PORTUGALIAE PHYSICA

PORTUGALIAE
PHYSICA

/17

BACK ANGLE ANOMALOUS SCATTERING IN AN ODD MASS SYSTEM : ^{19}F + ^{12}C

C. F. MAGUIRE and J. H. HAMILTON

Vanderbilt University, Physics Department, Nashville, TN 37235, USA

One of the most striking discoveries in heavy-ion induced reactions was the observation by Braun-Munzinger et al. [1] of anomalously large yields at backward angles in heavy-ion elastic and inelastic scattering. As first seen in the ^{28}Si + ^{16}O system (see Fig. 1), unexpected structure and enhancement occur in the backward hemisphere differential cross sections. Whereas the forward angle cross sections can be well fitted by a standard strong absorption optical potential [2], fitting the back angle yields requires new physics input such as the addition of a Regge pole [3-4]. Without such a refinement, the predicted back angle cross sections would be several orders of magnitude below that which is observed. An even more telling discovery, by Barrette et al [5] and by Clover et al. [6], was the association of the enhanced back angle yields with structures in the near 180° excitation functions ^{28}Si + ^{16}O and ^{28}Si + ^{12}C (Figs. 2 and 3). One observes in these excitation functions correlated, broad (1-2 MeV) gross structures, too wide to be compound elastic in origin and too narrow to come from conventional direct reaction processes. The importance of this discovery is that while simply weakening the absorption of the optical potential (surface transparency) is sufficient to enhance the predicted back angle cross sections, such optical potentials cannot reproduce the observed structures in the excitation function data.

Correlated excitation function structures ("resonances") have also been observed by Ford et al. [7] in ^{20}Ne + ^{12}C and ^{24}Mg + ^{12}C.

The phenomenon was seen to disappear almost entirely or at least to become substantially diminished when a non-α-conjugate nucleus was introduced: e. g. $^{28}Si + ^{9}Be$ or ^{13}C (Fig. 4, Refs. 8, 9), $^{28}Si + ^{18}O$ (Ref. 10), $^{27}Al + ^{12}C$ (Ref. 11), $^{29, 30}Si + ^{16}O$ (Ref. 12), and $^{32}S + ^{13}C$ (Ref. 9). Even for such α-conjugate systems such as $^{32}S + ^{12}C$
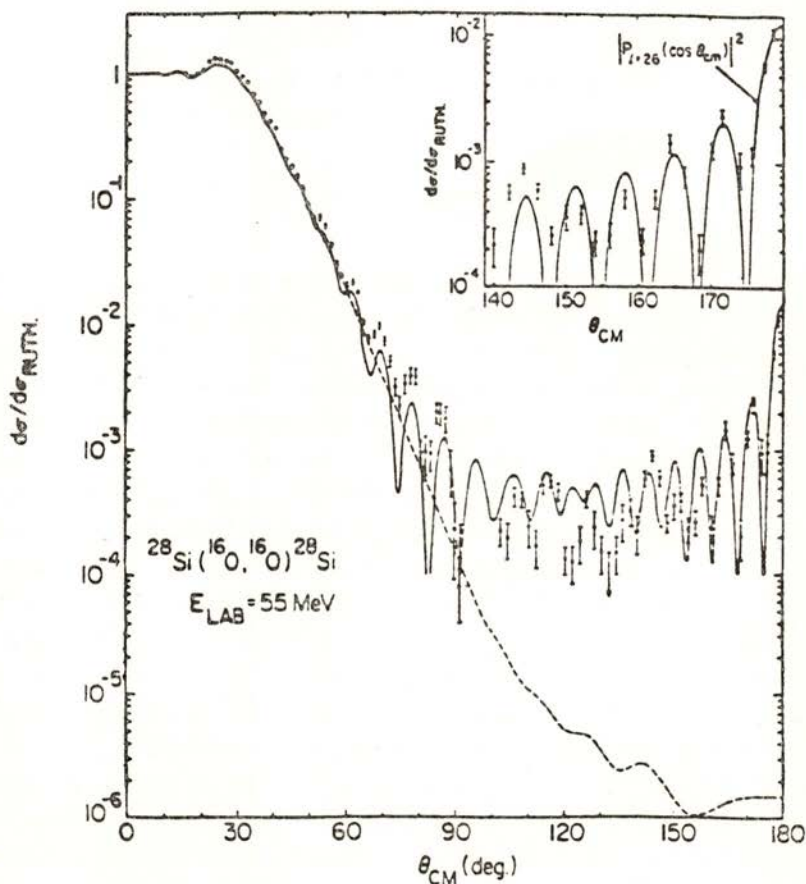
Fig. 1 — Elastic angular distribution for $^{16}O + ^{28}Si$ at a lab energy of 55 MeV (Ref. 1). The dashed line represents the predictions of the strongly absorbing optical potential set E18 (Ref. 2) which fits the forward angle region but can not fit the interior and back angle regions. The solid line is the prediction of optical potential set E18 modified to include a Regge pole contribution to the scattering matrix elements. In the inset is shown an expanded view of the back angle data which can be fitted by a $P_{L,0}$ (cos Θ) function.

(Refs. 8, 9, 13), $^{40}Ca + ^{12}C$ (Refs. 8, 14), and $^{24}Mg + ^{12}C$ (Fig. 5), the gross structures in the excitation function data are not nearly as prominent as in $^{28}Si + ^{16}O$ or ^{12}C. A major question arising from these experiments is whether the back angle anomalies represent the existence of resonances in the composite systems such as the quasi-molecules postulated for $^{16}O + ^{16}O$ scattering, or do they represent unknown characteristics of the ion-ion potential.

In an effort to further the understanding of this phenomenon we at Vanderbit, in collaboration with members of Los Alamos and Brookhaven National Labs, have begun to study the $^{19}F + ^{12}C$ *odd* mass system. On the basis of the preceding discussion, one
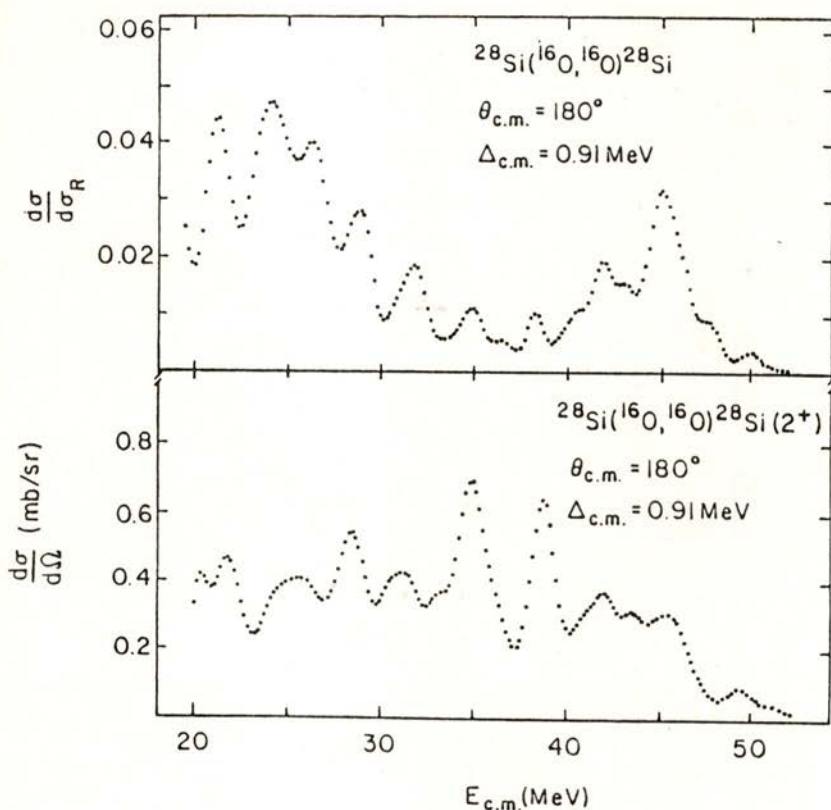
Fig. 2 — Elastic and inelastic excitation function data for the system $^{28}Si + ^{16}O$. The experimental data have been averaged over 0.91 MeV (c. m.) to emphasize the gross structures present in the data. (From Ref. 15).

Portgal. Phys. — Vol. 17, fasc. 1-2, pp. 1-19, 1986

3

might have anticipated that at best only weak anomalous structure would be present. The situation is further complicated because of the existence of two low-lying states in ^{19}F at 110 ($1/2^-$) and 197 ($5/2^+$) keV. In order to resolve this pair of states from the ground state and each other, it is necessary to use very thin
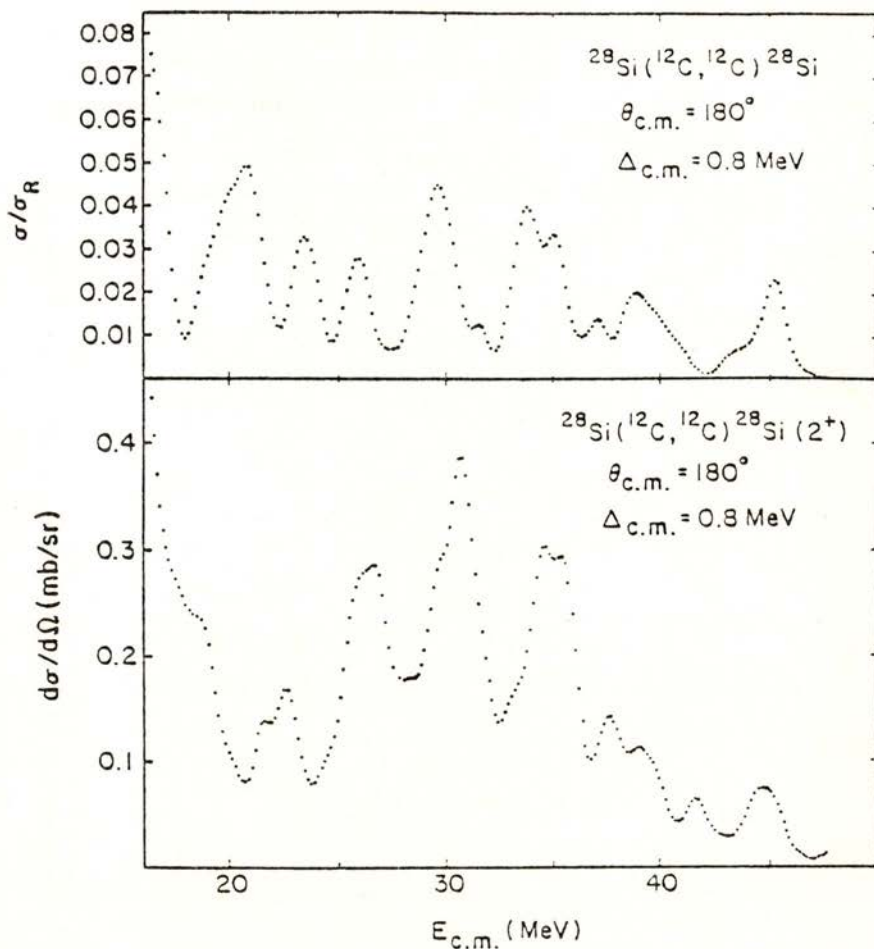
Fig. 3 — Elastic and inelastic excitation function data for the system $^{28}Si + ^{12}C$, where the actual experimental data are averaged over 0.80 MeV (c. m.) to emphasize the gross structure. Without this averaging procedure, fine structures of the order 100 keV would be visible. (From Ref. 15).

4
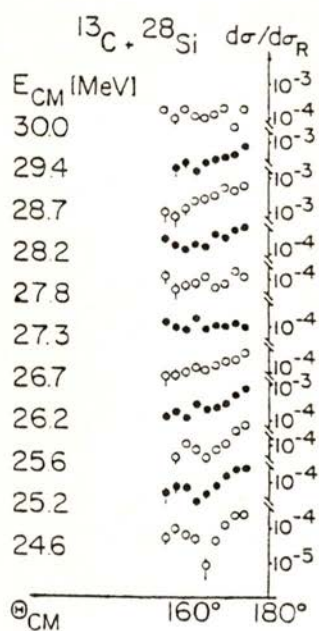
Fig. 4 — Elastic excitation function data for the system $^{28}Si + {}^{13}C$ taken at near 180° (Ref. 8). Note that compared to the $^{28}Si + {}^{12}C$ data in the previous figure, these cross sections are two orders of magnitude smaller. No structure is apparent in the excitation function nor is there pronounced oscilation in the angular distributions.
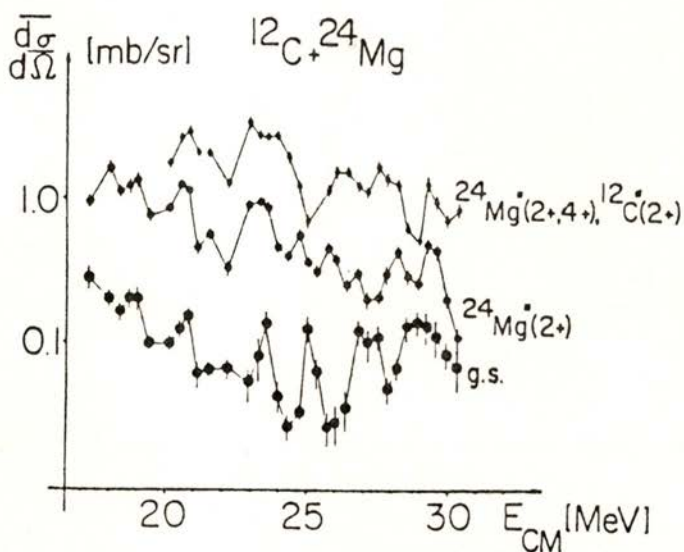
Fig. 5 — Elastic and inelastic excitation function data for the system $^{24}Mg + {}^{12}C$ taken near 180° (Ref. 7). The pattern here is more irregular than in $^{28}Si + {}^{16}O$ or ^{12}C.

Portgal. Phys. — Vol. 17, fasc. 1-2, pp. 1-19, 1986

5

(10 μg/cm²) targets. One cannot thus take advantage of the automatic energy averaging property of the thick (200 μg/cm²) targets normally used in this type of experiment. Furthermore,
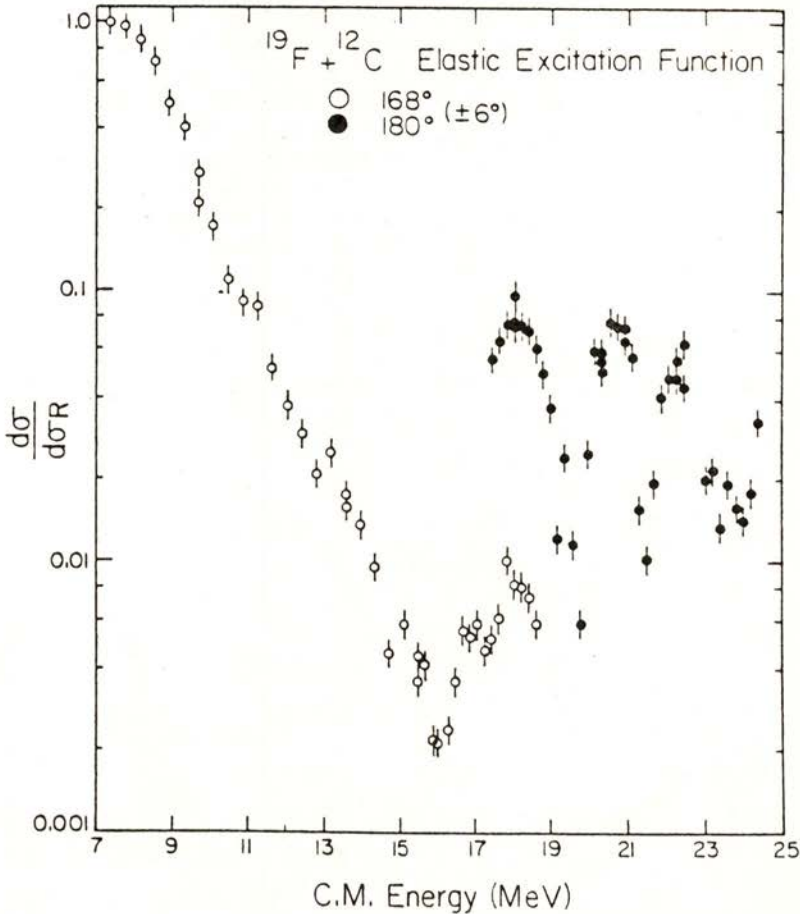
Fig. 6 — Elastic excitation function data for the system $^{19}F + {}^{12}C$ taken at 180 and at 168° c. m.

small energy steps must be taken in the excitation function in order to account for the possible presence of fine structure in the data. Rather startingly the data (Fig. 6) turned out to be com-

pletely different from what we expected. For this odd mass system the 180° gross structure excitation functions anomalies (elastic-to-Rutherford and peak-to-valley ratios) exceed even those of the prototype $^{28}Si + {}^{16}O$ or ^{12}C systems. Three very prominent structures are apparent in the elastic and inelastic excitation function where the elastic yield at 180° peaks between 6 and 8 % of the Rutherford scattering value and the excursion in the cross section from maximum to minimum is more than a factor of 20:1.

These excitation function data were measured at Brookhaven National Laboratory using a ^{19}F beam on a natural carbon target.
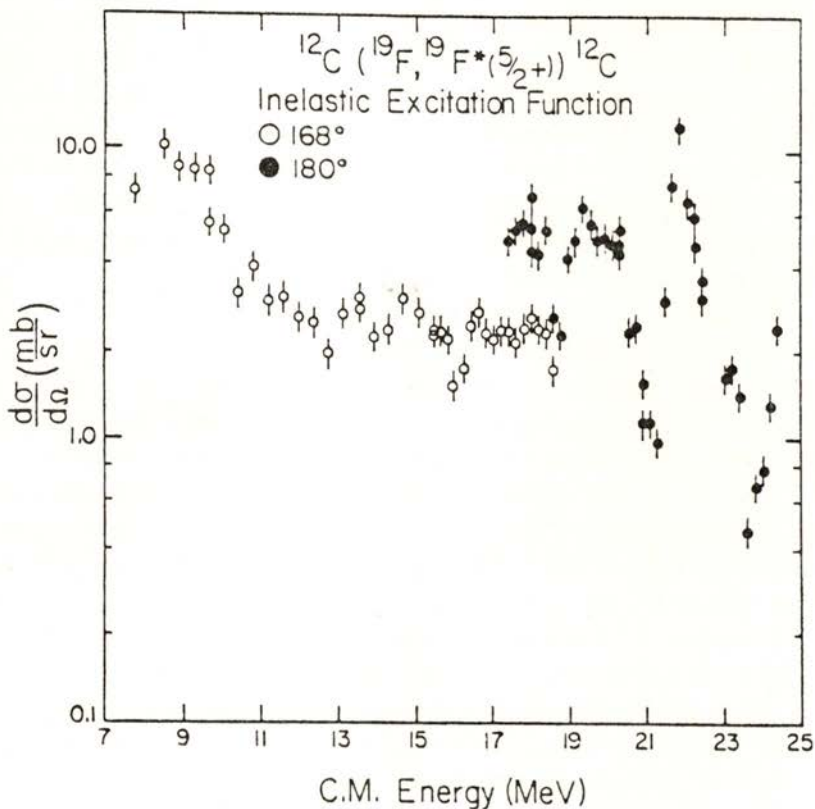
Fig. 7 — Inelastic excitation function data for the system $^{19}F + {}^{12}C$ populating the second excited state of ^{19}F.

Portgal. Phys. — Vol. 17, fasc. 1-2, pp. 1-19, 1986

7

The forward recoiling ^{12}C ions were momentum analyzed in the BNL QDDD magnetic spectrometer positioned at $0°$ ($\pm 3°$). A dual chamber gas detector system was used to identify the reaction products and it was found necessary to introduce nickel absorber foils (64 to 135 μ thickness) to prevent slit scattered primary beam from saturating the detector. Because of this degraded primary beam, no data could be taken below 45 MeV incident energy at $0°$. Excitation data were taken between 19 and 46.5 MeV incident energy at $6°$ lab (168° c. m.), where there was no slit scattering problem.

As can be seen in Fig. 6, for the system $^{19}F + {}^{12}C$ the gross structure in the elastic scattering is by far the dominant feature, almost completely overwhelming any trace of intermediate structure. Three very prominent structures are seen at center-of-mass energies of 18.0, 20.7, and 22.1 MeV, and there is the hint at the highest measured energy that a fourth structure will occur. In the 168° excitation function data, the 18.0 MeV structure is a factor of 10 below the 180° yield, indicating that the angular distribution at this energy must be backward rising. The 168° data also give some evidence of structures at lower energies, perhaps at 11.3, 13.0, and very slightly at 14.9 MeV.

No evidence was found for the excitation of the 110 keV state, as might be expected since this $1/2^-$ level must have a dominant p-shell hole admixture. However, the 197 keV $5/2^+$ state is strongly excited (Fig. 7) and its excitation function data display the same prominent gross structures as in the elastic channel.

Two points are especially striking with regard to these excitation function data. The first is the sheer prominence of the gross structures. The second is their existence in an *odd* mass system, given that a nearby α-conjugate system $^{24}Mg + {}^{12}C$ displays the phenomenon only relatively weakly. It has been thought that a necessary condition for the enhanced cross sections at back angles is a weak absorptive term in the optical potential. The absorption in odd mass systems should be greater than in the more strongly bound α-conjugate systems. In the face of such increased absorption, the diminution of the back angle anomalies in non-α-conjugate systems could be understood. The present data would appear to seriously undermine that argument.

8

Portgal. Phys. — Vol. 17, fasc. 1-2, pp. 1-19, 1986

A characteristic feature of the back angle anomaly is the highly oscillatory pattern of the near 180° differential cross section. In fact the shapes there can be fitted well by the square of a single Legendre polynomial $P_{L,0}^2(\cos\Theta)$, (see inset, Fig. 1). At first sight this might lend credence to the idea of isolated resonances as the interpretation for the phenomenon. For spin-zero on spin-zero scattering, the differential cross section is given by:

$$\frac{d\sigma}{d\Omega}(\Theta)_{el} = |f_C(\Theta) + (2ik)^{-1} \sum_L (2L+1) \exp(2i\sigma_L)$$
$$(S_L - 1) P_{L,0}(\cos\Theta)|^2 \qquad (1)$$

where $f_C(\Theta)$ and σ_L are the Coulomb scattering amplitude and phase, respectively, and S_L is the scattering matrix element for partial wave L. Since at 180° the Legendre polynomials vary as $(-1)^L$, there will tend to be a high degree of cancellation when the S_L vary smoothly in magnitude and phase, as usually is the case in heavy-ion elastic scattering. On the other hand, should one of the S_L become predominant, then the cross section at back angles will be very much a $P_{L,0}^2(\cos\Theta)$ function. In the case of $^{28}Si + {}^{16}O$ an L sequence of 9, 16, 16, 22, and 24 was extracted [15] from angular distributions taken at the maxima of the gross structures shown in Fig. 2. Although it turns out that these L values follow closely the grazing partial wave values, their irregular sequence is difficult to understand in terms of a band of resonant states. More seriously, Braun-Munzinger et al. [15] have shown that midway between two of these structures, the measured angular distribution cannot be described in terms of the interference of the two adjacent "resonant" structures. For $^{28}Si + {}^{12}C$ and for $^{32}S + {}^{12}C$, the L sequence was also determined to be irregular, and from 1 to 5 units *below* the grazing partial wave value. Most erratic of all is the behavior of the $^{20}Ne + {}^{12}C$ system for which the L sequence is 15, 14, and 19 in an energy region where the $l_{gr} = 20$-21. It should be noted that $^{20}Ne + {}^{12}C$ is the α-conjugate neighbor of the $^{19}F + {}^{12}C$ system presently under study.

Subsequent to the excitation function data analysis, we conducted an angular distribution experiment for $^{19}F + {}^{12}C$ at Los

Portgal. Phys. — Vol. 17, fasc. 1-2, pp. 1-19, 1986

9

Alamos National Laboratory. Angular distribution data were measured between 130 and 170° c. m. at the maxima of the three gross structures seen in the elastic excitation function data at 180°. A fourth angular distribution was measured at an intermediate energy, "off-resonance", of 21.3 MeV. These data for the ground and second excited state of ^{19}F are illustrated in Figs. 8 and 9.
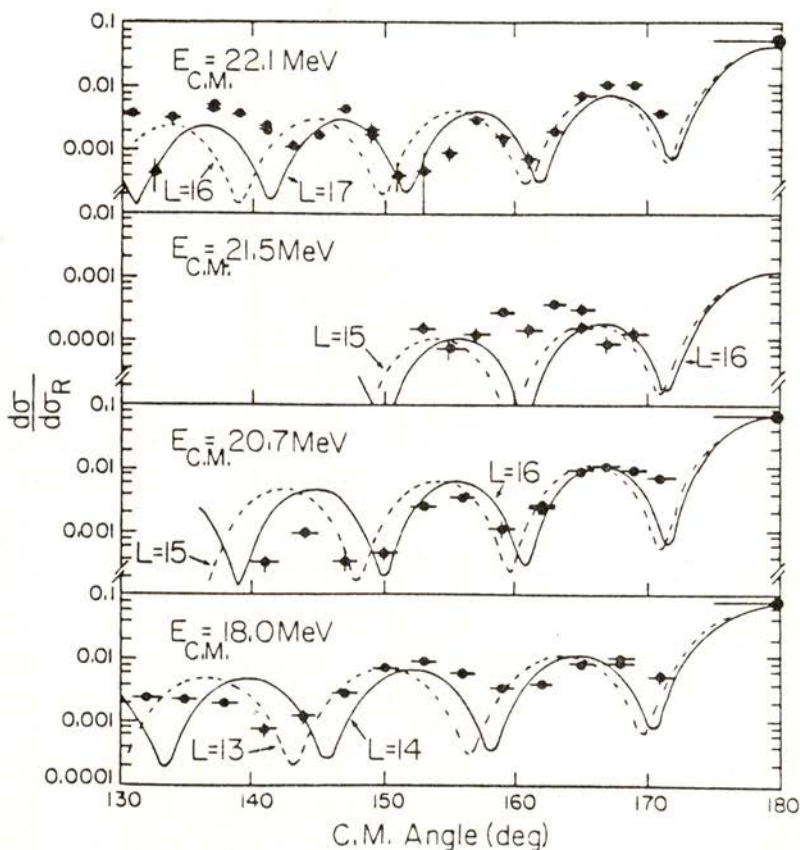
Fig. 8 — Elastic angular distribution data for the system $^{19}F + {}^{12}C$ measured at the maxima of the gross structures seen in the 180° excitation function. The lines drawn through the data point represent $P^2_{L,0}(\cos \Theta)$ fits to the oscillatory pattern. The 21.5 MeV data set correspond to a minimum in the excitation function data and no backward rising of the cross section is apparent.

10

Portgal. Phys. — Vol. 17, fasc. 1-2, pp. 1-19, 1986

At the three "resonance" energies both groups are seen to display oscillatory, backward rising angular distributions whose frequency increases with increasing beam energy. At the intermediate energy point, no oscillation is apparent.

Because of the spin 1/2 nature of ^{19}F, the formula for the
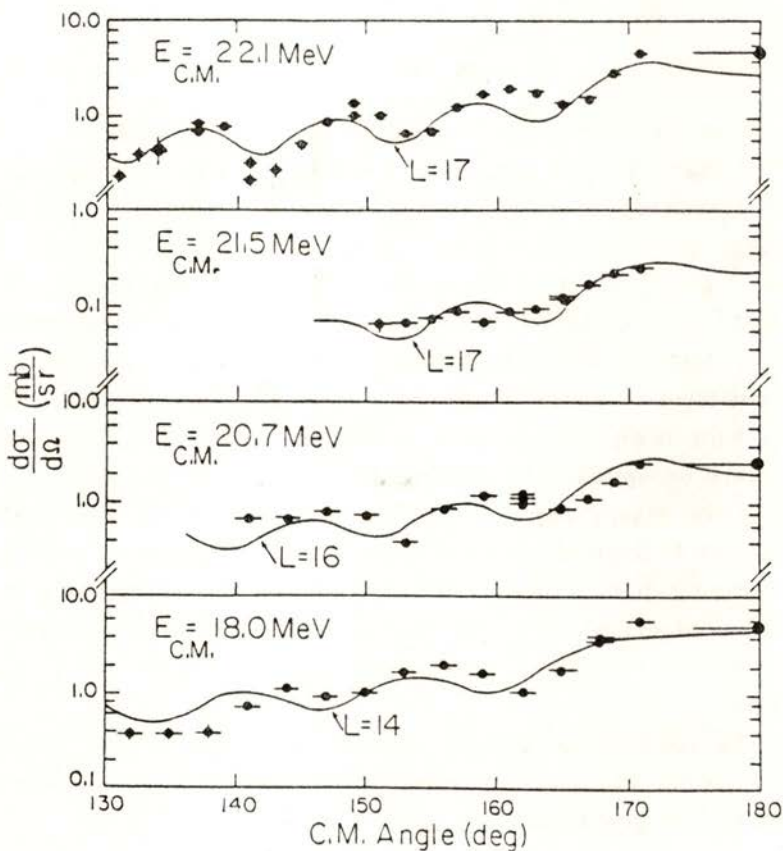
Fig. 9 — Inelastic angular distribution data for the system $^{19}F + ^{12}C$ exciting the second excited state of ^{19}F at 0.197 MeV (5/2+). The lines through the data represent an incoherent sum of associated Legendre polynominals having the same L values as in the elastic angular distribution fits. The exception is the "off-resonance" energy set (21.5 MeV) for which an L value of 17 is represented.

Portgal. Phys. — Vol. 17, fasc. 1-2, pp. 1-19, 1986

11

elastic differential cross sections is slightly more complicated than for spin-zero on spin-zero scattering:

$$\frac{d\sigma}{d\Omega}(\Theta)_{el} = \sum_{m_a, m'_a} |f_C(\Theta)\, \delta_{m_a, m'_a} + (2ik)^{-1} \sum_{J,L} < L\, 1/2\, 0 m_a | Jm_a >$$

$$< L\, 1/2\, (m_a - m'_a)\, m'_a | Jm_a > \sqrt{(L - M')!\,/\,(L + M')!}$$

$$(2L+1)\, e^{2i\sigma_L}\, (S^J_L - 1)\, P_{L,M'}(\cos\Theta)\, |^2 \qquad (2)$$

$$M' = |m_a - m'_a| = 0 \text{ or } 1$$

Now there is a sum over the total channel spin J and the partial wave L, and associated Legendre polynomials appear as well. However, for a given channel spin and parity, $J\pi$, there is a unique partial wave L which contributes. (This is not true for spins higher than 1/2). In terms of the resonance model, then, it is still correct to interpret the back angle angular distributions with a single L value. More restrictively, if the S matrix elements are assumed to be generated by a *central* ion-ion potential, then the J sum in Eq. (2) collapses to just an L sum, as in Eq. (1) for spin-zero on spin-zero scattering. In this manner we obtained the fits to the elastic angular distributions as shown in Fig. 8. The extracted L sequence here is quite regular and tracks well with the grazing partial wave value. Again, given the highly erratic behavior of neighboring system $^{20}Ne + ^{12}C$, this regular sequence in the $^{19}F + ^{12}C$ differential cross sections comes as a great surprise.

The oscillatory inelastic angular distributions can also be fitted within the single L model. The formula for the inelastic excitation is given by:

$$\frac{d\sigma}{d\Omega}(\Theta)_{inel} = \sum_{m_a, m'_a} |(2ik)^{-1} \sum_{J,L,L'} < L\, 1/2\, 0 m_a | Jm_a >$$

$$< L'\, 5/2\, (m_a - m'_a)\, m'_a | Jm_a > \sqrt{(2L+1)(2L'+1)}$$

$$e^{i(\sigma_L + \sigma_{L'})} \sqrt{(L - M')!\,/\,(L + M')!}\; S^J_{L,L'}\, P_{L', M'}(\cos\Theta)\, |^2$$

$$M' = |m_a - m'_a| = 0, 1, 2, 3 \qquad (3)$$

12

Portgal. Phys. — Vol. 17, fasc. 1-2, pp. 1-19, 1986

As in the elastic case, only one entrance channel partial wave L contributes for a given channel spin and parity J_π. However, three outgoing partial waves $L' = L - 2, L, L + 2$, can be coupled coherently to produce the differential cross section. If a single L is considered to be dominant in Eq. (3) at back angles, then the allowed Legendre polynomials are in phase and this can lead to a backward rising shape. Indeed, taking only the diagonal $L' = L$ term in Eq. (3) and making an *ad hoc* superposition of $P_{L,M}^2 (\cos \Theta)$ functions ($M = 0, 1, 2$), we obtain the fits to the inelastic angular distributions shown in Fig. 9. In these fits the $M = 2$ contribution is the most important, the $M = 1$ fills in the oscillations, and the $M = 0$ contribution yields the finite cross section at 180°. (The possible $M = 3$ contribution is ignored as it would not occur in spin-zero on spin-zero scattering). Hence, the fits depicted in Figs. 8 and 9 show that both the elastic and inelastic data are compatible with the interpretation of the same dominant L value. Of course this evidence is not conclusive and there is no prescription yet available for generating the observed sequence of L values.

The discussion so far has concentrated on the single L interpretation of the back angle phenomenon. An alternate explanation, proposed by Dehnhard et al. [16], is that there is a parity dependent component in the ion-ion potential. That is, to a standard optical potential $U(r)$ is added an L dependent term of the form $(-1)^L PU(r)$. The parity coefficient P is of the order 0.01. This approach is amazingly successful in describing the $^{28}Si + ^{16}O$ elastic excitation function data, as shown in Fig. 10. The back angle elastic and inelastic angular distributions are also fitted reasonably well [15, 16]. The theoretical justification for this parity dependence is the possible core exchange of a ^{12}C nucleus between the projectile ^{28}Si and the target ^{16}O. Such an exchange would lead to a Majorana component in the interaction potential. The inclusion of parity dependence in the optical potential upsets the delicate cancellation of the $P_{L,0} \cos(\Theta)$ in the summation of Eq. (1), leading instead to a coherent enhancement of all L contributions at the back angles. Although this approach is very successful, there is a serious question about the probability of the elastic transfer of a ^{12}C nucleus. The spectroscopic factor must be vanishingly small and it seems unlikely an effective parity

dependence would be present. Nonetheless, this idea has been also used in explaining the $^{32}S + ^{12}C$ back angle excitation function with a fair degree of success. As in the case of $^{28}Si + ^{16}O$, a positive parity coefficient P was found, meaning that the potential is more attractive for even than for the odd partial waves. Kubono [17] has also studied the question of parity dependence by comparing the 90° and the 180° $^{28}Si + ^{16}O$ excitation functions. Contradicting the other two studies, Kubono concluded that the parity coefficient should be negative, more attractive for odd rather than even partial waves.
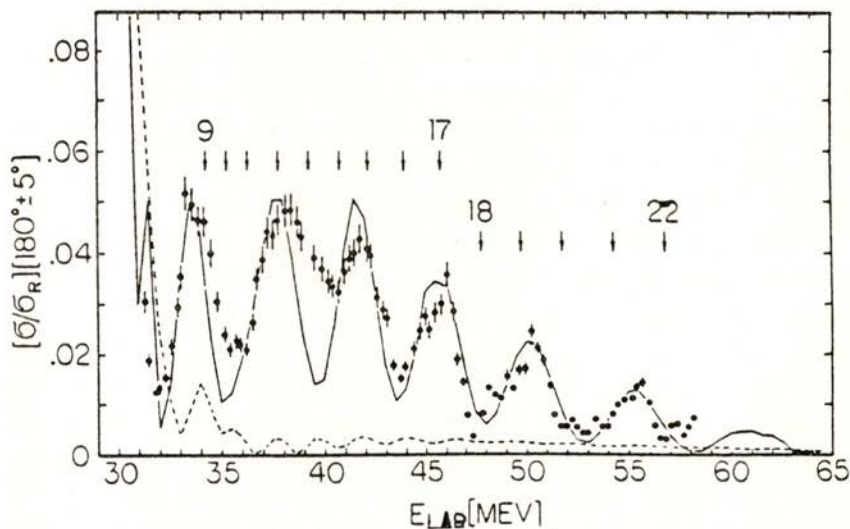
Fig. 10 — The $^{28}Si + ^{16}O$ elastic excitation function data at 180°. The solid curve through the data points represents the predictions of the parity dependent optical potential parameter set developed by Dehnhard et al. (Ref. 16). The broken curve represents the predictions of the same optical parameter set with the parity coefficient set to zero. The arrows in the figure represent the positions of the n = 0 shape resonances of the optical potential for which some of the L values are explicitly written.

We have investigated the question of parity dependence in the $^{19}F + ^{12}C$ system with mixed success. The result depends critically on the base optical potential U (r) which is used. Our

first attempt used the parameters of Voos et al. [18] ($V = 100$ MeV, $r_R = 1.19$ fm, $a_R = 0.48$ fm, $W = 23$ MeV, $r_I = 1.26$ fm, and $a_I = 0.26$ fm) which fits the forward angle elastic scattering of $^{19}F + ^{12}C$ in the incident energy regime under study here. This potential is rather strongly absorbing and a large parity coefficient ($P = 0.4$) was found to be necessary to enhance the back ángle yield to the level observed at 180° (8 % of Rutherford). It then turns out that no structure is produced in the excitation function with this choice of parity dependence. As a function of energy, the predicted back angle yield simply rises monotonically. Our next choice of optical potential was the parameter set used by Dehnhard to fit the $^{28}Si + ^{16}O$, for which the real and imaginary depths are a factor of 6 below those of the Voos set. With this new parameter set for $U(r)$, the parity dependence was much more successful in reproducing the $^{19}F + ^{12}C$ elastic excitation function data, as can be seen in Fig. 11. We find here also that a positive parity coefficient is necessary, although the coefficient is in this case a factor of 5 reduced from the $^{28}Si + ^{16}O$ analysis. If the opposite sign of the parity coefficient is used, the predicted structures become out-of-phase with those shown in Fig. 11. In the present case the parity dependence might arise because of the exchange of a ^{7}Li core between the ^{19}F and the ^{12}C. While the spectroscopic factor for this exchange might be higher than for ^{12}C in the $^{28}Si + ^{16}O$ experiment, the expected low probability for the process remains a troubling question.

Fortunately, an effective parity dependence in the S matrix elements can be obtained without introducing explicitly a parity dependent component in the optical potential. This approach was first developed by Lee [19] and extended by Braun-Munzinger et al. [15] for the $^{28}Si + ^{16}O$ data. The basic idea is that there can exist a pocket, of depth and width depending upon the partial wave number L, in the real potential. Incoming partial waves will be reflected at the exterior and interior boundaries of the pocket. Provided that the absorption inside the pocket is not too great, the wave reflected from the interior boundary of the pocket can interfere significantly with the wave reflected from the exterior boundary. With the use of the semi-classical approximation, the S matrix elements are parameterized in this model and a rather good

Portgal. Phys. — Vol. 17, fasc. 1-2, pp. 1-19, 1986

15

fit to the excitation function data in $^{28}Si + ^{16}O$ can be generated. A qualitative prediction of the model is that since the pocket in the optical potential tends to disappear at higher energies, the
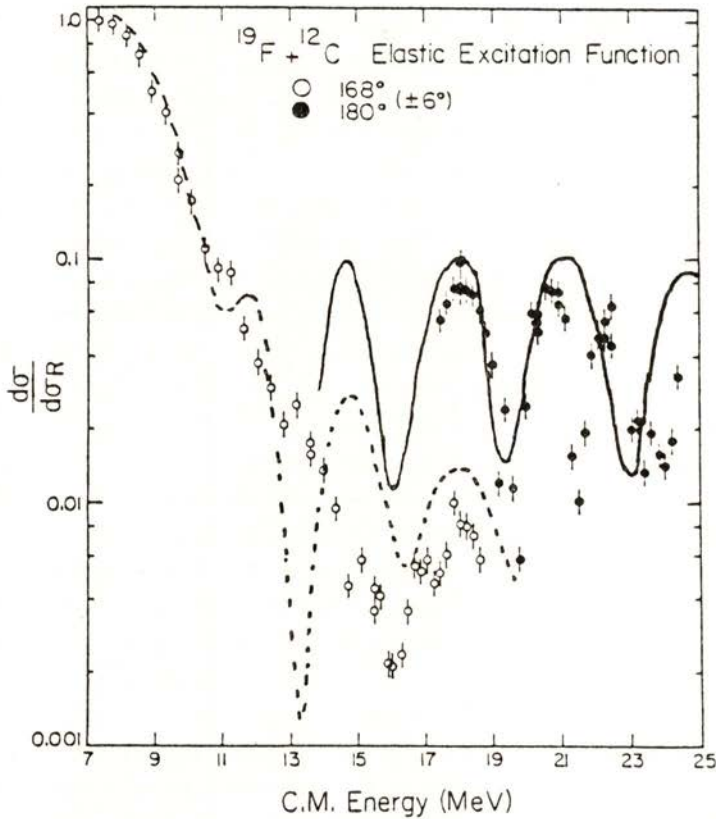
Fig. 11 — Elastic excitation function data for $^{19}F + ^{12}C$ fitted with the parity dependent optical potential parameter set developed by Dehnhard et al. [16]. Wile the qualitative agreement with the data is good, it should be noted that the minimum in the 168° data set near 16 MeV c. m. is predicted too early by this potential set.

back angle phenomenon should diminish also with increasing incident energy. A drawback of the model, however, is that there is no explicit parameterization of the underlying optical potential.

16

The back angle anomaly is most obvious in the elastic and inelastic channels. Attempts to correlate these structures with other reaction channels have not been particularly fruitful. The best investigated cas has been the α-particle transfer reaction channel, ^{24}Mg (^{16}O, ^{12}C) ^{28}Si, measured at both forward [20] and backward angles [21]. This reaction channel does show excitation function structures, but there is no clear correlation between those structures and the ones seen in the entrance or exit channel elastic scattering. Recently, Lichtenthaler et al. [22] have performed a two-step α-transfer reaction ($^{12}C + {}^{24}Mg \rightarrow {}^{16}O + {}^{20}Ne \rightarrow {}^{12}C + {}^{24}Mg$) which would coherently interfere with the elastic channel. This calculation indicated that this interference could account for the intermediate angle oscillations seen in the elastic differential cross section. It was speculated by these authors that the successive transfer of three α-particles could explain the back angle rise in the elastic cross section. Although the idea of α-transfer is of course attractive for the α-conjugate systems, it would not seem to be applicable to the $^{19}F + {}^{12}C$ elastic scattering. In fact this transfer reaction has been measured at 40, 60, and 68 MeV (Ref. 23) and the cross sections have been found to be rather small compared to the α-transfer cross sections between α-conjugate nuclei. On the other hand, the *triton* transfer reaction ^{12}C (^{19}F, ^{16}O) ^{15}N is a very strong channel (tens of millibarns) (Ref. 23). This channel could conceivably be interfering with the elastic channel to produce the structures observed in the $^{19}F + {}^{12}C$ excitation function.

Another avenue of exploration for the understanding of these structures is the light particle emission yields. So far this has not been done for the systems considered so far, but it has been measured in the case of $^{9}Be + {}^{12}C$. The back angle elastic yield in this system also exhibits structures [24] which may be related to the elastic transfer of a ^{3}He. In addition, the α-emission channel has also been observed. There are clear structures in this emission channel, structures which seem to be correlated with those seen in the elastic channel.

The back angle enhancement anomaly in heavy-ion elastic scattering presents a fascinating puzzle for the understanding of heavy-ion interactions. The phenomenon, already known to be

Portgal. Phys. — Vol. 17, fasc. 1-2, pp. 1-19, 1986

17

widespread for α-conjugate nuclei is now revealed to occur most prominently in an odd mass system. The present data thus provide a new challenge and new constraints on models proposed to interpret the data.

REFERENCES

[1] P. BRAUN-MUNZINGER, G. M. BERKOWITZ, T. M. CORMIER, C. M. JACHINSKI, J. W. HARRIS, J. BARRETTE, and M. J. LEVINE, *Phys. Rev. Lett.*, 38, 944 (1977).

[2] J. G. CRAMER, R. M. DEVRIES, D. A. GOLDBERG, M. S. ZISMAN and C. F. MAGUIRE, *Phys. Rev.*, C14, 2158 (1976).

[3] K. McVOY, *Phys. Rev.* C3, 1104 (1971).

[4] K. McVOY, in *Proc. of the Symposium on Heavy-Ion Elastic Scattering*, ed. R. M. DEVRIES (Univ. of Rochester, 1977), p. 430.

[5] J. BARRETE, M. J. LEVINE, P. BRAUN-MUNZINGER, G. M. BERKOWITZ, J. GAI, J. W. HARRIS and C. M. JACHINSKI, *Phys. Rev. Lett.*, 40, 445 (1978).

[6] M. R. CLOVER, R. M. DEVRIES, R. OST, N. J. A. RUST, R. N. CHERRY, JR. and H. E. GOVE, *Phys. Rev. Lett.*, 40, 1008 (1978).

[7] J. L. C. FORD, JR., J. GOMEZ DEL CAMPO, D. SHAPIRA, M. R. CLOVER, R. M. DEVRIES, B. R. FULTON, R. OST and C. F. MAGUIRE, *Phys. Lett.* 89, 48 (1979).

[8] R. OST, M. R. CLOVER, R. M. DEVRIES, B. R. FULTON, H. E. GOVE and N. J. RUST, *Phys. Rev.* C19, 740 (1979).

[9] Y-d. CHAN, R. J. PUIGH, W. L. LYNCH, M. Y. TSANG and J. G. CRAMER, *Phys. Rev.*, C25, 850 (1982).

[10] P. BRAUN-MUNZINGER and J. BARRETTE in *Proc. of the Symposium on Heavy-Ion Elastic Scattering*, (Univ. of Rochester, 1977), p. 45.

[11] A. ROY, A. D. FRAWLEY and K. W. KEMPER, *Phys, Rev.*, C20, 2143 (1979).

[12] P. BRAUN-MUNZINGER et al., *Bull. Am. Phys. Soc.*, 24, 571 (1979).

[13] C. K. GELBKE, T. C. AWES, U. E. P. BERG, J. BARRETTE, M. J. LEVINE and P. BRAUN-MUNZINGER, *Phys. Rev. Lett.*, 41, 1778 (1978).

[14] S. KUBONO, P. D. BOND and C. E. THORN, *Phys. Lett.*, 81B, 140 (1979).

[15] P. BRAUN-MUNZINGER, G. M. BERKOWITZ, M. GAI, C. M. JACHINSKI, T. R. RENNER, C. D. UHLHORN, J. BARRETTE and M. J. LEVINE, *Phys. Rev.*, C24, 1010 (1981).

[16] D. DEHNHARD, V. SHKOLNIK and M. A. FRANEY, *Phys. Rev. Lett.*, 40, 1549 (1978).

[17] S. KUBONO, P. D. BOND, D. HORN and C. E. THORN, *Phys. Lett.*, **84B**, 408 (1978).

[18] U. C. VOOS, W. VON OERTZEN and R. BOCH, *Nucl. Phys.*, **A135**, 571 (1969).

[19] S. Y. LEE, *Nucl. Phys.*, **A311**, 311 (1978).

[20] M. PAUL, S. J. SANDERS, J. CSEH, P. F. GESSMAN, W. HENNING, D. G. KOVAR, C. OLMER and J. P. SCHIFFER, *Phys. Rev. Lett.*, **40**, 1310 (1978).

[21] S. M. LEE, J. C. ADLOFF, P. CHEVALIER, D. DISDIER, V. RAUCH and F. SCHEIBLING, *Phys. Rev. Lett.*, **32**, 429 (1979).

[22] R. LICHTENTHALER, A. LEPINE-SZILY, A. C. C. VILLARI, W. MITTIG, V. J. G. PORTO and C. V. ACQUADRO, *Phys. Rev.*, **C26**, 2487 (1982).

[23] U. C. SCHLOTTHAUER-VOOS, R. BOCK, H. G. BOHLEN, H. H. GUTBROD and W. VON OERTZEN, *Nucl. Phys.*, **A186**, 225 (1972).

[24] G. VOURVOPOULOS, preprint (1984).

STUDY OF THE SQS MODE BY THE INDUCED CHARGE METHOD

E. P. DE LIMA, R. FERREIRA MARQUES, J. M. GARABATOS [1],
A. J. P. L. POLICARPO and C. M. RUELA

Departamento de Física, Universidade de Coimbra, 3000 Coimbra, Portugal

ABSTRACT — Preliminary data using the cathode induced charge method to study the self-quenching streamer (SQS) mode are reported. Very strong and reliable anisotropy has been detected. Several characteristics of these streamers are considered from the point of view of the physics of long sparks.

1 – INTRODUCTION

Detectors based on the self-quenching streamer (SQS) mode are now used in experiments in high energy physics. They are rugged, feature good position resolution along the wire and are associated to inexpensive electronics. At the moment, roughly as much effort is being put on the understanding of the process and on the measurement of some relevant intrinsic properties, as in its applications to detectors. This research goes on since the last few years.

During the last decades the engineering research on the U.H.V. transmission line insulation was actively pursued. In recent years it developed more and more towards the physics of long sparks, trying to reach a detailed knowledge of the mechanisms involved (space charge distribution, electron energy, gas temperature and density, etc.).

No doubt, the fundamental physics processes associated to the SQS mode and to the long spark formation are the same. However, the techniques used to initiate the discharge processes are different and the physical dimensions of the streamer may

---

[1] On leave from Universidade de Santiago, Spain.

vary by several orders of magnitude, between the conventional SQS detector and the point-to-plane arrangements, convenient to study the non uniform field geometries. In the SQS mode a steady high voltage (and this is an important feature for a detector) is applied to the anode wire and the streamer is triggered by an ionizing particle; in studies of the mechanism of long spark formation, in a non uniform long gap, a short high voltage pulse is applied to trigger the process. For a detailed review of the mechanisms of long spark formation see for example ref. [1].

The method of induced charges in a convenient set of electrodes is a powerful technique to study charge distributions. Spatial resolutions of about 5 microns have been achieved [2, 3], this accuracy being essentially limited by the number of bits of the digital charge measuring devices. The proportional counter mode has been studied using this techniques, the time evolution of the process was considered [4], and the so called left-right ambiguity in drift chambers is now currently solved by looking for induced charge asymmetries.

In this work we report preliminary results using the induced charge method applied to the study of the SQS mode. One can reasonably expect that work under these lines may be relevant to the fields of physics referred to above.

2 – EXPERIMENTAL SET-UP

For this study an adequate detector was built. It is a single wire chamber, the cathode of which consists of eight copper strips (copper clad epoxy board), about 8 mm wide and 144 mm long, spaced by about 1.5 mm. These strips were mounted parallel to the anode (nichrome wire, 60 micron diameter) in an octogonal arrangement with the anode located in the center. A cross section of the chamber is sketched in Fig. 1. This system of electrodes was inserted in a stainless steel cylinder and the anode wire was fixed to epoxy insulators.

The signal from each strip passes through a current sensitive output buffer ($Z_{in} = 50\,\Omega$, gain = 10, $Z_{out} = 50\,\Omega$), is delayed and fed to one channel of a current integrating CAMAC ADC (LRS 2249 W), gated during 150 ns by a discriminator triggered on the anode signal. This gating time is sligthly larger than the current pulse duration, as observed in a fast oscilloscope.

Each channel (both the current sensitive output buffer and the following ADC) was calibrated individually by electronic means and software corrections for linearity and bias were further checked by sending a fast pulse to the chamber's anode
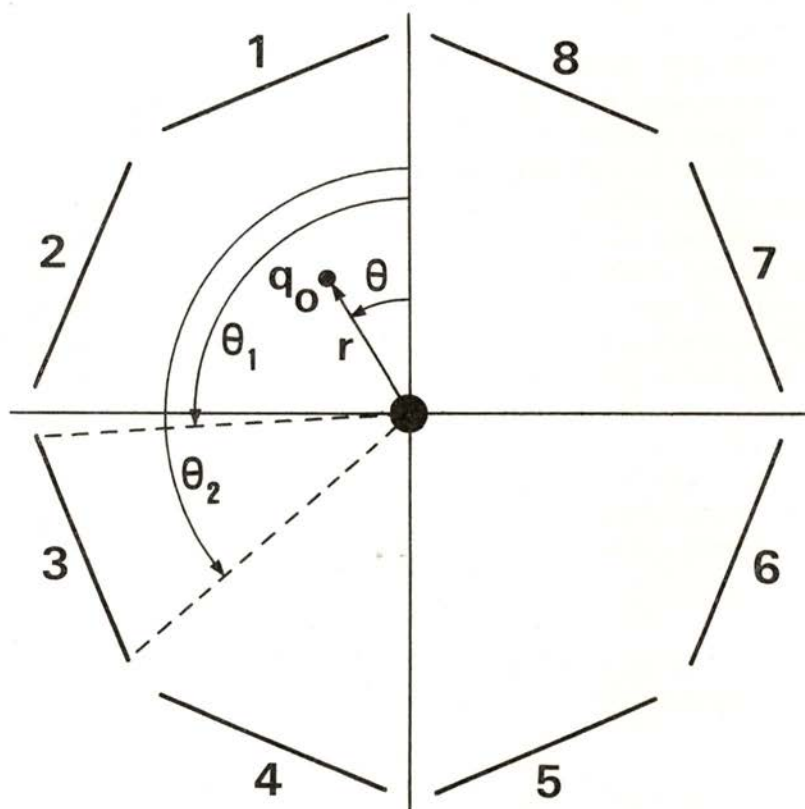
Fig. 1 — Schematic cross section of the detector, showing the coordinate system used in the theoretical calculations.

and looking to the capacitive coupled signals on the cathode strips. This technique should also provide information on the accuracy of the mechanical arrangement of the set of electrodes. Every observed event corresponds then to a set of eight numbers that are read-out to a microcomputer interfaced to the system.

Experimental data were recorded for a typical SQS mixture, 52 % argon + 48 % isobutane, at atmospheric pressure in a

constant flow regimen, at four different anode voltages (3500, 3700, 3900 and 4100 volts) using a ^{55}Fe X-ray source.

3 – THEORETICAL MODEL

Through optical measurements [5, 6] it is already known that, in the SQS discharge mode, the avalanche extends up to approximately 2-3 mm from the anode surface, for geometries similar to ours. It is then a case completely different from the proportional counter mode, where the dimensions involved are of the order of tens of microns and the ion motion determines the pulse shape. In the SQS mode, and using usual fast electronics, the total induced charge is essentially due to the contribution of the electron motion that, in a short time of about 150 ns, leaves a cloud of positive ions practically at rest. In this work, as a first approximation, a point like ion space charge is assumed to be responsible for the distribution of the induced charges on the several electrodes.

In the ideal coaxial counter (the geometrical conditions of this work are shown in Fig. 1), for a point charge q_0, located at $(r, 0)$ between two cylinders of radii a and b $(a < b)$, the total charge induced on the outer cylinder (cathode) is

$$Q_b = -q_0 \ln(r/a) / \ln(b/a) \qquad (1)$$

The charge induced on that part of the cathode which is bounded by angles zero and Θ is given, exactly, by [7]:

$$S(\Theta) = Q_b \frac{\Theta}{2\pi} - \frac{q_0}{\pi} \sum_{n=1}^{\infty} \frac{1}{n} \left(\frac{r}{b}\right)^n \frac{1-(a/r)^{2n}}{1-(a/b)^{2n}} \sin n\Theta \qquad (2)$$

So, for a point charge at (r, Θ) the charge induced on a sector of the cathode bounded by angles Θ_2 and Θ_1 is $Q = S(\Theta_2 - \Theta) - S(\Theta_1 - \Theta)$.

Approximate expressions for the usual case $b \gg a$, with $\Theta = 0$, are also available [8]:

$$Q = -(q_0/2\pi) \left\{ -[1/\ln(b/a)](\Theta_2 - \Theta_1) \ln(b/r) + 2\beta \right\}$$

where $\tan \beta = \dfrac{[1-(r/b)^2][\tan(\Theta_2/2) - \tan(\Theta_1/2)]}{(1-r/b)^2 + (1+r/b)^2 \tan(\Theta_2/2) \tan(\Theta_1/2)}$

Two computed distributions for the charge induced on the eight cathode strips, using the expression (2) for $\theta = 0$, and corresponding to two different values of r, typical of the SQS mode, are shown in Fig. 2.
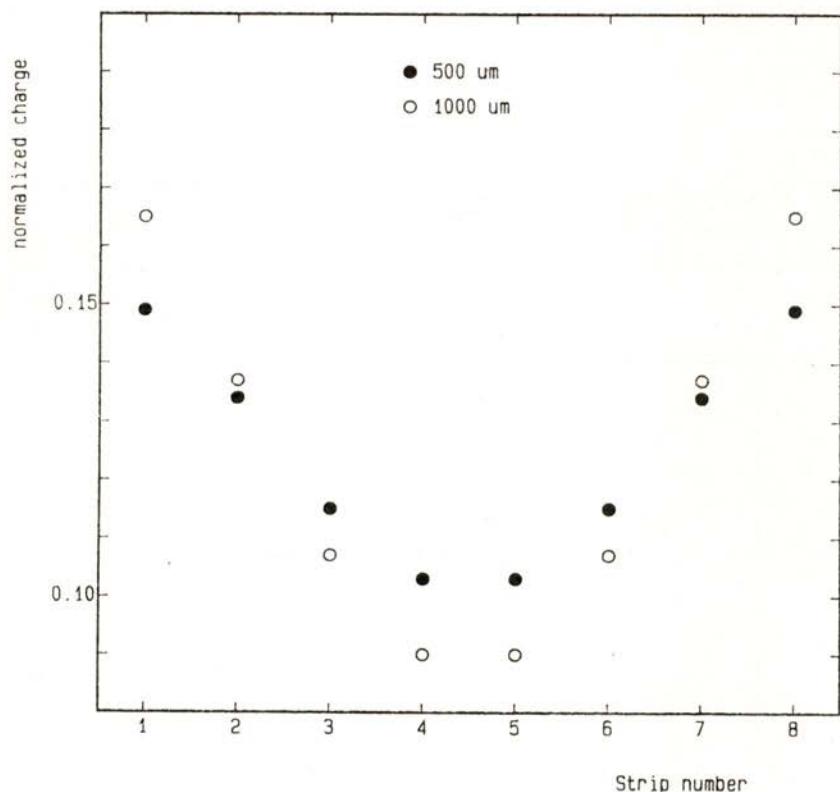
Fig. 2 — Calculated distribution of the charges induced on each cathode strip by a point charge located at $\theta = 0$, $r = 0.5$ mm (full circles) and $\theta = 0$, $r = 1$ mm (open circles).

To characterize the anisotropy of the distribution, two convenient parameters can be defined :

$$Y(r, \theta) = \ln [(q_1 + q_8) / (q_4 + q_5)]$$

$$X(r, \theta) = \ln [(q_7 + q_6) / (q_2 + q_3)] \tag{3}$$

q_i ' $i = 1, 2, ... 8$) being the charge induced in the ith cathode strip. Again for the ideal coaxial geometry, it can be shown that with errors less then 0.1 %

$$Y^2 (r, \Theta) + X^2 (r, \Theta) = R^2 (r) \tag{4}$$

and that the function $R(r)$ is, fortunately, an almost linear function of r.

4 — EXPERIMENTAL RESULTS

The pulse height spectrum obtained at 3900 V, using the total charge induced on the cathode strips ($Q_b = \Sigma \, q_i$), is displayed in Fig. 3. It corresponds essentially to a typical SQS
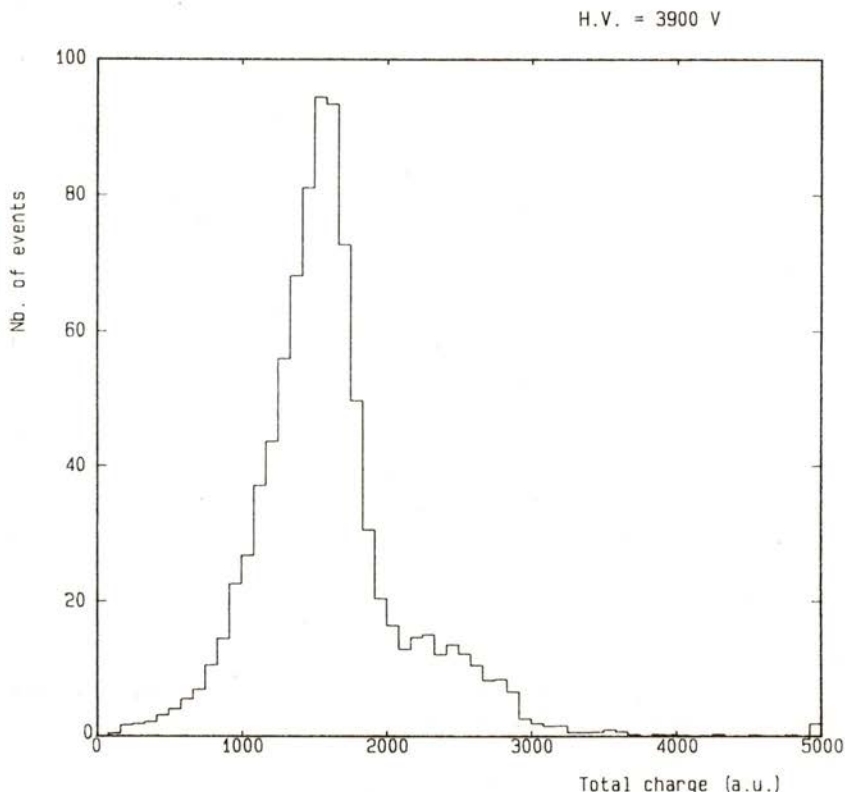
Fig. 3 — Pulse height spectrum, at 3900 V, of the total charge induced on the cathode strips.

distribution and the beginning of higher charge streamers can be observed. In these experimental conditions calculations with the observed data were accomplished, by substituting in eq. 3 the q_i by the corresponding ADC values suitably software corrected for linearity and bias.

H.V.= 3900 V
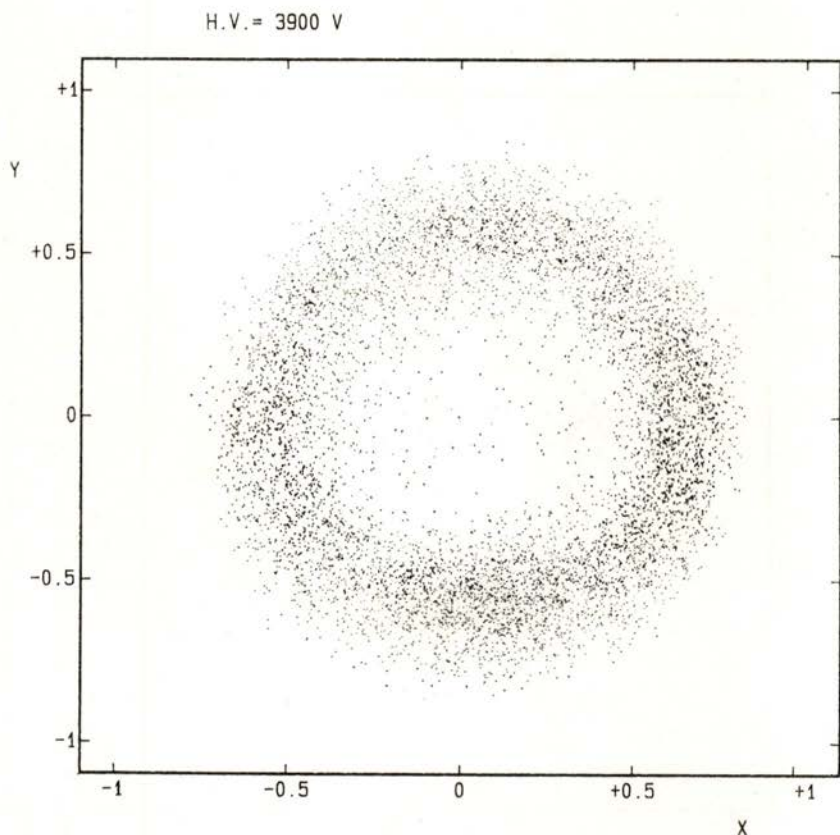
Fig. 4a) — Distribution of X, Y values defined by Eq. 3. Experimental data correspond to 10000 events taken at an anode voltage of 3900 volts.

Fig. 4a) is a typical plot of the resulting X, Y values for 10000 experimental events corresponding to all values of the charge distribution (see Fig. 3).

A more conventional way of defining a position would make use of the expressions $X' = \Sigma\, q_i\, x_i\, /\, \Sigma\, q_i$ and $Y' = \Sigma\, q_i\, y_i\, /\, \Sigma\, q_i$, where the x_i and y_i are the mean coordinates of the strip i.

A comparison of both techniques was made and Fig. 4b) shows the distribution obtained, for the same 10000 events, using the X′ and Y′ parameters. Since there was no obvious difference between the two distributions and in view of the properties of R(r), X and Y coordinates are used.

H.V.= 3900 V
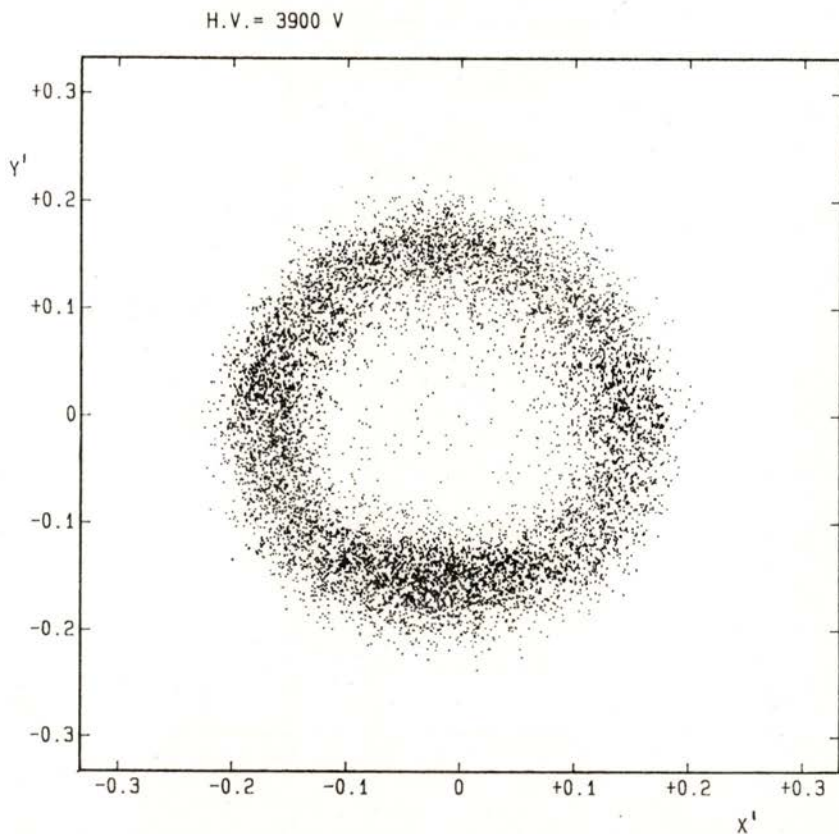
Fig. 4b) — Distribution obtained for the same events as in a), but making use of parameters X′ and Y′ (see text for their definition).

Using the relationship between r, the physical radius of the point like ion distribution, and R, referred to above, the data for all values of the total charge were analyzed in order to study the distribution of the mean radial position of the discharges. The

corresponding distribution (at 3900 V) is plotted in Fig. 5, where the events with positive and negative Y are separated. The two peaks have similar widths and mean values close to 1 mm.

H.V. = 3900 V
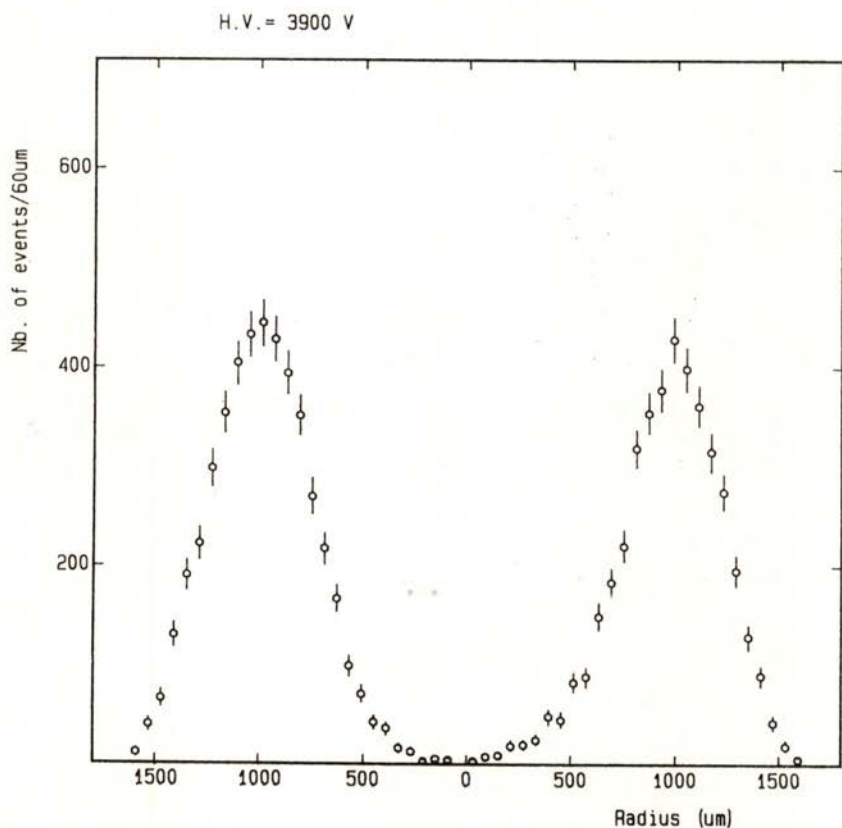
Fig. 5 — Distribution of the radial dimensions, r, of the discharge: right peak for streamers with Y > 0, left peak for the others.

Within the limitations of the model, knowledge of r and Q_b ($Q_b = \Sigma\, q_i$), allows the determination of q_0, in arbitrary units. The conversion into real charges simply requires a charge calibration.

The physical process of the SQS discharge strongly suggests a correlation between its radial extension and the total charge involved. Concerning this problems, two different situations should

be considered, namely when the applied field is constant and when it varies, as the quenching of the discharge is determined, among other parameters, by this one.

H.V. = 3900 V
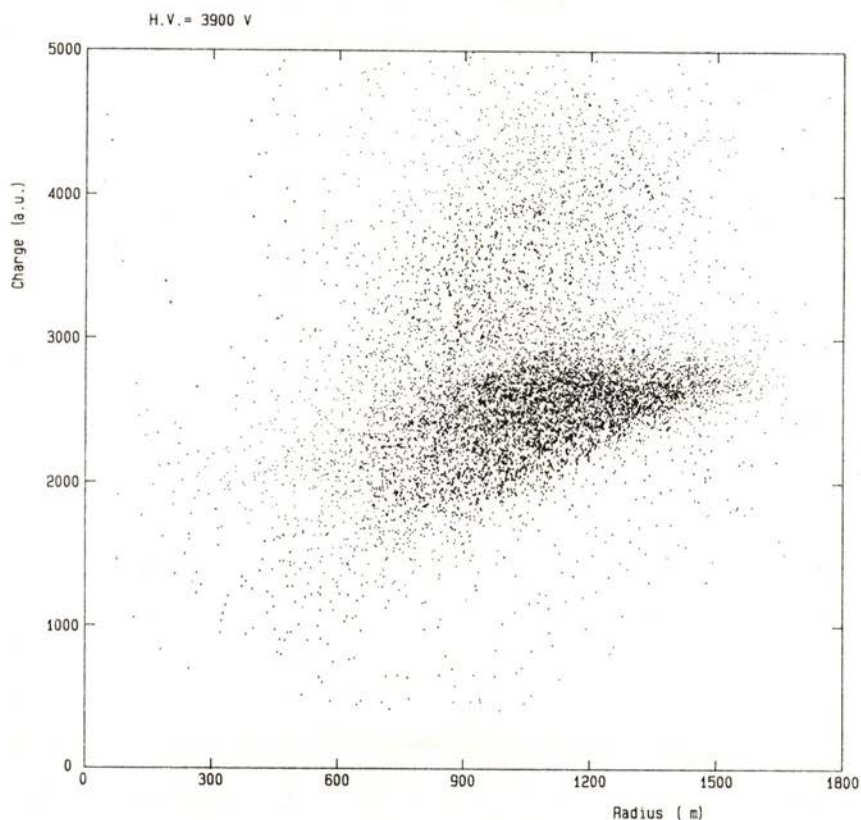
Fig. 6 — Correlation between the charge q_0 and its radial position r, for all values of the induced charges, for 3900 V anode voltage.

For the same high voltage used to obtain the data presented previously (3900 V), Fig. 6 displays the correlation between q_0 and r.

By varying the applied high voltage between 3500 and 4100 V and, for each voltage, using events corresponding to a thin slice in r around the peak (see Fig. 5), within the approach described

previously the mean values of q_0 were determined. In Fig. 7 are shown the mean values of r and the corresponding q_0 ; the bars correspond to the width of the slices defined in r.
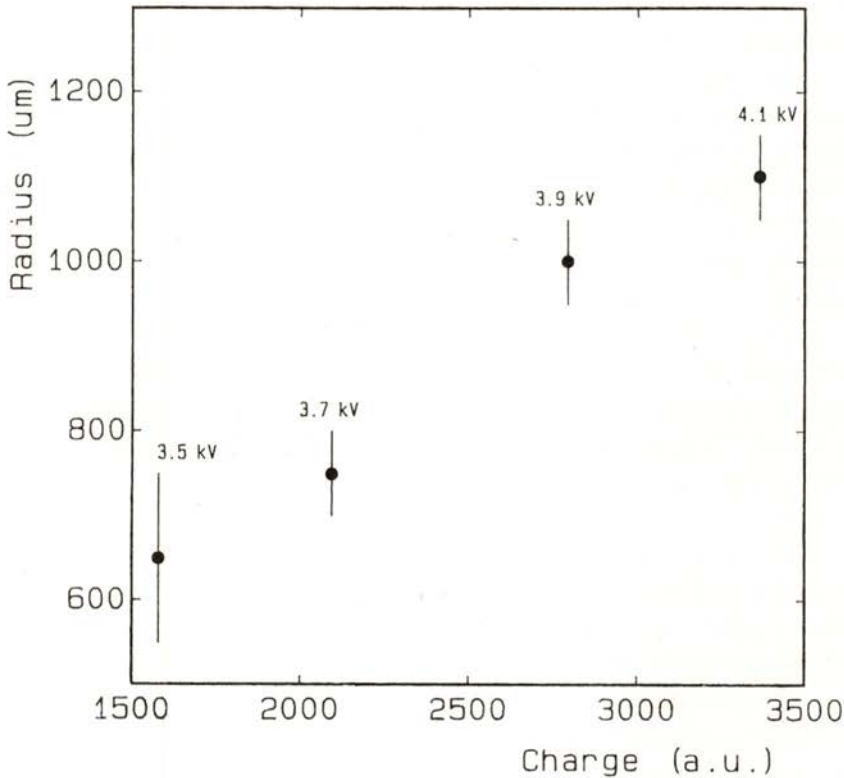
Fig. 7 — Mean value of r, black dot, as a function of the value of the mean charge q_0 of the streamer, for several values of the applied high voltage. Events near the peak of each radius distribution were used. The bars correspond to the width of the radial slices taken.

5 – CONCLUSIONS

Although the experimental data obtained reveal clearly features that are worth further investigation, only the main general characteristics will be referred to. A good example relates to Fig. 6 where most of the events reflect a strong correlation between charge q_0 and radial dimensions r, which, in any model for the

distribution of the space charge, is naturally related to the streamer length. According to the data, r increases with q_0, but for some events, an important increase in charge leads to small variation of r. Are these events related to higher charge streamers (see Fig. 3) and could they correspond to streamer branching or discharges that surround the wire?

An important result that arises out of this work is that, as one should expect for streamers orthogonal to the anode wire, the anisotropy of the induced signals is very large (about a factor two), such that it can be used with cheap electronics. And it is quite clear that this anisotropy should be even much larger for shorter gate duration, as one looks essentially to the furthermost part of the streamer.

Probably even more remarkable is the great stability of the streamer dimensions for a certain voltage, and then the stability of the anisotropy; only a negligible number of events are inside the main ring in Fig. 4; there are essentially no events with r ~ 0 that could arise from discharges built around the wire (see Fig. 5 and 6).

An important feature that was not studied in this work, is a possible correlation between the angle of arrival of the field lines that guide the electron to the anode and the angle of emergence of the streamer, Θ, which can be measured easily. In no way can one be sure that such a correlation exists, naturally disturbed by diffusion effects. Indeed, although it was quite clearly observed in the proportional counter mode, it is possible that a complete loss of memory occurs if, prior to the streamer formation, the avalanche surrounds the wire in the region of strong space charge effects [2]. The increase of the anode wire diameter or of the quencher concentration may eventually help to establish such a geometrical correlation that, in view of the strong anisotropy detected, could have important applications in instrumentation. A simple example could be in the localization of tracks in high energy physics by drift time measurements, the effort put in simple electronic hardware during data aquisition eventually paying, compared with the off-line computation time.

Assuming r as the approximate streamer length, considering that the streamer has a cross section corresponding to a radius

of about 30 micron (see ref. 9 for mean free path of ionizing photons) and since the total measured streamer charge at 3900 V is 62 pC, then one is dealing with space charges of about 10^{14} electrons/cm^3, a typical value associated with space charges in streamer tips of long sparks. The strong correlation observed between charges and "length" of the streamer, and of course also with high voltage (see Fig. 7), is in qualitative agreement with data for unbranching streamers arising from work in the long spark formation [1]. The influence of the applied electric field on the streamer quenching was also considered. For the high voltages 3500, 3700, 3900 and 4100 V the electric fields at the corresponding mean value of r for the streamers are 9.3, 8.4, 6.7 and 6.4 kV/cm, respectively. These results could be explained by the guiding effect of the cloud of primary electrons, if the streamer emerges along this cloud. This difficulty can be avoided by triggering the SQS mode with single electrons.

The model assumed in this work, in which the distribution of induced charges corresponds to a point like ion, can be easily improved. It provides a very clear first approach to the problem but, of course, extended space charge distributions can be computed. One of the problems would be to what extent the distributions of the induced charges is in practice sensitive to the model distribution for the density of charges in the streamer. Previous work on the mechanism of long spark formation lends us a relatively simple formalism that evolves out of the complex interaction of electromagnetic, hydrodynamic and thermodynamic elementary processes [1] and that allows the calculation of the variation of the charge in the streamer tip for every step of its propagation. In this work no study was made of the experimental shape of the induced charge distribution, but attention should be called to this problem. An interesting approach arises, using current sensitive output buffers with larger gains and fast enough, such that several time slices can be taken during the electron motion, each one providing information on the local ion space charge density along the streamer. Notice that for each time slice the charges involved are of the order of those associated to proportional counters.

Surely one of the important limitations to this type of work is related to mechanical accuracies, in particular deviations from

the ideal coaxial geometry. Although the electrostatics of the situation can be very accurately computed, simple algebraic formulae should be available if complex space charge situations are to be handled within a reasonable time and money scale.

REFERENCES

[1] I. GALLIMBERTI, *J. de Physique*, **40** (1979), C7-194.

[2] G. CHARPAK, G. PETERSEN, A. POLICARPO and F. SAULI, *Nucl. Instr. and Meth.*, **148** (1978), 471.

[3] J. FISCHER, H. OKUNO and A. H. WALENTA, *Nucl. Inst. and Meth.*, **151** (1978), 451.

[4] J. S. GORDON and E. MATHIESON, *Nucl. Inst. and Meth.*, **227** (1984), 267.

[5] G. D. ALEKSEEV, N. A. KALININA, V. V. KARPUKHIN, D. M. KHAZINS and V. V. KRUGLOV, *Nucl. Instr. and Meth.*, **177** (1980), 385.

[6] M. ATAC, A. V. TOLLESTRUP and D. POTTER, *Nucl. Instr. and Meth.*, **200** (1982), 345.

[7] G. A. ERSKINE, private communication.

[8] E. MATHIESON, private communication.

[9] E. P. DE LIMA, M. SALETE S. C. P. LEITE, A. J. P. L. POLICARPO and M. A. F. ALVES, *IEEE Trans. Nucl. Sci.*, **NS-30** (1983), 90.

MEASUREMENTS ON K X-RAY FLUORESCENCE YIELD RATIOS IN THE REGION OF 55 ≤ Z ≤ 82

N. Venkateswara Rao, Bh. Sankara Rao, Ch. Suryanarayana,
S. Bhuloka Reddy, G. Satyaranarayana and D. L. Sastry

Swami Jnanananda Laboratories for Nuclear Research,
Andhra University, Waltair — 530 003, India.

ABSTRACT — Accurate measurements on the $K_{\alpha_2}/K_{\alpha_1}$, $K_{\beta'_1}/K_{\alpha_1}$, $K_{\beta'_2}/K_{\alpha_1}$, K_β/K_α and $K_{\beta'_2}/K_{\beta'_1}$, X-ray intensity ratios in elements for the region of $55 \leqslant Z \leqslant 82$ have been made using natural targets with [241]Am as exciting source of radiation. The beta and electron capture decaying isotopes were studied to measure the K_β/K_α ratios in some elements. High resolution Si (Li) and HpGe systems were used for the detection of X-rays. The experimental values of K_β/K_α are consistent with theoretical predictions due to Scofield, which include exchange corrections, except for $K_{\beta'_2}/K_{\beta'_1}$. A second degree polynomial fit to the experimental values of intensity ratios is found to be most suitable for the computation of K_β/K_α ratios.

1 – INTRODUCTION

In recent years, accurate measurements on K-X-ray intensities have assumed great importance in view of the availability of high resolution solid state detectors and fast computers. Simultaneously, refined theories have been proposed which permit a comparison of the experimental values with theoretical predictions. Several authors [1-6, 12] have measured the K X-ray transition rates in the region $55 \leqslant Z \leqslant 82$, employing crystal spectrometers as well as solid state detectors. They used different modes of excitation, namely photons, electrons and heavy ions

Portgal. Phys. — Vol. 17, fasc. 1-2, pp. 35-48, 1986

35

as primary sources of radiation. Alternatively, the K X-ray intensities are measured via electron capture decay or internal conversion in radioactive isotopes. The K X-ray transition rates and K_β / K_α ratios measured using heavy ions are reported [7, 8] to be consistently higher than theoretical predictions due to Scofield [9]. It is also observed that this discrepancy between theory and experiment is found to be more pronounced as the charge of the bombarding ion increases. This is ascribed to the multiple ionisation of the atom in the case of heavy ions. Several authors have pointed out [1-6] that the K_β / K_α ratios determined via photoionisation caused by monochromatic X-rays or gamma rays, bremsstrahlung radiation and electron bombardment, are slightly higher than the Scofield theoretical values [9]. The original Scofield theory [9] assumes that the atomic electrons are in single particle states under the influence of a central potential given by the relativistic Hartree-Slater potential. Scofield modified his theory including exchange corrections [10] in the calculation in addition to the relativistic Hartree-Slater potential. The theoretical predictions of the modified Scofield theory [10] are seen to be in good agreement with the experimental K_β / K_α ratios. It may be noted that none of the earlier studies [1-6] on K_β / K_α ratios covers all the elements of the region considered here. Also, the available experimental results are due to different experimental techniques. A comparision of the predictions due to the modified Scofield theory [10] is made using these experimental values. This has prompted us to undertake a systematic experimental study of as many elements as possible in the region $55 \leqslant Z \leqslant 82$ employing high resolution solid state detectors with a computer facility, under identical conditions of experimentation, using ^{241}Am as the exciting source. In the case of some electron capture and beta decaying isotopes, a Hyper pure Germanium (HpGe) detector was used. The present work also covers the intensity ratios of several elements for which there were no previous measurements. The concerned elements are those with $Z = 55$, 57, 60, 65, 71 and 75. The values of the intensity ratios of K_β and K_α components are reported in this paper, compared to the theoretical predictions and discussed.

2 – EXPERIMENTAL DETAILS

The experiments were carried out in two phases. Under Phase I, a ^{241}Am source was used to create primary vacancies in the K-shell of an atom. Under Phase II, the intensity ratios were measured directly using radioisotopes. These isotopes are ^{137}Cs (beta), ^{133}Ba (EC), ^{152}Eu (EC, beta), ^{153}Gd (EC), ^{170}Tm (EC, beta), ^{185}W(beta), ^{203}Hg (beta), ^{204}Tl (EC, beta) and ^{207}Bi (EC). A high resolution fluorescence spectrometer was used for the detection and measurement of characteristic K X-rays. A block diagram of the present system including the source-target-detector geometry is shown in Fig. 1. The system includes a Si (Li) detector operated at liquid nitrogen temperature and coupled to a cooled FET preamplifier. It is also provided with a computer based 4K multichannel analyser and software programmes to process X-ray spectra and determine the final characteristic X-ray inten-
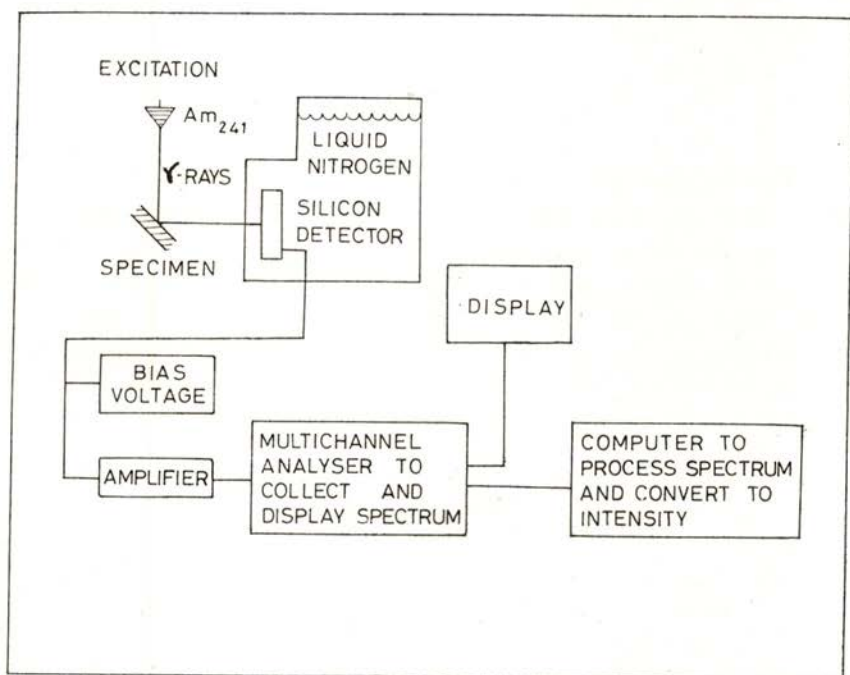

Fig. 1 — Block diagram of the experimental set-up

sities. The exciting source of radiation is a sealed 30 mCi ^{241}Am radioisotope. The resolution of the detector was measured to be 160 eV at 5.9 keV line of ^{55}Mn. Some of the radioisotopes were studied using a HpGe spectrometer facility of Bhabha Atomic Research Centre (BARC), Bombay, India. The energy resolution of the HpGe spectrometer was measured to be 180 eV at 5.9 keV. The resolution of the present systems is, thus, seen to be high enough to split close lying X-ray lines. The manipulation of the X-ray spectrum was done by a built-in computer of the type RT-11 with 32 K memory, using suitable software programmes.

3 – EFFICIENCY CALIBRATION

To determine X-ray intensities with the present detectors, a careful efficiency calibration is important. The low energy lines of well calibrated ^{57}Co, ^{133}Ba and ^{241}Am sources were used for the Si (Li) and HpGe spectrometers. The calibration was checked for the K/L ratios of X-rays following internal conversion in ^{137}Cs and ^{203}Hg.

4 – SOURCE-TARGET-PREPARATION

The natural targets like La, Ce, Pr, Nd, Tb, Dy, Ho and Lu were taken in their oxide form. They were pressed uniformly between two mylar films of thickness 0.00024 inches. The thickness of these samples ranges from 150 to 200 μg/cm^2. The radioactive sources ^{137}Cs, ^{133}Ba, ^{152}Eu, etc. of the present study were prepared by allowing a drop of the corresponding isotope on a mylar film to evaporate to dryness. A drop of insulin was also added to each source, so as to ensure an uniform spreading of the source material.

5 – DATA COLLECTION

The natural targets of different elements were excited by the 59.5 keV gamma rays from the 30 mCi ^{241}Am source. The characteristic X-ray spectra from different elements were recorded over long time intervals so as to ensure good statistics ($<$ .1 %). One typical characteristic X-ray spectrum from 'Ho' is shown in Fig. 2.

The figure shows that all the K X-ray components are well resolved. Fig. 3 shows the X-ray spectrum following electron capture decay of ^{207}Bi, as recorded by a HpGe system of BARC, Bombay, India. The intensities of X-ray lines were calculated using computer fits as well as by hand, after defining the
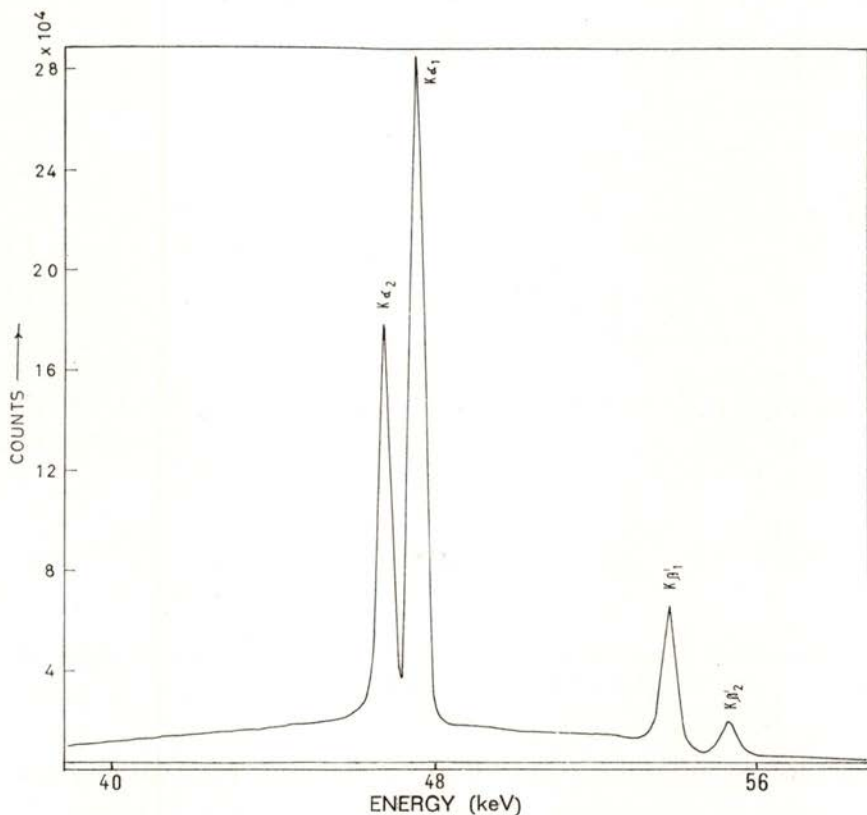
Fig. 2 — X-ray fluorescence spectrum from Ho recorded with a Si (Li) detector

background level. The two methods gave consistent values within 1 %. The areas thus obtained were corrected for self absorption and absorption in the air path between target and detector. Finally, they were corrected for the photopeak efficiency of the system used, in each case. The errors in the experimental values were estimated taking into consideration: 1) counting statistics,

2) instrument instability, 3) efficiency correction and 4) background correction. The experimental values of different ratios of K-components are summerized in Tables 1 through 5. The same tables
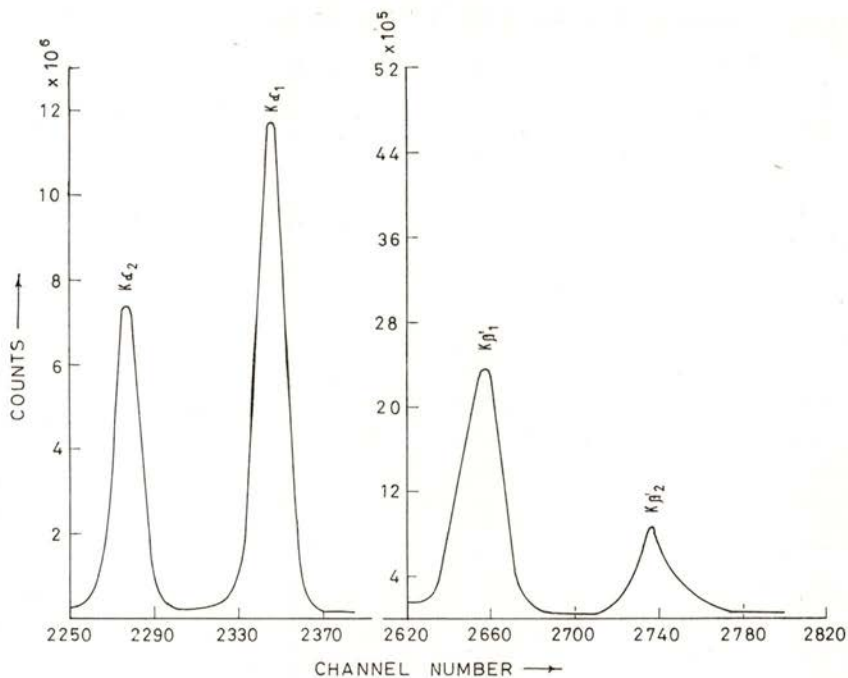
Fig. 3 — X-ray fluorescence spectrum from the electron capture decay of Bi-207, recorded with a HpGe detector system

include the theoretical predictions of Scofield, for both versions [9, 10] of his calculations. Figs. 4 through 8 show the behaviour of the $K_{\alpha_2}/K_{\alpha_1}$, $K_{\beta'_1}/K_{\alpha_1}$, $K_{\beta'_2}/K_{\alpha_1}$, K_β/K_α and $K_{\beta'_2}/K_{\beta'_1}$ ratios as functions of Z. The predictions due to Scofield [9, 10] are also shown in the same figures.

6 – RESULTS AND DISCUSSION

A polynomial fit was made to the experimental values of $K_{\alpha_2}/K_{\alpha_1}$, $K_{\beta'_1}/K_{\alpha_1}$, $K_{\beta'_2}/K_{\alpha_1}$, K_β/K_α and $K_{\beta'_2}/K_{\beta'_1}$ as a function of Z, for several degrees of freedom. The computations were

40

Portgal. Phys. — Vol. 17, fasc. 1-2, pp. 35-48, 1986

TABLE 1 — The experimental and theoretical values of the X-ray intensity ratios, $K_{\alpha_2}/K_{\alpha_1}$

Element	Z	Experimental values	Scofield theoretical values	
			Old, Ref. [9]	New, Ref. [10]
Cs	55	0.538 ± 0.011	0.542	0.542
Ba	56	0.540 ± 0.011	0.543	0.543
La	57	0.542 ± 0.011	0.545	0.544
Ce	58	0.544 ± 0.011	0.546	0.546
Pr	59	0.544 ± 0.011	0.548	0.548
Nd	60	0.545 ± 0.011	0.549	0.549
Sm	62	0.553 ± 0.012	0.553	0.553
Eu	63	0.551 ± 0.011	0.554	0.554
Gd	64	0.562 ± 0.011	0.556	0.556
Tb	65	0.559 ± 0.011	0.558	0.558
Dy	66	0.563 ± 0.011	0.560	0.560
Ho	67	0.559 ± 0.011	0.562	0.562
Er	68	0.560 ± 0.012	0.564	0.564
Yb	70	0.570 ± 0.011	0.567	0.567
Lu	71	0.569 ± 0.011	0.570	0.570
Re	75	0.576 ± 0.011	0.578	0.578
Hg	80	0.591 ± 0.011	0.590	0.590
Tl	81	0.594 ± 0.011	0.593	0.593
Pb	82	0.596 ± 0.011	0.595	0.595

TABLE 2 — The experimental and theoretical values of the X-ray intensity ratios, $K_{\beta'_1}/K_{\alpha_1}$

Element	Z	Experimental values	Scofield theoretical values	
			Old, Ref. [9]	New, Ref. [10]
Cs	55	0.294 ± 0.009	0.281	0.297
Ba	56	0.296 ± 0.009	0.283	0.300
La	57	0.296 ± 0.009	0.286	0.302
Ce	58	0.294 ± 0.009	0.288	0.304
Pr	59	0.295 ± 0.009	0.291	0.306
Nd	60	0.295 ± 0.009	0.293	0.309
Sm	62	0.300 ± 0.010	0.298	0.313
Eu	63	0.302 ± 0.009	0.300	0.315
Gd	64	0.305 ± 0.009	0.302	0.317
Tb	65	0.309 ± 0.009	0.304	0.319
Dy	66	0.310 ± 0.009	0.306	0.320
Ho	67	0.313 ± 0.009	0.308	0.322
Er	68	0.319 ± 0.010	0.310	0.324
Yb	70	0.327 ± 0.009	0.314	0.327
Lu	71	0.328 ± 0.009	0.315	0.329
Re	75	0.342 ± 0.009	0.323	0.335
Hg	80	0.342 ± 0.009	0.331	0.343
Tl	81	0.342 ± 0.009	0.333	0.344
Pb	82	0.342 ± 0.009	0.334	0.346

TABLE 3 — The experimental and theoretical values of the X-ray intensity ratios, $K_{\beta'_2} / K_{\alpha_1}$

Element	Z	Experimental values	Scofield theoretical values	
			Old, Ref. [9]	New, Ref. [10]
Cs	55	0.069 ± 0.003	0.065	0.073
Ba	56	0.071 ± 0.003	0.068	0.076
La	57	0.073 ± 0.003	0.070	0.077
Ce	58	0.077 ± 0.003	0.070	0.077
Pr	59	0.080 ± 0.003	0.071	0.078
Nd	60	0.083 ± 0.003	0.072	0.079
Sm	62	0.088 ± 0.004	0.073	0.081
Eu	63	0.088 ± 0.003	0.074	0.081
Gd	64	0.090 ± 0.003	0.076	0.083
Tb	65	0.090 ± 0.003	0.076	0.083
Dy	66	0.090 ± 0.003	0.076	0.083
Ho	67	0.091 ± 0.003	0.077	0.084
Er	68	0.090 ± 0.004	0.077	0.084
Yb	70	0.090 ± 0.003	0.078	0.085
Lu	71	0.088 ± 0.003	0.080	0.087
Re	75	0.088 ± 0.003	0.085	0.093
Hg	80	0.097 ± 0.003	0.093	0.100
Tl	81	0.101 ± 0.003	0.094	0.102
Pb	82	0.105 ± 0.004	0.096	0.104

TABLE 4 — The experimental and theoretical values of the X-ray intensity ratios, K_β / K_α

Element	Z	Experimental values	Scofield theoretical values	
			Old, Ref. [9]	New, Ref. [10]
Cs	55	0.236 ± 0.006	0.224	0.240
Ba	56	0.238 ± 0.006	0.227	0.243
La	57	0.239 ± 0.007	0.230	0.245
Ce	58	0.240 ± 0.007	0.232	0.247
Pr	59	0.243 ± 0.007	0.234	0.249
Nd	60	0.245 ± 0.007	0.235	0.250
Sm	62	0.250 ± 0.007	0.239	0.253
Eu	63	0.251 ± 0.007	0.241	0.255
Gd	64	0.253 ± 0.007	0.243	0.257
Tb	65	0.256 ± 0.007	0.244	0.258
Dy	66	0.256 ± 0.007	0.245	0.259
Ho	67	0.259 ± 0.007	0.246	0.260
Er	68	0.260 ± 0.007	0.248	0.261
Yb	70	0.265 ± 0.007	0.250	0.263
Lu	71	0.266 ± 0.007	0.252	0,265
Re	75	0.273 ± 0.008	0.258	0.271
Hg	80	0.276 ± 0.008	0.266	0.279
Tl	81	0.278 ± 0.008	0.268	0.280
Pb	82	0.280 ± 0.008	0.270	0.282

TABLE 5 — The experimental and theoretical values of the X-ray intensity ratios, $K_{\beta'_2} / K_{\beta'_1}$

	Z	Experimental values	Scofield theoretical values	
			Old, Ref. [9]	New, Ref. [10]
Cs	55	0.235 ± 0.011	0.230	0.244
Ba	56	0.240 ± 0.011	0.238	0.252
La	57	0.247 ± 0.011	0.245	0.253
Ce	58	0.262 ± 0.012	0.243	0.254
Pr	59	0.271 ± 0.012	0.244	0.256
Nd	60	0.281 ± 0.012	0.245	0.257
Sm	62	0.293 ± 0.012	0.247	0.258
Eu	63	0.291 ± 0.012	0.248	0.258
Gd	64	0.295 ± 0.012	0.251	0.263
Tb	65	0.291 ± 0.012	0.248	0.259
Dy	66	0.290 ± 0.012	0.249	0.260
Ho	67	0.291 ± 0.012	0.249	0.260
Er	68	0.282 ± 0.012	0.249	0.260
Yb	70	0.275 ± 0.012	0.250	0.261
Lu	71	0.280 ± 0.012	0.253	0.264
Re	75	0.257 ± 0.011	0.264	0.277
Hg	80	0.284 ± 0.013	0.280	0.295
Tl	81	0.295 ± 0.013	0.283	0.297
Pb	82	0.307 ± 0.014	0.288	0.302

made using a programme 'polyfit'. It was found that a quadratic fit yields the minimum chi-squared value. The coefficients of the polynomial are given in Table 6; the corresponding curves are shown as solid lines in figures 4-8. These figures show that the theoretical fits are consistent with the experimental behaviour of the K X-ray intensity ratio as a function of Z. The theoretical values of the intensity ratios of K components for elements not covered in the present study are given in Table 7; this table includes also the experimental values. From Table 7, it can seen that agreement between theory and the experimental values is satisfactory.

The intensity ratio measurements in elements Nd, Tb, Lu and Re were made for the first time in the present investigation; the same applies also to the $K_{\beta'_2} / K_{\beta'_1}$ ratios. It may be seen from Fig. 4, that there is a good agreement between the experimental values of $K_{\alpha_2} / K_{\alpha_1}$ and both versions of the theory due to Scofield.

TABLE 6 — Coefficients of the second degree polynomial fit to experimental values of the K X-ray intensity ratios

Coefficients	$K_{\alpha_2}/K_{\alpha_1}$	$K_{\beta'_1}/K_{\alpha_1}$	$K_{\beta'_2}/K_{\alpha_1}$	K_β/K_α	$K_{\beta'_2}/K_{\beta'_1}$
A_0	0.471351×10^0	0.133785×10^0	-0.108496×10^0	0.244827×10^{-1}	-0.250858×10^0
A_1	0.624179×10^{-3}	0.318455×10^{-2}	0.486874×10^{-2}	0.525117×10^{-2}	0.145837×10^{-1}
A_2	0.110417×10^{-4}	-0.720098×10^{-5}	-0.284165×10^{-4}	-0.261357×10^{-4}	-0.977562×10^{-4}

TABLE 7 — Values of K_β / K_α corresponding to the polynomial fit and experimental values (when available) for some elements

Atomic Number	Interpolated Values	Experimental values			
		Ref. [3]	Ref. [11]	Ref. [2]	Ref. [1]
61	0.248	—	—	—	—
69	0.260	—	—	—	—
72	0.267	0.269 ± 0.008	—	—	—
73	0.269	—	—	0.269 ± 0.014	0.262 ± 0.005
74	0.270	0.271 ± 0.008	—	—	—
76	0.273	—	—	—	—
77	0.274	—	—	0.275 ± 0.014	—
78	0.275	—	—	—	0.271 ± 0.005
79	0.276	0.276 ± 0.008	0.276 ± 0.02	0.272 ± 0.014	—

From Figs. 5-7, it may be noted that the experimental values of $K_{\beta'_1} / K_{\alpha_1}$, $K_{\beta'_2} / K_{\alpha_1}$ and K_β / K_α agree better with the theoretical values of Scofield when exchange corrections are included. However, one might note that the deviations that show up in figures 5 and 6 combine to give the disagreement in the
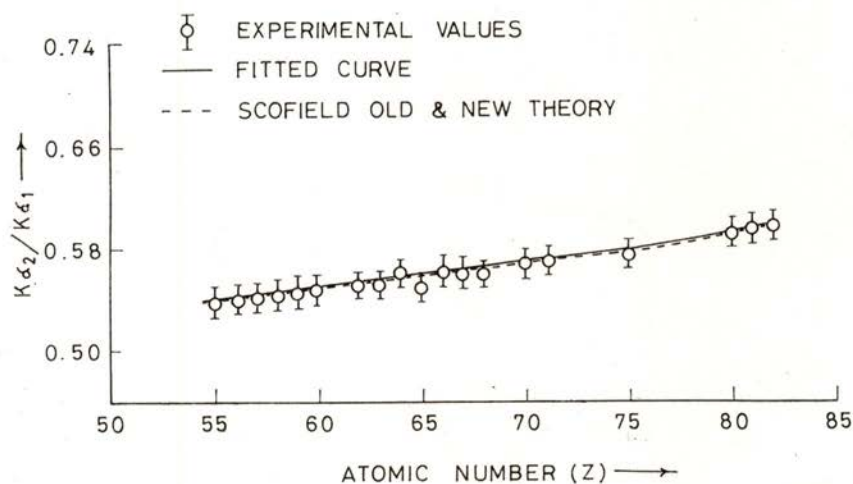

Fig. 4 — Experimental and theoretical curves showing $K_{\alpha_2} / K_{\alpha_1}$ versus atomic number Z

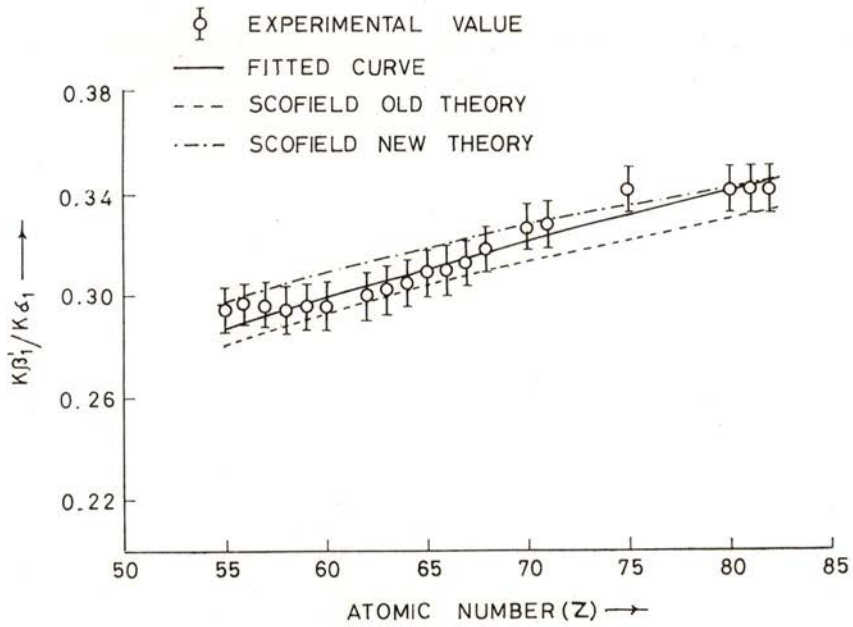*Portgal. Phys.* — Vol. 17, fasc. 1-2, pp. 35-48, 1986

45

Fig. 5 — Experimental and theoretical curves showing $K_{\beta'_1}/K_{\alpha_1}$ versus atomic number Z
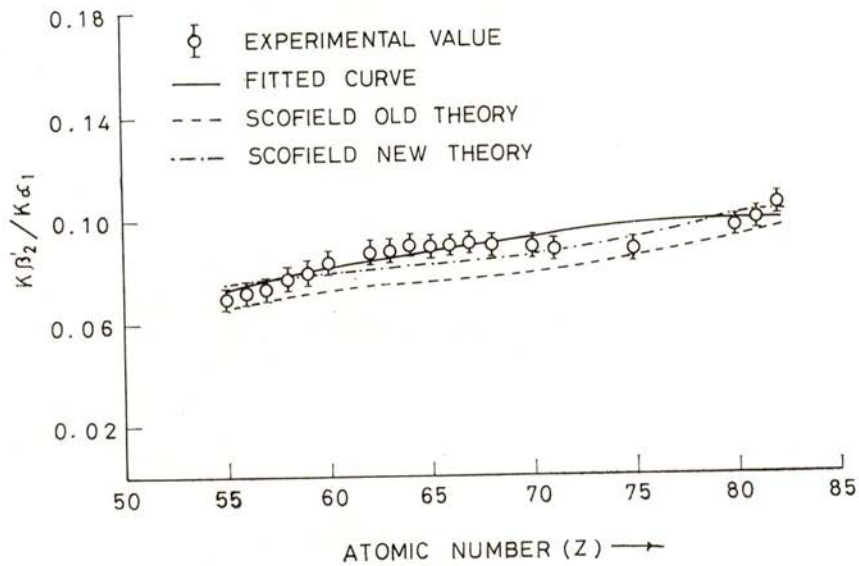

Fig. 6 — Experimental and theoretical curves showing $K_{\beta'_2}/K_{\alpha_1}$ versus atomic number Z
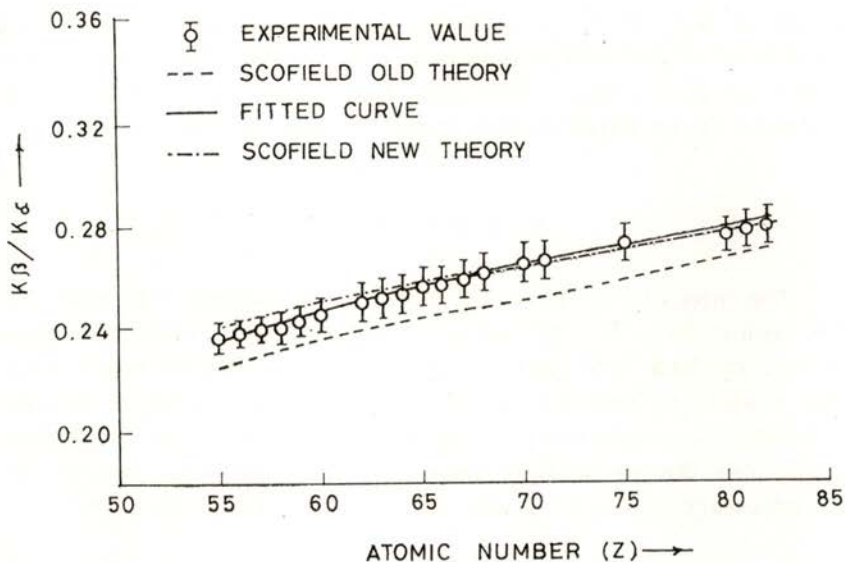
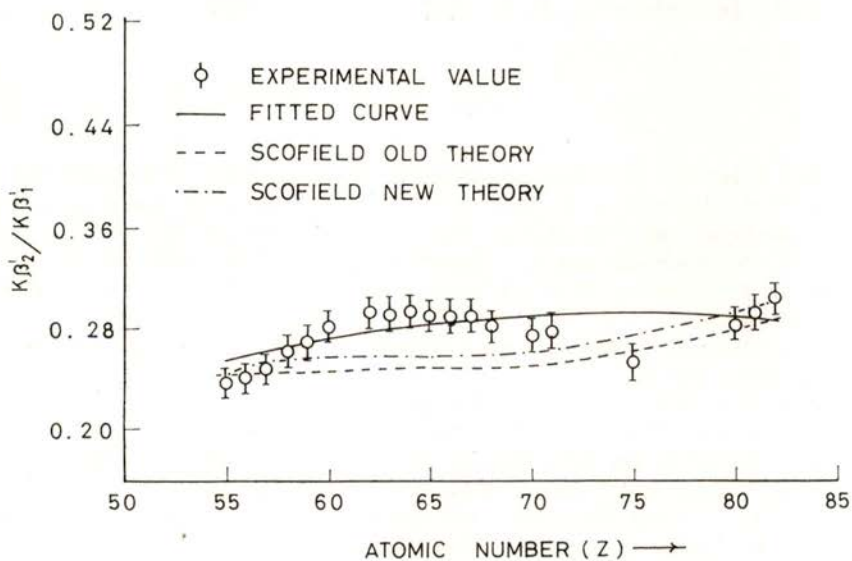Fig. 7 — Experimental and theoretical curves showing K_β / K_α versus atomic number Z

Fig. 8 — Experimental and theoretical curves showing $K_{\beta'_2} / K_{\beta'_1}$ versus atomic number Z

values of $K_{\beta'_2} / K_{\beta'_1}$ as evidenced in Fig. 8. Thus, it seems that the theory of Scofield is insufficient to explain the experimental values of $K_{\beta'_2} / K_{\beta'_1}$. One also sees from figure 8 that the quadratic fit to experimental points is not satisfactory.

7 – CONCLUSION

The intensity ratios of the K X-rays in different elements for the region $55 \leqslant Z \leqslant 82$, were measured using natural targets excited by 59.5 keV gamma rays of [241]Am. Radioisotopes were also studied to measure the K X-ray intensity ratios in certain elements. A comparison of experimental values and theoretical predictions due to Scofield shows that the exchange corrections are necessary to explain many of the observed K_β / K_α ratios.

REFERENCES

[1] J. S. HANSEN, H. U. FREUND and R. W. FINK. *Nucl. Phys.*, **A164** (1977) 604.

[2] J. H. McCRARY, L. V. SINGMANN, L. H. ZIEGLER, L. D. LOONEY, C. M. EDMONDS and C. E. HARRIS. *Phys. Rev.*, **A4** (1971), 1745.

[3] V. W. SLIVINSKY and P. J. EBERT. *Phys. Lett.*, **A29** (1969), 463.

[4] M. I. MARQUES, M. C. MARTINS and J. G. FERREIRA. *J. Phys.*, **B13** (1980), 41.

[5] D. BERENYI, G. HOCK, S. RICZ, B. SCHLENK and A. VALEK. *J. Phys.*, **B11** (1978), 709.

[6] A. G. DE PINHO. *Phys. Rev.*, **A3** (1971), 905.

[7] T. K. LI and R. L. WATSON. *Phys. Rev.*, **A9** (1974), 1574.

[8] Y. AWAYA, K. IZUMO, T. HAMADA, M. OKANO, T. TAKAHASHI, A. HASHIZUME, Y. TEMDOW and T. KATOU. *Phys. Rev.*, **A13** (1976), 992.

[9] J. H. SCOFIELD. *Phys. Rev.*, **179** (1969), 9.

[10] J. H. SCOFIELD. *Phys. Rev.*, **A9** (1974), 1041.

[11] V. D. MISTRY and C. A. QUARLES. *Nucl. Phys.*, **A164** (1971) 219.

[12] M. DOST, S. HOPPEUAU, S. ROHL and W. A. SCHONFELDT. *J. Phys.*, **B14** (1981), 3753.

48

Portgal. Phys. — Vol. 17, fasc. 1-2, pp. 35-48, 1986

A SIMPLE MODEL FOR THE PION FIELD AROUND
A STATIC SOURCE

M. FIOLHAIS and M. ROSINA [1]

Departamento de Física, Universidade de Coimbra, P — 3000 Coimbra, Portugal

ABSTRACT — We present a simple model for a system of static bare nucleon and bare delta, coupled linearly to a non-self-interacting pion cloud. The model space for the boson cloud consists of states with arbitrary number of $l = 1$ pions, having all the same radial wave function. Both axially symmetric and hedgehog coherent states of pions are studied, in order to compare their behaviour as a function of the coupling strength and to look at the relevance of the variation-after-projection method. The model may be used as a test of different approximations commonly applied in realistic calculations for meson clouds.

1 — INTRODUCTION

Several chiral invariant models have been proposed to describe the pion cloud around the nucleon: the chiral bag [1], the little bag [2], the cloudy bag [3] and the chiral soliton [4]. A fully quantum mechanical treatment of these models is possible only in the framework of perturbation theory. On the other hand, in the non-perturbative regime the solutions are obtained in the mean-field-approximation, assuming the so-called hedgehog form for the fields. These solutions are not eigenfunctions of the angular

momentum and the isospin operators and, therefore, they cannot directly describe the physical states. However, as it is well known from nuclear physics, the states with good spin and isospin quantum numbers may be obtained from them by means of the Peierls-Yoccoz projection technique [5].

In this paper we refer to a system of static bare nucleon and bare delta, coupled linearly to a non-self-interacting pion cloud, e. g. the cloudy-bag model [3]. We present a very simple model which is suitable for testing the validity of different approximation schemes to the meson cloud. In a given realistic model one should estimate the number of pions n and then, one can get some insight from the simple model, how different approximations behave in that range of n.

The contents of this paper are as follows. In section 2 the model is presented. The regimes of weak and strong coupling strengths are considered in section 3. Angular momentum and isospin projections from axially symmetric coherent states and hedgehog coherent state of pions are performed in sections 4 and 5. Section 6 contains the discussion of the different approximate solutions and the conclusions. The technical details of the spin-isospin projection are presented in the appendices.

2 – THE MODEL

For a system of p-wave pions interacting with static bare particles, the Hamiltonian can be written in the form [6]

$$H' = \sum_a \varepsilon_a c_a^+ c_a + \sum_{tmk} \{ \omega(k)\, a_{tm}^+(k)\, a_{tm}(k)$$

$$-\tilde{G}\, \rho(k)\, B_{tm}[a_{tm}(k) + (-1)^{t+m} a_{-t-m}(k)] \}$$

(2.1)

where c_a^+ is the creation operator for the bare particle and ε_a its energy; the operator $a_{tm}^+(k)$ creates a pion with momentum (magnitude) k, angular momentum one and (spherical) angular momentum and isospin components $m = 0, \pm 1$ and $t = 0, \pm 1$, respectively. We consider a model with bare nucleon

50

Portgal. Phys. — Vol. 17, fasc. 1-2, pp. 49-74, 1986

and bare delta. $\varepsilon_N = \varepsilon_\Delta = 0$ will be assumed. In (2.1) the operator B_{tm} is given by [6]

$$B_{tm} = \tau_t^{NN} \sigma_m^{NN} + \sqrt{72/25} \; (\tau_t^{N\Delta} \sigma_m^{N\Delta} + \tau_t^{\Delta N} \sigma_m^{\Delta N})$$

$$+ (4/5) \; \tau_t^{\Delta\Delta} \sigma_m^{\Delta\Delta} \qquad\qquad (2.2)$$

where τ_t^{NN} and σ_m^{NN} are the Pauli matrices acting on the isospin and the spin of the bare nucleon in the source; the operators $\tau_t^{\Delta\Delta}$ and $\sigma_m^{\Delta\Delta}$ do the same on bare delta; $\tau_t^{N\Delta} \sigma_m^{N\Delta}$ converts a bare delta in bare nucleon and $\tau_t^{N\Delta} \sigma_m^{N\Delta}$ vice-versa.

We shall not specify the spherically symmetric source density $\rho(k)$ in (2.1). However, for a given $\rho(k)$, the one pion radial wave function $F(k)$ can be determined by a self consistent mean-field calculation of the intrinsic state or, in a more reliable calculation, it can be determined variationally for a projected coherent state.

The creation operator $a_{tm}^+(k)$ can always be written in the form

$$a_{tm}^+(k) = F^*(k) \; a_{tm}^+ + \sum_n F_n^*(k) \; b_{tm}^+(n) \qquad\qquad (2.3)$$

where a_{tm}^+ and $b_{tm}^+(n)$ form a complete orthonormal set. Here, a_{tm}^+ creates a pion with angular momentum and isospin components m and t, respectively, and radial wave function $F(k)$; $b_{tm}^+(n)$ creates a pion with the same angular momentum and isospin quantum numbers but with radial wave function $F_n(k)$. These states are not occupied in the model space and therefore all $b_{tm}^+(n)$ can simply be ignored in the Hamiltonian.

In this paper we shall study the properties of approximate solutions for the Hamiltonian

$$H = \sum_{tm} \{ a_{tm}^+ a_{tm} - G B_{tm} [a_{tm} + (-1)^{t+m} a_{-t-m}^+] \} \qquad\qquad (2.4)$$

with

$$G = \tilde{G} \sum_k \rho(k) \; F(k) \qquad\qquad (2.5)$$

in energy units in which $\sum_k \omega(k) F^*(k) F(k) = 1$.

The Hamiltonian H is schematic in the sense that it contains no radial degree of freedom. It may be viewed as an effective Hamiltonian which is replacing (2.1).

3 — WEAK AND STRONG COUPLINGS

In the limit of small G, the second term in (2.4),

$$H_{coup} = - G \sum_{tm} B_{tm} (a_{tm} + (-1)^{t+m} + a^+_{-t-m}) \qquad (3.1)$$

may be considered as a perturbation to the first one. In this regime, the physical baryon states are superpositions of bare baryon, $| \phi_0 >$, and bare-baryon-plus-one-pion states, $| \phi_i >$. Up to second order in the coupling constant, the energy is

$$E^{pert} = E_0 + \varepsilon_1 + \varepsilon_2 \qquad (3.2)$$

where E_0 is the bare baryon energy,

$$\varepsilon_1 = < \phi_0 | H_{coup} | \phi_0 > \qquad (3.3)$$

and

$$\varepsilon_2 = \sum_i | < \phi_0 | H_{coup} | \phi_i > |^2 / (E_0 - E_i) \qquad (3.4)$$

In our simple model no chromomagnetic interaction is considered and for simplicity we have taken as zero both bare nucleon and the bare delta energies. Moreover, for the Hamiltonian (2.4), $E_i = 1$. From (3.1) and (3.3) it follows that the first order contribution for the energy, ε_1, vanishes. The evaluation of (3.4) yields for the energies of the physical nucleon and delta states the following results:

$$E_N = - 20.52 \ G^2 \qquad (3.5)$$

and

$$E_\Delta = - 11.88 \ G^2 \qquad (3.6)$$

where all these factors are exact fractions (multiples of $1/25$).

In the other limit, i. e. in a regime of very strong coupling strength, the cloud around the static source contains a large number of non-self-interacting pions and therefore the mean-field-approximation (MFA) is totally adequate. This consists in describing the pions by quantum mechanical coherent states [7]. In the MFA, the minimal energy for the Hamiltonian (2.4) is obtained for the hedgehog baryon configuration [8] and, as we shall see in section 5, is given by

$$E = - 9.72 \ G^2. \qquad (3.7)$$

52

Portgal. Phys. — Vol. 17, fasc. 1-2, pp. 49-74, 1986

In a regime of very large G, this is the leading term for the energy of the nucleon and its isobars. The quantum fluctuations are very small and all these states have the same energy.

As a starting point to the description of the pion cloud around the static source we shall consider the mean-field or coherent state approximation. The total trial wave function of the baryon reads as

$$| \psi > = \mathscr{N} (\xi) \, \exp (\underset{tm}{\Sigma} \, \xi_{tm} \, a_{tm}^{+}) \, | B > \qquad (3.8)$$

where $\mathscr{N} (\xi)$ is a normalization factor, $| B >$ is the bare baryon state and ξ_{tm} are amplitudes to be determined variationally. The state (3.8) has the following important property:

$$a_{tm} \, | \psi > = \xi_{tm} \, | \psi > . \qquad (3.9)$$

In the MFA, the energy is the expectation value of H in the state (3.8). Using (3.9) this 'intrinsic energy' is readily evaluated yielding

$$E^{(intr.)} = E_{kin}^{(intr.)} + E_{coup}^{(intr.)} , \qquad (3.10)$$

where

$$E_{kin}^{(intr.)} = \underset{tm}{\Sigma} \, \xi_{tm}^{*} \, \xi_{tm} \qquad (3.11)$$

and

$$E_{coup}^{(intr.)} = - G \underset{tm}{\Sigma} \, (\xi_{tm} + (-1)^{t+m} \, \xi_{-t-m}^{*}) \, v_{tm} , \qquad (3.12)$$

are respectively the intrinsic kinetic and interaction energies. Here, v_{tm} is the matrix element:

$$v_{tm} = < B \, | \, B_{tm} \, | \, B > , \qquad (3.13)$$

where B_{tm} is the operator (2.2). We notice that for the Hamiltonian (2.4) the kinetic energy is equal to the number of pions in the cloud.

The amplitudes ξ_{tm} are obtained performing a Ritz's variation, $\partial E^{(intr.)} / \partial \xi_{tm}^* = 0$, yielding

$$\xi_{tm} = (-1)^{t+m} \, G \, v_{-t-m} \, . \tag{3.14}$$

The solutions obtained in the MFA clearly violate the rotational symmetry of the Hamiltonian (2.4) both in coordinate and charge spaces. The trial coherent state (3.8) does not have the spin and isospin quantum numbers of the nucleon or its isobars. These physical states may be obtained by means of a Peierls-Yoccoz projection of the trial wave function onto states of good spin and isospin [5, 6, 9-11].

4 – PROJECTION FROM AXIALLY SYMMETRIC STATES

In this section we consider the projection from axially symmetric coherent states of pions. We assume the bare baryon state to be a mixture of a bare nucleon and bare delta, each having spin component 1/2 and charge +1:

$$| B(\delta) >_A = \cos \delta \, | N_{1/2}^+ > + \sin \delta \, | \Delta_{1/2}^+ > \tag{4.1}$$

Here, the mixing angle δ is another variational parameter. Now the amplitude (3.14) reads as

$$\xi_{tm} = \xi \, \delta_{to} \, \delta_{mo} \tag{4.2}$$

where

$$\xi = G \, [\cos^2 \delta + (8\sqrt{2}/5) \, \sin \delta \, \cos \delta + (1/5) \, \sin^2 \delta] \tag{4.3}$$

From (3.10-12) and (4.2-3) the kinetic, coupling and total intrinsic energies are given by:

$$E_{kin}^{(intr.)} = S = \xi^2 = G^2 \, f(\delta) \, , \tag{4.4a}$$

$$E_{coup}^{(intr.)} = -2 \, G \, \xi \sqrt{f(\delta)} = -2 \, G^2 \, f(\delta) \, , \tag{4.4b}$$

$$E^{(intr.)} = -G^2 \, f(\delta) \, , \tag{4.4c}$$

54

Portgal. Phys. — Vol. 17, fasc. 1-2, pp. 49-74, 1986

where

$$f(\delta) = [\cos^2 \delta + (8\sqrt{2}/5) \sin \delta \cos \delta + (1/5) \sin^2 \delta]^2 \qquad (4.5)$$

Here and in the sequel S denotes the average (intrinsic) number of pions in the cloud. This quantity is plotted in Figure 1, in dependence of G. The function (4.5) is plotted in Fig. 2 of ref [10].
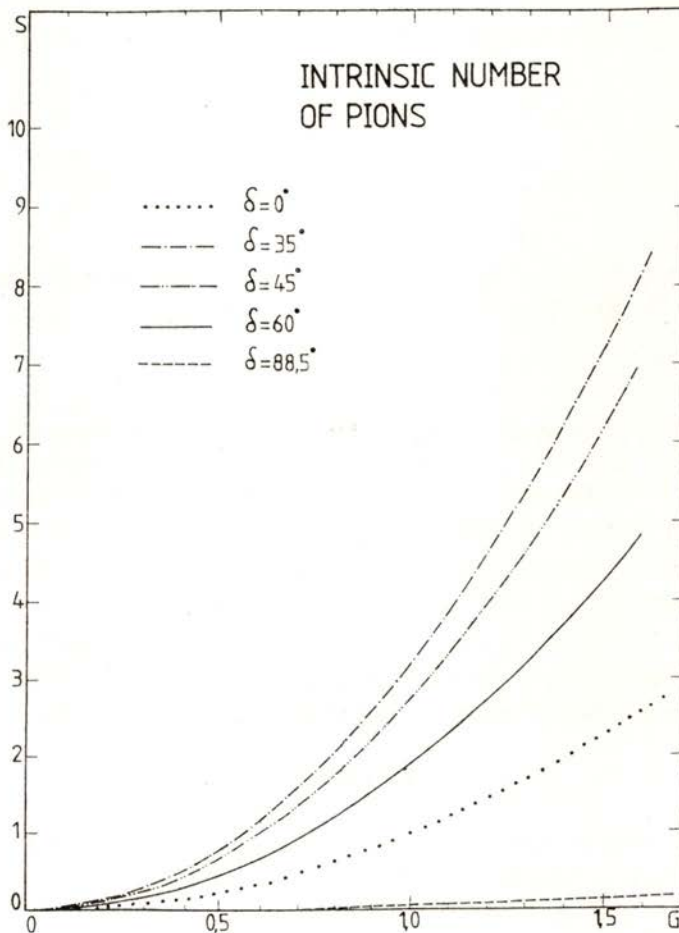

Fig. 1 — The average number of pions in the cloud of the non-projected axially symmetric state. The values are given in dependence of the coupling constant for different mixing angles.

It has an absolute maximum (a minimum for the energy) for $\delta = \text{arctg}\,(1/\sqrt{2}) \simeq 35°$, and the corresponding total energy is

$$E^{(\text{intr.})} = -3.24\ G^2 \,.\qquad (4.6)$$

Other values of $E^{(\text{intr.})}/G^2$, for several mixing angles, may be read directly from figures 3 and 5.

Let us use the following ansatz for the total trial wave function of the baryon:

$$|\psi> = \cos \delta\ |\psi_N> + \sin \delta\ |\psi_\Delta> \,;\qquad (4.7)$$

where

$$|\psi_N> = \exp(\xi\, a_{00}^+)\ |N_{1/2}^+>\qquad (4.8a)$$

and

$$|\psi_\Delta> = \exp(\xi\, a_{00}^+)\ |\Delta_{1/2}^+>\qquad (4.8b)$$

The state with the quantum numbers of a nucleon is extracted from (4.7) according to

$$|1/2\,,\ 1/2> = P_{1/2\,1/2}\,|\psi>\qquad (4.9)$$

where $P_{1/2\,1/2}$ is used as an abbreviation for the operator $P^T_{1/2\,1/2\,1/2}$ $P^J_{1/2\,1/2\,1/2}$; here, $P_{t\alpha\alpha'}$ projects out of a state with good third component α' of isospin (angular momentum), the state with good quantum number of isospin (angular momentum) t and rotates the third component into α. The norm (square) of the state (4.9) is $F = \cos^2 \delta\ F_N + \sin^2 \delta\ F_\Delta$, where $F_N = \ <\psi_N|\,P_{1/2\,1/2}\,|\psi_N>$ and $F_\Delta = \ <\psi_\Delta|\,P_{1/2\,1/2}\,|\psi_\Delta>$. The details of the calculation of these quantities are shown in Appendix A.

The number of pions in the cloud – see (A. 15) – is

$$n = S\,F^{-1}\,(S)\,F'\,(S)\,.\qquad (4.10)$$

F' denotes the derivative with respect to S. Using the property (3.9), the interaction energy is readily evaluated and the total projected energy for the nucleon reads as

$$E_{1/2\,1/2} = SF^{-1}\ F' - 2GF^{-1}\ \xi\ [\,\cos^2 \delta\ F_N$$
$$+\,(4\sqrt{2}/5)\ \sin \delta\ \cos \delta\ (F_N + F_\Delta) + (1/5)\ \sin^2 \delta\,]\qquad (4.11)$$

The energy of the physical nucleon is a function of the two variational parameters. Now, the appropriate procedure is to search for a minimum of $E_{1/2\,1/2}$ in the plane (ξ, δ). This is nothing but the variation-after-projection (VAP) method. Another procedure, the variation-before-projection (VBP) method, would be to insert in (4.11) the self-consistent values for the variational parameters obtained in the MFA. We shall study the behaviour of the solutions obtained in both methods.
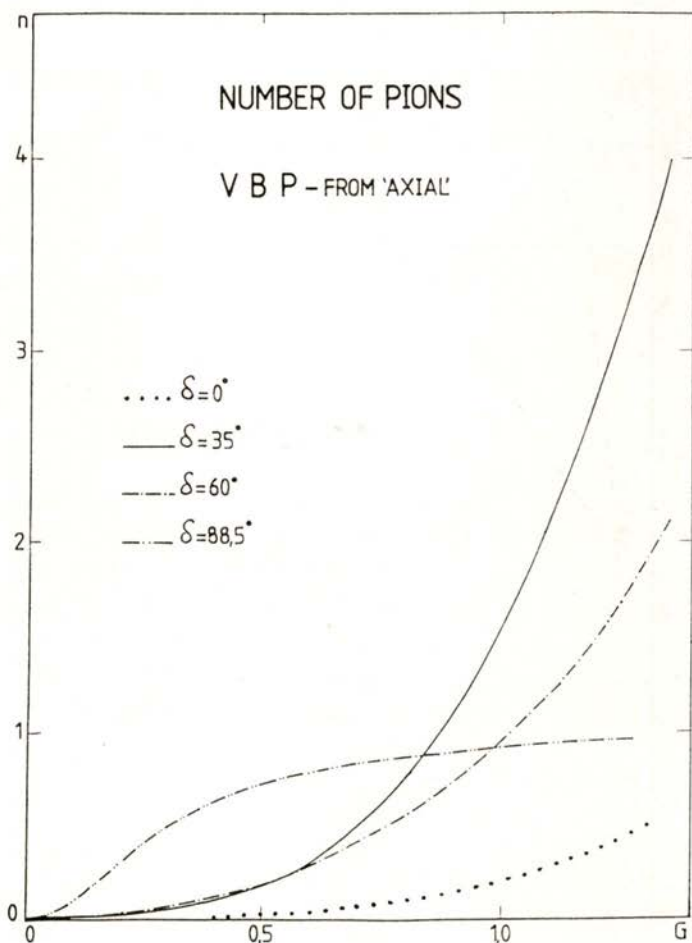

Fig. 2 — The number of pions in the pion cloud of the nucleon, for several mixing angles. The projected states have been obtained from axially symmetric coherent states of pions.

Portgal. Phys. — Vol. 17, fasc. 1-2, pp. 49-74, 1986

57

4.1 — Variation-before-projection

We have taken the self-consistent ξ, given by (4.3), and have considered the solutions for different values of δ.

The number of pions and the total energy of the projected state have been evaluated numerically from (4.10) and (4.11) using the power series expansions derived in Appendix A, for the norms of the projected coherent states. Figure 2 and 3 show the projected
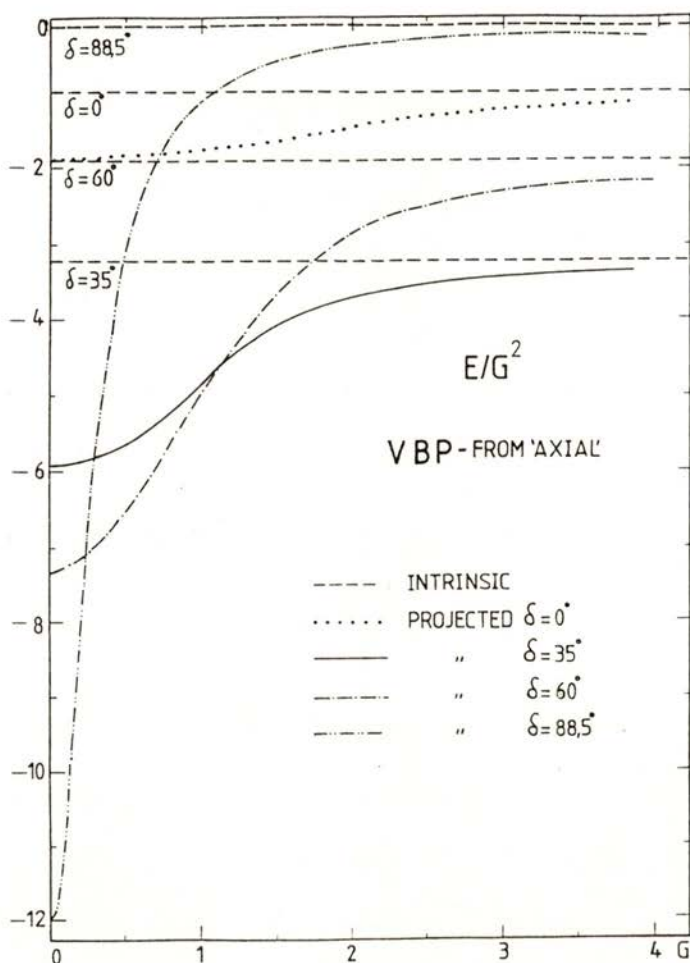

Fig. 3 — For the nucleon, E/G^2 is plotted versus coupling constant for various values of δ. The projected states have been obtained from axially symmetric coherent states of pions.

number of pions and $E_{1/2\,1/2} / G^2$, in dependence of G, for several mixing angles. A comparison between figures 1 and 2 shows that the number of pions gets reduced with the projection. The only exception is observed for angles close to 90°: the source is mainly bare delta and at least one pion is necessary to construct a state with the quantum numbers of a nucleon, whereas for the physical delta the main contribution comes from the zero pion state. Regarding the total energy, for very small values of the coupling constant, the best angle is also around 90°: the minimal energy in the limit $G \to 0$ is

$$\lim_{G \to 0} E_{1/2\,1/2} / G^2 = -12.02 , \qquad (4.12)$$

with $\delta = 88.5°$. This value is very far from (2.5), which is exact in this limit.

4.2 — *Variation-after-projection*

This procedure is more reliable, since it assumes that the eigenstate of the Hamiltonian is approximated by the trial wave function (4.9) which has already the quantum numbers of the nucleon.

For the projected energy (4.11), the variation with respect to ξ, $\partial E_{1/2\,1/2} / \partial \xi = 0$, yields

$$G = \xi\, T(S) \qquad (4.13)$$

where

$$T(S) = (FF' - SF'^2 + SFF'') \cdot \{ (F - 2SF') \cdot$$

$$[\cos^2 \delta\, F_N + (4\sqrt{2}/5) \sin \delta \cos \delta\, (F_N + F_\Delta) + (1/5) \sin^2 \delta\, F_\Delta] +$$

$$2SF [\cos^2 \delta\, F'_N + (4\sqrt{2}/5) \sin \delta \cos \delta\, (F'_N + F'_\Delta)$$

$$+ (1/5) \sin^2 \delta\, F'_\Delta] \}^{-1} . \qquad (4.14)$$

The numerical evaluation of the projected energy has been carried out in the following way: First ξ $(= \sqrt{S})$ was fixed; then, using (4.13-14) the coupling constant was determined; finally

Portgal. Phys. — Vol. 17, fasc. 1-2, pp. 49-74, 1986

59

the number of pions and the total projected energy were evaluated making use of the expressions (4.10-11).

Fig. 4 shows the number of pions in the cloud as a function of coupling strength, for different values of the mixing angle. In Figure 5 the quantity $E_{1/2\ 1/2} / G^2$ is plotted against G. This figure should be compared with Figure 3, where the curves have
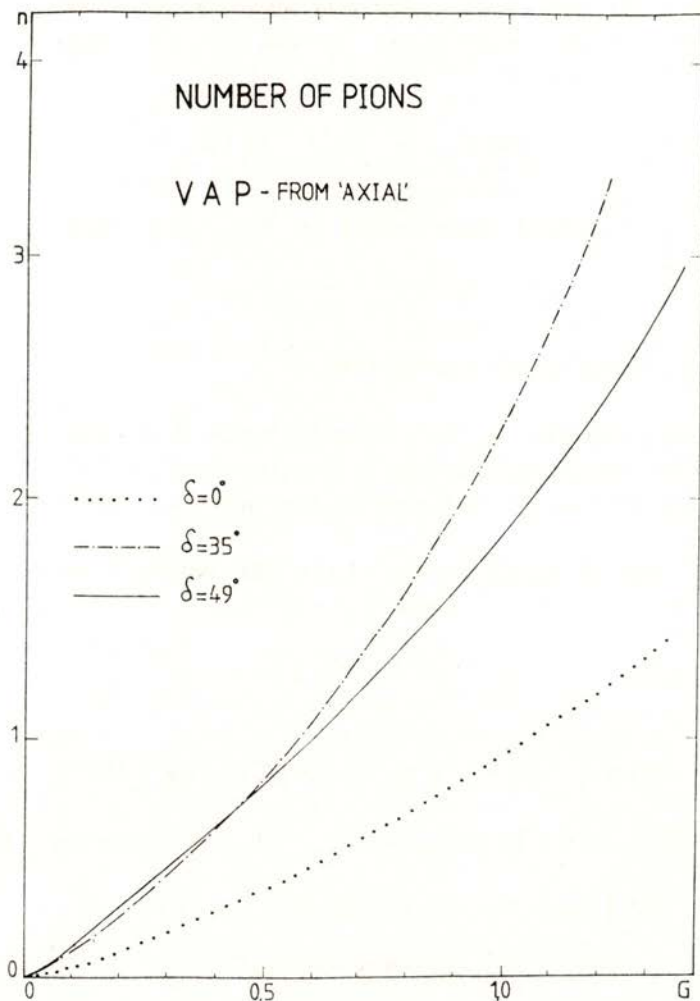

Fig. 4 — The number of pions in the pion cloud of the nucleon. The projected states have been obtained from axially symmetric coherent states of pions in a variation-after-projection calculation with respect to the pion amplitudes.

been obtained in a VBP calculation, in order to see the importance of the VAP procedure, for small values of the coupling constant.

The determination of the optimal parameters ξ and δ and, afterwards, the evaluation of $E_{1/2\ 1/2}/G^2$, may be done analytically for $G \to 0$. The minimization of $E_{1/2\ 1/2}$ with respect to ξ and δ yields $\delta = \text{arctg} (4\sqrt{2}/5)$, $\xi = 9\ G$ and the energy is

$$E_{1/2\ 1/2} = -20.52\ G^2. \tag{4.15}$$
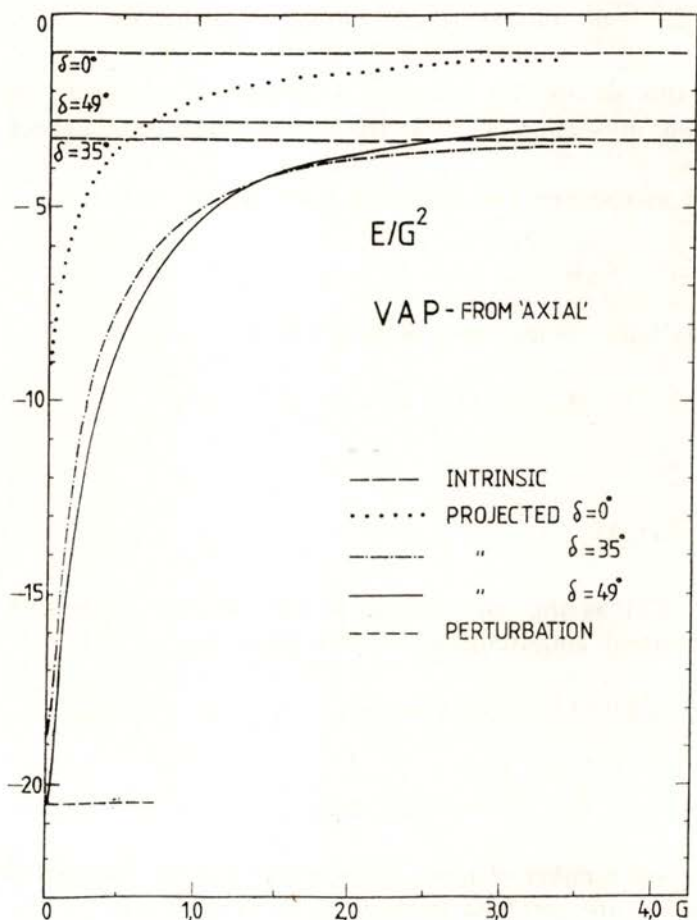
Fig. 5 — The quantity E/G^2 for the nucleon is plotted versus coupling constant for different values of the mixing angle. The physical states have been obtained from axially symmetric coherent states of pions. Here a scale different from the one of fig. 3 is used.

This agrees with (3.5), given by the perturbational calculation. Therefore one is led to the conclusion that the VAP from axially symmetric coherent states of pions should be a good approximation in the regimes of weak coupling strength. In regimes of very large G, the axially symmetric state considered in this section seems to be not so good: the energy (4.6) obtained in this limit is only one third of (3.7).

5 – PROJECTION FROM HEDGEHOG

In this section we consider a projection similar to the one presented in section 4, now from the hedgehog coherent state of pions.

Let us consider the following bare baryon state:

$$| B >_h = (1/\sqrt{2}) \; (| N >_h + | \Delta >_h) \qquad (5.1)$$

with the bare nucleon and delta states given by

$$| N >_h = (1/\sqrt{2}) \; (| N^{+}_{-1/2} > - | N^{0}_{1/2} >) \qquad (5.2a)$$

and

$$| \Delta >_h = (1/2) \; (| \Delta^{++}_{-3/2} > - | \Delta^{+}_{-1/2} > + | \Delta^{0}_{1/2} > - | \Delta^{-}_{3/2} >) \qquad (5.2b)$$

Taking (5.1) as the bare baryon in the coherent state (3.8), the self-consistent amplitudes (3.14) are given by

$$\xi_{tm} = (\xi /\sqrt{3}) \; (\delta_{t1} \, \delta_{m-1} + \delta_{t-1} \, \delta_{m1} - \delta_{t0} \, \delta_{m0}) , \qquad (5.3)$$

where

$$\xi = (9\sqrt{3}/5) \; G . \qquad (5.4)$$

The average number of pions in the cloud and the intrinsic interaction energy are obtained from (3.11-12) and (5.3-4):

$$S = E_{kin}^{(intr.)} = \xi^2 = (243/25) \; G^2 ; \qquad (5.5a)$$

$$E_{coup}^{(intr.)} = - (18\sqrt{3}/5) \; G \, \xi = - (486/25) \; G^2 . \qquad (5.5b)$$

The coherent state (3.8) now reads as

$$| Hh > = \mathcal{N}(\xi) \exp [(\xi/\sqrt{3}) (a_{1\text{-}1}^{+} + a_{\text{-}11}^{+} - a_{00}^{+})] \, | B >_h \qquad (5.6)$$

This state is known under the name 'hedgehog' and its energy, the sum of (5.5a) and (5.5b), is given by (3.7).

One should notice that the coherent state (5.6) contains bare nucleon and bare delta components exactly in the same proportion. It is interesting to study a generalized hedgehog coherent state which, like (4.7), allows different weights for the bare nucleon and the bare delta:

$$| Hh (\delta) > = \mathcal{N}(\xi) \exp [(\xi/\sqrt{3}) (a_{1\text{-}1}^{+} + a_{\text{-}11}^{+} - a_{00}^{+})] \, | B (\delta) >_h ,$$
$$(5.7)$$

where

$$| B (\delta) >_h = \cos \delta \, | N >_h + \sin \delta \, | \Delta >_h . \qquad (5.8)$$

The self-consistent pion amplitudes (3.14) are identical to (5.3) but now

$$\xi = G \sqrt{3} (1 + (8/5) \sin \delta \cos \delta) . \qquad (5.9)$$

The total intrinsic energy is

$$E^{(intr.)} = -3 G^2 (1 + (8/5) \sin \delta \cos \delta)^2 . \qquad (5.10)$$

Minimization with regard to δ yields $\delta = 45°$, i. e. the result (3.7) is recovered, according to ref. [8]. Obviously, if (5.7) is projected onto states with good isospin and angular momentum quantum numbers and, afterwards, the projected energies are varied with respect to the mixing angle, then δ will take values in general different from 45°.

The generalized hedgehog coherent state has grand spin zero, i. e. it only contains components with $J = T$ and $M = -M_T$. Therefore it is enough to perform the projection restricted to one space [8, 11]. The spin and isospin eigenstates are

$$| J ; T = J ; M ; -M > = P_{JM} | Hh (\delta) > , \qquad (5.11)$$

with P_{JM} the projector defined in Appendix B. There, the norms of the projected states are evaluated and the general expression for the kinetic energy of the projected states is derived. The evaluation of the expectation values for the coupling Hamiltonian is straightforward and the total projected energies read as

$$E_{1/2} = (\xi^2/3) \ [1 + f_{3/2}(\delta, \xi^2)/f_{1/2}(\delta, \xi^2)]$$

$$- 2G\sqrt{3}\,\xi \ [f_{1/2}(\delta, \xi^2) + (4/5) \ \sin\delta \ \cos\delta \ (f_{1/2}^N + f_{1/2}^\Delta)]/f_{1/2}(\delta, \xi^2)$$

$$(5.12)$$

$$E_{3/2} = (\xi^2/3) \ [1 + (f_{1/2}(\delta, \xi^2) + f_{5/2}(\delta, \xi^2))/f_{3/2}(\delta, \xi^2)]$$

$$- 2G\sqrt{3}\,\xi \ [f_{3/2}(\delta, \xi^2) + (4/5) \ \sin\delta \ \cos\delta \ (f_{3/2}^N + f_{3/2}^\Delta)]/f_{3/2}(\delta, \xi^2)$$

$$(5.13)$$

where f_J, f_J^N and f_J^Δ are given by (B. 6,14).

For $\delta = 45°$ these are the projected energies obtained from the normal hedgehog (5.6).

5.1 — *Variation-before-projection*

In a VBP calculation from the normal hedgehog, one gets the projected numbers of pions and energies, putting $\delta = 45°$ in (B. 20) and (5.12-13) respectively, and substituting ξ by its self-consistent value (5.4). For the nucleon, the projected number of pions is shown in Fig. 6, in dependence of G. The dashed curve in Fig. 7 refers to the quantity $E_{1/2} / G^2$ in a VBP from normal hedgehog. Figs. 6 and 7 also display the number of pions and $E_{1/2} / G^2$ obtained in the MFA and VAP.

In the limit $G \to 0$ one gets $E_{1/2} / G^2 = -14.58$, a value which is very far from the one given by (3.5) and well recovered in the VAP-from 'axial'.

5.2 — *Variation-after-projection*

In a VAP from normal hedgehog, the amplitude ξ is determined by means of a Ritz's variation of the projected energies (5.12-13) with $\delta = 45°$. For the numerical evaluation of the projected quantities we have used the procedure already explained in the previous section when the VAP-from 'axial' was considered.
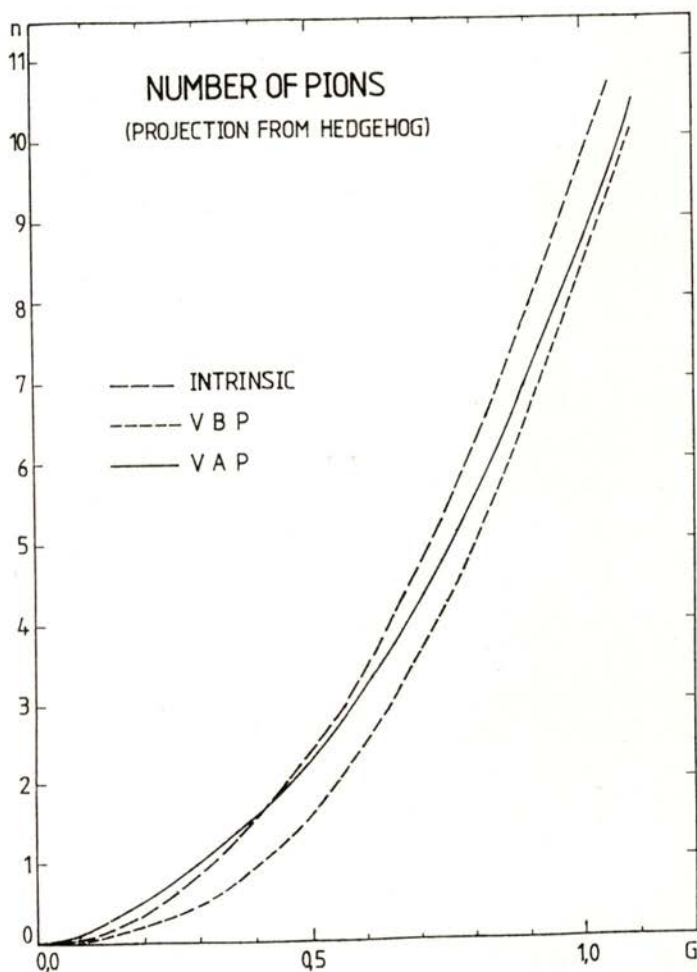

Fig. 6 — The number of pions in the pion cloud of the nucleon. The curves refer to the intrinsic hedgehog state and to the projected nucleon obtained from the hedgehog in VAP and VBP calculations.

The projected nucleon energy and number of pions are shown in Figs. 6 and 7 (solid lines). In the limit $G \to 0$ one gets $E_{1/2} = -19.44\ G^2$ for the nucleon and $E_{3/2} = -9.72\ G^2$ for the delta, i. e. the perturbative results given by (3.5-6) are almost reached. However, a full VAP calculation using the delta dependent hedgehog coherent state (5.7) improves the results obtained from
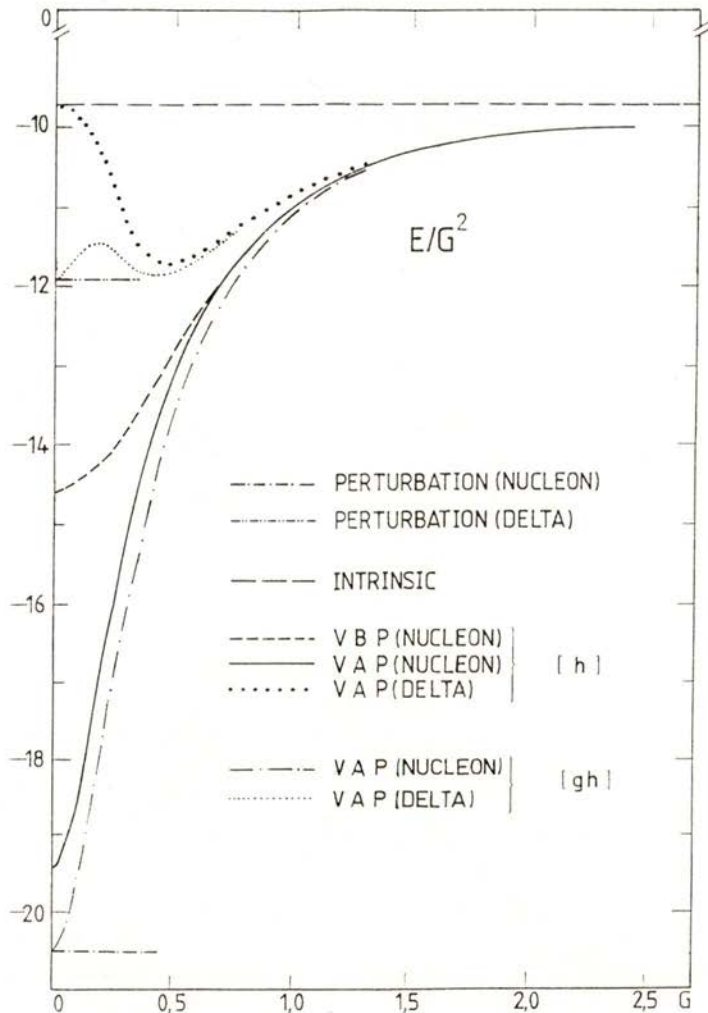

E/G^2

PERTURBATION (NUCLEON)
PERTURBATION (DELTA)

INTRINSIC

V B P (NUCLEON)
V A P (NUCLEON) [h]
V A P (DELTA)

V A P (NUCLEON) [gh]
V A P (DELTA)

Fig. 7 — For the nucleon and the delta, the quantities E/G^2 obtained in a projection from the hedgehog state (5.6), [h], and from the general hedgehog (5.7), [gh], are plotted versus coupling constant.

66

Portgal. Phys. — Vol. 17, fasc. 1-2, pp. 49-74, 1986

normal hedgehog, as it is shown in Fig. 7, in the whole range of G. In particular, the energies of the nucleon and the delta in the limit $G \to 0$, turn out to be exactly the perturbative values (3.5-6), for mixing angles $\delta = 58°$ (nucleon) and $\delta = 68.2°$ (delta).

In the limit $G \to \infty$, when a large number of pions is present in the cloud, the best value for δ is $45°$ in both cases. In this region the projection does not alter the MFA results, i. e. the nucleon and its isobars form a rotational band with a very large moment of inertia.

6 – CONCLUSIONS

In this paper we have studied different approximation schemes to the Hamiltonian for a system of non-self-interacting pions coupled to a static source with bare nucleon and bare delta.

In a realistic calculation, the approximation more suitable depends strongly on the size of source and the strength of the pion field. Here, the number of pions is a decisive parameter. We emphasize the usefulness of the simple model: for a given number of pions obtained in a realistic calculation one can read the bare coupling constant G from Figs. 1, 2, 4 or 6 and then, from Figs. 3, 5 and 7 one may compare the behaviour of the different approximations studied in this work, for that range of G.

We shall briefly discuss and compare the approximations considered in this work. The VAP is the right procedure to introduce quantum fluctuations in the mean-field or coherent state description of the pion cloud. The importance of this method is clearly demonstrated comparing the curves displayed in Figs. 3 and 5 (axial symmetric coherent state), on the one hand and Fig. 7 (hedgehog coherent state), on the other hand, for small values of G. From Figs. 3 and 5 one also concludes that the inclusion of bare delta in the intrinsic states, allowing for some nucleon-delta transitions, is very important.

The perturbative energy for the nucleon is exactly reproduced in the VAP-from 'axial' calculation, but a similar agreement with the energy (3.7) is not observed for $G \to \infty$. The hedgehog apparently is a much better ansatz. We reemphasize the following remarkable fact: using the generalized hedgehog one obtains the exact results (3.5-7), which refer to both the limits of very weak and very strong couplings, either for nucleon or delta.

Finally we refer a technical aspect: all projected quantities (energy, number of pions, etc.) may be expressed as functions of the norms, or their derivatives, of the projected states. For the axial state, these norms are given in terms of power series expansions which converge very fast. For the hedgehog they are expressed as functions of the modified Bessel functions $I_\nu(z)$, which are easily evaluated numerically by rapidly converging series in z or $1/z$.

APPENDIX A — THE NORM OF THE PROJECTED COHERENT STATE (AXIAL SYMMETRY)

From the intrinsic kets

$$|\psi_N> = \exp(\sqrt{S}\, a_{00}^+)\, |N_{1/2}^+> \tag{A.1}$$

and

$$|\psi_\Delta> = \exp(\sqrt{S}\, a_{00}^+)\, |\Delta_{1/2}^+>\,, \tag{A.2}$$

states with the quantum numbers of a nucleon are obtained according to

$$P_{1/2\,1/2}|\psi_N> = \iint d(\cos\beta)\, d(\cos\tilde\beta)\, d_{1/2\,1/2}^{1/2}(\beta)$$
$$d_{1/2\,1/2}^{1/2}(\tilde\beta)\, R(\beta)\, R(\tilde\beta)\,|\psi_N> \tag{A.3}$$

and

$$P_{1/2\,1/2}|\psi_\Delta> = \iint d(\cos\beta)\, d(\cos\tilde\beta)\, d_{1/2\,1/2}^{1/2}(\beta)$$
$$d_{1/2\,1/2}^{1/2}(\tilde\beta)\, R(\beta)\, R(\tilde\beta)\,|\psi_\Delta> \tag{A.4}$$

$P_{1/2\,1/2}$ is a projector with the properties: $P^2_{1/2\,1/2} = P^+_{1/2\,1/2} = P_{1/2\,1/2}$
The operator $R(\beta)$ rotates the unprojected state by an angle β around the y-axis and $R(\tilde{\beta})$ performs a similar rotation in isospin.

The overlap integrals are defined and evaluated as in ref. [5, 6, 9, 10]:

$$F_N(S) = \langle \psi_N | P_{1/2\,1/2} | \psi_N \rangle$$

$$= \iint d(\cos\beta)\, d(\cos\tilde{\beta})\, d^{1/2}_{1/2\,1/2}(\beta)\, d^{1/2}_{1/2\,1/2}(\tilde{\beta})\, d^{1/2}_{1/2\,1/2}(\beta)$$

$$d^{1/2}_{1/2\,1/2}(\tilde{\beta})\, e^{\,S\cos\beta\cos\tilde{\beta}}; \tag{A.5}$$

$$F_\Delta(S) = \langle \psi_\Delta | P_{1/2\,1/2} | \psi_\Delta \rangle$$

$$= \iint d(\cos\beta)\, d(\cos\tilde{\beta})\, d^{1/2}_{1/2\,1/2}(\beta)\, d^{1/2}_{1/2\,1/2}(\tilde{\beta})\, d^{3/2}_{1/2\,1/2}(\beta)$$

$$d^{3/2}_{1/2\,1/2}(\tilde{\beta})\, e^{\,S\cos\beta\cos\tilde{\beta}}. \tag{A.6}$$

The most practical way is to evaluate these integrals by power series expansion which converges rapidly for $S \lesssim 50$. By calling $\cos\beta = x$ and $\cos\tilde{\beta} = y$, we get

$$F_N(S) = \int_{-1}^{+1}\int_{-1}^{+1} dxdy\, (1+x)/2 \cdot (1+y)/2 \cdot [1 + Sxy +$$

$$(Sxy)^2/2! + \ldots] = f(S) + f'(S) \tag{A.7}$$

where

$$f(S) = \sum_{n=0}^{\infty} \frac{S^{2n}}{(2n)!\,(2n+1)^2} \tag{A.8}$$

and $f'(S)$ denotes derivative with respect to S. Similarly we get

$$F_\Delta(S) = \int_{-1}^{+1}\int_{-1}^{+1} dxdy\, (1+x)/2 \cdot (1+y)/2 \cdot (3x-1)/2 \cdot$$

$$\cdot (3y-1)/2 \cdot [1 + Sxy + (Sxy)^2/2! + \ldots]$$

$$= (1/4)\,f(S) + f'(S) + (9/4)\,f''(S) + g(S), \tag{A.9}$$

where

$$g(S) = -3/2 \sum_{n=0}^{\infty} \frac{S^{2n}}{(2n)!(2n+1)(2n+3)} \ . \qquad (A.10)$$

For the state

$$|\psi> = \cos \delta \, |\psi_N> + \sin \delta \, |\psi_\Delta>, \qquad (A.11)$$

the overlap integral is

$$F = <\psi \, | \, P_{1/2 \, 1/2} \, | \, \psi> = \cos^2 \delta \, F_N + \sin^2 \delta \, F_\Delta \qquad (A.12)$$

In order to calculate the number of pions in the projected state, we take into account the relation

$$\frac{\partial |\psi>}{\partial S} = \frac{1}{2\sqrt{S}} \, a_{oo}^+ \, |\psi> = \frac{1}{2S} \, a_{oo}^+ \, a_{oo} \, |\psi>, \qquad (A.13)$$

to evaluate the derivative of the overlap integral F. This gives

$$dF/dS = d<\psi \, | \, P_{1/2 \, 1/2} \, | \, \psi> /dS$$
$$= (1/S) <\psi \, | \, P_{1/2 \, 1/2} \, a_{oo}^+ \, a_{oo} \, | \, \psi> \ . \qquad (A.14)$$

The projected number of pions is easily obtained:

$$n = F^{-1} <\psi \, | \, P_{1/2 \, 1/2} \sum_{tm} a_{tm}^+ \, a_{tm} \, P_{1/2 \, 1/2} | \, \psi>$$
$$= F^{-1} <\psi \, | \, P_{1/2 \, 1/2} \sum_{tm} a_{tm}^+ \, a_{tm} | \, \psi>$$
$$= F^{-1} <\psi \, | \, P_{1/2 \, 1/2} \, a_{oo}^+ \, a_{oo} \, | \, \psi> = (S/F) \ dF/dS, \qquad (A.15)$$

since only $a_{oo} \, |\psi>$ in non-zero.

APPENDIX B — THE NORM OF THE PROJECTED COHERENT STATE (HEDGEHOG)

The generalized hedgehog coherent state is defined by

$$| \, Hh(\delta)> = \cos \delta \, | \, \tilde{N}>_h + \sin \delta \, | \, \tilde{\Delta}>_h \qquad (B.1)$$

70

Portgal. Phys. — Vol. 17, fasc. 1-2, pp. 49-74, 1986

where

$$| \tilde{N} >_h = \exp [\sqrt{S/3} \; (a^+_{1-1} + a^+_{-11} - a^+_{00})] \, | N >_h \qquad \text{(B.2)}$$

and

$$| \tilde{\Delta} >_h = \exp [\sqrt{S/3} \; (a^+_{1-1} + a^+_{-11} - a^+_{00})] \, | \Delta >_h ; \qquad \text{(B.3)}$$

$| N >_h$ and $| \Delta >_h$ are defined by (5.2). The state (B.1) has grand spin zero:

$$(J + T) \, | \, Hh (\delta) > \, = 0 , \qquad \text{(B.4)}$$

i. e. it only contains components with $J = T$ and $M_T = - M$. Thus, separate projections for spin and isospin are not required. The eigenstates of spin and isospin are obtained from (B.1) according to [11]

$$| \, J , \, T = J ; \, M , - M > \, = P_{JM} \, | \, Hh (\delta) >$$
$$= (2J + 1)/8\pi^2 \int d^3 \Omega \; \mathscr{D}^J_{MM} (\Omega) \, R (\Omega) \, | \, Hh (\delta) > . \qquad \text{(B.5)}$$

Here Ω represents the three Euler angles α, β and γ and $R (\Omega)$ stands for the rotation operator. The operator P_{JM} is a projector: $P^2_{JM} = P^+_{JM} = P_{JM}$.

We shall always consider $M = J$; the norm of this state is

$$f_J (\delta , \, S) = \, < Hh (\delta) \, | \, P_{JJ} | \, Hh (\delta) >$$
$$= \cos^2 \delta \; f^N_J (S) + \sin^2 \delta \; f^\Delta_J (S) , \qquad \text{(B.6)}$$

where

$$f^N_J (S) = (2J + 1)/8\pi^2 \int d^3 \Omega \; \mathscr{D}^J_{JJ} (\Omega) \, \mathscr{K}_N (\Omega , \, S) \qquad \text{(B.7a)}$$

$$f^\Delta_J (S) = (2J + 1)/8\pi^2 \int d^3 \Omega \; \mathscr{D}^J_{JJ} (\Omega) \, \mathscr{K}_\Delta (\Omega , \, S) . \qquad \text{(B.7b)}$$

In these expressions, the kernels $\mathscr{K}_N$ and $\mathscr{K}_\Delta$ are given by

$$\mathscr{K}_N (\Omega , \, S) = \, _h < \tilde{N} \, | \, R (\Omega) \, | \, \tilde{N} >_h$$
$$= \mathscr{K}_\pi (\Omega , \, S) \, \cos \beta/2 \, \cos (\alpha + \gamma)/2 \qquad \text{(B.8a)}$$

and

$$\mathscr{N}_\Delta (\Omega , S) = {}_h< \tilde{\Delta} \mid R(\Omega) \mid \tilde{\Delta} >_h$$

$$= \mathscr{N}_N (\Omega , S)(2\cos^2 \beta/2 \ \cos^2 (\alpha + \gamma)/2 - 1), \quad \text{(B.8b)}$$

where

$$\mathscr{N}_\pi (\Omega, S) = \exp\{ S/3 \ [(1 + \cos\beta)\cos(\alpha + \gamma) + \cos\beta]\} \quad \text{(B.9)}$$

refers to the overlap between rotated pion clouds. To calculate the norms (B.7) we use the expression

$$\mathscr{D}^J_{JJ}(\Omega) = e^{-iJ(\alpha + \ )} (\cos\beta/2)^{2J} \quad \text{(B.10)}$$

and define the following new variables: $z = 2S/3$, $x = \cos^2 \beta/2$, $k = J-1/2$ and $\varphi = \alpha + \gamma$ ($d\alpha d\gamma = d\alpha d\varphi$, and the integral over α is trivial, giving 2π). The expressions for f_J^N and f_J^Δ reduce to

$$f_J^N = (k + 1) \ e^{-z/2} \int_0^1 dx \ x^{k+1} \ e^{zx}$$

$$\left\{ \frac{1}{2\pi} \int_0^{2\pi} d\varphi \ [\cos k\varphi + \cos(k + 1)\varphi] \ e^{zx \cos\varphi} \right\} \quad \text{(B.11a)}$$

$$f_J^\Delta = -f_J^N + \frac{k + 1}{2} \ e^{-z/2} \int_0^1 dx \ x^{k+2} \ e^{zx} \left\{ \frac{1}{2\pi} \int_0^{2\pi} d\varphi \ e^{zx \cos\varphi} \right.$$

$$\left. \cdot [\cos(k - 1)\varphi + 3\cos k\varphi + 3\cos(k + 1)\varphi + \cos(k + 2)\varphi] \right\}$$

$$\text{(B.11b)}$$

and we recognize the integrals over φ as the modified Bessel functions of integer order $I_y(t)$ (see (9.6.19) of ref. [12]):

$$f_J^N = (k + 1) \ e^{-z/2} \ z^{-(k+2)} \int_0^z dt \ e^t \ t^{k+1} \ [I_k(t) + I_{k+1}(t)]$$

$$\text{(B.12a)}$$

$$f_J^\Delta = -f_J^N + \frac{k + 1}{2} \ e^{-z/2} \ z^{-(k+3)} \int_0^z dt \ e^t \ t^{k+2}$$

$$[I_{k-1}(t) + 3I_k(t) + 3I_{k+1}(t) + I_{k+2}(t)], \quad \text{(B.12b)}$$

72

Portgal. Phys. — Vol. 17, fasc. 1-2, pp. 49-74, 1986

where $t = xz$. Defining the function $g_{\mu,\nu}(z)$ (see (11.3.1) of ref. [12], with $p = -1$) as

$$g_{\mu,\nu}(z) = \int_0^z dt\, e^t\, t^\mu\, I_\nu(t) \qquad (B.13)$$

the above expressions for the overlaps read as

$$f_J^N = (k+1)\, e^{-z/2}\, z^{-(k+2)}\, [\, g_{k+1,k}(z) + g_{k+1,k+1}(z)\,] \qquad (B.14a)$$

$$f_J^\Delta = -f_J^N + (k+1)\, e^{-z/2}\, z^{-(k+3)}\, [\, g_{k+2,k+1}(z) + g_{k+2,k+2}(z)$$
$$+ (k/2)\, g_{k+1,k}(z) + 3(k+1)/2\, g_{k+1,k+1}(z)\,]. \qquad (B.14b)$$

In order to write f_J^Δ in this form, we have used the recursion relation for the modified Bessel functions ((9.6.26) of ref. [12]) and the definition (B.13) of the g-functions.

The expressions in brackets in (B.14) can be written as functions of $I_\nu(z)$. Using the formulas (11.3.3,6,12) and (9.6.26) of ref. [12], one gets

$$f_J^N(S) = (1/z)\, \exp(z/2) \cdot (k+1)\, I_{k+1}(z) \qquad (B.15a)$$

$$f_J^\Delta(S) = 1/(2z)\, \exp(z/2)\, [\, k\, I_k(z) + (k+2)\, I_{k+2}(z)\,] \qquad (B.15b)$$

where $k = J - 1/2$ and $z = 2S/3$.

The modified Bessel functions $I_\nu(z)$ are evaluated by rapidly converging power series in z, or, for $z > 3.75$, by the asimptotic series in z^{-1} (see ref. [12]).

In order to evaluate the kinetic energy one should note that, for the state (B.1) the property (3.9) reads as

$$< Hh(\delta)\,|\, a_{tm}^+ = \sqrt{S/3}\, \delta_{t-m}(-1)^{t+1}\, < Hh(\delta)\,|. \qquad (B.16)$$

The projected kinetic energy is

$$E_{kin}^J = f_J^{-1}(\delta, S)\, < Hh(\delta)\,|\, P_{JJ} \sum_{tm} a_{tm}^+ a_{tm} P_{JJ}\,|\, Hh(\delta) >, \qquad (B.17)$$

where $f_J(\delta, S)$ is defined by (B.6). The first projector can be commuted to the right of the kinetic energy operator and dropped. Next we use the property (B.16) and take into account the com-

mutation relation of P_{JJ} with the operator a_{t-t} (see Appendix B of ref. [6]):

$$a_{t-t} P_{JJ} = \sum_{J'} P_{J' J-t} \, a_{t-t} \, [\mathcal{C}^{JJ}_{J' J-t\,1\,t}]^2 + \text{other terms}, \quad \text{(B.18)}$$

where the sum is over all values of J' such that

$$|J' - 1| \leqslant J \leqslant |J' + 1|. \quad \text{(B.18a)}$$

In (B.18) the 'other terms' contain the operator a_{tm} with $t \neq -m$ which gives zero acting on the hedgehog ket according to (B.16) and therefore can be ignored. Noticing that $< Hh(\delta) \,|\, P_{J' J-t} \,|\, Hh(\delta) >$ is independent of $J - t$ and using the property of the Clebsh-Gordan coefficients

$$\sum_t [\mathcal{C}^{JJ}_{J' J-t\,1\,t}]^2 = 1, \quad \text{(B.19)}$$

one gets

$$E^J_{kin} = (S/3) \, f^{-1}_J (\delta, S) \sum_{J'} f_{J'} (\delta, S). \quad \text{(B.20)}$$

REFERENCES

[1] A. Chodos and C. B. Thorn, *Phys. Rev.*, **D 12** (1975), 2733.

[2] G. E. Brown and M. Rho, *Phys. Lett.*, **82 B** (1979), 177.

[3] S. Théberge, A. W. Thomas and G. A. Miller, *Phys. Rev.*, **D 22** (1980), 2838.

[4] S. Kahana, G. Ripka and V. Soni, *Nucl. Phys.*, **A 415** (1984), 351; M. C. Birse and M. K. Banerjee, *Phys. Lett.*, **136 B** (1984), 284; *Phys. Rev.*, **D 31** (1985), 118.

[5] J. da Providência and J. N. Urbano, *Phys. Rev.*, **D 18** (1978), 4208.

[6] B. Golli, M. Rosina and J. da Providência, *Nucl. Phys.*, **A 436** (1985), 733.

[7] J. da Providência, *Nucl. Phys.*, **B 57** (1973), 536.

[8] M. Fiolhais, J. N. Urbano and K. Goeke, *Phys. Lett.*, **150 B** (1985), 253.

[9] J. N. Urbano and K. Goeke, *Phys. Lett.*, **143 B** (1984), 319.

[10] J. N. Urbano and K. Goeke, *Phys. Rev.*, **D 32** (1985), 2396.

[11] B. Golli and M. Rosina, *Phys. Lett.*, **165 B** (1985), 347.
      M. C. Birse, *Phys. Rev.*, **D 33** (1986), 1934.

[12] M. Abramowitz and I. A. Stegun, *Handbook of Mathematical Functions*, Dover Publications Inc., New York (1970), 375-378, 483.

MODEL SIMULATION OF DIFFERENTIAL CROSS SECTIONS IN ION-PAIR FORMATION COLLISIONS

M. J. P. Maneira (¹), R. F. M. Lobo (¹) and A. M. C. Moutinho (¹)

Centro de Física Molecular das Universidades de Lisboa

(Instituto Nacional de Investigação Científica) Complexo I, I.S.T.

Av. Rovisco Pais, 1000 Lisboa, Portugal

ABSTRACT — A simple method to simulate differential cross sections in ion-pair formation collisions is presented and discussed. The colliding system is assumed to be described by a two state interaction, where an ionic diabatic potential crosses a covalent one at a certain internuclear distance r_c. At that point the possibility of an electronic transition is taken into account. The ionic diabatic potential is the addition of a Coulomb attraction and a Born-Mayer repulsion. The same type of repulsion is used to describe the covalent diabatic potential. Both deflections due to attractive and repulsive forces are obtained analytically. Straight line trajectories and impulsive interactions are assumed and the small angle approximation is used. The simulated differential cross sections for the Na + I system are compared with calculations and with experimental results from other authors.

1 – INTRODUCTION

In the last ten years much has been done in ion-pair formation in neutral collisions. Experimental results and theoretical models are giving some insight into the understanding of fast collisions between alkali atoms and several targets. Total cross sections as well as single and double differential ones were obtained by several groups [1, 2, 3].

The differential cross sections $\sigma(\Theta)$ are normally presented as plots of $\sigma(\Theta) \cdot \sin\Theta$ as a function of $\tau = E \cdot \Theta$, where E is the energy of the collision and Θ the scattering angle of the ionized projectile (all symbols refer to the center of mass system and atomic units are used unless stated otherwise). These plots show

---

(¹) Departamento de Física, Faculdade de Ciências e Tecnologia (Universidade Nova de Lisboa), Quinta da Torre — 2825 Monte da Caparica — Portugal.

Portgal. Phys. — Vol. 17, fasc. 1-2, pp. 75-91, 1986

75

in general two or three maxima, more or less hidden by the smoothing effects of different resolutions of the molecular beam experiments. The theoretical models attribute the maximum nearer the forward direction (i. e., lower $\tau = E. \theta$ values) to projectile particles coming through "covalent" trajectories. This means that for internuclear distances lower than the electron jump distance, r_c, the interaction has been a covalent one because an electronic adiabatic transition did not occur at the first crossing. The remaining structure at higher τ values is attributed to projectile particles coming through "ionic" trajectories: this means that for internuclear distances lower than r_c the interaction has been mainly ionic because an adiabatic electronic transition has occurred at the first crossing.

Using such basic features, ion pair formation both in atom-atom and atom-molecule collisions has been interpreted [4]. However special attention has been paid to the alkali atom-halogen atom collisions as an example of an electron transfer involving two well defined states.

Delvigne and Los [5], measured the differential cross sections for the collisions $Na + I \rightarrow Na^+ + I^-$, and have done calculations using the deflection function, the Landau-Zener-Stueckelberg probability (LZS), the stationary-phase approximation and JWKB phase shifts. They used a Rittner ionic potential that includes a Coulomb term, a screened polarization term, a dipole-dipole interaction, a Van der Waals and a Born-Mayer term; for the covalent potential they adopted the two last terms. They calculated the deflection functions using a method of preset error, relying heavily on programming facilities. Remarkable agreement was obtained with the main features of the experimental results, namely the ionic structure (made up of an intermediate ionic peak and rainbow ionic one), the covalent peak as well as some of the Stueckelberg oscillations.

Faist and Levine [6] simulated the processes $(Na, Li) + I \rightarrow (Na^+, Li^+) + I^-$ at post-threshold energies considering a more sophisticated Rittner potential than that of Delvigne and Los and solving the matrix Schroedinger equation for two states with a JWKB method. The main features of the experimental results were reproduced. However comparisons made with the LZS model showed only qualitative agreement; quantitatively there were some deviations.

Later on Gillen et al. [7], using a much simpler model, were able to explain partly the general behaviour of the results of Delvigne and Los. They deleted completely the repulsive forces in the covalent as well as in the ionic potential curves, used only a Coulomb potential to describe the attractive forces in the ionic curves, and disregarded completely the Landau-Zener probability influence. Such drastic simplifications allowed an analytic exact solution for the deflection function, explaining the position of the covalent and ionic intermediate maxima and the minimum in between them. Moreover, at an energy of 38.7 eV, they succeeded in reproducing their relative intensities. In fact that was possible because the Landau-Zener probability is about one half at this collisional energy. However, the ionic rainbow at higher τ was not reproduced since repulsive forces were not taken into account.

The present work is situated between the drastic assumption of Gillen leading to rather straightforward calculations, and the more detailed models and realistic potentials used by Delvigne and Faist, with their inherent calculation difficulties. Repulsive forces were introduced through Born-Mayer short range repulsions both in covalent and ionic diabatic potential curves, therefore obtaining a simulation more realistic than that of Gillen. We disregard some terms considered by Delvigne and Faist, simplifying considerably the calculations and the number of parameters of the model. It was possible then to obtain analytical solutions for the ionic and covalent deflection curves. The Landau-Zener probability is calculated at the crossing of the potential energy curves and depends on the diabatic coupling matrix element H_{12}, which is obtained from an empirical expression by Moutinho [8]. The model is entirely classical, except for the transition probabilities, where quantum mechanics is involved. Therefore interference effects could not be reproduced. However the most relevant structure found experimentaly by Delvigne for Na + I was reproduced, namely the position of minima and maxima, as well as the relative intensities.

II — THE MODEL

The collision is described using a two-state approach of an interaction between states of the same symmetry. When the alkali atom is at a large distance (in the ingoing part of the collision)

the system is described by a "covalent" state, as neutral particles are approaching. In the far outgoing, the system will be described by an "ionic" state, as charge exchange occurs. It is at the crossing of the two potential curves that the electronic transition ("electron jump") between the two states can occur. In general in one single collision the crossing can occur twice, giving two chances for the electron to jump. It is clear that the electron transition may occur in the neighbourhood of the crossing and not necessarily at the crossing itself, as a consequence of the uncertainty principle. This fact, however, is disregarded in the model, as the Landau-Zener probability is calculated at the point of crossing. The deflection of the probe particle (the alkali projectile) depends mainly on the interaction inside the sphere of radius r_c. If the electron jump has occured at the first crossing the interaction will be an ionic one from there to infinity and a large deflection is obtained. If the electron jump occurs at the second crossing, the ionic potential acts only in the far outgoing part of the collision, leading to a lower deflection.

To calculate the differential cross sections and present them as plots of $\sigma(\theta) \cdot \sin\theta$, as a function of $E. \theta$, one makes use of

$$\sigma(\theta) \ \sin\theta = \sum_k p(1-p) \ b_k \ |db_k/d\theta| \tag{1}$$

where p is the probability of a diabatic transition at the crossing, $\sigma(\theta)$ is the differential cross section and $db/d\theta$ is the derivative of the impact parameter b with respect to the deflection angle θ. As the deflection function is not single valued, and net repulsive trajectories cannot be distinguished from the net attractive ones, the summation of equation (1) must be carried out over the single valued branches of the absolute value of the deflection function, which is taken into account by the index k. To obtain the deflection curves, ionic and covalent potential energy curves must be assumed. For the covalent curve a purely repulsive Born-Mayer potential $V_c(r)$ of the form,

$$V_c(r) = A_c \ \exp(-r/B_c) - \Delta E \tag{2}$$

is used. ΔE is the endoergicity of the process, that is, the asymptotic energy difference between ionic and covalent states. A_c and B_c are constants. This potential seems reasonable because short range interactions can be represented by exponentials, even in the case

of molecular interactions, as pointed out by Bohm and Ahlrichs [9], as a result of SCF calculations.

For the ionic potential curve $V_i(r)$, a repulsive potential also of the Born-Mayer type is added to the Coulomb attraction, giving

$$V_i(r) = -1/r + A_i \exp(-r/B_i) \tag{3}$$

Assuming the potentials of equations (2) and (3), the validity of the model is restricted to the validity of the relation

$$r_c = 1/\Delta E \tag{4}$$

Any time the internuclear distance in a trajectory with a certain impact paremeter b reaches a value $r = r_c$ a commutation from one potential to the other can be done. For ion pair formation only two families of paths are contributing, the one where the "electron jump" occurs at the first crossing and the one where it occurs at the second crossing. The relative weight of these trajectories is determined by the Landau-Zener probability. The deflection depends on how much attraction and repulsion is experienced during the collision, and therefore it depends also on the point where the commutation takes place.

If the target particle can be considered initially at rest in the laboratory system and the impulse approximation is assumed, the total deflection can be calculated as the sum of the deflections τ_a and τ_r due to attraction and repulsion independently, as the net effect of longitudinal forces is neglected [10]. Let us consider a collision with energy E, impact parameter b, and energy loss ΔE. Suppose the electron jump has occurred at the first crossing. The total deflection τ^i corresponding to the ionic trajectory, will be given by

$$\tau^i = \tau_a^i + \tau_r^i \tag{5}$$

where τ_a^i and τ_r^i are the attractive and repulsive ionic deflections. Suppose now that the electron jump occurs at the second crossing. The total deflection τ^c corresponding to the covalent trajectory, will be given by

$$\tau^c = \tau_a^c + \tau_r^c \tag{6}$$

where τ_a^c and τ_r^c are attractive and repulsive covalent deflections.

Analytic expressions for covalent and ionic attractive deflections were deduced from Gillen [7] and in the small angle approximation are given by

$$\tau_a^c = E \left[\alpha^{-1} \left(1 + \beta \right)^{1/2} - 2\gamma \right] \tag{7}$$

and

$$\tau_a^i = - E \; \alpha^{-1} \left(1 + \beta \right)^{1/2} \tag{8}$$

where

$$\alpha = 2b \left[E \left(E - \Delta E \right) \right]^{1/2}$$

$$\beta = 1 - b^2 \; E \left(E - \Delta E \right)^{-1} \left[r_c^2 + r_c \left(E - \Delta E \right)^{-1} \right]^{-1}$$

$$\gamma = \left[1 + 4b^2 \; E \left(E - \Delta E \right) \right]^{-1/2}$$

As it can be seen, ionic and covalent atractive deflections depend only on b, E and ΔE.

If the repulsive energy terms in equation (2) and (3), can be neglected for values of $r \geqslant r_c$, the repulsive deflections are mainly a function of what happens inside the sphere of radius r_c, and equation (4) is satisfied. In this case, repulsive deflections τ_r (τ_r standing for τ_r^i or τ_r^c) can be calculated as function of the impact parameter b, A and B (A standing for A_i or A_c and B for B_i or B_c). In the straight line and impulse approximation, τ_r is given by [10, 11]

$$\tau_r (b) = -b \int_b^\infty \left(dV/dr \right) \left(r^2 - b^2 \right)^{-1/2} dr \tag{9}$$

For the Born Mayer potentials and after some algebraic manipulations, the analytical solution found for equation (9) is

$$\tau_r (b) = (A/B) \; b \; K_0 (b/B) \tag{10}$$

where $K_0 (b/B)$ is a modified Bessel function of order 0.

The derivatives $db/d\tau$ necessary to calculate $\sigma (\Theta) . \sin \Theta$ are determined analytically by differentiating (5) and (6). For the terms involved in the derivatives of the attractive deflections we have

$$d\tau_a^i / db = E \left\{ bE \left[\alpha (E - \Delta E) \beta^{1/2} (r_c^2 + r_c (E - \Delta E)^{-1}) - 1 \right] \right.$$
$$\left. + 2\alpha^{-2} \left[1 + \beta^{1/2} \right] \left[E (E - \Delta E) \right]^{1/2} \right\} \tag{11}$$

and

$$d\tau_a^c / db = 8bE^2 \gamma^3 (E - \Delta E) - d\tau_a^i / db \qquad (12)$$

In the case of $d\tau_r / db$, from equation (10) a simple expression is found:

$$d\tau_r^{i,c} / db = (A/B) [K_0(b/B) - (b/B) K_1(b/B)] \qquad (13)$$

where K_1 is a modified Bessel function of the first order.

The Landau-Zener probability is calculated at the crossing point of the potential curves using the expression,

$$p = \exp(-2\pi H_{12}^2 r_c^2 / v) \qquad (14)$$

where v is the radial velocity at the crossing point, and H_{12} is the coupling potential between the diabatic states. This potential can be estimated with the help of

$$H_{12} / I(M) = 2.467 \exp(-0.969 r_c \sqrt{I(M)}) \qquad (15)$$

where $I(M)$ is the ionization potential of the projectile. This empirical expression (8) was obtained by least squares fitting to estimated values for several systems derived from experiment and theory.

Finally the $\sigma(\Theta) . \sin \Theta$ dependence on $\tau = E . \Theta$ is determined, using expression (1). To simulate the experimental results the smoothing of the values is done by convolution with the apparatus function. As apparatus function we have used a Gaussian curve with a standard deviation σ_g given by

$$\sigma_g \simeq 0.42 \ \delta\tau \qquad (16)$$

with

$$\delta\tau = \Theta \cdot \delta E + E \cdot \delta\Theta \qquad (17)$$

where δE is the full width at half maximum of the energy distribution (due to projectile and target beam energy spread), and $\delta\Theta$ is the angular resolution due to beam and detection geometry [12].

According to this model the differential cross sections depend on the endoergicity and the collisional energy, on the four repulsive

potential parameters used, on the ionization potential of the projectile and finally on the mass of the colliding partners.

A simpler version of the model can be obtained by making $A_c = A_i = A$, and $B_c = B_i = B$. These assumptions satisfy also relation (4), and allow that at $r = r_c$ the potential be already repulsive. They are equivalent to make the repulsive forces from covalent and ionic potentials identical. In other words, in the scope of this simplified two-parameter version of the model, and with respect to short range repulsions it makes no difference whether the valence electron is on the alkali projectile (electron donor) or on the target (electron acceptor).

All the calculations involved in the model were performed in a mini computer (H. P. 9821A); the programs were developed in a simplified version of Basic. To obtain at each energy the plot of a differential cross section, about thirty minutes are needed in this slow computer.

III — DISCUSSION

The two-parameter version of the model was mainly used to simulate differential cross sections for the collision $Na + I \rightarrow Na^+ + I^-$. Limitations and advantages of the four- and two-parameter version of the model will be referred.

The parameters A and B were obtained by fitting the simpler version of the model to experimental results of Delvigne and Los (Table 1). With these parameters, potential curves were constructed (Fig. 1) and deflection functions at different energies were obtained, (e. g. Fig. 2). The quality of the fitting can be judged from Fig. 3. It is clear from figure 1 that the potentials we used are more realistic than the ones of Gillen, because the inclusion of the repulsion in the ionic potential originates the minimum near the equilibrium distance in the NaI molecule and because our covalent potential is repulsive whereas Gillen's is not. However the covalent repulsion is not so strong as the one obtained by Delvigne. It is worthwhile to refer also that the potential energy curve obtained with our two parameter version of the model, agrees reasonably well with other experimental results mentioned by Rittner [13], and Huber and Herzberg [14]. On the one hand, our minimum occurs at an internuclear distance 2.5 Å, a value

0.1 Å lower than the one obtained by Delvigne and Los (see Fig. 1) and 0.2 Å lower than the one presented in reference [14]. On the other hand, for the ionic potential depth we got 4.85 eV, which is also near the value presented by Delvigne and Los (about 5.25 eV, as shown in Fig. 1). Both values agree with that predicted from solid state studies made by Rittner [13], which ranges from 4.7 to 5.2 eV. Moreover, the result of our model fitting agrees reasonably with a well depth of 5.12 eV obtained with an adiabatic dissociation energy of 3.02 eV, estimated from Herzberg [14].

TABLE 1 — Parameters involved on model fittings

Parameters	This work	Delvigne's work
ΔE (eV)	2.075 (1)	2.075
H_{12} (eV)	0.051 (2)	0.065 (3)
A (eV)	2448.0 (4)	—
B (Å)	0.3175 (4)	—
A_i (eV)	2312 (6)	2760 (3)
B_i (Å)	0.3069 (6)	0.3489 (5)
A_c (eV)	2992 (6)	3150 (3)
B_c (Å)	0.3969 (6)	0.435 (3)

(1) $- \Delta E = $ I-EA, where I is the ionization potential of Na and EA the electron affinity of iodine. (2) − From expression (15) of this work. (3) − Proposed by Delvigne [5]. (4) − Fitting from this work using the two-parameter model. (5) − From [15]. (6) − Fitting from this work using the four-parameter model.

The deflection function at an energy of 13.1 eV is shown in Fig. 2 together with those of the authors refered to. Two features can be observed in our deflection function that are not present in Gillen's case. In the first place an absolute minimum responsible

for the ionic rainbow is obtained and, secondly, net repulsive ionic and covalent branches are present. It can be also observed that
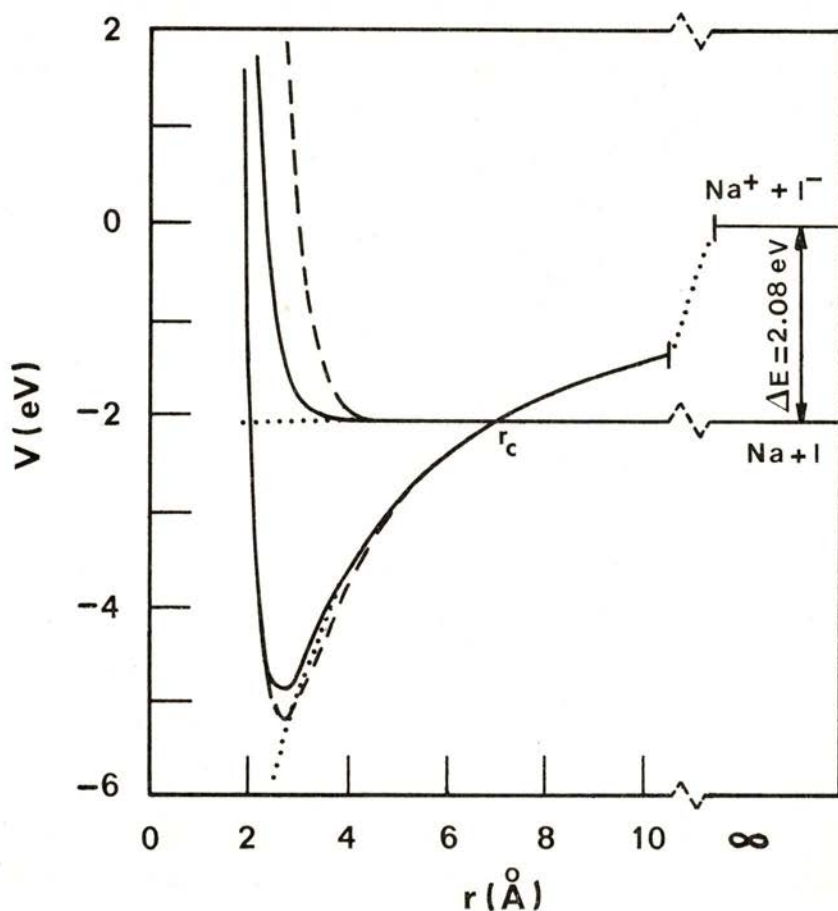
Fig. 1 — Ionic and covalent potential energy curves involved in differential cross section simulations for the Na + I collisions [5, 7]: (.........) used by Gillen; (- - - -) Delvigne and Los; (————) after fitting of 2-parameter version of this work to experimental results from [5] (see Fig. 3).

between the impact parameter of the minimum in the ionic branch, and the crossing distance r_c, our ionic deflection is less attractive. It is less attractive than in Delvigne's case because we did not include as many attractive terms as they did. It is less attractive

than in Gillen's case because to the purely attractive Coulomb term we add the exponential repulsion which has some influence even at large impact parameters.
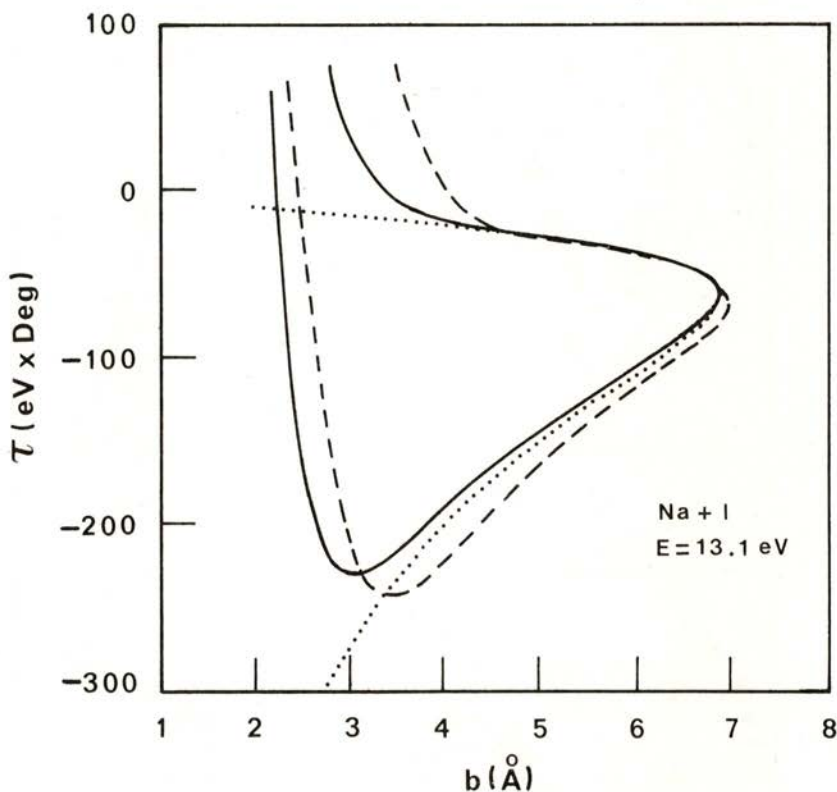
Fig. 2 — Deflection function corresponding to the potential curves of Figure 1 at an energy of 13.1 eV. In our case and in Gillen's $r_c = 6.94$ Å; in Delvigne's $r_c = 6.98$ Å, as more attractive terms are included in the potential.

The differential cross sections simulated with the two-parameter potential version are shown in Fig. 3, in comparison with experimental results of Delvigne and Los at two different energies. The position of maxima, minima and relative intensities are in quite reasonable agreement. Three peaks constitute the structure of this polar differential cross section. On the left hand side one has the covalent peak, which corresponds to an inflection in the covalent branch of the deflection function. The intermediate one

Figure (a): Na + I → Na⁺ + I⁻, E = 13.1 eV

Figure (b): Na + I → Na⁺ + I⁻, E = 18.2 eV
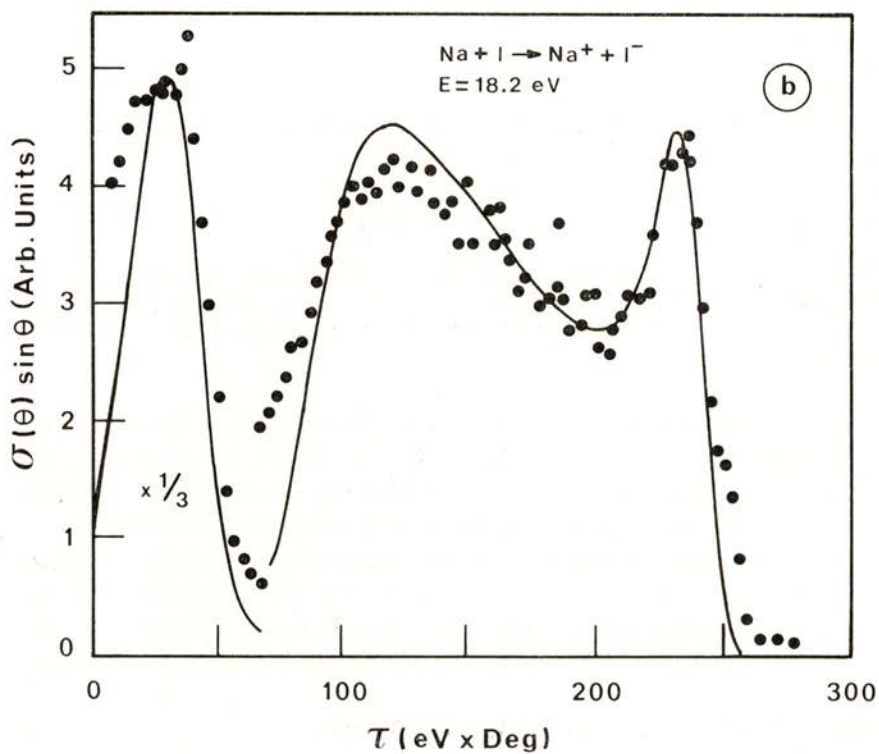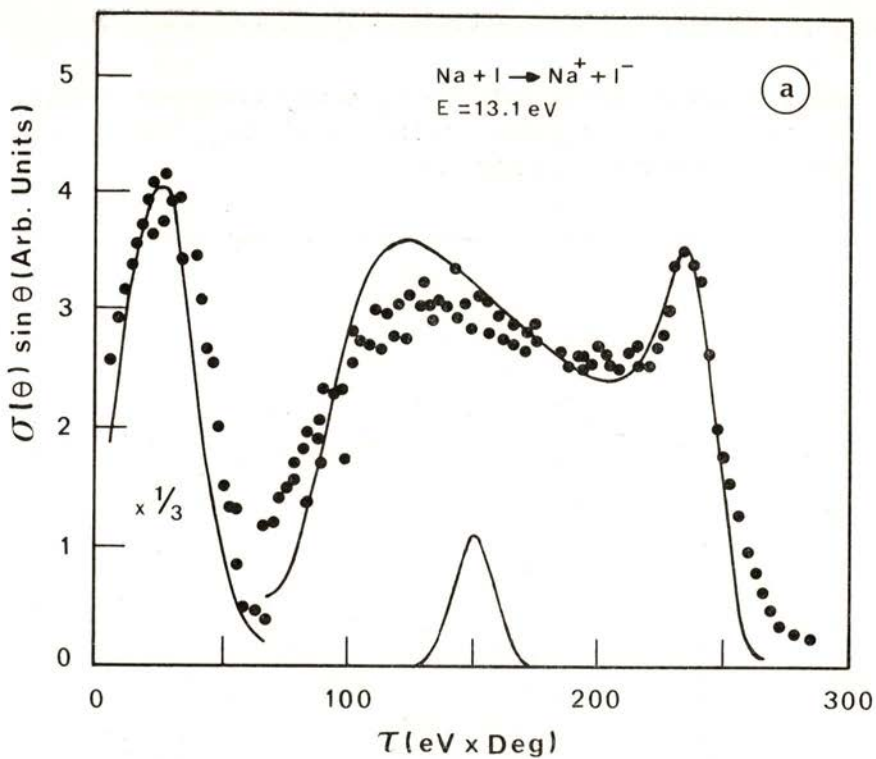
is due to a similar inflection in the ionic branch, both cases corresponding to b values where $d^2b / d\Theta^2 = 0$. On the right hand side the ionic rainbow maximum corresponds to the b value for which $db / d\Theta \to \infty$ (absolute minimum of the deflection function). Covalent and intermediate ionic peaks had already been obtained by Gillen with his simple model, and by the more sophisticated calculations of Delvigne and Los. These peaks depend mainly on the attractive forces, and correspond to impact parameters closer to r_c. Their angular positions can be reproduced by the three types of calculations under comparison, since in the three cases those forces are taken into account. However the rainbow ionic peak, which corresponds to the zone of the deflection function where the repulsive forces begin to overcome the attractive ones (in the minimum of the deflection function) is not present in Gillen's calculations.

Our calculation can be also compared with the semiclassical calculations of Delvigne and Los (Fig. 4). Their model used more sophisticated potentials that include, in addition to our terms, attractive ones depending on r^{-4} and r^{-7}, expressing polarization and dipole-dipole interactions, respectively. They included also a Van der Waals attraction $\propto r^{-6}$. To obtain the deflection function and their derivatives $db/d\Theta$ they used numerical calculations. The Landau-Zener probability was calculated in a way analogous to ours. In order to get the oscillating structure, the phase shifts were estimated by integration of the deflection function, assuming the stationary-phase and JWKB approximations. Obviously, in our calculation Stueckelberg oscillations cannot appear. Nevertheless our results seem to follow closely the average of the quantum oscillations they obtained. A covalent maximum, as well as intermediate ionic and rainbow peaks are in both cases present and in 'agreement' with ref. [5].

Fig. 3 — Simulated differential cross sections $\sigma(\Theta) \sin \Theta$ for the Na + I → Na+ + I− collision, in comparison with the experimental data redrawn from [5], at two different energies. To avoid overcrowding some points were skipped. The fitting was obtained with our 2-parameter version of model, corresponding to the A and B values of Table 1. The Gauss curve simulating apparatus function is shown in a at 150 eV. degree. Because of the large differences in intensity, covalent peak values were divided by 3 to get proper scaling.

As referred in the introduction, Faist and Levine [6] performed also calculations on the Na + I ion-pair formation collision. They used a generalized JWKB method to solve the S-matrix. The differential cross sections they obtained, considering a flat potential
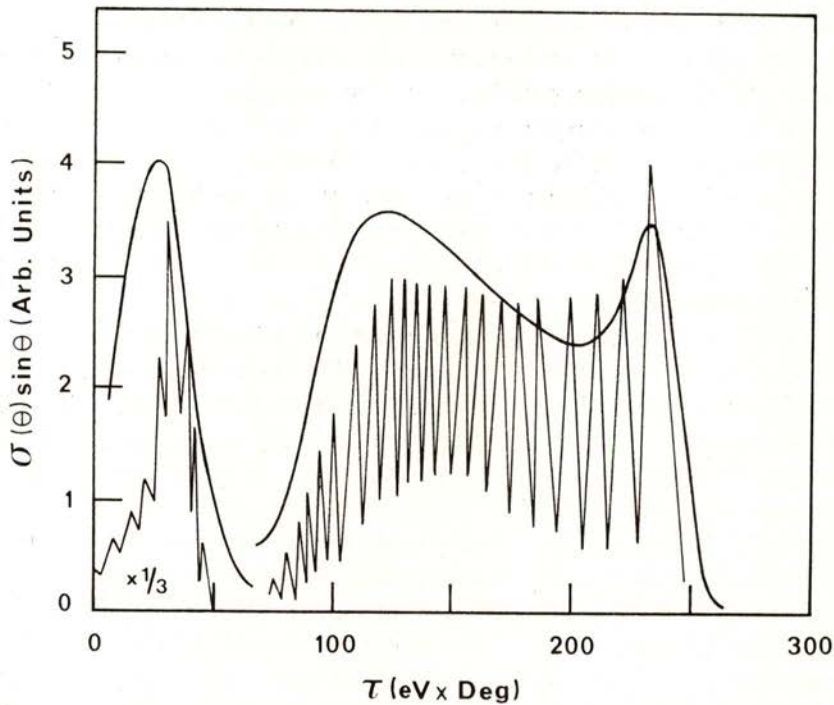
Fig. 4 — Comparison of the simulated differential cross sections, obtained with the two-parameter model at an energy of 13.1 eV with the calculations, redrawn from reference [15], showing quantum oscillations.

at short distances, agree with Delvigne's work when using the same potential parameters, although the Rittner potential was not exactly the same. The differential cross section obtained at 55 eV in the scope of our two-parameter version (see Fig. 5) and using the same values of Table 1, agree reasonably well with that of ref. [6]: our curve follows the average of the fast oscillations.

In all the differential cross sections from this work the smoothing effect of the apparatus was simulated by convoluting

calculated values with a Gaussian function of $\sigma_g = 7.5$ eV. degree. This value was estimated from the experimental conditions of Delvigne and Los at 18.2 eV and at a value of $\tau = 150$ eV. degree, using expression (16) and (17).
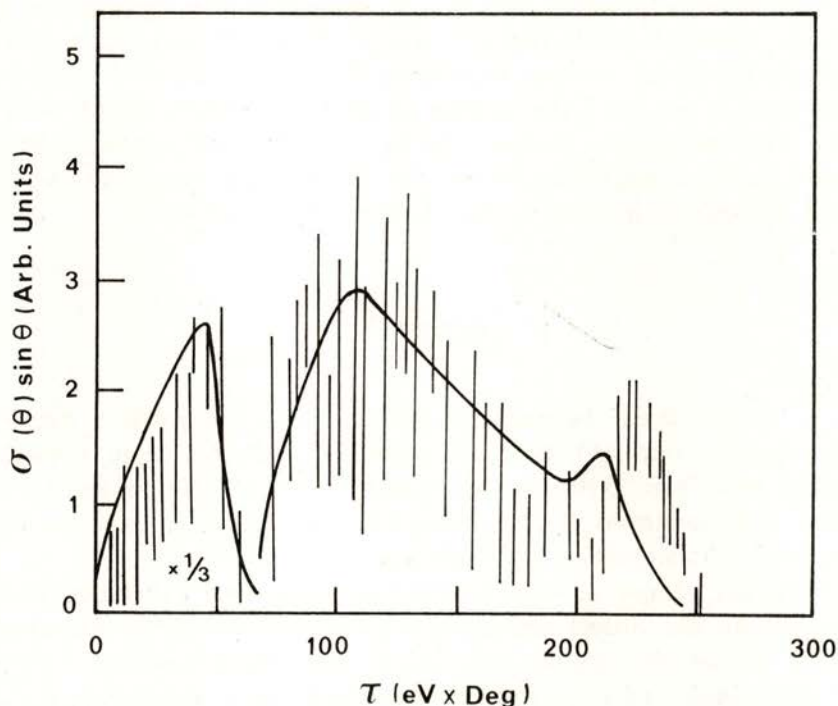
Fig. 5 — Calculated differential cross sections at an energy of 55.0 eV. Vertical bars represent very fast quantum oscillations obtained by Faist and Levine [6], some of which were skipped to avoid overcrowding. The full line shows the results of the two-parameter version of the model.

A trial with the four-parameter version of the model was done by fitting the deflection function presented by Delvigne. The parameters obtained in this way are also shown in Table 1. Comparison with the experimental results shows no improvement. In principle, the four-parameter version of the model is more precise than the two-parameter one. However it can be used only if covalent and ionic structures are well resolved in the experimental cross sections and if repulsion is inefficient outside the crossing

radius. If the latter condition is not fulfilled an error will arise from the fact that the repulsive deflection imposed before the first crossing is different from the one produced after the second one.

A comparison (Table 1) of the prarameters involved in the model fittings, either in the two or four-parameter versions, with those obtained in Delvigne's work, show an underestimation of the ionic and covalent repulsions. This is due to the oversimplication of the attraction, which we reduced to the Coulomb term.

The comparison between the two and four parameter models also shows a slight overestimation in the ionic repulsion (5 %) and an underestimation in the covalent one (~ 20 %).

IV – CONCLUSION

In short it can be said that the model we present is a simple but realistic one [16]. Indeed it reproduces all the main features of the experimental differential cross sections, at different energies. This was achieved by an extension of Gillen's model which maintains its simplicity and analytical character.

When compared with Delvigne's model, one concludes that except for the Stueckelberg oscillations, the qualitative explanations of the phenomena are equivalent, because covalent, intermediate ionic and ionic rainbow peaks are explained equally well. From a quantitative point of view, under-estimation of repulsive parameters results from the attempt to take into account the effects of some attractive forces that we did not really include in the model. This handicap does not seem too important, because good fittings are possible, giving good reproduction of peak positions and relative intensities. Moreover the model can be used without further modifications in cases where electron affinity of the target is negative, and can be modified in order to be used in atom-molecule collisions, by the inclusion of some aspects of molecular behaviour.

Although the two-parameter version of the model is, in principle, not so precise as the four-parameter one, it is twice as fast for computing. Moreover it has the advantage that it can be used even when repulsion is important in the crossing point, and

90

Portgal. Phys. — Vol. 17, fasc. 1-2, pp. 75-91, 1986

when no values from other sources are available for the sake of comparison.

REFERENCES

[1] J. LOS, A. W. KLEYN, *Alkali Halide Vapors*, Academic Press (1979).

[2] A. P. M. BAEDE, *Adv. Chem. Phys.*, **30** (1975), 463.

[3] K. LACMANN, *Adv. Chem. Phys.*, **42** (1980), 513.

[4] A. W. KLEYN, J. LOS, E. A. GISLASON, *Phys. Reports*, **90** (1982), 1.

[5] G. A. L. DELVIGNE, J. LOS, *Physica*, **67** (1973), 166.

[6] M. R. FAIST, P. R. JOHNSON, R. D. LEVINE, *Chem. Phys. Letters*, **32** (1975), 1.

[7] K. T. GILLEN, A. P. HICKMAN, *Chem. Phys.*, **53** (1980), 383.

[8] A. M. C. MOUTINHO, *Portgal. Physica*, **15** (1984), 157.

[9] K. J. BOHM, R. AHLRICHS, *J. Chem. Phys.*, **77** (1982), 2028.

[10] J. BAUDON, *J. Phys. B*, **6** (1973), 850.

[11] F. T. SMITH, R. P. MARCHI, W. ALBERTH, D. C. LORENTS, O. HEINZ, *Phys. Rev.*, **161** (1967), 31.

[12] M. J. P. MANEIRA, A. J. F. PRAXEDES, A. M. C. MOUTINHO, *Proc. 13th Symp. Rarified Gas Dynamics* (1982).

[13] E. S. RITTNER, *J. Chem. Phys.*, **19** (1951), 1030.

[14] K. P. HUBER, G. HERZBERG, *Molecular Spectra and Molecular Structure.* Vol. IV, Van Nostrand (1979).

[15] K. G. SPEARS, *J. Chem. Phys.*, **57** (1972), 1842.

[16] M. J. P. MANEIRA, Tese de doutoramento, Universidade Nova de Lisboa, Julho de 1984 (Cap. II).

TENSILE STRENGTHS OF PERFECT CRYSTALS: ANISOTROPY AND EFFECT OF INTERATOMIC POTENTIAL

M. A. Fortes and J. Brito Correia

Departamento de Engenharia de Materiais, Instituto Superior Técnico
Av. Rovisco Pais, 1000 Lisboa, Portugal

ABSTRACT — Computer calculations of various properties related to the behaviour of perfect crystals at high strains were undertaken using a pairwise potential approach. Three tensile deformation modes were considered, two of uniform deformation (constrained and unconstrained) and one of localized deformation, and the effect of the orientation of the tensile axis was studied. The emphasis was put on the maximum stress that can be supported in each deformation mode.

The potentials used were of the Mye type with three combinations of the exponents in the attractive and repulsive terms. In this way conclusions were drawn on the effect of potential ranges on the anisotropy of the elastic constants and maximum stresses, in each deformation mode. The anisotropy is found to increase as the ranges increase, in contrast with the effect on the anisotropy of surface energy.

Correlations between tensile properties and between these and surface energy were investigated and their accuracy assessed.

1 – INTRODUCTION

The subject of the ideal strength of crystals was recently reviewed by Macmillan [1]. In the calculations of the ideal strength, the atoms are assumed to interact by a pairwise central potential and the energy of the crystal is calculated as a function of the imposed strain: the maximum (or ideal) strength is simply related to the slope of the energy curve at the inflection point. Ideal strengths of simple crystals in uniform tension and in uniform

Portgal. Phys. — Vol. 17, fasc. 1-2, pp. 93-115, 1986

93

shear have been calculated by this method for various directions of the applied stress, both for constrained and unconstrained deformation, e. g. [2-6], leading to values that are in all cases of the order of 0.1M, M being the relevant elastic modulus.

Calculations of ideal stresses for non-uniform deformation have not been attempted in these studies, although they would be relevant to the understanding of fracture by the usual mechanism of crack propagation. Attemps at computer modelling of cracks have nevertheless been made recently, e. g. [7, 8], based on a lattice dynamics approach.

In this paper we report on results of computer calculations of ideal strengths in tension under various regimes. Results were obtained for several orientations of the tensile axis, allowing a detailed study of the anisotropy of the ideal strength. Three Mye type potentials have been used, with the purpose of studying the effect of the potential range on the ideal strength and on its anisotropy.

In uniform constrained tension no transversal relaxation of the atomic positions is allowed, implying that stresses must be applied in transversal directions. In the unconstrained mode of uniform deformation, the equilibrium positions of the atoms in each plane perpendicular to the applied tension are calculated; the crystal is now stress-free transversally. Calculations of this type were only undertaken for tension applied along symmetry axes.

The special, simple mode of non-uniform deformation that is analysed in this work is such that the interplanar distances remain unaltered except for a pair of planes perpendicular to the tensile axis.

All calculations were made for a f. c. c. monoatomic crystal using three Mye potentials, with exponents 6|9, 6|12 (Lennard-Jones) and 9|12. The stored elastic energy for each potential and each deformation mode is found by calculating the appropriate lattice sums which will be derived in the paper. Equations that enable the calculation of the rests of the lattice sums were also derived with which we were able to avoid the necessity, common to all previous calculations, of considering a crystal of finite arbitrary dimensions. The results obtained for the 6|12 potential are compared with those available in the literature [1, 5].

For each deformation mode and each potential we calculate the maximum tensile stress σ_{max}, the elastic energy stored at maximum stress and Young's modulus, Y, for various directions of tension. A correlation between these properties and also a correlation with the surface energies, γ, previously determined [9], was attempted. In particular, we calculate the values of α_0 in the equation, e. g. [1, 10, 11],

$$\sigma_{max} = \alpha_0 \ (\ Y \gamma \ / \ r_0\ )^{1/2} \tag{1}$$

where r_0 is the interatomic spacing in the crystal (^{1}).

In unconstrained uniform deformation it may happen that the crystal reaches a state of unstable equilibrium before the maximum stress is reached. The problem of stability under load was first discussed by Born ([12]; see other references to Born's work in ref. [13]) and is reviewed in refs. [1] and [13]. The difficulty with Born's stability criterion is that it is not coordinate independent, as first pointed out by Hill [14]. Furthermore, the criterion defines stability with respect to a homogeneous perturbation and not with respect to a general perturbation. At any rate, the stress at the onset of instability is an alternative and in principle more correct definition of the ideal stress. But several ideal stresses can then be defined. Various papers on the problem of stability under load have been published in recent years, particularly by Hill and by Milstein; they are reviewed in ref. [13]. A remarkable finding in these studies [15, 6, 13] is that a deformation path under load may bifurcate leading to different crystal structures. These stress-free structures are reached along paths that go beyond the maximum stress.

Considering the difficulties in assessing stability under load, we identify, in this paper, the ideal strength with the maximum stress attained under unconstrained deformation. This is equivalent to assume that all deformation states up to the one at maximum stress are stable. Consequently, we shall not attempt to address the problem of crystal structure transformations induced by stress or strain.

(^{1}) In the original form of eq. 1 (see ref. 1), r_0 is the interplanar spacing of planes perpendicular to the tensile axis. However, as will be shown, nearly constant values of α_0 in eq (1) are obtained only if r_0 is the interatomic spacing (or proportional to it).

2 – UNIFORM DEFORMATION

Consider a crystal with an atom per lattice point, in which the lattice planes $(p_1 \, p_2 \, p_3) = (p)$ are at a variable but uniform spacing, equal to $\mu \, d_0 \, (\mu \geqslant 1)$, d_0 being the spacing in the unstressed crystal (Fig. 1). In the unconstrained mode of defor-
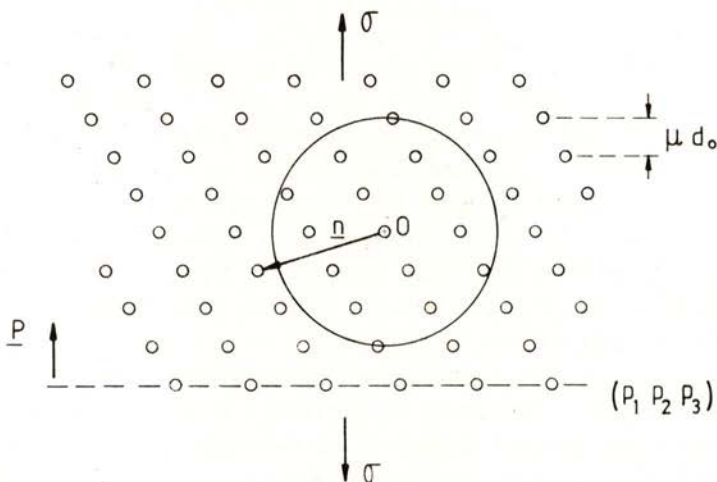
Fig. 1 — A crystal under uniform deformation in tension. The direction of tension is perpendicular to the lattice planes $(p_1 \, p_2 \, p_3)$. The interplanar spacing of these planes is $\mu \, d_0$, d_0 being the unstrained value.

mation, the atoms in each plane (p) relax to new equilibrium positions which can be calculated by minimizing the energy of the crystal, for fixed μ. The nominal strain is $(\mu - 1)$. A general method to find the minimum energy configuration for each strain is as follows.

We take a vector basis in the crystal lattice, e_1, e_2, e_3 (not necessarily a primitive basis), in relation to which we define the Miller indices (p). The unit vector perpendicular to (p) is denoted by **P**.

Let t_3 be a vector between adjacent unstrained planes (p) and perpendicular to them

$$t_3 = d_0 \, \mathbf{P} \qquad (2)$$

96

Portgal. Phys. — Vol. 17, fasc. 1-2, pp. 93-115, 1986

and t_1, t_2 two vectors in the plane (p) defining a convenient basis (not necessarily primitive) for the planar lattice in (p). The set t_i is related to the e_i by a matrix T

$$[t_1 \, t_2 \, t_3] = [e_1 \, e_2 \, e_3] \, T \tag{3}$$

or, in a more condensed notation,

$$[t] = [e] \, T \tag{4}$$

where $[e] = [e_1 \, e_2 \, e_3]$, for example, is to be regarded as a row matrix. When the crystal is stretched, t_3 changes to

$$t'_3 = \mu \, t_3 \tag{5}$$

and t_1, t_2 are transformed into t'_1, t'_2:

$$[t'_1 \, t'_2] = [t_1 \, t_2] \begin{bmatrix} \alpha_1 & \alpha_3 \\ 0 & \alpha_2 \end{bmatrix} \tag{6}$$

We can always take a non-diagonal element of this transformation matrix as zero, without loss of generality. The atomic positions in the planes of the strained crystal are given by linear combinations of t'_1, t'_2 with the same coefficients that define, in terms of t_1, t_2, the positions in the unstrained crystal. In the constrained deformation mode the matrix in eq. 6 is the identity matrix.

The two sets t'_i and t_i ($i = 1, 2, 3$) are then related by a matrix D such that

$$[t'] = [t] \, D \; ; \quad D = \begin{bmatrix} \alpha_1 & \alpha_3 & 0 \\ 0 & \alpha_2 & 0 \\ 0 & 0 & \mu \end{bmatrix} \tag{7}$$

The general form of a vector n between two atoms is

$$n = \sum_i n_i \, e_i = [e] \, (n) \tag{8}$$

where (n) denotes a column matrix with elements n_i. The n_i satisfy certain selection rules, dependent on the crystal structure

and vector basis e_i chosen. For example, if the e_i are a lattice basis, the n_i are any integers. Eq. 8 can be written as

$$n = [t] \, T^{-1} \, (n) \tag{9}$$

When the crystal is deformed, this vector changes to n^* given by

$$n^* = [t'] T^{-1} \, (n) = [e] \, TDT^{-1} \, (n) \tag{10}$$

Consider an arbitrary atom for origin. The other atoms are at distances ρ, which, in the deformed crystal, are the moduli of the n^* vectors. If we denote by $\varepsilon(\rho)$ the pairwise potential, the potential energy per atom, in the field of all other atoms in the deformed crystal, is given by

$$E(\mu; \alpha_1, \alpha_2, \alpha_3) = \sum_{n \neq 0} \varepsilon(n^*) \tag{11}$$

with n^* given by eq. 10. The sum is for all values of $n \neq 0$. In the unstrained crystal $-E = 2 \varepsilon_c$, where ε_c is the cohesive energy per atom. For each μ, the lattice sum (11) is minimized in relation to the α_i. We denote this energy by $\bar{E}(\mu)$ and the volume per atom by v. The applied (nominal) tensile stress, σ, for each μ, is then obtained from

$$\sigma = (1/v) \, d\bar{E}/d\mu \tag{12}$$

because the strain increment is $d\mu$.

Young's modulus, Y_u, can be determined from the slope of $\sigma(\mu)$ as $\mu \to 0$. However it is easier and more accurate to obtain the modulus from the elastic constants (see section 4).

When the deformation is constrained, the vectors n^* are simply related to μ through

$$n^* = n + (\mu - 1) \, (n \cdot P) \, P \tag{13}$$

and the elastic energy is obtained from eq. 11. In this case, Young's modulus Y_c was calculated directly for each direction P by the following method. Since

$$Y_c = (1/v) \, (d^2E(\mu)/d\mu^2)_{\mu=0} \tag{14}$$

and noting that (eq. 13)

$$dn^{*2} / d\mu = 2 (n \cdot P) (n^* \cdot P) \tag{15}$$

we find upon simple calculations

$$Y_c = \frac{2}{V} \left\{ \sum_{n.P>0} (n \cdot P)^2 \, \varepsilon'(n) + 2 \sum_{n.P>0} (n \cdot P)^4 \, \varepsilon''(n) \right\} \tag{16}$$

where ε' and ε'' denote derivatives of $\varepsilon(\rho)$ with respect to ρ^2, and the sums are for all n such that $(n \cdot P) > 0$. From the values of Y_c determined in this way for a number of tensile directions it is possible to obtain the elastic constants of the crystal, as we exemplify in section 4. From the elastic constants we then calculate the unconstrained moduli.

3 — LOCALIZED DEFORMATION

Suppose that the distance between two, and only two, crystal planes (p) is changed from d_0 to $d_0 + \delta$ as shown in Fig. 2. The displacement is δP. The strain will be defined as δ / r_0
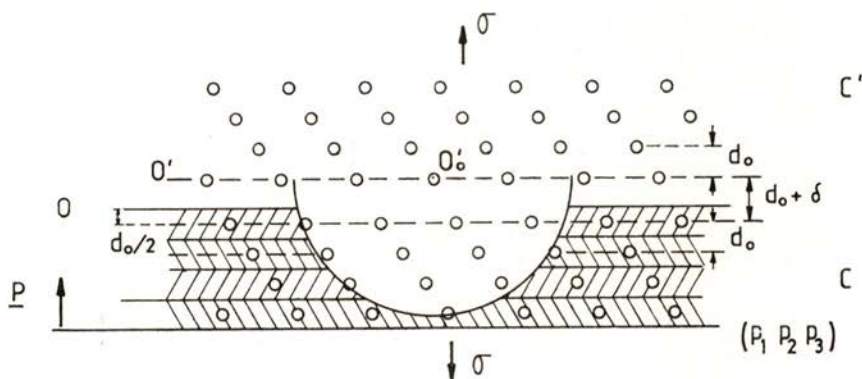
Fig. 2 — A crystal under localized deformation in tension. The direction of tension is perpendicular to the lattice planes ($p_1 p_2 p_3$). The interplanar spacing between a pair of these planes is $d_0 + \delta$, while the other planes remain at the unstrained spacing d_0.

where r_0 is the interatomic spacing [1]. The two half-crystals C and C' limited by these two planes are rigid. Let $E^*(\delta)$ be the interaction energy between C and C' per unit area in the plane (p), as a function of δ. The applied stress is

$$\sigma = d E^*(\delta) / d\delta \qquad (17)$$

The potential energy $E^*(\delta)$ is easily derived from the well-known equation [e. g. 9] for the potential energy of interaction, $E^*(0)$, of two half-crystals separated by a plane **P** through an unstrained crystal ($\delta = 0$):

$$E^*(0) = \frac{1}{V} \sum_n (n \cdot P) \, \varepsilon(n) \; ; \quad n \cdot P > 0 \qquad (18)$$

where the sum is for $n \cdot P > 0$. The quantity $(n \cdot P)$ is proportional to the number of pairs of interacting planes at a given spacing and is unaltered when the two half-crystals suffer a relative translation δP, in which case **n** in $\varepsilon(n)$ changes to

$$n' = n + \delta P \qquad (19)$$

Therefore

$$E^*(\delta) = \frac{1}{V} \sum_n (n \cdot P) \, \varepsilon(n') \; ; \quad n \cdot P > 0 \qquad (20)$$

Young's modulus is defined as the stress increment for a unit increment of the strain δ / r_0 as $\delta \to 0$. Therefore

$$Y_1 = r_0 \left(\frac{d^2 E^*(\delta)}{d \delta^2} \right)_{\delta = 0} \qquad (21)$$

Using a procedure similar to that described in the derivation of eq. 16 we find

$$Y_1 = 2 \frac{r_0}{V} \left[\sum_n (n \cdot P) \, \varepsilon'(n') + 2 \sum_n (n \cdot P)^3 \, \varepsilon''(n') \right] \qquad (22)$$

where the sums are, again, for all **n** such that $n \cdot P > 0$.

---

[1] The strain has to be defined in relation to a reference length in the crystal, the same for all orientations of the tensile axis. It is misleading to define strain in relation to the interplanar spacing d_0.

4 – APPLICATION TO F.C.C. CRYSTALS, MYE POTENTIALS

The general equations derived above were applied to f.c.c. crystals in which the atoms interact by a Mye potential with exponents e, e' :

$$\varepsilon(\rho) = \varepsilon_0 \left[(\sigma/\rho)^{e'} - (\sigma/\rho)^{e} \right], \quad e' > e \tag{23}$$

In this equation ε_0 and σ are constants that can be related to the cohesive energy ε_c and to the interatomic distance r_0 in the crystal (see ref. 9). The values of e, e' used were combinations of 6, 9 and 12. A quantity of interest is the second derivative of $\varepsilon(\rho)$ at the minimum, which is a measure of the elastic stiffness of the bond between a pair of atoms. These values and other relevant parameters of each potential (taken from ref. 9) are included in Table 1.

TABLE 1 — Various parameters of the Mye potentials used

	6 | 9 Potential	6 | 12 Potential	9 | 12 Potential
σ / r_0	0.91710	0.91729	0.91747
$\varepsilon_0 / \varepsilon_c$	0.69769	0.46456	1.39026
$(d^2\varepsilon / d\rho^2)$ *	5.0646	7.8880	15.5292

* Second derivative at the minimum $\varepsilon(\rho)$ in ε_c units.

With unit vectors, $\mathbf{e}_1 \mathbf{e}_2 \mathbf{e}_3$, parallel to the cube axes, the form of $\mathbf{n}$ is

$$\mathbf{n} = (a/2) \sum_i n_i \mathbf{e}_i \tag{24}$$

where a is the lattice parameter (cube edge, $a = \sqrt{2}\, r_0$) and the n_i are integers such that

$$\sum_i n_i = \text{even integer} \tag{25}$$

In the following equation, $\mathbf{n}$ and n are expressed in $a/2$ units.

The lattice sums that intervene in the calculation of the energy in the three deformation modes are of the following types.

To obtain the energy in uniform deformation, it is necessary to calculate series of the type

$$S_e = \sum_{n \neq 0} \left(\frac{1}{n^*} \right)^e \tag{26}$$

where n^* is related to n by eqs. 10 and 13, respectively for the unconstrained and constrained deformation modes.

In the localized deformation mode the lattice sums for the energy are of the form

$$C_e(\delta) = \sum_n \frac{n \cdot P}{(n')^e} \tag{27}$$

where n' is defined by eq. 19 and the sum is for all n such that $n \cdot P > 0$.

Finally the sums that enter in Young's moduli (eqs. 16 and 22) are of the types

$$\sum (n \cdot P)^\alpha \, n^{-(e+\alpha)} \text{ and } \sum (n \cdot P)^{\alpha-1} \, n^{-(e+\alpha)} ; \; \alpha = 2,4 \tag{28}$$

summed for all n such that $n \cdot P > 0$. As already pointed out, in eqs. 26-28, n is expressed in $a/2$ units, so that the components n_i are integers satisfying eq. 25.

The sums S_e and C_e were calculated with great precision. A direct sum was obtained up to a chosen value of n; the rest of the sum was obtained by replacing the corresponding part of the crystal by a continuum. The appropriate equations are derived in the Appendix.

The sums (28) for Young's moduli were calculated by direct sum up to $n = 10$ (in $a/2$ units). The maximum error in such truncated sums, estimated from values obtained for $n = 15$, is 1 %.

Calculations in the unconstrained mode were done exclusively for the tensile axis parallel to [002] and [111] directions. The method developed in section 2 was used to find the relaxed configuration which, in both cases, depends on one parameter only [1].

---

[1] This restriction to one parameter calculations is a constant in the literature. The method outlined in section 2 can, of course, be used to extend the calculations to other directions of tension.

The vectors t_1, t_2 in the plane perpendicular to the tensile axis were chosen parallel to $<110>$, both for [002] and [111] tension, as shown in Fig. 3. The matrix D (eq. 7) then has $\alpha_3 = 0$ and $\alpha_1 = \alpha_2 = \alpha$.
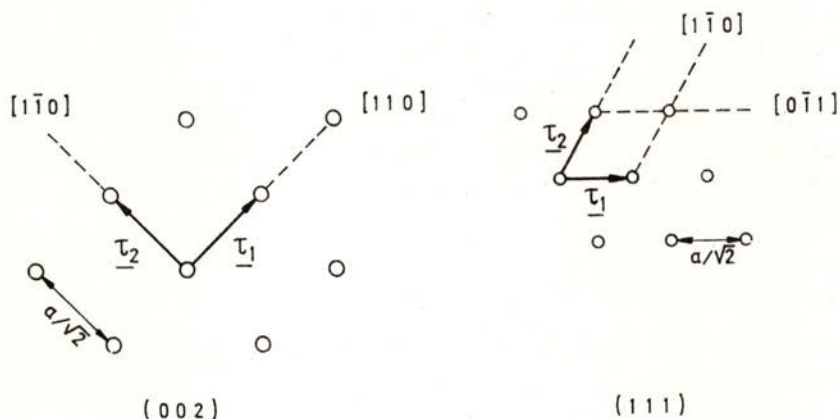
Fig. 3 — Choice of vector bases in (002) and (111) planes.

The elastic moduli in uniform deformation can be expressed in terms of the elastic constants. In the unconstrained mode, the modulus for tension in the direction $[p_1\, p_2\, p_3]$ is easily found to be

$$Y_u^{-1} = (1/p^4)\, [\, A\, s_{11} + B\, (2\, s_{12} + s_{44})\,] \qquad (29a)$$

where

$$A = p_1^4 + p_2^4 + p_3^4$$

$$B = p_1^2\, p_2^2 + p_2^2\, p_3^2 + p_3^2\, p_1^2 \qquad (29b)$$

and the s_{ij} are the elastic compliances. It is also easy to obtain equations for the Poisson ratio corresponding to [002] and [111] tension. In the constrained mode of deformation, the modulus is given by

$$Y_c = (1/p^4)\, [\, A\, c_{11} + B\, (2\, c_{12} + 4\, c_{44})\,] \qquad (30)$$

where the c_{ij} are the stiffnesses, related to the s_{ij} by well-known equations [e. g. 16]. It is then possible, by calculating the con-

strained moduli for a few directions, to obtain all the c_{ij}, making use of Cauchy's relation $c_{44} = c_{12}$. The s_{ij} are then calculated and, from them, the unconstrained moduli can be determined for the various directions of tension.

In unconstrained deformation, the stress obtained from eq. 12 is a nominal stress (force divided by the initial area). The true stress can easily be found from the values of α in the equilibrium configurations; it is obtained by multiplication of the nominal stress by α^{-2}. Finally, it is possible to obtain the transversal stress in constrained tension parallel to [002] and [111]. The transversal stress is a negative two-dimensional pressure p, which, for each μ is given by

$$p = 1/(\mu d_0) \cdot dE(\mu, \alpha)/dS = 1/(\sqrt{2}\mu) \cdot dE/d\alpha \qquad (31)$$

where S is the area per atom in the plane perpendicular to the tensile axis ($S_{002} = 1/2 \ \alpha^2 a^2$; $S_{111} = \sqrt{3}/4 \ \alpha^2 a^2$). The derivative is taken for $\alpha = 1$.

5 – RESULTS AND DISCUSSION

All quantities will be expressed by taking ε_c (the cohesive energy per atom) and r_0 (the interatomic spacing in the crystal) as units. For example, elastic stiffnesses and Young's moduli will be expressed in ε_c / r_0^3 units.

Table 2 gives the values of the elastic constants c_{ij} and s_{ij} for each potential. The anisotropy ratio is also included. The anisotropy increases as the exponents in the potential decrease (increasing range). The elastic stiffnesses increase as the curvature of the potential at the minimum increases (cf. values in Table 1).

TABLE 2 — Elastic constants *

Potential	c_{11}	$c_{12} = c_{44}$	s_{11}	s_{12}	s_{44}	$2c_{44}/(c_{11}-c_{12})$
6 | 9	23.21	13.88	0.0780	-0.0292	0.0720	2.977
6 | 12	31.69	18.12	0.0540	-0.0197	0.0552	2.672
9 | 12	48.62	26.60	0.0335	-0.0119	0.0376	2.415

* c_{ij} in ε_c / r_0^3 units for each potential; s_{ij} in $r_0^3/$ c units.

104

Portgal. Phys. — Vol. 17, fasc. 1-2, pp. 93-115, 1986

However, a simple correlation between the c_{ij} and the curvature cannot be established. This is not surprising considering that the equilibrium distance in the crystal is always smaller than the equilibrium distance of a pair of atoms [9].

Fig. 4 shows the energy curves for constrained tension in the [111] direction for the three potentials. The location of the
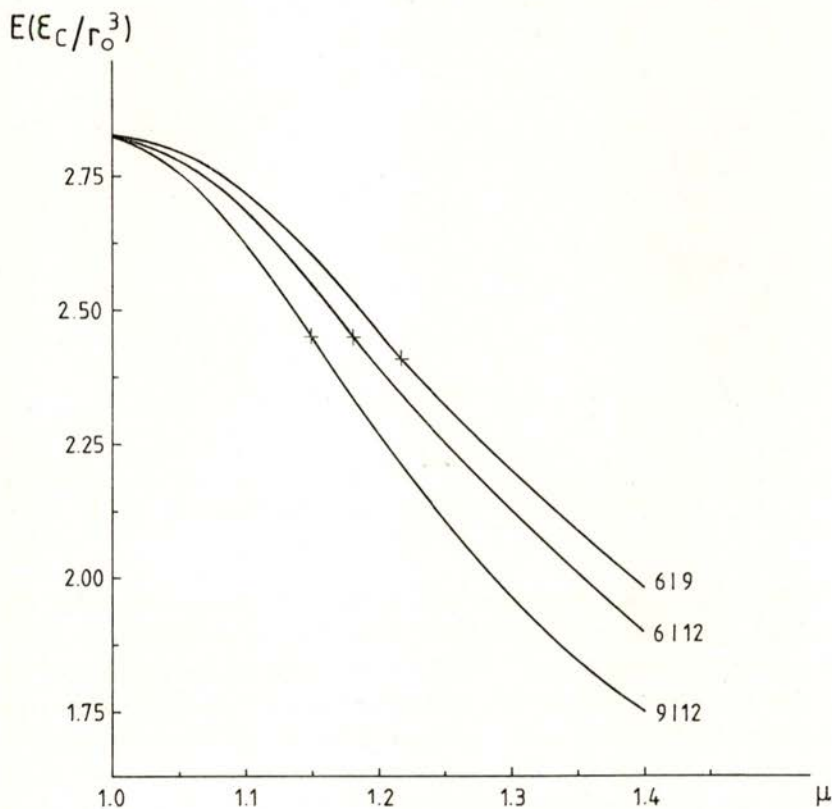
Fig. 4 — Energy (in ε_c / r^3_0 units) as a function of uniform strain μ for tension parallel to [111] in the constrained deformation mode. Each curve is for the Mye potential indicated. The location of the inflection points is shown.

inflection points is indicated. In Fig. 5 are shown the stress-strain curves corresponding to Fig. 4. Similar curves are obtained for other directions and for other deformation modes.

$\sigma(\varepsilon_c/r_o^3)$
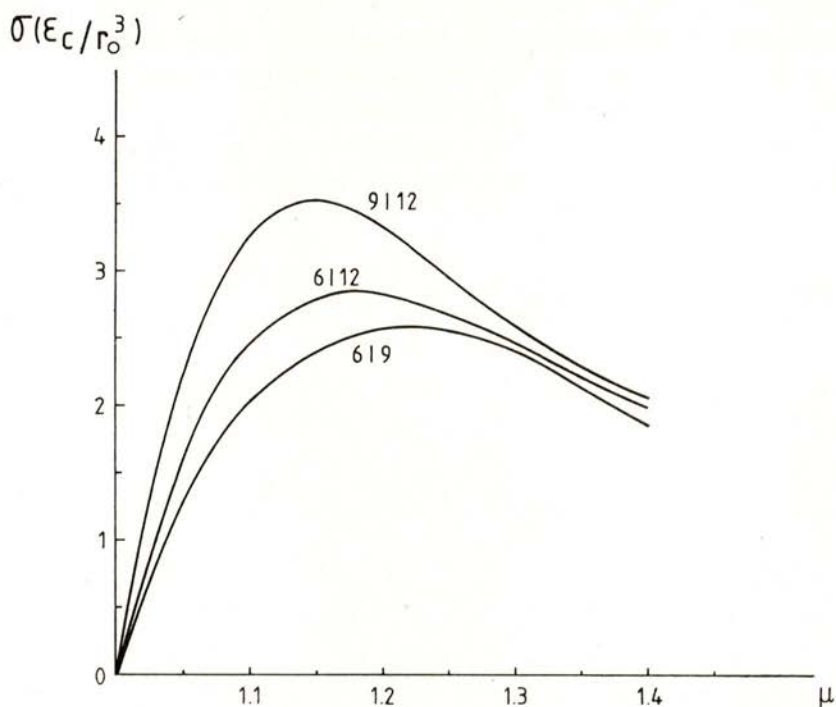
Fig. 5 — Nominal stress-strain curve for [111] uniform constrained tension. Each curve is for the Mye potential indicated.

In Table 3 are indicated the values of Young's modulus for various orientations of the tensile axis in each deformation mode. As already explained, the moduli for the constrained and localized modes were determined directly from eqs. 15 and 22, while the unconstrained moduli were calculated from the elastic constants. The values included in Table 3 for the constrained and localized modes are for tensile directions perpendicular to the more close packed lattice planes up to (135). Many other directions were calculated but in Table 3 we include only one more, for [1 15 19] tensile axis. The ratio of the moduli for [111] and [002] is also shown in Table 3, confirming that the anisotropy increases as the range of the potential increases. It is remarkable that the anisotropy of surface energy (and also of evaporation energy) varies in the opposite way with the range of the potentials [9]. It is also noticeable that the unconstrained moduli are only slightly smaller

106

Portgal. Phys. — Vol. 17, fasc. 1-2, pp. 93-115, 1986

TABLE 3 — Young's moduli (c / r_0^3 units) and Poisson ratios

Constrained; Localized

Tensile axis	6 | 9 Potential		6 | 12 Potential		9 | 12 Potential	
	constrained	localized	constrained	localized	constrained	localized
111	35.50	23.81	46.81	30.33	69.40	43.37
002	23.21	19.58	31.69	25.24	48.62	36.57
022	32.43	21.15	43.03	27.20	64.20	39.31
113	29.00	20.68	36.81	26.61	58.41	38.48
133	33.32	21.89	44.13	28.08	65.71	40.45
024	29.11	20.23	38.94	26.12	58.59	37.88
224	32.43	21.95	43.03	28.15	64.20	40.53
115	25.79	19.90	34.86	25.66	52.98	37.17
135	31.01	20.91	41.28	26.93	61.80	38.96
1 15 19	31.97	20.98	42.46	27.01	69.39	39.08
Ratio extreme values	1.53	1.22	1.48	1.20	1.43	1.19

Unconstrained (Values in brackets are calculated Poission's ratios).

Tensile axis	6 | 9 Potential	6 | 12 Potential	9 | 12 Potential
111	32.75 (0.179)	42.93 (0.185)	63.32 (0.190)
002	12.82 (0.374)	18.52 (0.364)	29.85 (0.354)
Ratio extreme values	2.56	2.32	2.12

than the constrained ones for [111], but appreciably smaller for [002]. This is related to the small relaxation associated with tension along [111], reflected in the small value of the Poisson ratio, also listed in Table 3. In all modes, the extreme moduli are for [111] (maximum) and [002] (minimum). It is also noted that Poisson's ratio increases with the range of the potential for [002] tension but decreases with the range for [111] tension. The behaviour in unconstrained tension was found to be anomalous at high strains in the sense that the transversal dimensions go through a minimum and then increase as the tensile strain increases. This result was previously reported in ref. [5].

The maximum stresses are indicated in Table 4 for various orientations of the tensile axis in each deformation mode studied. The largest maximum stress is in all cases for [111] tension while the smallest value was obtained for [0 30 38] among the directions investigated. The maximum stress is larger in the unconstrained mode than in the constrained one, but the difference is small. The maximum stress in localized deformation is appreciably smaller than in uniform deformation, by a factor that varies between 1.40 and 1.95. This factor increases from the 6 | 9 to the 9 | 12 potential.

The transversal tension, p , at maximum stress in constrained deformation was calculated from eq. 31. The values of p are about 9 % and 31 % of the maximum stress, respectively for [111] and [002] tension. The lower value for [111] tension is related to the smaller transversal contraction that occurs in this case.

Our results on maximum stresses and Young's moduli for the 6 | 12 potential were compared with those obtained by Macmillan and Kelly [5] for argon, using the same potential and appropriate values of the potential constants. The agreement is excelent, as we show with the following examples. The ratio of the extreme maximum stresses in constrained tension is $3.42/2.64 = 1.295$ in ref. [5], while our value is $2.856/2.215 = 1.289$. The ratio σ_{max} / Y_c in [002] constrained tension is 0.083 in both calculations. The ratio of maximum true stresses in [002] unconstrained and constrained tension is $3.45/3.17 = 1.088$ in ref. [5] and $2.861/2.645 = 1.082$ in the present work.

Other characteristics of the critical state at maximum stress were determined in the calculations, related to the stored elastic energy and to the deformation at maximum stress. In Table 5 are

TABLE 4 — Maximum stress (ε_c / r_0^3 units)

	6 | 9 Potential		6 | 12 Potential		9 | 12 Potential	
	constrained *unconstrained*	localized	constrained *unconstrained*	localized	constrained *unconstrained*	localized
111	2.582 *2.607 - 2.640 (a)*	1.461	2.856 *2.882 - 2.922*	1.551	3.539 *3.566 - 3.616*	1.814
002	2.323 *2.388 - 2.548*	1.414	2.645 *2.703 - 2.861*	1.524	3.420 *3.476 - 3.649*	1.815
022	1.944	1.401	2.223	1.499	2.828	1.774
113	2.068	1.411	2.362	1.509	3.024	1.789
133	2.125	1.412	2.403	1.508	3.032	1.779
024	1.950	1.389	2.243	1.492	2.888	1.774
224	2.221	1.417	2.500	1.513	3.157	1.784
115	2.129	1.414	2.458	1.515	3.147	1.801
135	2.008	1.397	2.292	1.496	2.926	1.775
0 30 38	1.935	1.391	2.215	1.493	2.827	1.772
Ratio extreme values	1.33 *1.09*	1.05	1.29 *1.07*	1.04	1.25 *1.03*	1.02

(a) First value in italic is nominal stress; second value in italic is true stress.

TABLE 5 — Deformation and stored energy at maximum stress

Constrained

Property	6 | 9 Potential	6 | 12 Potential	9 | 12 Potential
μ	1.21 - 1.28 (1.06)	1.18 - 1.24 (1.05)	1.15 - 1.20 (1.04)
Stored energy (ε_c / r_0^3 units)	0.324 - 0.472 (1.46)	0.321 - 0.465 (1.45)	0.340 - 0.500 (1.47)

Unconstrained

Property	6 | 9 Potential [111] [002]		6 | 12 Potential [111] [002]		9 | 12 Potential [111] [002]	
μ	1.207	1.283 (1.063)	1.170	1.257 (1.074)	1.147	1.210 (1.055)
α^{*}	0.9937	0.968 (1.026)	0.9932	0.972 (1.022)	0.9930	0.976 (1.017)
Stored energy (ε_c / r_0^3 units)	0.386	0.439 (1.14)	0.353	0.476 (1.35)	0.361	0.494 (1.37)

Localized

Property	6 | 9 Potential	6 | 12 Potential	9 | 12 Potential
δ (r_0 units)	0.18 - 0.24 (1.33)	0.16 - 0.18 (1.13)	0.13 - 0.14 (1.08)
E_{max} (ε_c / r_0^2)	0.197 - 0.262 (1.33)	0.178 - 0.209 (1.17)	0.169 - 0.188 (1.11)

Values in brackets are the ratios of extreme values.

110

Portgal. Phys. — Vol. 17, fasc. 1-2, pp. 93-115, 1986

indicated, for each potential and each deformation mode, the ranges of values found for the various tensile directions. The extreme values of the deformation parameter, μ, at maximum stress occur for [111] and [002] tension, respectively for the largest and smaller μ. The values of the stored energy vary only slightly with orientation; the extreme values correspond to tensile directions which depend on the potentital and are not in general low index directions. Neverthless the larger values seem to occur near [024] and the smaller values near [002] in uniform deformation and near [111] in localized deformation. It is also noted that the energy stored at maximum stress is not much different in the two modes of uniform deformation.

The ratio between maximum stress and Young's modulus is listed in Table 6. Nominal stresses were used in the case of unconstrained deformation. There is a fair uniformity in the values,

TABLE 6 — Ratio between maximum stress and Young's modulus (x 100)

Direction of tension	6 | 9 Potential			6 | 12 Potential			9 | 12 Potential		
	unconst.	const.	local.	unconst.	const.	local.	unconst.	const.	local.
111	8.0	17.3	6.1	6.7	6.1	5.1	5.6	5.1	4.2
002	18.6	10.0	7.2	14.6	8.3	6.0	11.6	7.0	5.0
022		6.0	6.6		5.2	5.5		4.4	4.5
113		7.1	6.8		6.4	5.7		5.2	4.6
133		6.4	6.5		5.4	5.4		4.6	4.4
024		6.7	6.9		5.8	5.7		4.9	4.7
224		6.8	6.5		5.8	5.4		4.9	4.4
115		8.5	7.1		7.0	5.9		5.9	4.8
135		6.5	6.7		5.6	5.6		4.7	4.6

although the ratios for unconstrained deformation in [002] are noticeably larger. In general, then, the maximum stress ranges from Y/5 to Y/23.

Using the values of (unrelaxed) surface energies calculated in ref. [9] for the same potentials, we determined the values of α_0

defined by eq. (1). The results are as follows. In constrained deformation α_0 increases from the 6 | 9 to the 9 | 12 potential. The extreme values for the 6 | 9 potential are 0.48-0.69; for 6 | 12: 0.51-0.70; and for 9 | 12: 0.57-0.82. The first value corresponds to [022] and the second to [002]. The values for unconstrained deformation (nominal stresses) are as follows (first value for [111], second for [002]): 6 | 9: 0.66-0.95; 6 | 12: 0.67-0.94: 9 | 12: 0.78-1.07.

Finally, the values of α_0 for localized deformation are surprisingly uniform: they range from 0.42 to 0.44 for each of the 6 | 9 and 6 | 12 potentials and from 0.45 to 0.50 for the 9 | 12 potential.

Various correlations involving the energy stored at maximum stress have been attempted. For example, the ratio between the maximum stored energy and the surface energy ranges from 0.41 to 0.53 in localized deformation.

6 – SUMMARY

The calculations described in this paper were aimed at studying the effect of the interatomic potential on various crystal properties with interest for the mechanical behaviour of materials. The tensile properties at low stresses (elastic stiffness) and at maximum stress (ideal strength, stored energy and deformation) were calculated for each Mye potential as a function of the direction of the tensile axis. The anisotropy of these properties was found to increase as the range of the attractive and/or repulsive terms in the potential increases. This is in contrast with the effect of range on the anisotropy of the surface energies. The anisotropy of the maximum stress is fairly small for all potentials, indicating that there is not a well-defined cleavage plane.

The consideration of different tensile modes is another matter of interest in the paper. It was concluded that in the localized deformation mode, the maximum stress is reduced by a factor of 1.5-2 compared to the values in uniform deformation. Finally, correlations between tensile properties and surface energy, such as eq. 1, were analysed and the numerical factors in the correlations were determined.

APPENDIX — CALCULATION OF LATTICE SUMS

The sum S_e defined in eq 26 is calculated term by term for all combinations of integers n_i satisfying eq. 25 and such that

$$n_1^{*2} + n_2^{*2} + n_3^{*2} \leqslant M^2$$

and the corresponding number of terms, or atoms, N, is counted. The vector n^* is defined by eqs. 10 or 13. The rest of the sum is obtained from an integral over a continuum distribution in the region outside the sphere where the N atoms are located (Fig. 1). Since the volume per atom is $(a^3/4) D$, where $D = |\det D|$ is the volume ratio between the strained and unstrained crystal, the radius $R_0 (a/2)$ of the sphere is given by

$$4\pi R_0^3 / 3 = 2ND$$

The rest of the series, S_e', is obtained by integration in ρ over the region outside the sphere, where the atomic density is $4(a^3 D)^{-1}$:

$$S_e' = (4\pi/2 D) \int_{R_0}^{\infty} \rho^{2-e} \, d\rho = 2\pi \, R_0^{3-e} \, D^{-1} / (e-3)$$

The series S_e is then calculated from

$$S_e = \sum_{\rho \leq M} \rho^{-e} + S_e'$$

When the value of M is changed from 10 to 15 the relative changes in the energy values obtained for the 6|9 potential are less than 2.10^{-3} %. The accuracy is even better for the other potentials.

The series $C_e(\delta)$ defined by eqs. 27 and 19 is calculated term by term for all values of n_i such that

$$n_1'^2 + n_2'^2 + n_3'^2 \leqslant M^2 \; ; \quad n_i' = n_i + \delta p_i / p$$

where δ is expressed in $a/2$ units. The corresponding N atoms are within a hemisphere centred at atom $0_0'$ in the first plane $0'$ of

crystal C′ (see Fig. 2). The radius of this hemisphere, R_0 (a/2), is given by (see ref. 9)

$$(2\pi/3)\ R_0^3 - \pi R_0^2\ (\delta + 1/p) = 2N$$

Note that $1/p + \delta$ is the interplanar spacing (in a/2 units) across the two half-crystals. Crystal C, outside the hemisphere, is replaced by a continuum distribution of lamella of thickness d_0, centred in each plane, with an atomic density $4/a^3$ (Fig. 2). The procedure is similar to that used for the sums that give the surface energy [9]. The integration region, outside the hemisphere, is the difference between: i) the volume below plane 0′ outside the hemisphere; ii) the volume of a lamella of thickness $d_0/2 + \delta$, adjacent to plane 0′, and outside the hemisphere.

The integrals over these two regions are calculated in spherical coordinates, ρ (in a/2 units), θ and ϕ. But

$$\mathbf{n} \cdot \mathbf{P} = \rho\ \cos \theta - \delta$$

The integrals that give the rest of sum $C_e (\delta)$ are of the form (upon integration in ϕ)

$$\frac{2\pi}{2} \iint (\rho \cos \theta - \delta)\ \rho^{2-e}\ \sin \theta\ d\rho\ d\theta$$

where a factor $1/2$, corresponding to the atomic density in a/2 units, has been introduced.

The integral over region i) is for ρ between R_0 and ∞ and for θ between 0 and $\pi/2$. The result is

$$C'_e = \frac{\pi}{2 (e - 4)}\ \frac{1}{R_0^{e-4}} - \frac{\pi}{e - 3}\ \frac{\delta}{R_0^{e-3}}$$

The integration limits for region ii) are: ρ between R_0 and $(1/p + \delta)/\cos \theta$ and θ between $\cos^{-1} [(1/p + \delta)/R_0]$ and $\pi/2$. The result is

$$C''_e = \frac{\pi}{2p^2}\ \frac{1}{e - 2}\ (1 - p^2\ \delta^2)\ \frac{1}{R_0^{e-2}}$$

The series C_e is then calculated from

$$C_e(\delta) = \sum_{\rho \leq M} (\mathbf{n} \cdot \mathbf{P})\, \rho^{-e} + C_e' - C_e''$$

Note that for $\delta = 0$ the result corresponds to that derived in ref. 9 for the sums used in the calculation of surface energies (the series C_e in that paper is related by a factor $2/p$ to the one being used here).

When M is changed from 10 to 15, the relative change in the interaction energy $E(0)$ obtained by this method for (002), potential $6 \mid 9$, is 6.10^{-3} %. For the other potentials the error is even smaller.

REFERENCES

[1] N. H. MACMILLAN, *The Ideal Strength of Solids* in Atomistics of Fracture, Ed. R. M. Latanision and J. R. Pickens, Nato Conference Ser.; Plenum Press (1983), p. 98-164.

[2] M. BORN and R. FÜRTH, *Math. Proc. Camb. Phil. Soc.*, **36**, 454 (1940).

[3] W. R. TYSON, *Phil. Mag.*, **14**, 925 (1966).

[4] G. M. BARTENEV and E. G. KORYAK-DORONENKO, *Phys. Stat. Sol.*, **24**, 443 (1967).

[5] N. H. MACMILLAN and A. KELLY, *Proc. Roy. Soc.* **A330**, 191 (1972).

[6] F. MILSTEIN and B. FARBER, *Phil. Mag. A*, **42**, 19 (1980).

[7] G. J. DIENES and A. PASKINS, *Computer Modelling of Cracks*, in Atomistics of Fracture, Ed. R. M. Latanision and J. R. Pickens, Nato Conference Ser., Plenum Press (1983), p. 671-705.

[8] A. PASKIN, B. MASSOUMZADEH, K. SHULA, K. SIERADZKI and G. J. DIENES, *Acta Met.*, **33**, 1987 (1985).

[9] M. A. FORTES and J. B. CORREIA, *Portgal. Phys.*, **16**, 137 (1985).

[10] E. OROWAN, *Rep. Prog. Phys.*, **12**, 185 (1940).

[11] A. H. COTTRELL, *Mechanical Properties of Matter*, Willey (1964), p. 234.

[12] M. BORN, *Proc. Cambridge Phil. Soc.*, **36**, 160 (1940).

[13] F. MILSTEIN, *J. Mat. Sci.*, **15**, 1071 (1980).

[14] R. HILL, *Math. Proc. Cambridge Phil. Soc.*, **77**, 225 (1975).

[15] K. HUANG, F. MILSTEIN and J. A. BALDWIN Jr., *Phys. Rev. B*, **10**, 3635 (1974).

[16] G. E. DIETTER, *Mechanical Metallurgy*, Chap. 2, McGraw-Hill (1961).

RBS / CHANNELING, SEM AND LAMMA ANALYSES
OF SCANDIUM SINGLE CRYSTALS

M. F. DA SILVA

Departamento de Física, LNETI, 2685 Sacavém, Portugal

A. A. MELO and J. C. SOARES

Centro de Física Nuclear da Universidade de Lisboa, 1699 Lisboa, Portugal

H. J. HEINEN

Leybold — Heraeus GmbH, Cologne, West Germany

P. M. J. WINAND and R. VIANDEN

Institut fuer Strahlen und Kernphysik der Universitaet, Bonn, West Germany

ABSTRACT — It is shown how RBS/Channeling, SEM and LAMMA techniques can be combined in the surface characterization and analysis of scandium single crystals for channeling experiments. Scandium oxide layers and iron rich particles have been identified and conclusions about the solid solubility of iron in scandium are given.

1 – INTRODUCTION

Lattice location measurements in scandium single crystals are relevant to confirm recent theoretical predictions related with volume effects upon alloying of two transition metals [1], and to explain a very high field gradient measured in a scandium matrix, using an iridium probe produced by osmium implantation [2, 3].

The success of the lattice location studies is, however, very dependent not only on the possibility of growing crystals of high purity and good quality but also on the ability to prepare conveniently the crystal surface so that dechanneling will be minimized.

In order to start a systematic investigation in this metal, two random oriented single crystals acquired from different producers were prepared and studied. Results on the surface characterization of these crystals are given. It is the aim of the present work to show how well known techniques like RBS/channeling and SEM can be complemented with LAMMA analysis to characterize phenomena which appear at the near surface region of the scandium metal during annealing, and after bombardment with the analysing helium beam.

2 – EXPERIMENTAL DETAILS

The scandium samples, 1 mm thick disks, were spark cut from two random oriented 6 mm diameter and 1 mm thick scandium single crystals. The sample surface was mechanically polished with diamond paste up to $1/4 \mu$m. One of the samples was implanted with osmium ions at 80 keV and with a dose of about 10^{14} atoms/cm^2 at room temperature and at a pressure of 5×10^{-6} mbar. Annealing treatments were carried out in an oven at a pressure of about 2×10^{-6} mbar. Different temperatures and times for the annealing have been tested. The best conditions were found to be an annealing temperature of 800°C during three hours.

In one case a short time annealing of about 10 min has been tried at 1280°C. Since at this temperature the scandium vapour pressure is much higher than 10^{-6} mbar, the scandium contact surface reacted with the alumina crucible and formed a melted layer which has been analysed with the SEM technique. In order to analyse the bulk material this layer has been removed and, after polishment, a layered structure has been observed and completely characterized by RBS, SEM and LAMMA analyses. Details on these techniques are described elsewhere [4, 5].

3 – RESULTS

Although the samples of both crystals showed quite different purity (Fig. 1), reasonable channeling quality could only be obtained

after annealing at 800°C for three hours as presented in Fig. 2 and Fig. 3. The amount of particles at the surface of the annealed crystal increased during annealing (Fig. 4). Combining SEM and

a)
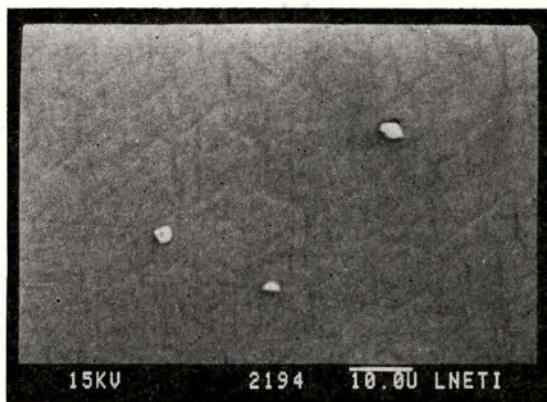
b)

Fig. 1 — SEM micrographs of two Sc single crystals which were mechanically polished: a) Sc crystal with many iron particles; b) Sc crystal with higher purity.

RBS analyses it has been possible to prove that these particles are enriched in iron. The RBS spectra confirm also the increase of iron at the surface after annealing treatment. The SEM analysis of the helium irradiated region is presented in Fig. 5. Bubbles have been formed during annealing and large iron rich crystals were observed not far from the bubbles. In one case, evidence could be found for the formation of an aglomerate of small iron rich
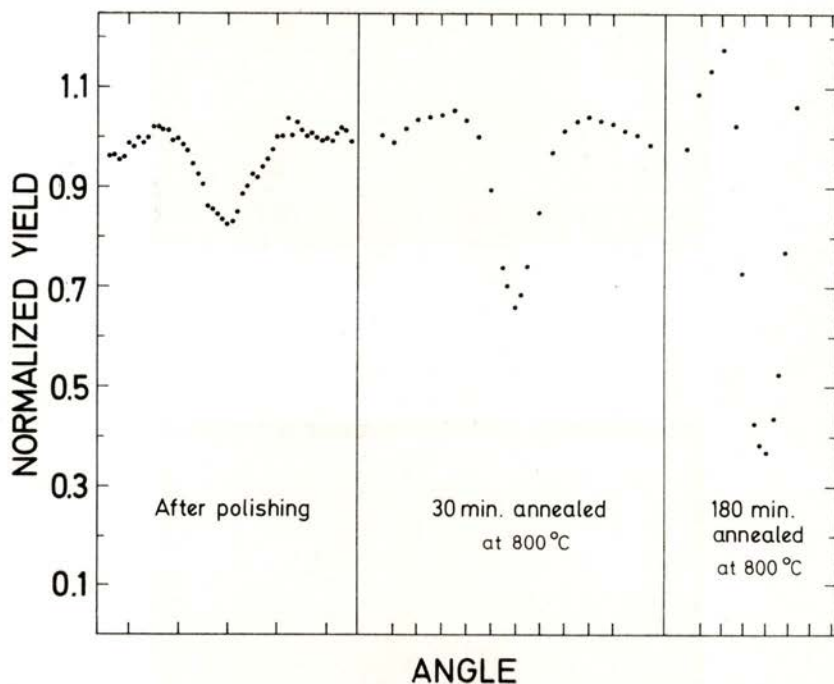
Fig. 2 — (0001) planar scans for a Sc single crystal.

particles (Fig. 6). In the case shown in Fig. 5 the crystal formed presents well defined surfaces. The composition of these particles can be derived from the SEM spectra of Fig. 7. These particles are, most probably, $FeSc_3$ which is stable up to 800°C according to the phase diagram [6].

The melted surface obtained after annealing at 1280°C and

the corresponding bulk structure observed after the mechanical polishing are shown in Figs. 8 a) and b). RBS analysis confirms that scandium remained iron free. The layered structure could be identified through the LAMMA results presented in Fig. 9 as being alternated scandium and scandium oxide layers. Finally, Fig. 10 and Fig. 11 compare the near surface region of an osmium
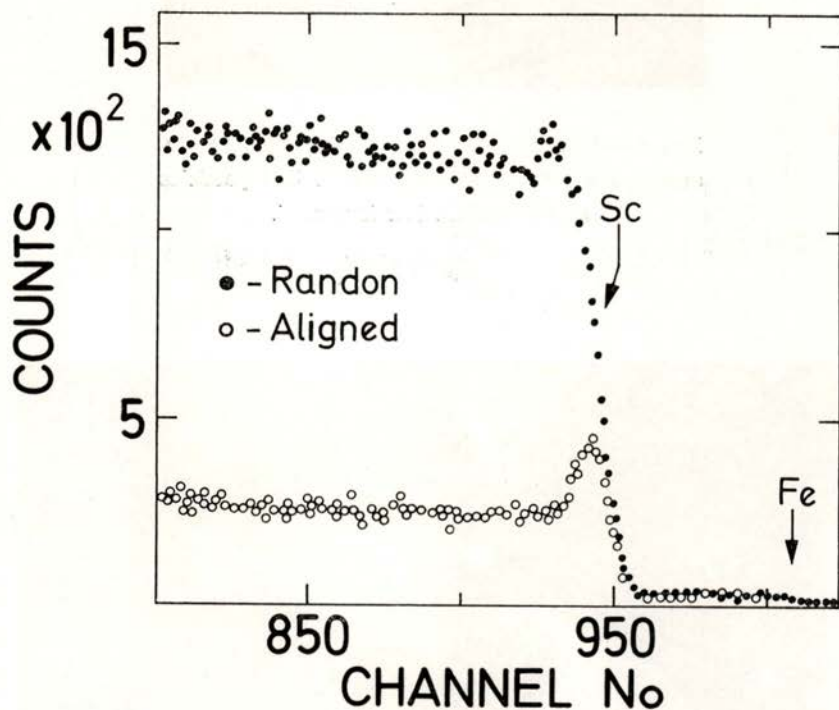
Fig. 3 — Random and aligned $< 11\bar{2}0 >$ RBS spectra after annealing at 800°C for three hours.

implanted and not implanted crystal after annealing. It is clear that dechanneling at the surface increases with the presence of the osmium implanted ions. This can be explained by an enhancement of the surface oxidation during annealing.
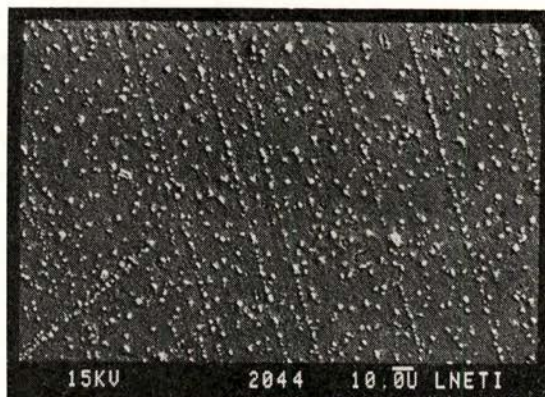
Fig. 4 — SEM micrograph of a Sc single crystal
annealed at 800°C. The number of iron particles
at the surface has increased.
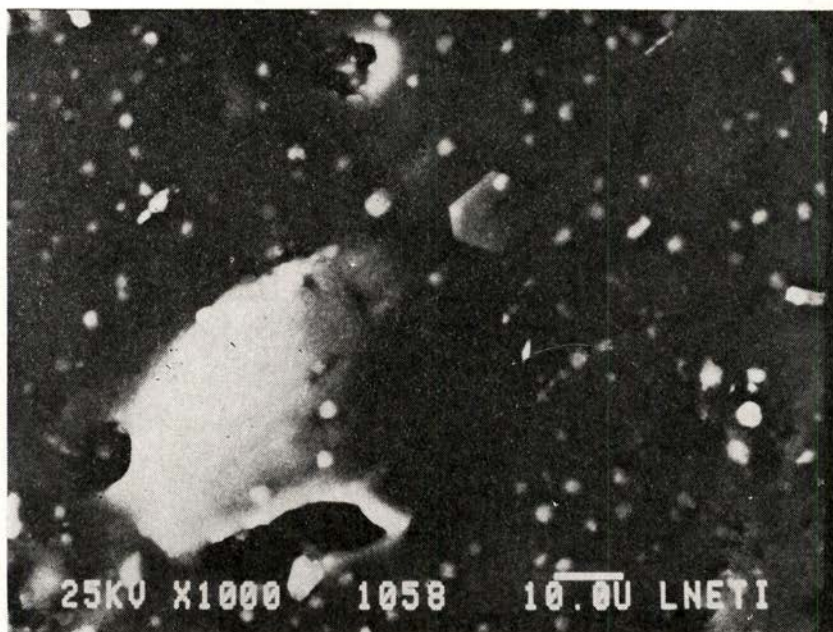
Fig. 5 — SEM micrograph of the helium irradiated region, after annealing.

Fig. 6 — SEM micrograph showing an aggregate
of iron particles.
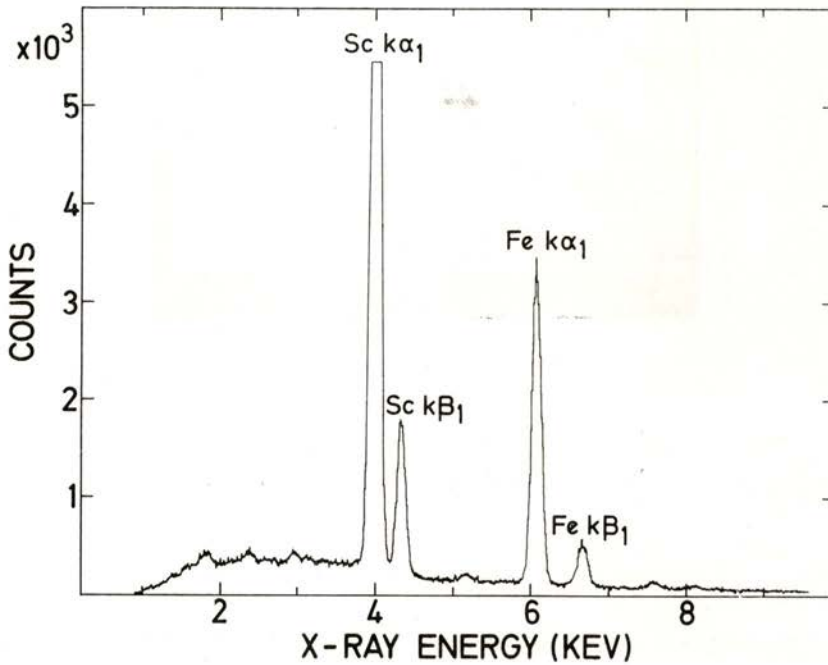
Fig. 7 — X-ray spectrum from the SEM analysis of the iron rich particles.
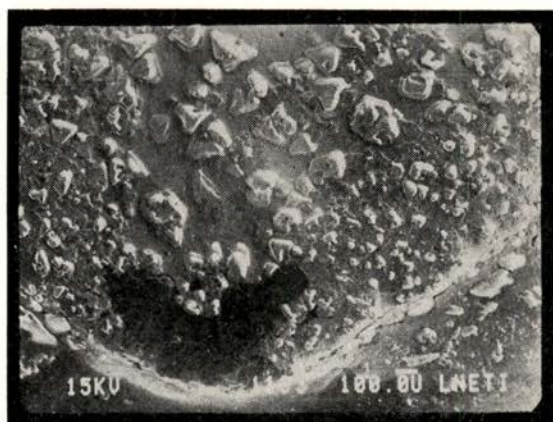
a)
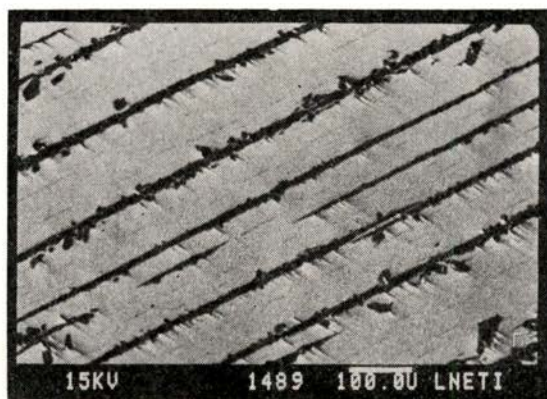
b)

Fig. 8 — SEM micrograph of the scandium annealed at 1280°C:
a) melted surface; b) after polishment.

4 — DISCUSSION AND CONCLUSIONS

From the results presented above some significant information on the solid solubility of iron in scandium can be obtained. Solubility of about 1 % to 2 % is predicted as probable in the phase

diagram [6]. The results of the present work do not confirm this prediction and on the contrary they support the idea that the solubility must be very low. This conclusion agrees with the hyperfine interaction measurements where the samples were prepared by melting a small amount of iron with scandium [2, 3]. The very high field gradients measured indicate also that inter-
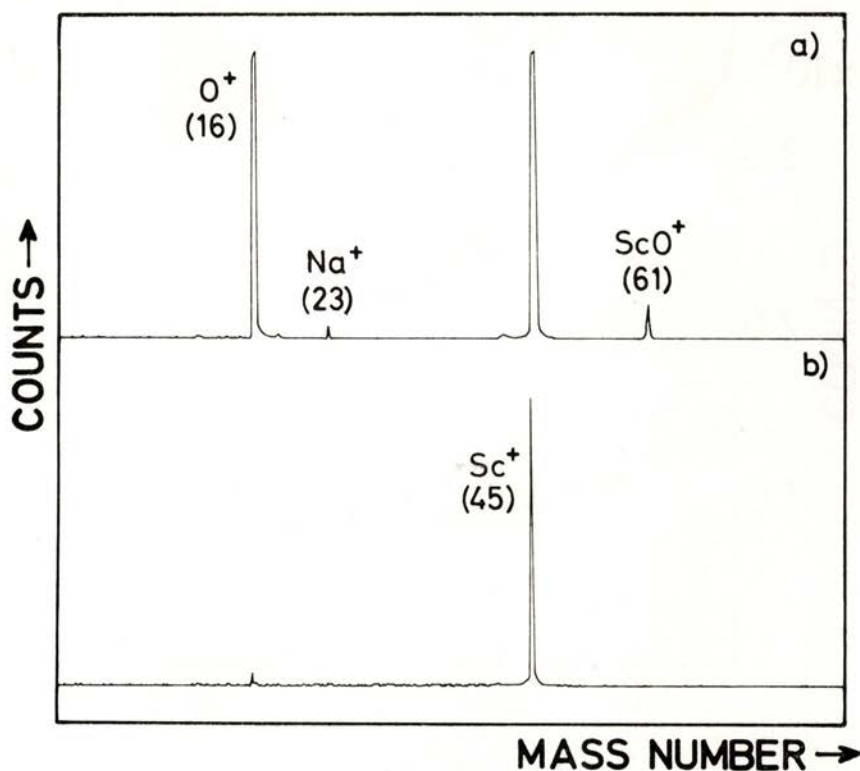
Fig. 9 — LAMMA analysis of the layered structure shown in Fig. 8 b):
a) dark lines; b) white zones.

metallic compounds were formed. Our observation that the number of iron rich particles increases with the annealing temperature agrees also with the strong dependence of the hyperfine results on the way the samples are prepared.

The improvement in the channeling quality of the single crystal shown in Fig. 2 might be related with the segregation of the iron content. When big aggregates are formed the scandium lattice shows a higher channeling quality because the number of dislocations in the lattice has decreased. In order to improve the
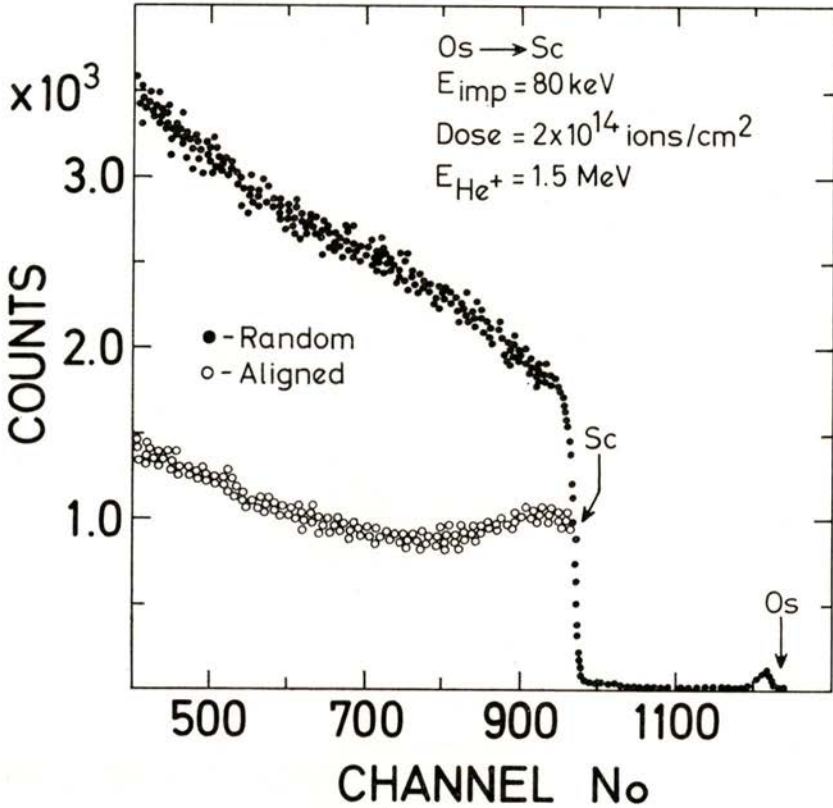
Fig. 10 — Random and aligned RBS spectra of an osmium implanted Sc crystal after annealing.

channeling performance one needs much higher purity and also cleaner surfaces. It could be shown that, at a pressure of 10^{-6} mbar, scandium reacts with the residual oxygen and this reaction is enhanced when impurities like osmium are present.

The analysis of the annealed scandium surface in the helium beam spot shows that, probably, helium is not soluble in scandium and, therefore, bubbles are formed when very high doses of helium ions are implanted. Also the radiation induced damage enhances the formation of aggregates of iron rich particles near
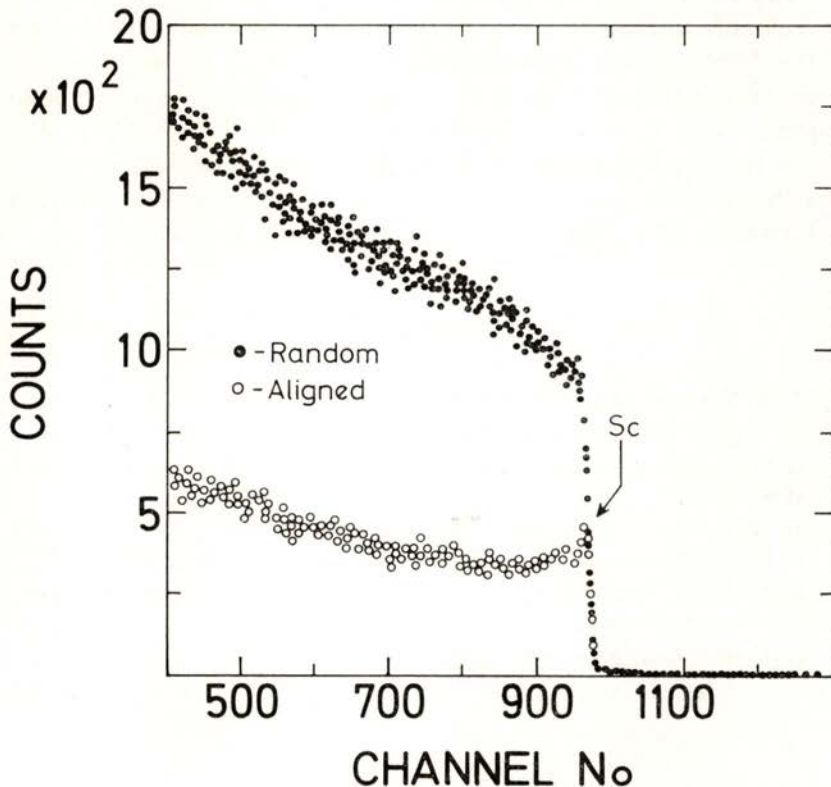
Fig. 11 — Random and aligned RBS spectra of a not implanted Sc crystal after annealing.

the bubbles as is shown in Fig. 6. With these results one can conclude that the RBS analysis using protons might be more useful and that the annealing in a pure helium atmosphere might improve the crystal surface quality.

Short annealings at very high temperature did not improve the channeling quality. They can originate a mixture of scandium-α

and scandium-β, and a contamination of the scandium crystal with scandium oxide layers as those shown and identified with LAMMA. Although the complete segregation of iron has been achieved, the channeling quality of the crystal was hindered by the big amount of Sc_2O_3 formed along planar dislocations of the crystal.

REFERENCES

[1] A. R. MIEDEMA and A. K. NIESSEN, *Physica*, **114B** (1982), 367.

[2] M. FORKER and K. KRUSCH, *Phys. Rev.*, **B21** (1980), 2090.

[3] G. WORTMAN, B. PESCHEID, G. KAINDL and F. E. WAGNER, *Hyp. Int.*, **9** (1981), 343.

[4] M. R. DA SILVA, A. A. MELO, J. C. SOARES, E. ALVES, M. F. DA SILVA, P. M. J. WINAND and R. VIANDEN, *Portgal Phys.*, **14** (1983), 175.

[5] H. J. HEINEN, S. MEIER, H. VOGT and R. WECHSUNG, *Int. J. Mass Spectrom. Ion Phys.*, **47** (1983), 19.

[6] O. P. NAUMKIN, *Russ. Met.*, **3** (1969), 125.

PORTUGALIAE PHYSICA publishes articles or research notes with original results in theoretical, experimental or applied physics; invited review articles may also be included.

Manuscripts, with an abstract, may be written in English or French; they should be typewritten with two spaces and in duplicate. Figures or photographs must be presented in separate sheets and be suitable for reproduction with eventual reduction in size; captions should make the figures intelligible without reference to the text. Authors are requested to comply with the accepted codes concerning references.

There is no page charge. Author(s) will get 50 free reprints (without covers); these are to be shared among all the authors of the article. Authors interested in more reprints should say so when sending their manuscripts; quotations shall be sent with the proofs.

Subscription rates for volume 17:

> 3.600 Escudos (US$24) — individuals
> 9.000 Escudos (US$60) — libraries

PORTUGALIAE PHYSICA may also be sent on an exchange basis; we wellcome all suggestions to such effect.

All mail to be addressed to

PORTUGALIAE PHYSICA

VOL. 17 · NUMB 1/2 · 1986

CONTENTS

PORTUGALIAE PHYSICA

PORTUGALIAE
PHYSICA

ZINN-JUSTIN AND PRIVMAN-FISHER ESTIMATORS FOR THREE-DIMENSIONAL UNDIRECTED LATTICE ANIMALS

M. C. T. P. Carvalho

Departamento de Física, Universidade de Aveiro, 3800 Aveiro, Portugal

ABSTRACT — The recent appearance of markedly different non-overlapping ranges for the first correction exponent of undirected lattice animals in 2 and 3 dimensions is examined. One of the earliest estimated ranges (in 2 dimensions) stood for nearly 8 years (the three-dimensional one is 2 years old) and we try to gain a clear perspective on the question using newly extended series data. To the best of the present accuracy we feel the newly-analysed three-dimensional results favour a value closer to 0.64 than to any value below 0.5. (New central estimates of 0.45 from a Monte-Carlo randomization method have been proposed for the radius of gyration of lattice animals in 3 dimensions.)

INTRODUCTION

Lattice animals are by now a classical area of lattice statistics whose studies have influenced an enormous mass of material in most phenomenological subjects relating to cluster growth and kinetics, with a special emphasis on gelation, aggregation, polymers and percolation models. They are, of course, their essential geometrical substrate (in discrete models) and the corpus of exact (and well established) results on topological properties and their influence on critical exponents, growth parameters and dimensional dependence can be used as a testing ground for new developments in series studies, transfer matrix calculations or Monte-Carlo generation procedures.

Real interest in lattice animals, per se, always an overlooked by-product of percolation enumeration in the 1970's, was spurred on by Lubensky's lengthy field theory on animal partitions

Portgal. Phys. — Vol. 17, fasc. 3-4, pp. 129-142, 1986

129

according to site valence and cyclomatic number [1], which predicted that the upper critical dimensionality was $d_c = 8$ and that the restricted set of lattice animals with no closed loops (or cycles), called 'lattice trees', shared the same critical exponent as the complete set of animals for all dimensions and problems. Family [2], with small-cell renormalization, Seitz and Klein [3], with Monte-Carlo tree generation in 2 and 3 dimensions, and Duarte and Ruskin [4], using series expansions, proved these results on lattice trees. The latter authors have also identified a restricted subset of lattices on which lattice trees collapse into neighbour-avoiding walks (a very different universality class from lattice animals). Ruskin and Duarte [5], have completed the series study for all dimensions using the hypercubic system.

No radius of gyration or generating function exponent predictions appear in [1] for animals with cycles. Also a very troublesome gap in exponent evolution for dimensions higher than 3 hindered any significant refining of the estimated interval for the generating function exponent (quoted as $\theta = 1.55 \pm 0.10$ in [4] for 3 dimensions). Parisi and Sourlas [6] have established $\theta = 1$, in 2 dimensions, and $\theta = 1.5$, in 3 dimensions, as well as $\nu = 0.5$, in 3 dimensions, exactly, while, two years later, Whittington, Torrie and Gaunt [7] have shown that a hierarchy of exponents was hidden in the cycle partition. No statements have been made on the correlation exponent ν and its possible cycle dependence. Numerical results (limited to series expansion evidence) were not outstanding, particularly for the higher cycle values, but a consideration of the equivalent model for directed lattices, [8], where some growth constants are known exactly, lent additional (and better) support to the existence of such an hierarchy of exponents.

Under the influence of all these results, attention has inevitably shifted from the leading exponents to the next correction exponent — the so-called first confluent singularity exponent, [9]. The earliest such attempt, due to Guttmann and Gaunt [10], virtually established a central estimate of 0.86 ± 0.05 in 2 dimensions, which was successively extended to the radius of gyration series [11], to the first moment of the bond distribution [12] and later reobtained by alternative numerical manipulations [13]. Reference [11] also first proposed a value for the confluent

exponent in 3 dimensions ($\Omega = 0.64 \pm 0.06$), while trees (from an even shorter series than that available for animals) led to the same radius of gyration interval in 2 dimensions [14].

In the last 12 months, a much heralded breakthrough on series extensions (for lattices that can be divided into two equivalent sublattices — the so-called 'bipartite' or 'loose-packed' lattices) saw its first published results [15], while a successful Monte-Carlo thermal algorithm was put forward by Glaus as an efficient and precise tree-generator, giving growth parameters and generating function exponents as well as ν estimates [16]. On the other hand, the 'incomplete enumeration method' of Dhar and Lam [17], grafting a Monte-Carlo randomization onto the exhaustive series enumeration process, has been tested by Lam [18, 19], on studies of the anisotropy and cycle partition of animals in 2 and 3 dimensions. Lam has also presented studies of the radius of gyration for total animals that show a considerable difference from the accepted confluences of all the other authors, quoting $\Omega = 0.5 \pm 0.05$ and $\Omega = 0.45 \pm 0.10$, in 2 and 3 dimensions respectively. Cycle studies through an equivalent randomization have been independently undertaken by Wilkinson [20].

Our own approach to the subject [9] has followed the historical mainstream of animal statistics, particularly drawing on a significant amount of published but not analysed data (se also [12]) and it seems fair to assert the importance of such a viewpoint now that the subject is coming close to an explosive loss of overall perspective: references [8], [14] and [16], for example, have virtually no overlapping bibliography and reports on dynamics and growth (where the area is termed 'static lattice animals') emphatically ignore the historical perspective as if lattice animals were freshly born in the past 3 years.

In this paper we undertake an analysis of the generating function for lattice animals in 3 dimensions, using the exact leading singularity exponent, $\Theta = 1.5$, and studying the first moment of the site and bond distributions enumerated in [21] to scan the usual three-dimensional lattices. Our aim is to analyse these numbers in the light of Lam's markedly different exponents for the radius of gyration — Glaus data analyses have always assumed the absence of non-analytical terms while reptation algorithms [3, 22] have not yet specialized to the evaluation of confluent corrections. We also

use the extended body-centered cubic evidence [15] to assess the gain represented in practical terms by the code-method developments in 3 dimensions.

ANALYSIS AND DISCUSSION

As stated in the Introduction we report here on the attempt to get the confluent singularity, using the Privman-Fisher and Zinn-Justin estimators, for all series data in 3 dimensions available to us, either on pure or bond- and site-weighted lattice animals [15, 21]. Most of them and particularly the weighted distributions (see appended lists) appeared to be long enough to allow already a safe comment on the bound limits of the sequences.

TABLE 1 — Tabulated values of $\Sigma_b \, bg_{sb}$ (g_{sb} being the number of animals with s sites and b bonds) worked out from refs. [15] and [21]

s	Simple Cubic	Body-centered Cubic	Face-centered Cubic
2	3	4	6
3	30	56	108
4	261	660	1 602
5	2 184	7 400	22 452
6	17 937	81 344	308 118
7	146 160	887 352	4 192 260
8	1 187 049	9 651 836	56 841 252
9	9 631 140	104 896 328	769 801 944
10	78 150 654	1 140 176 604	10 425 240 712
11	634 544 034	12 400 948 880	
12		134 992 129 128	
13		1 470 871 228 200	

For s sites or bonds the asymptotic number of different animals is usually assumed as

$$N_s = As^{-\Theta} \lambda^s \, (1 + Bs^{-\Omega} + g(s))$$

132

Portgal. Phys. — Vol. 17, fasc. 3-4, pp. 129-142, 1986

TABLE 2 — Tabulated values of Σ_s sg_{sb} worked out from ref. [21]

b	Simple Cubic	Face-centered Cubic	Diamond
1	6	12	4
2	45	198	18
3	380	3 712	88
4	3 402	74 217	455
5	31 614	1 542 120	2 448
6	300 980	32 866 554	13 494
7	2 915 160	713 112 984	75 640
8	28 595 115	15 678 677 670	429 255
9	283 236 544		2 459 052
10	2 827 120 098		14 191 320
11			82 387 836
12			480 652 244
13			2 815 642 168

where Θ and Ω are the universal leading and confluent singularities respectively, λ, A and B lattice dependent constants and $g(s)$ more rapidly vanishing confluences. Neglecting such power law correction terms higher than Ω and assuming Θ to be known exactly [6], we took the successive ratios (Privman-Fisher, [13])

$$\lambda_{s,k}(\Omega) = [R_s s - R_{s-k}(s-k)]/[s^w - (s-k)^w]$$

for $k = 1, 2, \ldots \ll s$, with

$$R_s = [s^{\Theta+\Omega} N_s]/[(s-1)^{\Theta+\Omega} N_{s-1}]$$

and $w = 1 - \Omega$.

We expected to be able to identify the range of the confluent singularity as a region of intersection of the $\lambda_{s,k}$'s close to the values previously predicted for each lattice. The patterns were rather deceptive (even in 2 dimensions) as they failed to predict

a confluent singularity below 1 and gave the estimated values of λ in the limit of Ω going to zero instead - probably a sign that such ratios actually overemphasize the relevance of the dominant behaviour.

A more straightforward adaptation of the method introduced in [13] would be to assume both λ and Θ as known, using the values of λ obtained from standard extrapolants that mostly neglect confluent singularities despite the shortness of the series. We thus considered the ratios

$$A_{s,k} (\lambda, \Omega) = [R_s - R_{s-k}] / [s^{\Omega} - (s-k)^{\Omega}]$$

with $R_s = s^{\Theta + \Omega} \lambda^{-s} N_s$ and $k \ll s$, that should display the values of the prefactor constant A for any s, and used them to establish bounds for Ω in a manner essentially dependent upon the trend of each curve. Fortunately, the regions of overlap for the various s values were highly sensitive to the varying values of Ω, inside the quoted ranges, and this led us to reasonable estimates of both A and λ that, for $\Omega = 0.64$, do not conflict with the values pointed out before and even allow for a not overly optimistic narrowing of the error bounds for both values (to be compared with the values fitted in [10] to the ansatz $N_s = As^{-\Theta} \lambda^s esp (Bs^{-\Omega}))$. The central values of A we found are lower, for most lattices and problems, than the earlier tentative ones of Guttmann and Gaunt [10].

In the light of previous estimates for the bond problems, considerable gain in the evolution of the sequences was brought up during the analysis just by trying a whole shift of the numbers of animals up to their corresponding size in bonds plus (or minus) one, an operation whose effects are negligible for large s. In fact, this implicitly defines new values A' and B' such that

$$N_s = As^{-\Theta} \lambda^s [1 + Bs^{-\Omega} + g(s)]$$
$$= A' (s+1)^{-\Theta} \lambda^{s+1} [1 + B'(s+1)^{-\Omega} + g(s)]$$

with $A' = (A/\lambda) ((s+1)/s)^{\Theta}$ and $B' = B ((s+1)/s)^{\Omega}$, that go to A/λ and B, respectively, for large s. Our results are summarized on Tables 3 and 4.

From our figures, in general, we think we can safely argue that, again due to the sensitivity of the plots (whose intersection regions are also monotonic as a function of Ω), one may really accept the value of Ω in [11] for the animal generating function (note that the authors proposed it for the radius of gyration) if the published bounds of λ are to be taken as granted. These bounds cover the whole range of allowed values of Ω in the inter-

TABLE 3 — Results of $\Omega = 0.64$ – intersection curves for three dimensional bond animals

Lattice	λ	A/λ
Body-centered cubic	15.306 ± 0.006	0.0205 ± 0.0002
Site-weighted simple cubic	10.655 ± 0.006	0.0338 ± 0.0003
Site-weighted face-centered cubic	23.984 ± 0.006	0.0114 ± 0.0002
Site-weighted diamond	6.137 ± 0.001	0.0787 ± 0.0004

TABLE 4 — Results of $\Omega = 0.64$ – intersection curves for three dimensional site animals ([1], [2] are overall estimates and (a), (b), (c), (d) the amplitude ranges consistent with them)

Lattice	λ	A
Simple cubic	8.347 ± 0.005 [1]	0.180 ± 0.002 (a)
Bond-weighted simple cubic	8.334 ± 0.005 [1]	0.209 ± 0.001 (b)
Body-centered cubic	11.182 ± 0.006 [2]	0.139 ± 0.001 (c)
Bond-weighted body-centered cubic	11.168 ± 0.005 [2]	0.163 ± 0.001 (d)
Bond-weighted face-centered cubic	13.900 ± 0.005	0.168 ± 0.001

[1] $\lambda = 8.350 \pm 0.015$ (a) $A = 0.183 \pm 0.005$ (c) $A = 0.141 \pm 0.005$
[2] $\lambda = 11.175 \pm 0.015$ (b) $A = 0.206 \pm 0.005$ (d) $A = 0.161 \pm 0.005$

val there proposed although we do not feel confident enough to narrow this range (see Figs. 1-9).

In a sense we have just stressed the problem of relying on biased parameter estimates, a common practice with short series
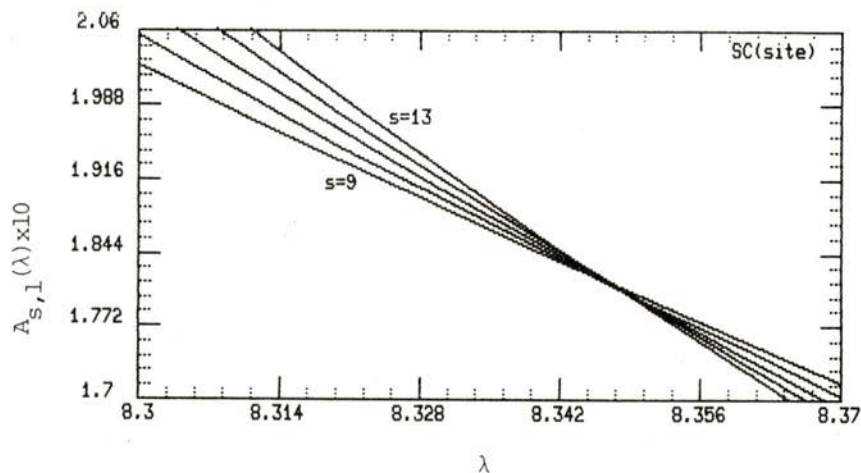
Fig. 1 — Intersections of $A_{s,1}$ (λ) for the Simple Cubic site animals for $s = 9, 10, \ldots, 13$ and the input $\Omega = 0.64$.
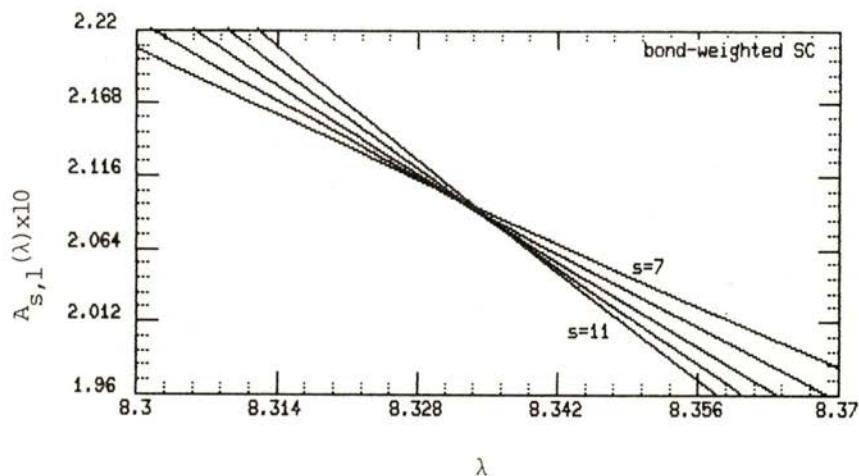
Fig. 2 — Intersections of $A_{s,1}$ (λ) for the bond-weighted simple cubic lattice animals for $s = 7, 8, \ldots, 11$ and the input $\Omega = 0.64$.

where any induced variations are quickly propagated. The Zinn-Justin estimators [23] are the simplest version of a direct
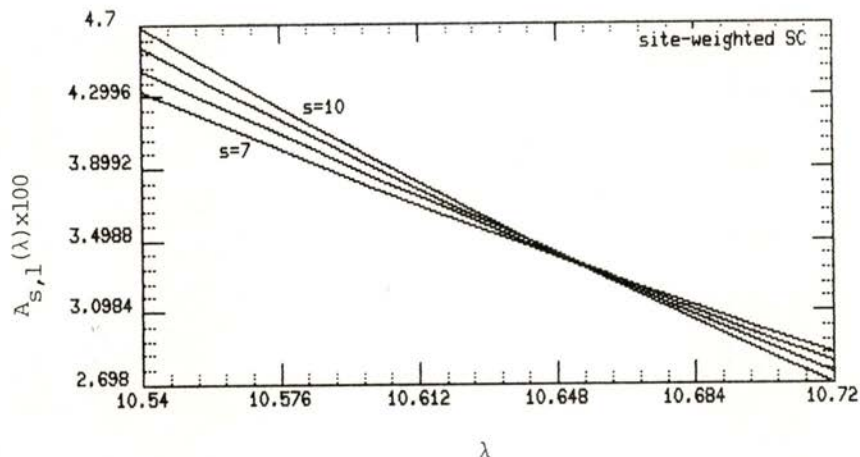
Fig. 3 — Intersections of $A_{s,1}$ (λ) for the site-weighted simple cubic lattice animals for s = 7, 8, ..., 10 and the input $\Omega = 0.64$.
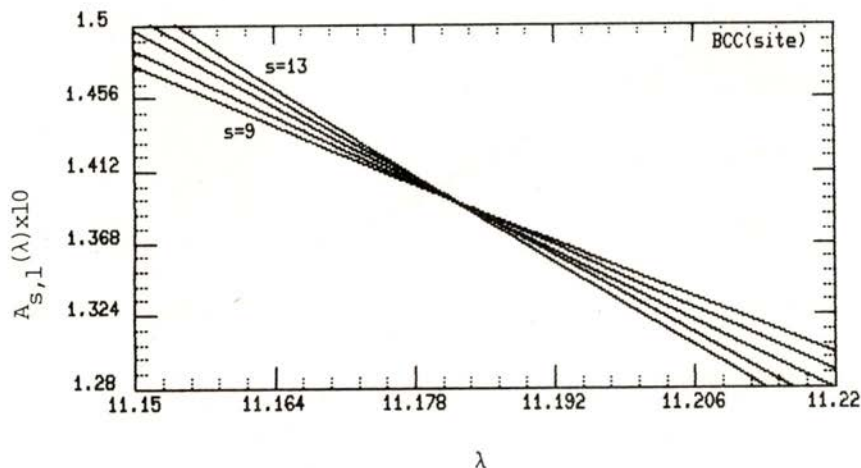
Fig. 4 — Intersections of $A_{s,1}$ (λ) for the body-centered cubic site animals for s = 9, 10 ..., 13 and the input $\Omega = 0.64$.

evaluation of the confluent singularity (up to corrections of order $O(1/s)$), provided we can use a reasonably good estimate
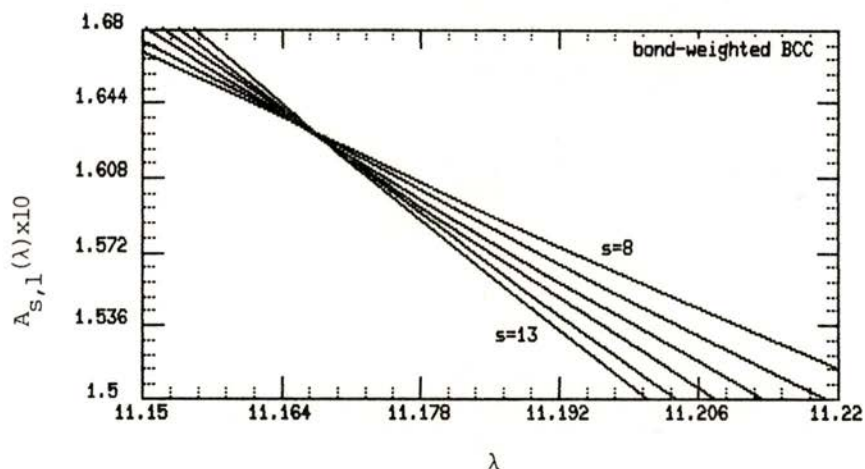
Fig. 5 — Intersections of $A_{s,1}(\lambda)$ for the bond-weighted body-centered cubic lattice animals for $s = 8, 9, ..., 13$ and the input $\Omega = 0.64$.
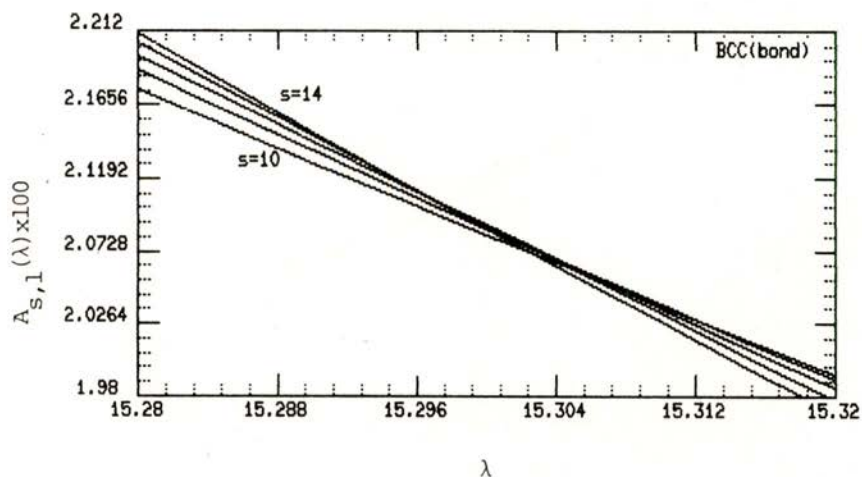
Fig. 6 — Intersections of $A_{s,1}(\lambda)$ for the body-centered cubic bond animals for $s = 10, 11, ..., 14$ and the input $\Omega = 0.64$.

of the leading exponent (ideally it should be exactly known). It involves considering, for large s, the consecutive differences

$$\Omega_s = (R_s - R_{s-1})^{-1} - 2$$
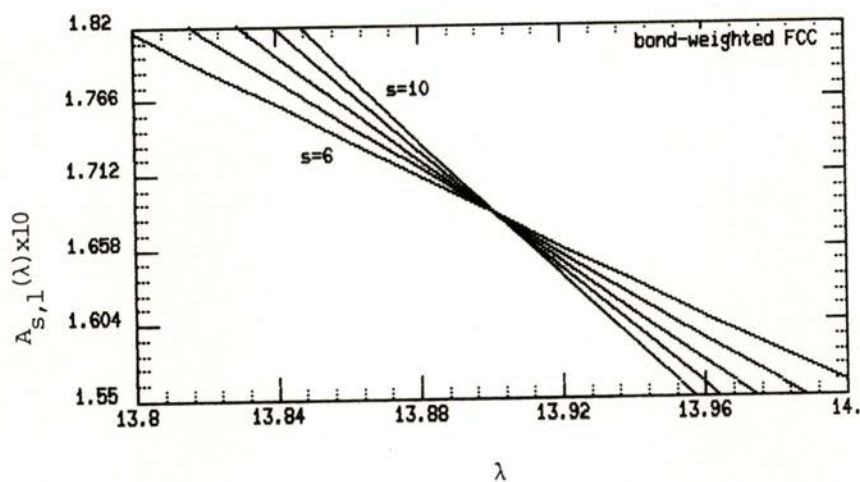
Fig. 7 — Intersections of $A_{s,1}$ (λ) for the bond-weighted face-centered cubic lattice animals for s = 6, 7, ..., 10 and the input $\Omega = 0.64$.
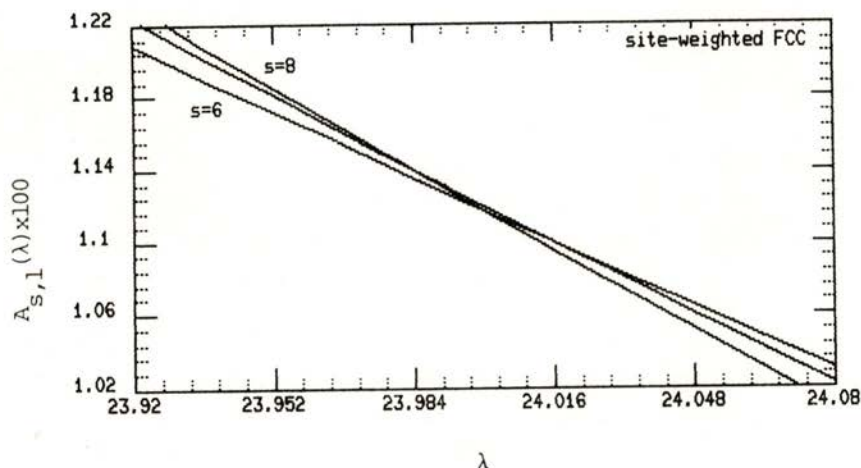
Fig. 8 — Intersections of $A_{s,1}$ (λ) for the site-weighted face-centered cubic lattice animals for s = 6, 7, 8, and the input $\Omega = 0.64$.
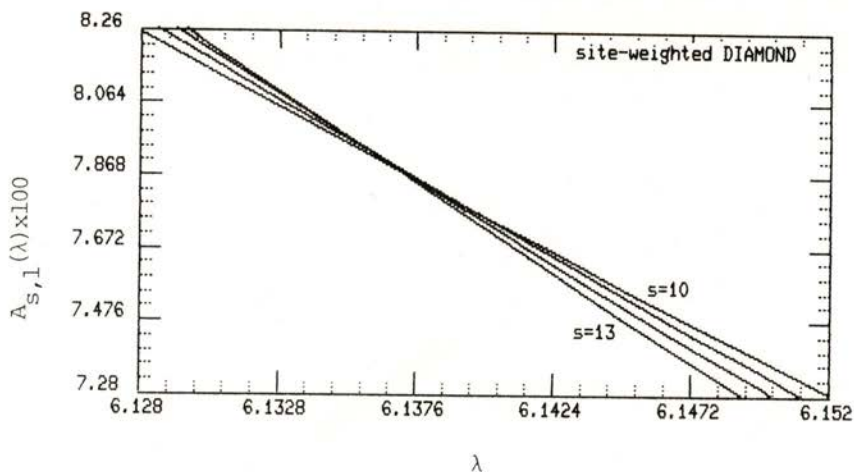
Fig. 9 — Intersections of $A_{s,1}$ (λ) for the site-weighted diamond lattice
animals for $s = 10$, 11, ..., 13 and the input $\Omega = 0.64$.

from the log-ratios

$$R_s = (\ln T_s / T_{s-1})^{-1} \doteq - [(\Omega + 2) \ln (s - 1)/s]^{-1} \doteq s/(\Omega + 2)$$

where

$$T_s = \ln (W_s W_{s-2} / W_{s-1}^2) \doteq B \Omega (\Omega + 1) / s^{\Omega+2}$$

and $W_s = s^\Theta N_s$. In other words, the T_s's are successive dis-
crete logarithm derivatives,

$$T_s = (\ln W_s - \ln W_{s-1}) / (s - (s - 1))$$
$$- (\ln W_{s-1} - \ln W_{s-2}) / ((s - 1) - (s - 2))$$

which makes them less than ideal for short series. Finally,
an averaging of two consecutive Ω_s's may be required in order to
damp any oscillations. They have been plotted against $1/s$ in Fig. 10
where only bond-weighted body- and face-centered cubic sequences
remain above 1 but with acceptably fast descending slopes. Their
spreading makes it hard to believe that the picture will be dras-
tically altered by adding a few more terms, however tempting a
clue this might provide for the presence of more distant singu-
larities, although the simple cubic site data show a troublesome
final slope (line *e*, fig. 10).

140

Portgal. Phys. — Vol. 17, fasc. 3-4, pp. 129-142, 1986

In summary and to conclude we note that we have sampled two kinds of estimators in the search for a decisive position of the series approach concerning the disparity of values proposed for
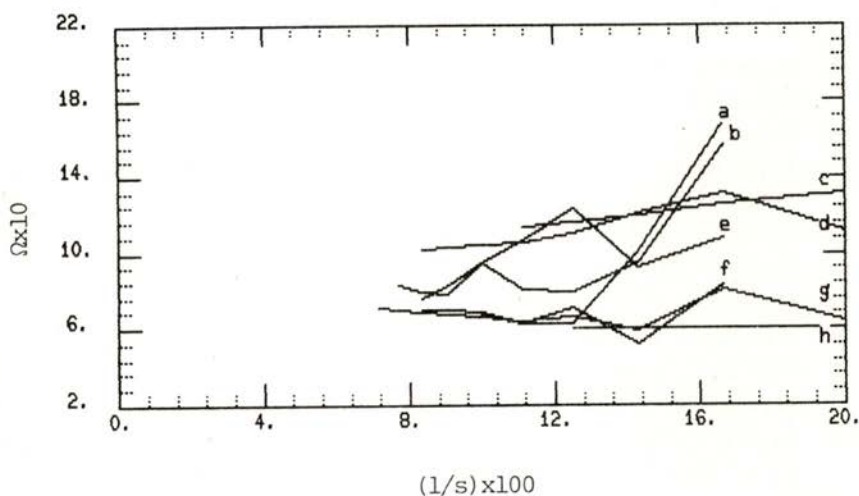
Fig. 10 — Estimates of the confluent singularity exponent for the *a*: body-centered cubic site, *b*: site-weighted diamond, *c*: bond-weighted face-centered cubic, *d*: bond-weighted body-centered cubic, *e*: simple cubic site, *f*: site-weighted simple cubic, *g*: body-centered cubic bond and *h*: site-weighted face-centered cubic animals.

the first confluent exponent of lattice animals in 3 dimensions. Falling into a band between 0.6 and 1.1, our results for the confluence of the generating function support the higher range ($\Omega = 0.64 \pm 0.06$) and certainly do not put in doubt the reliability and control of the methods used to locate singularities. For the Zinn-Justin estimators the extended series of [15] mainly confirm the trends one already obtains with data from [21] while in the Privman-Fisher version the last body-centered cubic figures added improve the tendency to a more favourable overlapping region.

This paper contains the results of a communcation to the Conferência Nacional de Física, Braga 1986.

REFERENCES

[1] LUBENSKY, T. C., ISAACSON, I., *Phys. Rev.* **A20**, 2130 (1979).

[2] FAMILY, F., *J. Phys.* **A13**, L 325 (1980).

[3] SEITZ, W. A., KLEIN, D. J., *J. Chem. Phys.* **75**, 5190 (1981).

[4] DUARTE, J. A. M. S., RUSKIN, H. J., *J. Physique* **42**, 1585 (1981).

[5] RUSKIN, H. J., DUARTE, J. A. M. S., *Phys. Rev.* **A26**, 1791 (1982).

[6] PARISI, G., SOURLAS, N., *Phys. Rev. Lett.* **46**, 871 (1981).

[7] WHITTINGTON, S. G., TORRIE, G. M., GAUNT, D. S., *J. Phys.* **A16**, 1695 (1983).

[8] DUARTE, J. A. M. S., *J. Physique Lettres* **46**, L 253 (1985).

[9] CARVALHO, M. C. T. P., DUARTE, J. A. M. S., *Portgal. Phys.* **16**, 1 (1985).

[10] GUTTMANN, A. J., GAUNT, D. S., *J. Phys.* **A11**, 949 (1978).

[11] MARGOLINA, A., FAMILY, F., PRIVMAN, V., *Z. Phys.* **B54**, 321 (1984).

[12] DUARTE, J. A. M. S., CARVALHO, M. C. T. P., *Z. Phys.* **B58**, 155 (1985).

[13] PRIVMAN, V., FISHER, M. E., *J. Phys.* **A16**, L 295 (1983).

[14] FAMILY, F., VICSEK, T., MEAKIN, P., *Phys. Rev. Lett.* **55**, 641 (1985).

[15] SYKES, M. F., *J. Phys.* **A19**, 1007, 1027 (1986).

[16] GLAUS, U., *J. Phys.* **A18**, L 609 (1985).

[17] DHAR, D., LAM, P. M., *Phys. Rev.* B (submitted).

[18] LAM, P. M., *Z. Phys.* **B64**, 227 (1986).

[19] LAM, P. M., *J. Phys.* A preprints (1987).

[20] WILKINSON, M., poster at STATPHYS 16, Boston (August 1986).

[21] DUARTE, J. A. M. S., *Portgal. Phys.* **15**, 119 (1984).

[22] DUARTE, J. A. M. S., *J. Phys.* **A19**, 1979 (1986).

[23] ZINN-JUSTIN, J., *J. Physique* **42**, 783 (1981).

A STUDY OF CHEMICAL EFFECTS ON K_β / K_α X-RAY INTENSITY RATIOS IN 3d ELEMENTS

N. Venkateswara Rao, S. Bhuloka Reddy, C. V. Raghavaiah,
S. Venkataratnam and D. L. Sastry

Swami Jnanananda Laboratories for Nuclear Research, Andhra University,
Waltair — 530 003, India.

ABSTRACT — The K_β / K_α X-ray intensity ratios were measured in some pure elements belonging to the 3d shell as well as in their compounds, to look for the influence of the chemical environment on the fluorescence yield ratios. A high resolution Si (Li) detector system was used for the experimental measurements and a low power X-ray generator was used for the excitation. It is found that the K_β / K_α X-ray intensity ratios measured with compounds deviate up to 5 % from the corresponding values of the pure elements. No such deviations are observed for the elements Mo and Ag belonging to the 4d shell.

1 — INTRODUCTION

Brunner et al. [1] have reported that the K_β / K_α X-ray intensity ratio is sensitive to the chemical environment for 3d elements. Their results show deviations up to 4 % between compounds and pure elements. These deviations were attributed to the variations in K_β transition probabilities of valence electrons with change in chemical environment. The same cannot be expected in the case of elements belonging to the N shell, since the K_β transition probability of electrons of this shell is very small. The K shell vacancies in an atom of any element can be caused either via photoelectric effect or through radioactive decay, like K-electron capture or internal conversion of K-electrons. Paić and Pečar [2] have reported different values of the K_β / K_α ratio for elements of the 3d shell following electron capture decay and photon induced

excitation. They have attributed this difference in K_β / K_α values to the difference in the mode of excitation. In the above study the chemical environment of the decaying isotope and the one used in the photon induced excitation are not the same. This might be another explanation for the difference in the K_β / K_α values in the two experiments. To confirm this idea, we have studied [3] the dependence on the mode of excitation of the K_β / K_α values using electron capture decaying isotopes and photon induced excitation of natural elements, covering two regions, $Z=20$ to 28 and $Z = 49$ to 82. Our studies reveal dependence of K_β / K_α ratio on the mode of excitation for the 3d shell elements but such a dependence is not found for the high Z elements. Our conclusion is that the apparent small dependence of the K_β / K_α ratio on the mode of excitation is in fact due to different chemical states of the element, consistently with the conclusions of Brunner et al. [1]. If the K_β / K_α ratio dependence on the mode of excita-tion is possible, then it should manifest itself in the case of high Z elements also, which we have not observed. It is to be noted [4, 5] that the K_{β_5} transition probability is significantly affected by the chemical environment in the case of 3d shell elements, but is not appreciable for the 4d shell elements. The present study concerns a measurement of K_β / K_α X-ray intensity ratios, using a high resolution Si (Li) detector system in some 3d shell and 4d shell elements and their compounds, to look for the chemical effects. The compounds of 3d elements we studied are different from previous ones, and the compounds of 4d elements are studied for the first time in the search for chemical effects. Preliminary results are reported in this paper.

2 – EXPERIMENTAL

The elements Fe, Cu, Zn, Ag and Mo were taken in the form of self supporting foils of thickness ranging from 2 to 3 μm. The chemical compounds $Fe_2(SO_4)_3(NH_4)_2SO_4$, $CuSO_4$, ZnO, $ZnSO_4$, NH_4MoO_3 and Ag_2SO_4 were taken in powdered form and pressed uniformly between two X-ray mylar films of thickness 6 μm. The thickness of these powdered samples was of the order of 250 to 500 μgcm^{-2}.

The present system comprises a high resolution Si (Li) detector (FWHM = 160 eV at 5.9 keV) coupled to a 4K multi-channel annalyser with a microprocessor base. The energy calibration of the present system was made in the usual way. The X-ray generator consists of an X-ray tube with Rh target and operates at a maximum power of 25 watts. The tube voltage can be varied from 5 kV to 50 kV and the tube current from 10 to 500 μA. The tube-target-detector geometry is shown in Fig. 1. For
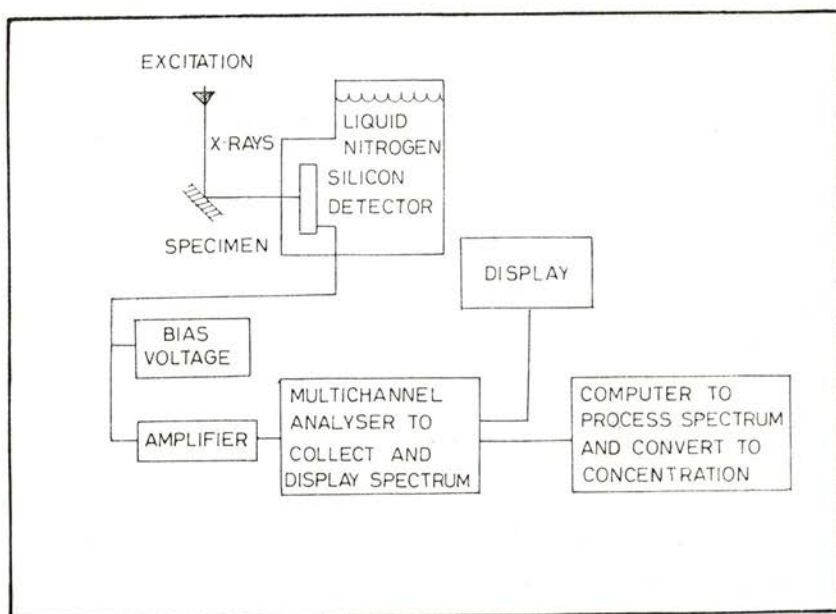

Fig. 1 — Block diagram of the experimental set-up.

the present experiments, the tube was operated at a voltage of 25 kV and a current of 200 μA. Each target of present interest was properly positioned in the sample chamber and excited in order to study the corresponding characteristic X-ray spectrum. The spectra from Fe and its compound are shown in Figs. 2 and 3, respectively. Similar spectra were recorded for the cases of Mo and Ag over a time period of 2 hours each. Since we have used, for excitation of the samples, an X-ray tube which provides high incident flux, the time of collection of data necessary to ensure good

statistics is considerably reduced. After defining the background level (assumed to be linear), the K_α and K_β line intensities were determined using the computer as well as by hand. These two
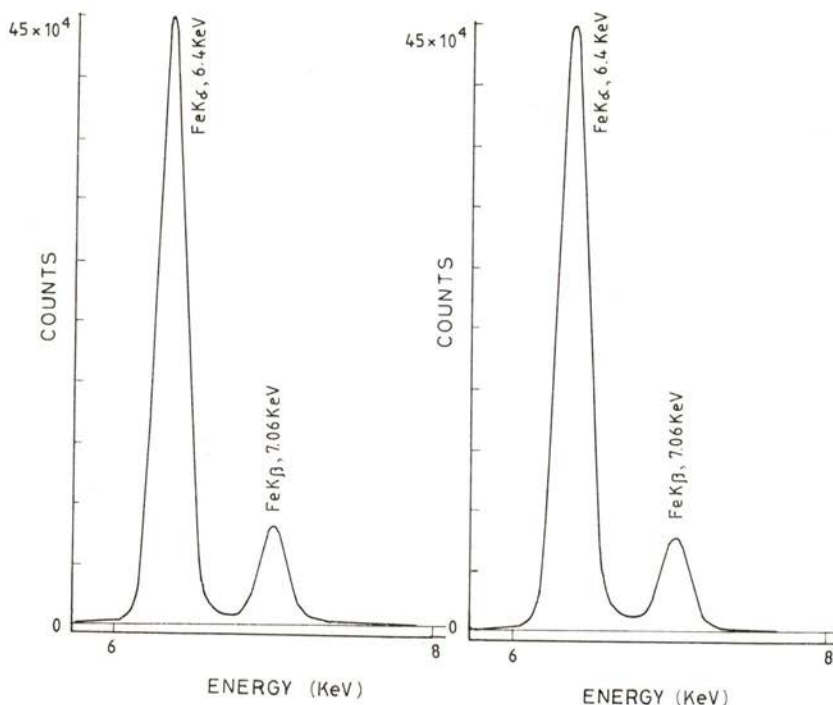
Figs. 2 and 3 — Characteristic X-ray spectrum from Fe foil (left) and from $Fe_2(SO_4)_3(NH_4)_2SO_4$ (right).

methods have yielded consistent intensities in each case. The intensities thus obtained were corrected for self absorption in the target (pure elements), using the usual relationship

$$I/I_o = (1 - e^{-\mu t}) / (\mu t)$$

where μ is the mass absorption coefficient and t the thickness in g cm^{-2}. The relevant absorption coefficients at appropriate X-ray energies were taken from the tables of NBS [6] and UCRL [7]. In the case of compounds the self absorption correction was

calculated using the sum rule [8]. The errors that arise in the computation of intensities are mainly due to the efficiency correction. In the present case one considers the ratios of X-ray intensities 'element/compound' eliminating thus the efficiency correction. The errors that arise in the estimate of the intensities are, thus, essentially due to counting statistics and they are less than 0.5 %. The final values of K_α and K_β X-ray intensity ratios were computed and are summarized in Table 1.

3 – RESULTS AND DISCUSSION

The K_α and K_β lines have fine structure which cannot be resolved by our Si (Li) detector system. Thus, the variation in the intensity of the K_{β_5} component due to chemical effects will manifest itself in the present study only in the variation of the total intensity of the K_β components. It is then justifiable to consider the K_β / K_α ratio when studying the effect of the chemical environment, instead of the K_{β_5} / K_α ratio. From Table 1, it can be seen that the K_β / K_α X-ray intensity ratio for the Cu compound deviates from pure Cu by 2.5 % while for Fe it deviates 5 %. Brunner et al. [1] reported values of the K_β / K_α ratio for Fe an Cu compounds which differ from Cu and Fe by 2 % and 1 %, respectively. However, the chemical compounds they used were different. Thus, it may be concluded that the K_β / K_α X-ray intensity ratio depends on the chemical environment for the partially filled 3d shell elements. From Table 1 it may be noted that the K_β / K_α

TABLE 1 — K_β / K_α X-ray intensity ratios for elements and compounds

Element	Compound	(K_β/ K_α) elem. $/ (K_\beta/ K_\alpha)$ comp.
Fe	$Fe_2(SO_4)_3(NH_4)_2SO_4$	0.950 ± 0.011
Cu	$CuSO_4$	0.975 ± 0.010
Zn	ZnO	0.985 ± 0.010
	$ZnSO_4$	0.980 ± 0.010
Mo	NH_4MoO_3	1.000 ± 0.010
Ag	Ag_2SO_4	0.990 ± 0.010

X-ray intensity ratio for Ag and Mo and their corresponding compounds agree with each other within experimental uncertainty. This is ascribed to the fact that the K_β transition probabilities for the 4d electrons are very small.

Further work is in progress to study the dependence of the K_β / K_α ratio on the oxygen content of the compound for each element of the 3d shell.

REFERENCES

[1] G. Brunner, M. Nagel, E. Hartmann and E. Arndt, *J. Phys.*, **B15**, 4517 (1982).

[2] G. Paić and V. Pečar, *Phys. Rev.*, **A14**, 2190 (1976).

[3] N. Venkateswara Rao, S. Bhuloka Reddy and D. L. Sastry, *Il Nuovo Cimento* (to be published).

[4] Y. Tamaki, T. Okori and T. Shiokawa, *Radiochem. Radioanal. Lett.*, **20**, 255 (1975).

[5] Y. Tamaki, T. Omori and T. Shiokawa, *Radiochem. Radioanal. Lett.*, **37**, 39 (1979).

[6] R. T. McGimics, *X-ray Atten. Coeff.*, NBS Circular., **583**, 10 (1959).

[7] M. C. McMaster, N. Kerrdel Grando, J. H. Mallet and J. H. Huddel, *UCRL Report* N.° 50174, Lawrence Radiation Lab., California.

[8] J. H. Hubbel, *Radiation Research.*, **70**, 558 (1977).

CRITICAL BEHAVIOUR OF SbSBr (*)

J. L. Ribeiro, M. Renata Chaves, Abílio Almeida,
M. Helena Amaral, António Ramalho

Centro de Física da Universidade do Porto, 4000 Porto, Portugal

S. Ziolkiewicz

Laboratoire d'Ultrasons, Université Pierre et Marie Curie, Place Jussieu,
75230 Paris Cedex 05, France

M. Balkanski

Laboratoire de Physique des Solides, Université Pierre et Marie Curie,
Place Jussieu, 75252 Paris Cedex 05, France

ABSTRACT — A study of critical behaviour in SbSBr is presented and compared with reported data. Critical exponents β, δ, γ and γ' are determined. These values are in disagreement with those predicted by a mean field theory.

1 – INTRODUCTION

SbSBr is one of the $A_V B_{VI} C_{VII}$ ferroelectric compounds. At room temperature it has an orthorhombic structure described by D_{2h}^{16} space group [1]. It is photoconductive and becomes ferroelectric at low temperatures. There has been a large discrepancy on the reported values of the critical temperatures (T_c) of this material. Pikka et al. [1] and Nitsche et al. [2] reported a 'ferroelectric phase transition' at about 90K and Fridkin et al. [3] reported the existence of another phase transition at 178K. Raman scattering measurements suggested a critical temperature of about 39K [4]. Inushima et al. observed the ferroelectric phase transition

at 22.8K by studying Raman scattering birefringence and electrical permittivity [5, 6, 7, 8].

This rather confusing situation is probably due to the sensitivity of dielectric properties in SbSBr on domains, mechanical strains and impurities.

SbSBr crystals are among the pure ferroelectric materials with lower critical temperature; it lies in the same range of the critical temperatures observed in $K Ta_{1-x} Nb_x O_3$ and $K_{1-x} Na_x TaO_3$ [9]. For such systems quantum-statistical fluctuations can be predominant and determine the range of stability of the polar phase [9]. The existence of quantum effects on ferroelectric transitions at very low temperatures is a matter of considerable interest and those effects in a quantum crystal can lead to a critical behaviour different from that in a classical crystal. In this work we report an experimental study of electrical permittivity (ε), hysteresis loops and pyroelectric effect, as a function of the temperature, in a SbSBr crystal grown by a vapour transport method. Particular attention is focused on the analysis of the critical behaviour of the electric permittivity and spontaneous polarization.

2 — EXPERIMENTAL

The sample studied was carefully cut with a thickness of 1.4 mm along the c axis (polar axis). The cross section area is 0.73 mm². The electrodes were made of silver paste.

Electrical permittivity was measured at a frequency of 10 kHz along the polar direction by using a Hewlett Packard LCR meter 4262A. Hysteresis loops were obtained with a modified Sawyer-Tower circuit at 0.2 Hz frequency.

Fig. 1 (a) shows the relative electrical permittivity (ε_r) as a function of the temperature. A clear anomaly is observed in ε_r (T) and its maximum value takes place at $T_{max} = 23.8K$. A plot of ε_r^{-1} versus T can be seen in Fig. 1 (b). A detailed behaviour of ε_r and ε_r^{-1} versus T in the critical region are displayed in Fig. 2 (a) and Fig. 2 (b), respectively. Near T_c there is a deviation from the Curie-Weiss law over an appreciable range of temperatures, above and below T_c. In the higher temperature region of the paraelectric phase we remark a kind of saturation of ε_r^{-1} (T).

Temperature dependence of the spontaneous polarization (P_s) in the same sample was determined by studying ferroelectric
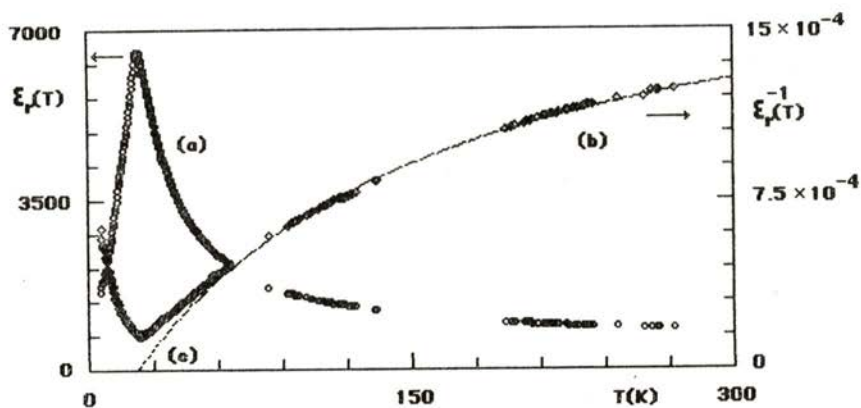
Fig. 1 — Temperature dependence of electrical permittivity parallel to c axis, ε_r (a) and inverse electrical permittivity (b), of SbSBr.
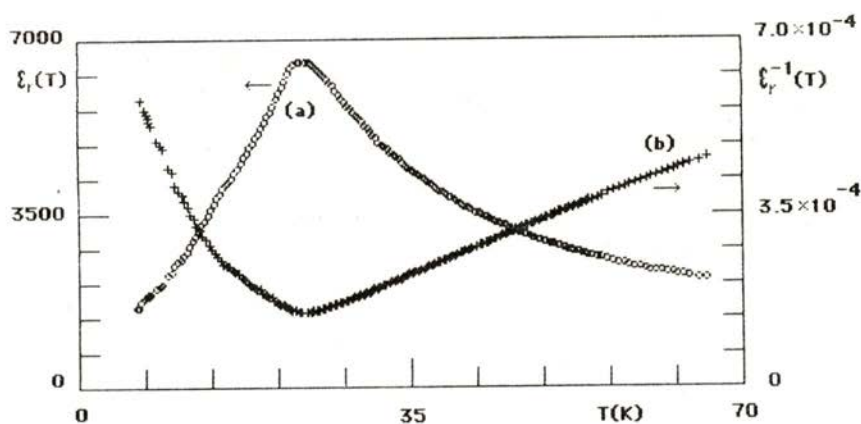
Fig. 2 — Temperature dependence of electrical permittivity parallel to c axis, ε_r (a) and inverse electrical permittivity (b), of SbSBr.

hysteresis loops. No double loops were observed. Fig. 3 shows a plot of P_s versus T; for $4 < T < 10K$, P_s is approximately constant and its value is $6 \mu Ccm^{-2}$. A very sharp decrease of P_s is observed around T_c, but above this temperature some residual

polarization is still observed up to about 39K. We have also studied the pyroelectric effect in order to see if that important tailing off of polarization was an intrinsic effect or a polarization induced by
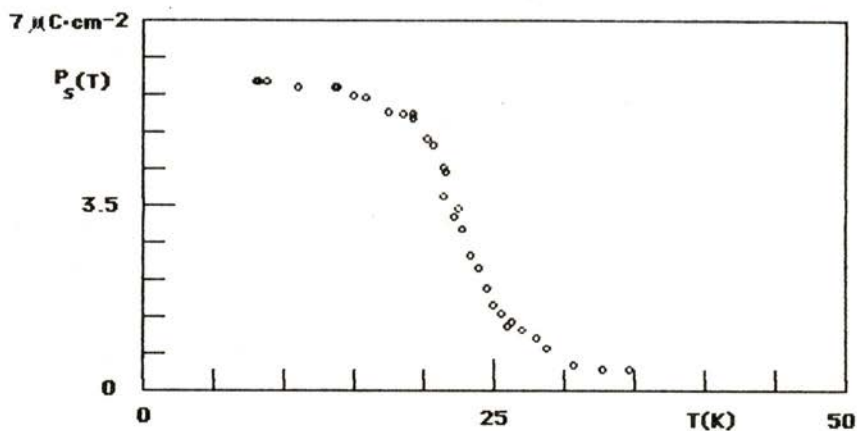
Fig. 3 — Temperature dependence of the spontaneous polarization (P_s) parallel to c axis of SbSBr, obtained from D-E hysteresis loops.

the applied a.c. electric field used to obtain the hysteresis loops. Preliminary results on the pyroelectric effect show a clear anomaly in the critical region (Fig. 4 (a)). Temperature dependence of P_s
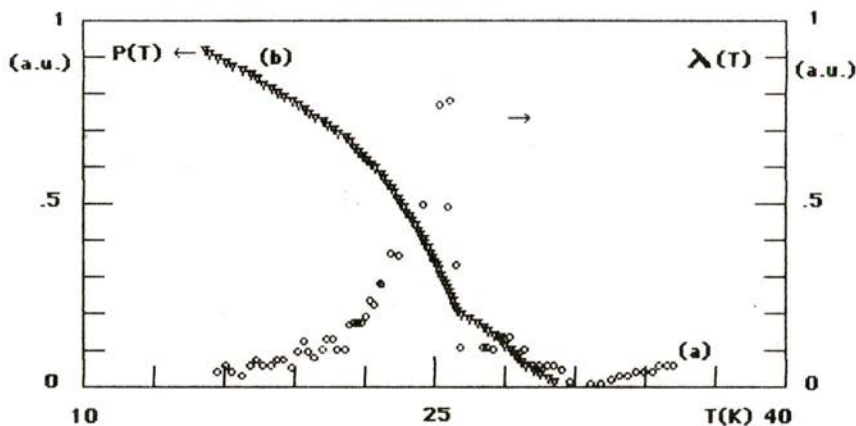
Fig. 4 — Temperature dependence of the pyroelectric coefficient λ (a) and spontaneous polarization, P_s (b) parallel to c axis, of SbSBr.

deduced by integration of the pyroelectric coefficient is similar to that obtained by the hysteresis loops study (Fig. 4 (b)).

In Fig. 5 we can see a plot of the coercive electric field versus temperature and remark a coercive field tailing off.
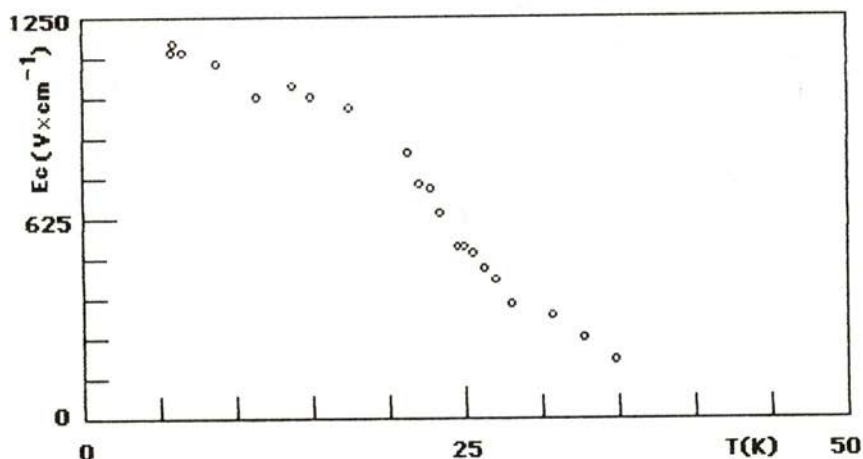
Fig. 5 — Temperature dependence of the coercive electric field (E) in SbSBr.

3 – ANALYSIS AND DISCUSSION

Our experimental results are in good agreement with those previously found in samples of SbSBr, $T_c \sim 23K$ [8]. In all these results we can observe clear deviations from Landau theory predictions and so it seems meaningless to analyse the experimental results in the scope of that theory. It seems that short range interactions must be taken into account for a better understanding of data. Those interactions can arise from intrinsic properties associated with a peculiar behaviour of fluctuations and correlation functions in ferroelectrics with low T_c. Point defects, spatial charges or internal strains in the sample, can also give an important contribution to the critical behaviour.

In order to see to what extent short range interactions would be important, our analysis of the experimental results focuses on

the question of existence of single exponent laws and the determination of those exponents.

It is difficult to find an experimental criterion to determine the critical temperature from a study of hysteresis loops. As usual we take the temperature of the maximum of the dielectric constant as the critical temperature.

Fig. 6 shows a plot of $\ln P_s$ versus $\ln |t|$, with $t = (T - T_c) / T_c < 0$. From the slope of the straight line drawn in the figure $(0.01 < |t| < 0.6)$ we have determined a critical
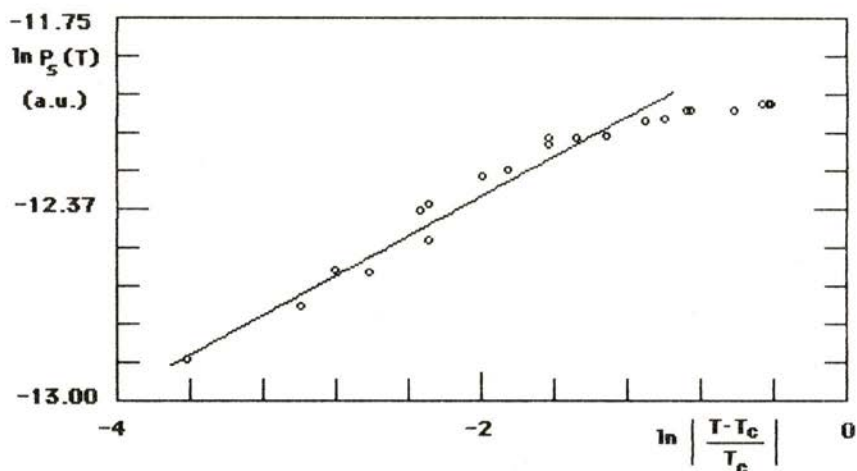
Fig. 6 — Logarithmic plot of the spontaneous polarization (P_s) versus reduced temperature (t).

exponent $\beta = 0.31$. This value closely agrees with $\beta = 0.30 \pm 0.05$, obtained from Raman scattering in SbSBr [4]; it is also of the same order of magnitude as the value $\beta = 0.26$ reported in [8], obtained from a birefringence study. Fig. 7 shows the logarithm of the applied a. c. field (E) versus $\ln P$, for several temperatures near T_c; the data are fitted by lines $\ln E = \tilde{\delta} (T) \ln P + \text{const.}$ A plot of $\tilde{\delta}$ versus T can be seen in Fig. 8: $\tilde{\delta} (T)$ is a function with a rapid variation and so it is difficult to determine precisely the critical exponent δ ($E \sim P^{\delta}$ for $T = T_c$ [10]). The value of $\tilde{\delta}$ for $T_c = 23.8K$ is 4.1.
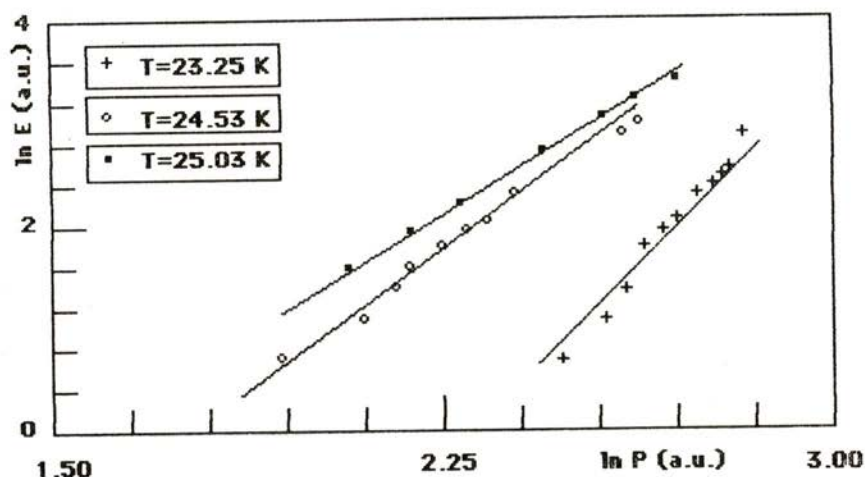
Fig. 7 — Logarithmic plot of electric polarization (P) versus electric field (E), at different temperatures: + 23.25 K, o 24.53 K, ■ 25.03 K.
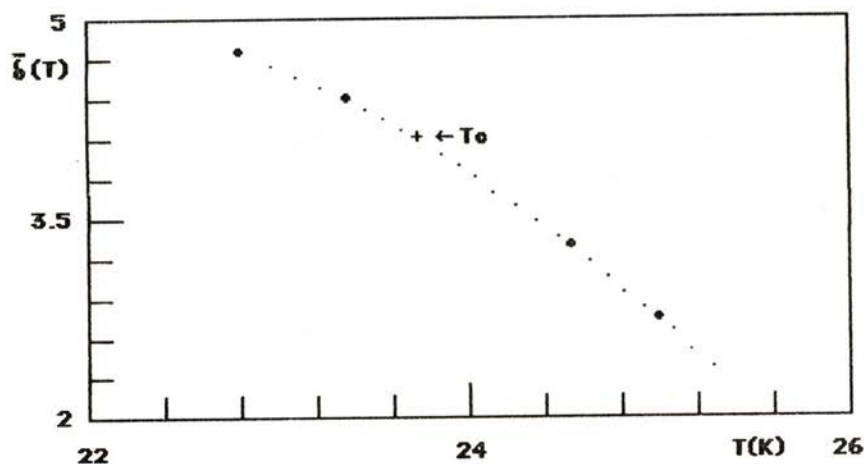
Fig. 8 — $\tilde{\delta}$ (see text) versus temperature (T).

Fig. 9 shows ln ε_r versus ln $|t|$. We can see a flattening of the electric permittivity close to T_c. This situation is commonly encountered in ferroelectrics with low T_c [9]. Well below

T_c the experimental data can be fitted to the expression $\ln \varepsilon_r = -1.38 \ln |t| + 6.99$ $(0.3 < |t| < 0.8)$, and the exponent associated with the electrical susceptibility is $\gamma' = 1.38$.
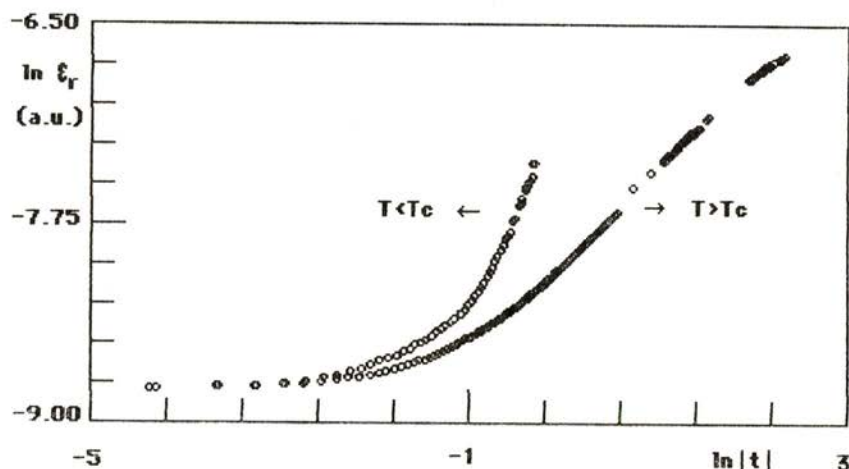
Fig. 9 — Logarithmic plot of electrical permittivity (ε_r) versus reduced temperature (t), for $T < T_c$ and $T > T_c$.

The critical exponents we found for $T < T_c$ clear deviate from those predicted by a mean field theory and can be associated with the role played by fluctuations in the phase transition. In particular, fluctuations can be enhanced by defects of the asymmetric type and it seems plausible that critical exponents in defective systems deviate more from the mean field exponents than those in the pure system [12]. The theoretical values of critical exponents in a 3-dimension short range model with just one order parameter component are $\beta = 0.325$ and $\gamma = \gamma' = 1.241$ [13].

In the paraelectric region the plot of ε_r^{-1} versus T (Fig. 9) allows us to distinguish three regions. Above $T \sim 50K$ the experimental data can be fitted to a modified Curie-Weiss law [11] $\varepsilon_r^{-1} = A_0 (T - T_0) / (T - T_0 + \tilde{T})$, with $T_0 \sim 22.5 \pm 0.5K$, $A_0 \sim (1.96 \pm 0.01) \times 10^{-3}$ and $\tilde{T} = 147.4K$. A similar behaviour is reported in [14]. This law is predicted by a quasi-one dimension shell model which takes into account interactions between two

sublattices (rigid cations and polarisable anions) [11]. A single exponent law is verified between 36 K and 50 K and in that region data can be fitted to $\ln \varepsilon_r = -0.59 \ln |t| + 8.02$; which leads to the exponent 0.59. Near T_c there is a considerable roundness in ε_r. A behaviour similar to this one was observed in $K H_2 PO_4$ under a pressure of 15.4 kbar ($T_c = 32K$), as can be seen in Fig. 4c of reference [9].

REFERENCES

[1] T. A. Pikka and V. M. Fridkin, *Sov. Phys. - Solid State* 10, 2668 (1968).

[2] R. Nitsche, H. Roetschi and P. Wild, *Appl. Phys. Lett.* 4, 210 (1964).

[3] V. M. Fridkin, E. I. Gerzanich, I. I. Groshik and V. A. Lyakhovitskaya, *Sov. Phys. - JETP Letters* 4, 139 (1966).

[4] E. Furman, G. Brafman and J. Makovsky, *Phys. Rev. B* 8, 2341 (1973).

[5] T. Inushima, K. Uchinokura, K. Sasahara and E. Matsuura, *Phys. Rev. B* 26, 2525 (1982).

[6] T. Inushima, K. Uchinokura, K. Sasahara, E. Matsuura and R. Yoshizaki, *Ferroelectrics* 38, 885 (1981).

[7] T. Inushima, A. Okamoto, K. Uchinokura and E. Matsuura, *J. Phys. Soc. Japan* 48, 2167 (1980).

[8] T. Inushima, K. Uchinokura, L. Matsuura and A. Okamoto, *J. Phys. Soc. Japan* 49, Suppl. A. 753 (1980).

[9] D. Rytz, U. T. Hochli and H. Bilz, *Phys. Rev. B* 22, 359 (1980).

[10] H. E. Stanley, *Introduction to phase transitions and critical phenomena*, Clarendon Press, Oxford 1971.

[11] M. Balkanski, M. K. Teng, M. Massot and H. Bilz, *Ferroelectrics* 26, 731 (1980).

[12] J. C. Tolédano, *Annales des Télécommunications* 39, 277 (1984).

[13] J. C. Le Guillou, J. Zinn-Justin, *Phys. Rev.* B21, 3976 (1980).

[14] M. R. Chaves, M. H. Amaral, A. Almeida, S. Ziolkiewicz, J. Y. Prieur and M. Balkanski, *Ferroelectrics* 54, 261 (1984).

DOMAINS AND IMPERFECTIONS IN FERROELECTRIC TGS

Manuela Lopes dos Santos, Abílio Almeida,
Maria Renata Chaves, António Ramalho,
Maria Helena Amaral

Laboratório de Física, Faculdade de Ciências, Uuiversidade do Porto, 4000 Porto, Portugal

ABSTRACT — Dielectric constant, polarization and pyroelectric coefficient of ferroelectric TGS are investigated near the phase transition. The values of the critical exponents β, δ, γ and γ' are in agreement with those predicted by a mean field theory. The dielectric constant values are strongly influenced by domain formation. Domain relaxation seems to obey a «stretched» exponential law.

1 – INTRODUCTION

Triglycine Sulfate (TGS) – $(NH_2 CH_2 COOH)_3 \cdot H_2SO_4$ – is a uniaxial, order-disorder ferroelectric with a second order phase transition at ~322K [1]. Deuteration has a small effect on its ferroelectric properties.

TGS crystallizes with the symmetry of the monoclinic system. In the high temperature phase its symmetry group is C_{2h} with the binary axis parallel to the b axis of the monoclinic system. In the ferroelectric phase the symmetry group is C_2 and the polarization in TGS is associated with the glycine molecules [2].

Although intense study has been made on triglycine sulfate's dielectric behaviour and a good agreement with the Mean Field Theory is usually obtained, there are still a few aspects that need to be clarified. In fact the ratio of the slopes of the reciprocal dielectric constant (ε^{-1}) versus the temperature below and

above T_c (m_1 / m_2) yields values higher than the value 2 predicted by Landau's theory of phase transitions [3, 4, 5, 6]. The adiabatic correction suggested by Triebwasser [7] is not enough to obain a value of 2. The factors that are usually presented as being responsible for such a behaviour are: the existence, in the sample, of superficial layers with a small dielectric constant [8, 9, 10] and, in polydomain samples, the electrostriction effect caused by the formation of differently oriented domains. In addition, the study done by Gonzalo [11] and Sekido & Mitsui [10] suggests an infinite value for the dielectric constant at the transition, while other authors [12] find that it has a finite value.

Our purpose is to try to clarify this situation, as well as to verify the importance of surface treatments. Fatigue caused by the application of electric fields, and the influence of domains in TGS are also studied. We measured the dielectric constant, pyroelectric coefficient and spontaneous polarization as functions of temperature in differently prepared samples and we analysed the results obtained.

2 – EXPERIMENTAL PROCEDURE

The samples (1, 2 and 3) used in our study had the shape of thin slices, of different surface shapes, perpendicular to the b axis,

TABLE I — Dimensions and preparation of the measured samples

Samples		1	2	3
Extraction from mother crystal		cleavage	cleavage	cut
Surface polishment		water	water	diamond paste (1μ)
Dimensions	Area (mm²)	37.1	13.5	32.0
	Thickness (mm)	1.2	1.0	1.6
Max. temperature (°C) subjected during preparation		70-80	70	room temp.

160

Portgal. Phys. — Vol. 17, fasc. 3-4, pp. 159-172, 1986

and were obtained from different parts of the same TGS single crystal. Their characterization is summarized in Table I.

All samples had excellent transparency and no tensions or defects could be detected when analysed in a polarization microscope. We used silver paste as electrodes, and during measurements all samples were free from any clamping.

To measure the complex dielectric constant, we used a five terminal coaxial method [13] with a resolution of about 0.01 pF.
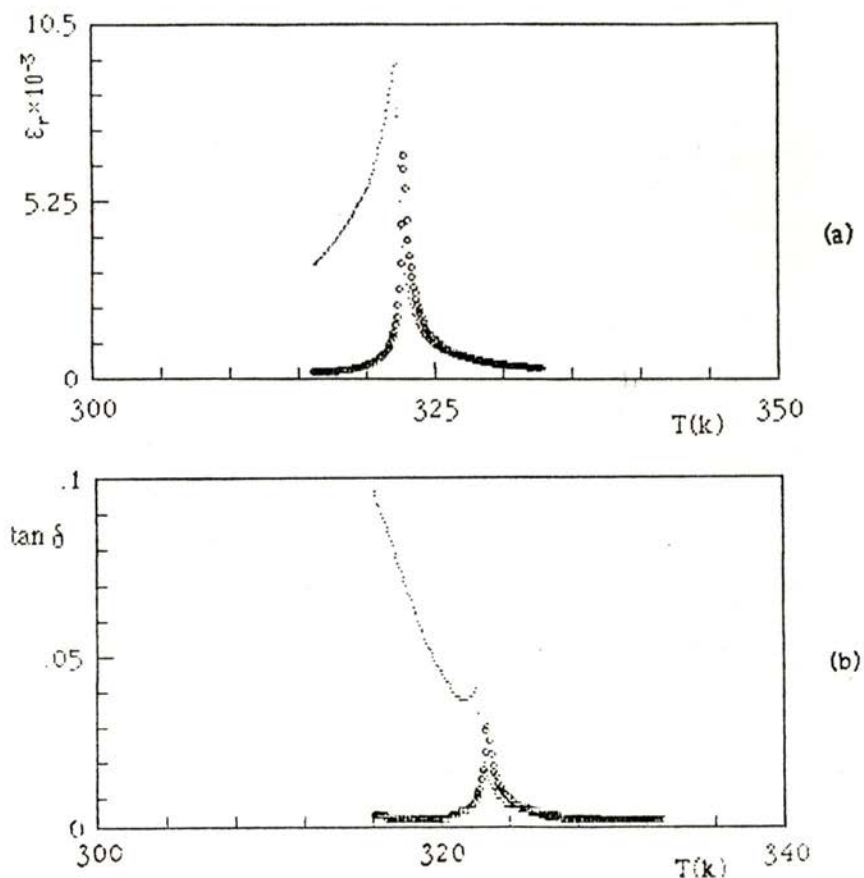

Fig. 1 — Relative dielectric constant (a) and loss, tan δ (b) as function of temperature, in sample 3, during: o $\rightarrow$ heating; • $\rightarrow$ subsequent cooling down. These measurements were taken at 1 kHz.

The data acquisition was done automatically through an IEEE bus. We chose a 1V amplitude measuring signal with frequencies of 1 kHz or 10 kHz.

A copper-constantan thermocouple was used to measure the sample's temperature and we had a temperature stability of about 0.02K.

The pyroelectric coefficient was measured by studying the pyroelectric current under short-circuit conditions [14] using an electrometer with a resolution of about 1×10^{-14}A. The data acquisition was done automatically through a BCD bus. To achieve a monodomain the samples were always cooled from the paraelectric phase under an electric field of about 0.8 kV.cm^{-1}. When the intended temperature was attained, the field was removed and the samples' electrodes shortcircuited during a few hours, eliminating in this way any residual spatial charges. Measurements of the pyroelectric current were then taken, when warming up the sample at a heating rate of about 0.1K per minute at the transition.
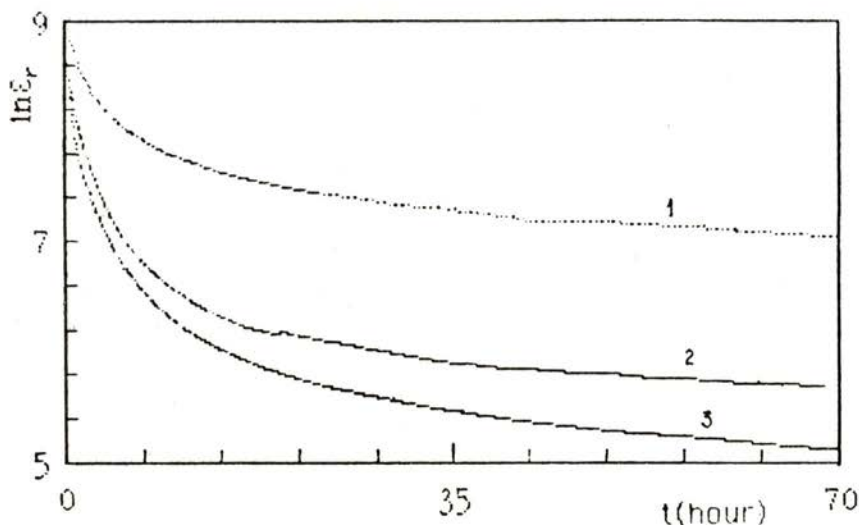
Fig. 2 — ln ε_r vs. time in the ferroelectric phase at constant temperatures $T_1 < T_2 < T_3$. These measurements were taken after cooling the sample through the phase transition.

To study the polarization reversal we used a modified Sawyer-Tower circuit [13]. The alternating electric tension applied to the samples had a frequency of 0.2 Hz and an amplitude of about 500 V.

3 — RESULTS AND DISCUSSION

The results obtained by us clearly show that the values of the relative dielectric constant ε_r and loss tanδ are systematically smaller on heating the samples through the phase transition than on the subsequent cooling down. An example of this behaviour is shown in Fig. 1 and it is associated with the fact that the domain structure of TGS ferroelectric phase takes some days to relax to equilibrium. Until it does, the response (ε_r) to the measuring field has a higher value than the equilibrium one, due mostly to domain wall motion. This behaviour is shown in the time dependence of ln ε_r depicted in Fig. 2, for a sample other than the three already referred. In this figure we can see that the relaxation behaviour is not an exponential one. We found that
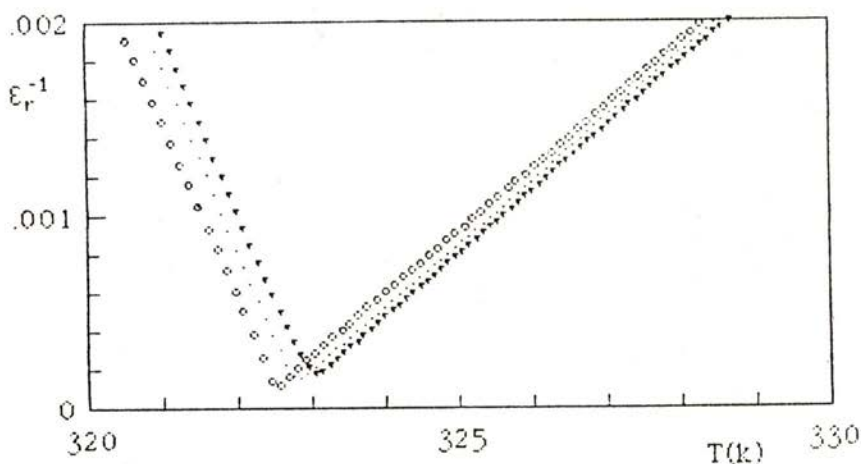
Fig. 3 — Inverse of relative dielectric constant ε_r^{-1} vs. temperature T, for three consecutive heatings relating to sample 3: o → heating on virgin sample; • → first heating on monodomain sample; ▼ → third heating on monodomain sample.

TABLE II — Values of ε_r max., temperature at ε_r max. and ratios m_1/m_2 calculated in the ranges of 2K or 5K around T_0, for the three samples studied. The electric field used on the samples to achieve a monodomain was 0.8 kV cm^{-1} except on the first heating of monodomain sample 1. In this case the electric field was ~0.4 kV cm^{-1}.

Number of sample	Consecutive warm ups of the sample	ε_r max.	Temperature T_0 at ε_r max. (K)	m_1/m_2 in the range of	
				2K around T_0	5K around T_0
1	1st heating on monodomain sample	10285.71	323.06		2.6
	2nd heating on monodomain sample	9218.33	322.94		2.83
2	heating on virgin sample	59925.93	322.59	3.42	3.23
	1st heating on monodomain sample	39185.19	322.66	3.62	3.30
3	heating on virgin sample	8998.87	322.59	2.76	2.82
	1st heating on monodomain sample	6612.65	322.86	2.72	2.90
	3rd heating on monodomain sample	6046.38	323.05	2.83	3.03

164

Portgal. Phys. — Vol. 17, fasc. 3-4, pp. 159-172, 1986

the data concerning ε_r versus time could be satisfactorily fitted to the expression [15]:

$$\varepsilon_r = \varepsilon_0 \exp\left[-(Ct)^m\right]$$

where $\varepsilon_0 = \varepsilon_r$ for $t = 0$ and C and m are parameters.

Because of this, only measurements when heating a sample with its domain structure in equilibrium — virgin or monodomain sample — were analysed. To achieve a monodomain, we followed
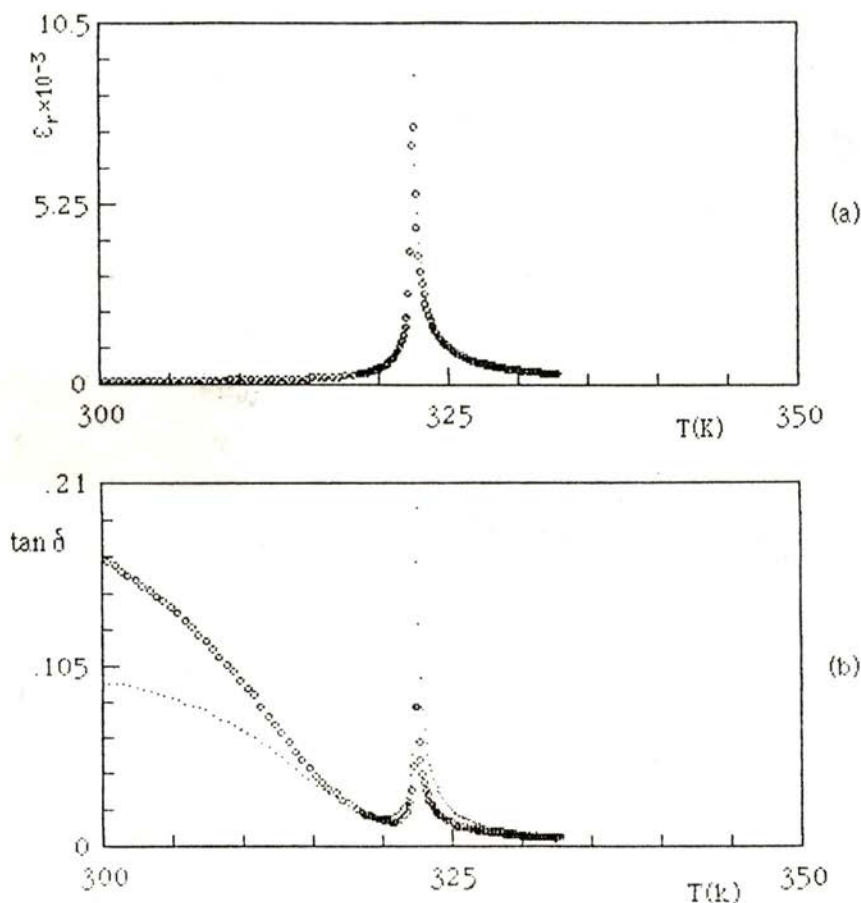
Fig. 4 — Relative dielectric constant ε_r vs. temperature T (a) and loss tangent tan δ, vs. T (b) relating to virgin sample 3. These measurements were taken when heating the sample at the frequency of: ● → 1 kHz; o → 10 kHz.

the same procedure as in the pyroelectric measurements. Although the electric field used to achieve a monodomain was not high, it still caused some 'fatigue' in the material, as can be seen from results concerning sample 3 (Table II and Fig. 3). One should also note in Fig. 3 that ε_r has finite values at the phase transition, in agreement with the results obtained by Graig [13].

The influence of the sample surface treatment on the behaviour of ε_r vs. temperature can be observed in the maximum values of ε_r for the three samples, and is presented in Table II. In this table we can also see that the values for the ratios m_1 / m_2 in monodomain sample 3 (no clamping by domains) are definitely higher than Landau's value. The adiabatic factor correction can be responsible, at the most, for a reduction of 20 % [7]. But even with this correction the value obtained is higher than 2.

Hill & Itchiki [16] found that in the ferroelectric phase, when the frequency of the measuring signal is increased, the loss tangent has lower values than at lower frequencies. We have found the inverse, as can be seen in the example presented in Fig. 4. It is also displayed in this figure the temperature dependence of the dielectric constant, which is quite similar at the frequencies of 1 kHz and 10 kHz.
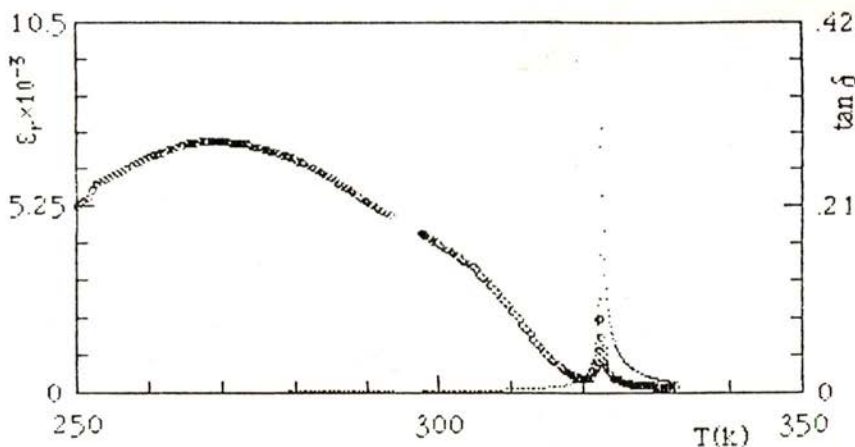
Fig. 5 — Measurements of ε_r vs. T (•) and tan δ vs. T (o) relating to sample 3. The virgin sample was cooled from room temperature to ~250K and then heated at the frequency of ~10 kHz. The data acquisition was momentarily interrupted at around ~295K.

166

Portgal. Phys. — Vol. 17, fasc. 3-4, pp. 159-172, 1986

Itoh & Mitsui [17] observed round peaks in the temperature dependence of the dielectric constant at low temperatures. Our results (Fig. 5) show that only the loss tangent has a round peak at low temperatures.

From the pyroelectric current I measured as a function of the temperature in samples 1 and 3, we obtained the pyroelectric coefficient and the spontaneous polarization P_s shown in Fig. 6.
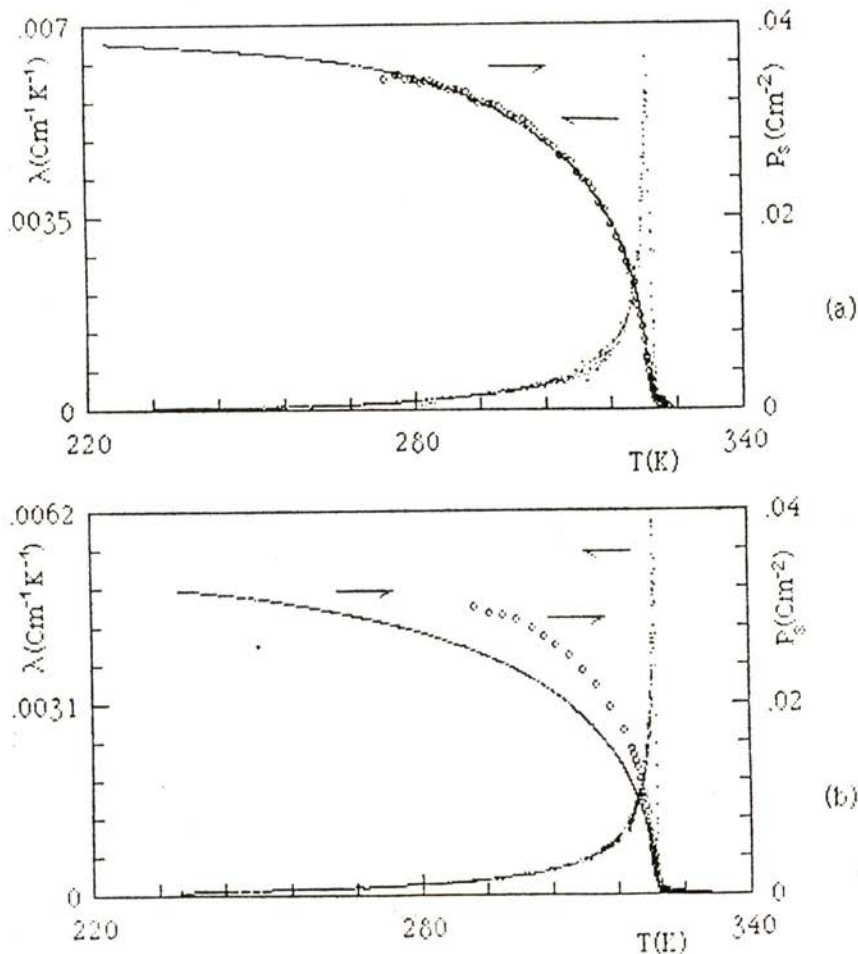

Fig. 6 — Spontaneous polarization P_s and pyroelectric coefficient λ vs. temperature T on sample 1 (a) and on sample 3 (b). $\bullet \rightarrow \lambda$ vs. T; $o \rightarrow P_s$ vs. T, obtained from hysteresis loops; $- \rightarrow P_s$ vs. T, obtained from integration of λ.

Using the procedure previously described we obtained hysteresis loops in samples 1 and 3, examples of which are depicted in Fig. 7.

The 'squareness' of the hysteresis loops obtained for samples 1 and 3 proves the good quality of the samples. The fact that we always obtained a good saturation of the hysteresis loops for any of the samples shows that a monodomain is actually achieved when following the procedure referred in the previous pages. It is worth noting (Fig. 7) that while the lower coercive
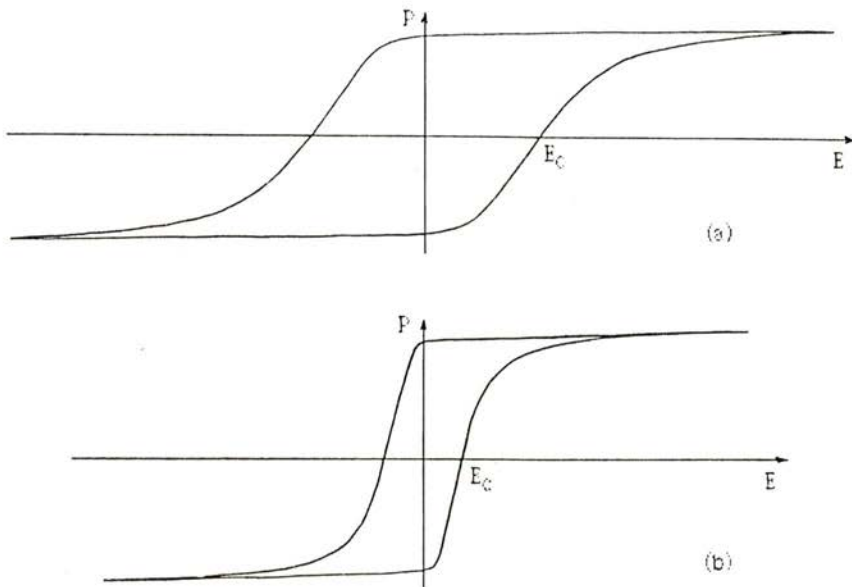
Fig. 7 — Hysteresis loops relating to sample 1 (a) at temperature T = 319.75K and sample 3 (b) at temperature T = 319.85K. The coercive fields are E_c (a) = 3,9 kV/cm and E_c (b) = 0.7 kV/cm, respectively.

field value of sample 3 shows the good condition of this sample's surface, the higher one obtained for sample 1 is surely a consequence of the excessive temperature which the sample attained when it was prepared. This is believed to cause the formation of viscous superficial layers which on cooling have a different behaviour from that of the initial crystal [9].

The spontaneous polarization P_s obtained from hysteresis loops, in both samples, is shown in Fig. 6 with the corresponding results obtained from pyroelectric measurements. In sample 1, the coincidence of the polarization curves obtained with both methods is somewhat surprising. As a matter of fact, we believe that the polarization values obtained from hysteresis loops should be higher than the pyroelectric ones, because of the inducing effect of the applied electric field.

We found that the ε_r^{-1} data could be satisfactorilly fitted to the expression:

$$\varepsilon_r^{-1} \propto |T - T_0| \; , \; T > T_0 \; ; \; \varepsilon_r^{-1} \propto |T_0' - T|^{\gamma'} , \; T < T_0' \, .$$

with $\gamma = \gamma' \simeq 1.0$. These values for γ and γ' are the ones predicted by Landau's theory. However in this theory $T_0 = T_0'$, which is not the case in our experiments (Fig. 2), where we obtained $|T_0 - T_0'| < 0.28K$.

The critical exponent β associated with the spontaneous polarization ($P \propto |(T - T_c)/T_c|^{\beta}$) was calculated choosing the critical temperature T_c as the one corresponding to the maximum value of the pyroelectric coefficient. This value is close to the temperature corresponding to the maximum of the dielectric constant versus temperature (Table I). The β values for samples 1 and 3 obtained from the pyroelectric effect as well as from

TABLE III — β values for samples 1 and 3 obtained both from the pyroelectric effect and from hysteresis loops.

Number of sample	T_c (K)	$\beta \pm 0.02$ obtained from	
		Pyroelec. effect	Hysteresis loops
1	322.73	0.49	0.52
3	322.87	0.48	
	322.95	0.50	

hysteresis loops (Table III) are coherent with the predicted Landau value of 1/2.

It should be emphasized that the choice of T_c has a significant influence in the β value, as can be seen in Table III for sample 3.

The critical exponent δ is obtained from hysteresis loops. It relates the polarization with the applied electric field at T_c ($E \propto P^{\delta}$, for $T = T_c$). The values obtained for sample 3, at temperatures near T_c are represented in Table IV, and are com-

TABLE IV — δ values for temperatures near $T_c = 322.87$ K, concerning sample 3

T (K)	δ
322.73	3.02
322.60	2.90
322.46	3.14

parable to the predicted Landau value of 3. The deviations from this value can be attributed to the difference between the temperature at which δ is calculated and T_c .

Following Gonzalo [18, 19] we checked for scaling behaviour and considered the rescaled values of polarization p and electrical field e ,

$$ p \,=\, P \,/\, | \,(\,T - T_c\,) \,/\, T_c \,|^{\beta} \,, \quad e \,=\, E \,/\, | \,(\,T - T_c\,) \,/\, T_c \,|^{\beta\delta} $$

where P is the polarization and E is the electric field corresponding to a point in a hysteresis loop at temperature T , T_c is the critical temperature, $\beta = 1/2$ and $\delta = 3$. We plotted ln p vs. ln e in the temperature range $| T - T_c | < 0.5$K in Fig. 8, for sample 3. These results are in a quite reasonable agreement with those previously determined by Gonzalo [16]. The differences obtained must result from the fact that the temperatures of the hysteresis loops we have considered were not near enough to T_c .
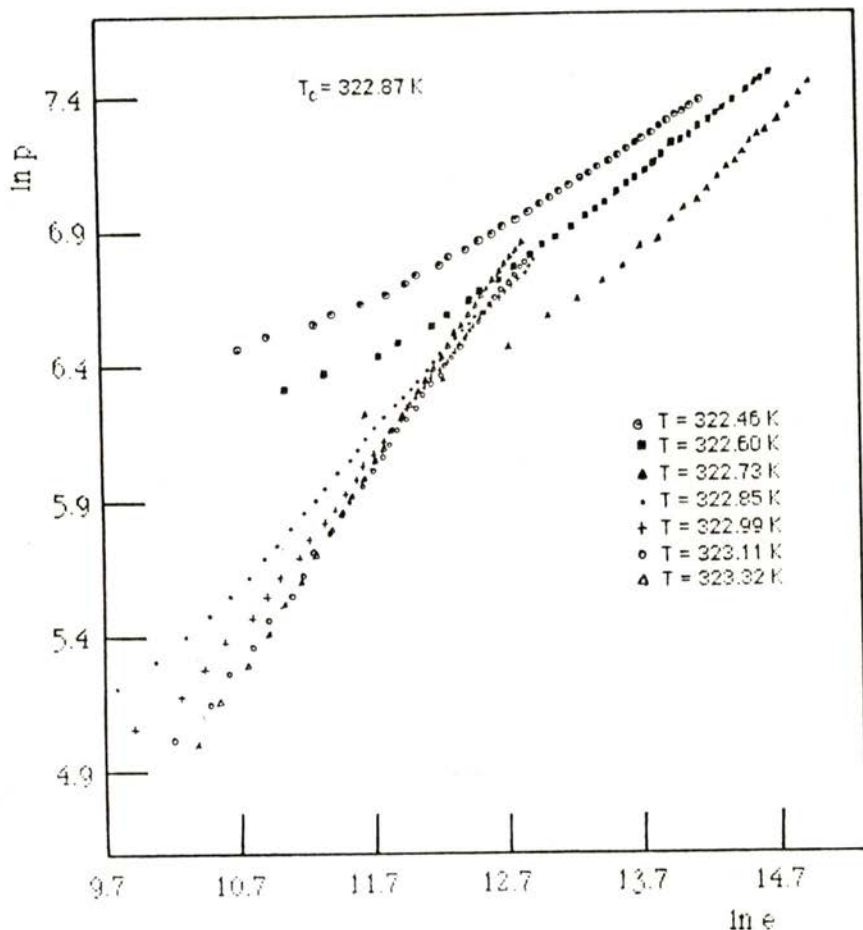
Fig. 8 — ln p vs. ln e relating to sample 3, for the indicated temperatures, with $T_c = 322.87$K.

4 — CONCLUSIONS

The main interest of this work lies in the presentation of a systematic and quite complete study of experimental macroscopic properties of triglycine sulfate. We have shown that: (i) the dielectric constant has finite values at the transition temperature in all the samples studied; (ii) the value for the ratio m_1 / m_2 is not in agreement with the value 2 predicted by Landau theory and the difference cannot be caused by domain clamping; (iii) the

values of the critical exponents γ, γ', β and δ agree with those predicted by the Mean Field Theory and verify the predicted scaling relations; (iv) the rescaled values of the polarization and field can follow an equation of state; (v) the relaxation of domains in TGS does not follow an exponential law.

A study regarding the relaxion of domains in TGS at different temperatures near T_c is presently in progress.

REFERENCES

[1] B. T. Mattias, C. E. Miller and J. P. Remeika, *Phys. Rev.*, **104**, 849 (1956).
[2] S. Hoshino, Y. Okaya, R. Pepinsky, *Phys. Rev.*, **115**, 323 (1951).
[3] R. M. Hill and S. K. Ichiki, *Phys. Rev.*, **132**, 1663 (1963).
[4] S. Hoshino, T. Mitsui, F. Jona and R. Pepinsky, *Phys. Rev.*, **107**, 1255 (1957).
[5] R. M. Hill and S. K. Ichiki, *Phys. Rev.*, **128**, 1140 (1962).
[6] F. Jona and G. Shiran, *Phys. Rev.*, **117**, 139 (1960).
[7] S. Tribwasser, *IBM J. Res. and Develop.*, **2**, 212 (1958).
[8] A. Mansingh and S. R. J. Prasad, *J. Appl. Phys.*, **48**, 4307 (1977).
[9] A. G. Chynoweth, *Phys. Rev.*, **117**, 1235 (1960).
[10] T. Sekido and T. Mitsui, *J. Phys. Chem. Solids*, **28**, 967 (1967).
[11] J. A. Gonzalo, *Phys. Rev.*, **144**, 662 (1966).
[12] P. P. Graig, *Phys. Lett.*, **20**, 140 (1966).
[13] M. E. Lines and A. M. Glass, *Principles and applications of ferroelectrics and related materials*, Clarendon Press, Oxford 1977.
[14] R. Chaves, H. Amaral, S. Ziolkiewicz, *J. Phys.*, **41**, 259 (1980).
[15] R. Palmer, D. Stein, E. Abrahams & P. Anderson, *Phys. Rev. Letters.*, **53**, 958 (1984).
[16] R. M. Hill & S. K. Ichiki, *Phys. Rev.*, **132**, 1603 (1963).
[17] K. Itoh & T. Mitsui, *Journal Phys. Soc. of Japan*, **23**, 334 (1967).
[18] J. Gonzalo, *Phys. Rev.*, **B1**, 3125 (1970).
[19] R. Ramirez & J. A. Gonzalo, *II Simpósio Ibérico de Física de la Matéria Condensada*, p. 2, Sevilha Proceedings (1986).

ELECTRON DENSITY IN THE LAVES PHASE Ti Mn₂

M. M. R. Costa and M. J. M. de Almeida

Centro FCl (INIC), Departamento de Física da Universidade de Coimbra, 3000 Coimbra — Portugal

ABSTRACT — Structure factors for the hexagonal Laves phase TiMn₂ have been measured by X-ray diffraction, using Mo-Kα radiation. The refinement of structural and temperature parameters using a full matrix least-squares technique was carried out.

The main features of the electron density are presented and discussed in terms of Fourier difference maps.

1 – INTRODUCTION

The Laves phase compounds crystallize in three different structures — Mg Zn₂ (C 14), Mg Cu₂ (C 15) and Mg Ni₂ (C 36) — which have been investigated by Friauf [1] and Laves et al. [2]. A review of the crystal and band structures, as well as of the properties of these alloys, has been more recently given by Sinha [3].

The crystalline structure of all Laves phase compounds — which have, in general, a stoichiometric composition AB₂ — can be described in terms of triangular nets of A and B atoms, stacked between a Kagomé net of B atoms. There are several possibilities for the stacking of these layers, giving rise to the three crystallographic structures mentioned above. The difference among them is only in the local symmetry of the nearest neighbours of A and B atoms, their number being the same in all structures.

These alloys have been considered as size factor compounds; the closest packing of the constituent atoms occurs when the

radius ratio R_A / R_B is 1.225. Deviations from this ideal value exist, however, in several Laves phases where R_A / R_B varies between 1.05 and 1.68.

The study of several pseudo-binary systems of these compounds, carried out by Laves et al. [4] and Lieser et al. [5] suggested that a close relationship exists between the crystal structure and the electron concentration, e/a; in fact, the phase boundaries of the three possible types of structure appear, in all systems investigated, at the same values of e/a. In the alloy Ti Mn₂ the radius ratio is $R_A / R_B = 1.10$. The fact that it deviates from the ideal value suggests that changes in the valences of the constituent elements may occur, which cause the necessary adjustments of atomic volumes so as to preserve the closest possible packing.

This can be investigated by carrying out a careful determination of the electron distribution in this Laves phase. A comparative study of the electron distribution in Laves phase compounds which have a common A element and a B transition metal varying along one line of the periodic table, may be of interest to clarify which of the two factors — atomic size or electron concentration — is dominant in these structures. This work has already been undertaken in our Laboratory on the Laves phases Ti Fe₂, Ti Mn₂ and Ti Co₂.

2 — EXPERIMENTAL

The Laves phase Ti Mn₂ has the Mg Zn₂ (C 14) hexagonal type of structure, with space group P6₃ / mmc. The manganese atoms occupy two types of position with different point symmetry; they will be hereafter denoted by Mn (I) — at the origin — and Mn (II) with general coordinates $(x, \bar{x}, 1/4)$.

A single crystal of Ti Mn₂ with approximate dimensions $(0.07 \times 0.06 \times 0.10)$ mm³ was selected from an ingot kindly offered by Dr. M. Nevitt, Argonne National Laboratory, Illinois, U.S.A. The specimen had a somewhat irregular shape which could be approximated by an irregular polyhedron with six faces; Laue photographes confirmed that it was a single crystal.

The diffraction experiment was carried out using a single crystal four-circle diffractometer (CAD4). Lattice parameters were determined by a least-squares standard technique using a set of 25 pre-selected and carefully centered reflections:

$$a = b = (4.8333 \pm 0.0009) \text{ Å}$$
$$c = (7.9384 \pm 0.0011) \text{ Å}$$
$$\alpha = \beta = 90° \,; \; \gamma = 120°$$

These values are in good agreement with those determined by photographic methods and reported by the authors in a previous paper [6]. The integrated intensities of 4915 reflections out to $(\sin \theta)/\lambda = 1.08 \text{ Å}^{-1}$ were measured in ω - 2θ scans, using Mo - Kα radiation, monochromated by a graphite crystal. Each reflection h k *l* was considered to be observed if the corresponding intensity, I_{hkl}, was greater than $3\sigma_{hkl}$, σ_{hkl} being the standard deviation of I_{hkl}.

A set of up to 24 symmetry equivalent reflections was measured for each h k *l*, in order to evaluate and correct for the effects of absorption and secondary extinction. The intensities of six medium and strong reflections were measured periodically; these were subsequently used as standards to correct the intermediate data for any eventual systematic variation of the main beam intensity.

3 – DATA ANALYSIS

Lorentz and polarization corrections were applied to the reflection data in the usual way.

The empirical absorption correction suggested by North et al [7] brought the integrated intensities of equivalent reflections into agreement within 3 %. Least squares refinements including only reflections with $(\sin \theta) / \lambda \geqslant 0.6 \text{ Å}^{-1}$ and assuming spherically symmetric scattering factors [8] were carried out in order to refine the scale factor, as well as the positional and thermal parameters for Ti an Mn atoms. The inclusion of only higher order data in these refinements should yield a more reliable value for the scale

TABLE 1

	x	y	z	β_{11}	β_{22}	β_{33}	β_{12}
Mn (I)	0	0	0	.00428 (19)	.00428 (19)	.00109 (9)	—
Mn (II)	.82786 (9)	.17214 (9)	1/4	−.00026 (25)	.00985 (27)	.00130 (4)	.00492 (14)
Ti	1/3	2/3	.06398 (13)	.00436 (14)	.00436 (14)	.00144 (7)	—

$S = 0.3347\ (24)$ $g = 6.0\ (1) \times 10^{-6}$ $R = 2.7\ \%$ $R_w = 4.4\ \%$

176

Portgal. Phys. — Vol. 17, fasc. 3-4, pp. 173-180, 1986

factor, essentially free from correlation with extinction and asphericity effects, as discussed in a previous paper [9].

Structure factors were then calculated for each observed reflection, based on the atomic coordinates and anisotropic temperature factors thus refined. Comparison between calculated and observed structure factors showed that the effect of extinction could not be neglected. Therefore, an extinction coefficient was further refined by least-squares fixing all parameters except the scale factor, and including all the observed reflections.

The results of the above mentioned refinements are shown on table 1. A final set of structure factors was calculated with the refined positions, thermal and extinction parameters, and postulating a spherical distribution of the atomic electrons.

4 – FOURIER ANALYSIS AND RESULTS

Difference Fourier syntheses with coefficients ($SF_{obs} - F_{calc}$) were carried out. The results represent the deviations of the observed electron density in Ti Mn₂ from the postulated spherical distribution. They can be visualized by drawing difference density maps for several sections of the hexagonal unit cell, as show in figs. 1a) and 1b). The results of Fourier syntheses of the corresponding standard deviations can be seen in figs. 2a) and 2b).

Alternating positive and negative densities (highs and valleys) along vertical lines Ti-Ti are observed on sections parallel to [10.0] at x = 1/3. Such oscillations cannot be related to any real charge density effect; their reproducibility will be investigated using another crystal.

The most interesting features, however, are observed on sections parallel to [00.1] at z = 1/4: negative contour levels representing a defficiency of about 1.7 e/Å³ are present along directions joining a pair of Mn (II) atoms (fig. 1a)). This agrees with the contraction of Mn (II)-Mn (II) distances which can be calculated from the results shown on table 2.

The fraction of electrons delocalised from Mn (II)-Mn (II) bonds appears as significant positive contours around the Mn atom on the section parallel to [10.0] at x = 1/3 (fig 1b)).
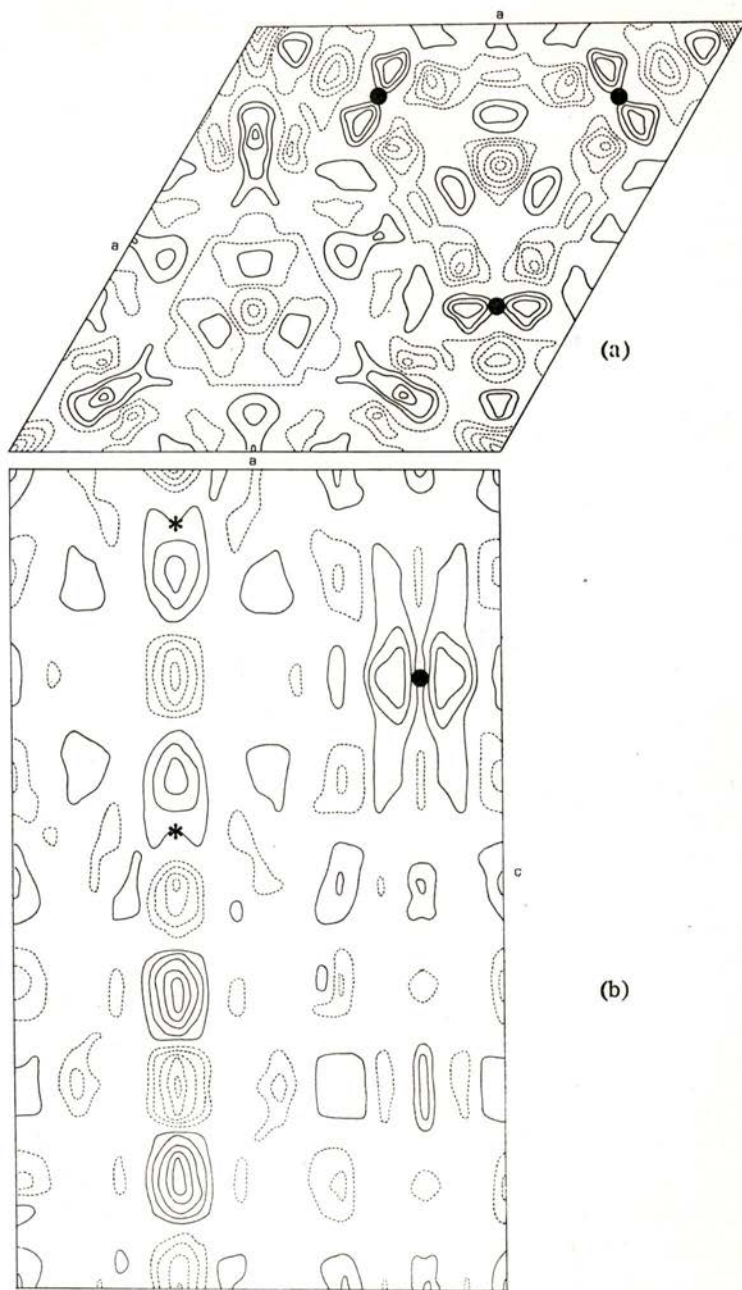
Fig. 1 — Fourier difference maps, SF_o - F_c. Contour levels at 0.43 e/Å^3. Broken lines represent negative contours. ● Mn atoms; * Ti atoms.

(a)   Section [00.1] of the unit cell at $z = 1/4$
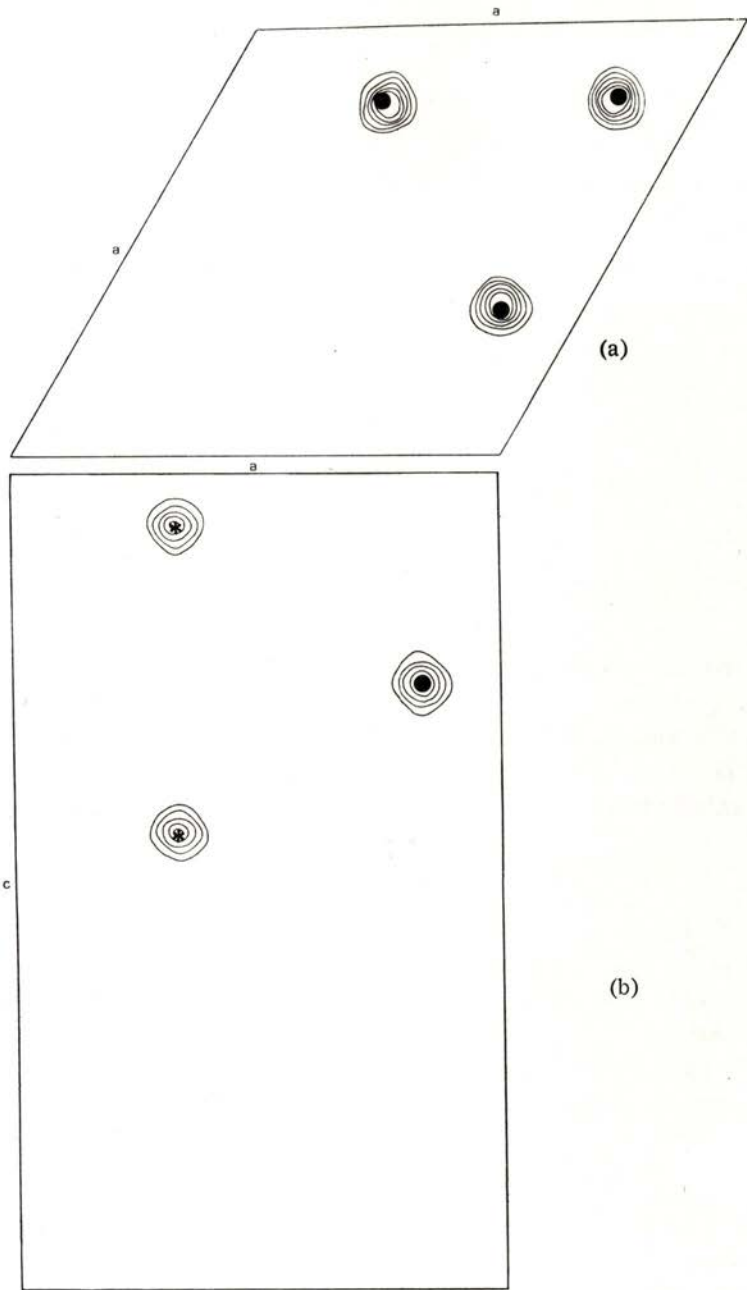(b)   Section [10.0] of the unit cell at $x = 1/3$

Fig. 2 — Fourier maps representing the distribution of errors.
Contour levels at 0.43 e/Å³.

(a) Section [00.1] of the unit cell at $z = 1/4$
(b) Section [10.0] of the unit cell at $x = 1/3$

TABLE 2

Position	Atom	Neighbours	Distance	Atomic radii (CN12)
f	A (Ti)	1 f	2.953 (1)	1.45
		1 f	2.970 (2)	
		6 a	2.836 (2)	
		3 h	2.834 (2)	
a	B (Mn)		2.453 (2)	1.30
h	B (Mn)		2.337 (2)	

We are indebted to the Cultural Service of the German Federal Republic Embassy, the Deutscher Akademischer Austauschdienst (DAAD) and the German Agency for Technical Cooperation (GTZ) for the offer of a CAD4 automatic diffractometer which enabled the experimental work to be carried out.

REFERENCES

[1] FRIAUF, J. B., *J. Am. Chem. Soc.*, **49**, 3107 (1927).
[2] LAVES, F. and WITTE, H., *Metallwirtsch. Metallwiss. Metalltech.*, **14**, 645 (1935).
[3] SINHA, A. K., *Progress in Materials Science*, **15**, 93 (1972).
[4] LAVES, F. and WITTE, H., *Metallwirtsch. Metallwiss. Metalltech.*, **15**, 840 (1936).
[5] LIESER, K. H. and WITTE, H., *Z. Metallkd.*, **43**, 396 (1952).
[6] ALMEIDA, M. J. M., COSTA, M. M. R., ALTE DA VEIGA, L., ANDRADE, L. R. and MATOS BEJA, A., *Portgal. Phys.*, **11**, 219 (1980).
[7] NORTH, A. C. T., PHILLIPS, D. C. and MATHEWS, F. S., *Acta Cryst.*, **A24**, 351 (1968).
[8] *International Tables for Crystallography*, vol. III.
[9] ALMEIDA, M. J. M. and COSTA, M. M. R., *Portgal. Phys.*, **16**, 181 (1985).

RAPPORTS DE RAYLEIGH, CONSTANTES DE RAYLEIGH ISOTROPES ET ANISOTROPES, FACTEURS DE DIFFUSION MOLÉCULAIRE ANISOTROPES (F_an) ET ANISOTROPIES OPTIQUES MOLÉCULAIRES DU PHYTOL ET DE QUELQUES SOLVANTS ORGANIQUES MESURÉS A 632,8 nm AVEC UN LASER He-Ne

M. SREĆKOVIĆ [1], S. BLANCHARD [2], A. M. TISTCHENKO [2]
et J. P. LEICKNAM [2]

ABSTRACT — The paper reports and discusses measurements on the Rayleigh scattering of He-Ne radiation (632.8 nm), at room temperature, by phytol and phytyl acetate, as well as by several organic solvents. Infrared spectra seem to confirm the result concerning the formation of dymers in $C_{20}H_{39}OH$, but not in $C_{20}H_{39}C_2H_3O_2$.

1 – RESUMÉ

L'importance biologique du radical phytyle justifie cette étude; on rappelle tout d'abord succinctement son rôle biologique.

L'absence dans la littérature de renseignements concernant la conformation et le comportement de ce radical ou du phytol

---

[1] Faculty of Electrical Engineering of Belgrade P.O. Box 816, 11001 Belgrade, Yugoslavia.

[2] I.R.D.I., D.E.S.I.C.P., Département de Physico-Chimie, Laboratoire d'Optique Moléculaire, Centre d'Etudes Nucléaires de SACLAY, 91191 Gif-sur-Yvette Cedex, France.

lui même nous a conduit à sélectionner les techniques et méthodes permettant d'obtenir des renseignements structuraux sur le phytol et sur les interactions moléculaires dans lesquelles cette molécule peut être engagée.

Nous avons choisi de travailler par diffusion Rayleigh dépolarisée, cette technique s'étant révélée particulièrement efficace pour déterminer la conformation des alcanes normaux et pour mettre en évidence les corrélations de translation et d'orientation de ces composés à l'état liquide.

Dans un premier temps, pour disposer d'une méthode fiable et commode, on a mesuré les rapports Rayleigh isotropes et anisotropes, les facteurs de diffusion moléculaire anisotrope et les divers paramètres d'anisotropie optique moléculaire de quelques liquides organiques, ce qui nous a permis d'une part de choisir parmi les méthodes proposées celle qui paraissait la mieux adaptée au cas du phytol et d'autre part de vérifier la précision de nos mesures.

Le paramètre d'anisotropie optique moléculaire apparent γ^2_{ap} est plus spécialement intéressant car la littérature fournit de nombreuses valeurs de cet observable pour des séries de composés homogènes (par exemple: molécules hétérocycliques, hydrocarbures normaux ou ramifiés etc...).

Nous avons déterminé les γ^2_{ap} du phytol et de l'un de ces dérivés, l'acétate de phytyle, qui a été préparé pour la première fois à cette occasion. Ces deux valeurs sont confrontées à celles obtenus avec les alcanes normaux.

Pour compléter les informations obtenues par cette comparaison, on a enregistré les spectres infrarouges du phytol et de l'acétate de phytyle à l'état liquide.

L'anisotropie optique moléculaire apparente de ce dernier correspond pratiquement exactement à celle d'un alcane normal ayant une chaîne hydrocarbonée de même longueur; ce qui permet de conclure que les interactions moléculaires dans l'acétate de phytyle sont orientées de telle façon que les molécules tendent à se placer parallèlement les unes aux autres (disposition caractérisant le paratropisme), comme elles le font dans l'alcane liquide correspondant.

Pour le phytol, le paramètre γ_{ap}^2 est l'un des plus élevés de ceux qui ont été mesurés avec les liquides organiques. D'autre part, la spectrométrie infrarouge montre que le phytol est entièrement autoassocié par liaison hydrogène. La valeur exceptionnellement élevée du paramètre d'anisotropie optique moléculaire apparent du phytol nous conduit à supposer que dans ce liquide les corrélations d'orientation moléculaire conduisent les dimères formés par liaison hydrogène à s'ordonner également de façon paratropique.

Les techniques permettant d'obtenir des renseignements sur la structure des liquides sont peu nombreuses et difficiles à mettre en oeuvre. Ce travail montre que l'emploi conjoint de la spectrométrie vibrationnelle et de la diffusion de la lumière (plus spécialement la détermination de l'intensité diffusée dépolarisée) permet d'avoir aisément et rapidement des indications sur les interactions moléculaires dirigées responsables de l'ordre à courte distance qui existe dans certains liquides et plus spécialement dans les divers milieux denses d'intérêt biologique.

2 – INTRODUCTION

Dans le cadre d'une étude générale des propriétés physico-chimiques de la chlorophylle, il nous a semblé indispensable de compléter nos études antérieures [25] concernant les interactions moléculaires dans lesquelles cette molécule peut être engagée, par l'examen du comportement structural de la plus longue chaîne latérale de cette molécule, le radical phytyle (de formule brute $C_{20} H_{39} OH$).

Cette chaîne hydrophobe est fixée sur le propionyle situé en position 7 de la chlorophylle. Elle joue en effet certainement un rôle dans l'insertion de cette molécule dans la membrane thylacoïde et peut-être permet-elle aussi aux molécules de phéophytine et de chlorophylle, qui se trouvent au voisinage l'une de l'autre dans les centres réactionnels des bactériochloroplastes, de se positionner de façon à permettre un bon transfert électronique et une séparation de charge suffisamment efficace au cours du premier stade de l'acte primaire photosynthétique.

En outre le radical phytyle fait partie de la structure de deux vitamines liposolubles dont l'importance biologique est extrêmement grande:

1.°) — la vitamine K_1 (α-phylloquinone ou 2 méthyle-3 phytyle-1,4 naphtoquinone), vitamine de la coagulation du sang, vitamine antihémorragique.

2.°) — l'α-tocophérol ou vitamine E, vitamine de la fertilité, qui résulte de la condensation d'une triméthyl-hydroquinone avec le phytol, suivie d'une cyclisation permettant d'obtenir le noyau chromane triméthylé.

Rappelons aussi qu'il existe un effet de synergie entre l'axérophtol, la vitamine A (ou rétinol) et la vitamine E, ce qui fait que le radical phytyle joue sans doute un rôle dans l'insertion du rétinal dans la membrane rétinienne.

Le phytol, isolé pour la première fois par Willstätter par hydrolise de la chlorophylle, joue donc in vivo un rôle de première importance. Or aucune donnée structurale de base concernant cet alcool polyterpénique n'existe dans la littérature.

Dans une première approche de l'étude du comportement du radical phytyle, nous nous sommes fixés comme objectif d'avoir des informations sur la structure du phytol liquide lui-même. Le choix de la technique à utiliser a été simplifié par la remarque suivante: bien que les propriétés des liquides dépendent essentiellement de leur organisation (qui peut s'étendre jusqu'à 100 Å, comme dans le cas des cristaux liquides), les techniques permettant de mettre en évidence l'existence de corrélation d'orientation et/ou de translation dans les liquides ne sont à notre connaissance qu'au nombre de trois ([1]): diffraction des rayons X et des neutrons, diffusion de la lumière.

Nous avons choisi cette dernière technique car de nombreux résultats antérieurs ont montré que la diffusion Rayleigh dépolarisée était effectivement très sensible aux modifications structurales subies par les molécules à l'état liquide ou en solution [3, 16, 23, 24].

([1]) Contrairement aux nombreuses méthodes permettant de mettre en évidence les délocalisations électroniques des molécules à l'état liquide: mesure du courant de cycle décelable par R.M.N., exhaltation de la susceptibilité diamagnétique, rotation magnéto-optique (effet Faraday), calcul de l'énergie de résonance.

permet de conclure que la formation de liaisons hydrogène phytol-phytol loin de réduire la tendance paratropique de cette dernière molécule semble au contraire la renforcer par un effet coopératif entre interactions par liaison de Van der Waals et par liaison hydrogène, effet coopératif qui a certainement une très grande importance dans tous les milieux denses d'intérêt biologique; effet qui peut donc être mis en évidence par une étude simultanée par D.R.D. et par spectrométrie vibrationnelle.

BIBLIOGRAPHIE

[1] FARINATO R. S., ROWELL R. L., *J. Chem. Phys.* **65**, 593 (1976).

[2] BOKOV O. G., *Optika i spektroskopia* **39**, 43 (1975).

[3] CLEMENT C. et BOTOREL P., *J. Chim. Phys.* **61**, 878 (1964).

[4] SREĆKOVIĆ M., *Thèse*, Belgrade 1979.

[5] KIELICH S., *J. Chem. Phys.* **46**, 4090 (1967).

[6] DEŽELIĆ D., *Pure Appl. Chem.* **23**, 327 (1970).

[7] a) UTIYAMA H., in *Light Scattering from Polymer Solutions*, London 1972, b) UTIYAMA H., KURATA M., *Bull. Inst. Chem. Res.*, Kyoto Univers. **42**, 128 (1964).

[8] VUKS M. F., *Rassejanie sveta v gazah, zidkostjah i rastvorah*, Izd. Leningr. univers., Leningrad 1977.

[9] PORTO S. P. S., LEITE R. C. C., MOORE R. S., *J. Chem. Phys.* **40**, 2741 (1964).

[10] FABELINSKI I. L., *Molekuljarnoe rassejanie sveta*, Moskva 1965.

[11] CHU B., *Laser Scattering*, New York 1974.

[12] COUMOU D. J., HIJMANS J. E. L. MACKOR, *Trans. Farad. Soc.* **60**, 2244 (1964).

[13] FLEURY P. A., BOON J. P., *Laser Scattering in Fluid Systems*, in Advances in Chem. Phys. Ed. Prigogine, I., Rice A. S., Vol. **24**, Intersc. Public. Wiley Sons, New York 1973.

[14] CABANNES J., *La diffusion moléculaire de la lumière*, Les Presses Univers. de France, Paris 1929.

[15] MOREL A., *Journ. de chim. Phys.* **10**, 1359 (1966).

[16] BOTHOREL P., SUCH C., CLEMENT C., *J. Chim. Phys.* **69**, 1453 (1972).

[17] TONNELAT J., *Biophysiques* T. II., Paris 1973.

[18] ROCCARD J., *Thermodynamique*, Masson Cie, Paris 1952.

[19] PRINCE J. A. W., *Physica* 22, 576 (1956).

[20] LALLANE J. R., MARTIN F. B., BOTHOREL P., *Journ. of Colloid and Interf. Science,* 39, 601 (1972).

[21] ŠAHPARONOV M. I., *Metodi issledovanija teplovogo dviženija molekul i stroenija židkostei,* Moskva 1963.

[22] COHEN C., EISENBERG H., *J. Chem. Phys.* 43, 3881 (1965).

[23] CLÉMENT C. et BOTHOREL P., *Compt. Rend Acad. Sci. Paris* 255, 494 (1962) et *J. Chim. Phys.,* 61, 878 (1964).

[24] CANSELIER J. P. et CLÉMENT C., *J. Chim. Phys.,* 75, 880 (1978).

[25] LEICKNAM J. P., ANITOFF O. E., GALLICE M. J., HENRY M. et TAYEB A. E. K., *J. Chim. Phys.* 78, 587 (1981); 79, 171 (1982).

[26] PLA F., FROMENT P., CAPITINI, R., TISTCHENKO A. M. et ROBERT A., *Cellulose Chem. Technol.,* 11, 711 (1977).

[27] LALANNE J. R. et BOHTOREL P., *J. Chim. Phys.* 63, 1538 (1966).

En outre, l'emploi d'un laser comme source de lumière permet d'accroître la précision tout en réduisant le volume diffusant.

L'objectif principal de ce travail étant de voir s'il est possible d'obtenir des informations d'ordre structural sur le groupement phytyle par diffusion quasi élastique de la lumière, nous avons mesuré les grandeurs suivantes concernant le phytol à l'état liquide: Constante absolue de Lord Rayleigh (ou rapport Rayleigh), facteurs de dépolarisation en lumière naturelle et en lumière polarisée, ce qui a permis de calculer la constante dépolarisée de Lord Rayleigh d'où on a déduit les constantes anisotropes et isotropes correspondantes, ainsi que son facteur de diffusion moléculaire anisotrope et divers paramètres d'anisotropie optique moléculaire. Pour comparaison les mêmes grandeurs ont été déterminées dans les mêmes conditions avec divers solvants organiques, ainsi qu'avec l'acétate de phytyle, qui a été spécialement préparé pour ce travail.

En outre, pour complément d'information on a enregistré le spectre infrarouge du phytol.

Avant de présenter et de discuter ces résultats, on indique le formalisme retenu pour cette étude.

Symboles, définitions et choix d'une Systématique.

λ, est la longueur d'onde du faisceau lumineux incident;

N, le nombre d'Avogadro;

T, la température absolue;

k, la constante de Boltzmann, rapportée à une molécule réelle;

M, la masse moléculaire du liquide pur;

d, sa masse volumique en gcm^{-3};

d', sa densité en nombre de molécules par cm^3;

n, son indice de réfraction;

$\bar{\alpha}$, sa polarisabilité moyenne définie comme $\bar{\alpha} = 1/3 \, (\alpha_{xx} + \alpha_{yy} + \alpha_{zz})$ où les α_{ij} sont les composantes du tenseur de polarisabilité moléculaire $|\alpha|$ attachées à un référentiel cartésien xyz;

R_M sa réfraction moléculaire, qui est une fonction simple des polarisabilités principales, $R_M = (4/3) \, \pi N \bar{\alpha}$;

V, est le volume diffusant;

E, l'amplitude maximale du champ électrique incident dans le vide;

r, distance d'observation: distance séparant le volume diffusant du détecteur.

D'autre part on désigne les trois facteurs de dépolarisation de la molécule considérée par:

ρ_n le facteur de dépolarisation en lumière naturelle;
ρ_v le facteur de dépolarisation en lumière polarisée verticalement;
ρ_h le facteur de dépolarisation en lumière polarisée horizontalement;

les trois facteurs étant liés par la relation (Krishnan [17])

$$\rho_n = (1 + \rho_h^{-1}) / (1 + \rho_v^{-1})$$

qui pour une observation à 90°, devient

$$(\rho_n)_{90} = 2 \rho_v / (1 + \rho_v) \qquad ([1] \text{ et } [17]);$$

et l'on désigne par:
R, son rapport de Rayleigh (ou constante absolue de lord Rayleigh relative à l'intensité diffusée totale:

$$R = (I_{90} / I_0) \cdot r^2 / V \tag{I}$$

où I_0 est l'intensité du faisceau incident et I_{90} l'intensité diffusée à 90° de celui-ci);
R_i, sa constante dépolarisée de Rayleigh donnée par:

$$R_i = R \rho_n / (1 + \rho_n) ;$$

R_{is}, sa constante de Rayleigh 'isotrope' relative aux fluctuations de densité, que correspond à son rapport de Rayleigh corrigé du facteur de Cabannes:

$$R_{is} = R (6 - 7 \rho_n) / (6 + 6 \rho_n) \tag{II}$$

R_{an}, sa constante de Rayleigh 'anisotrope' relative aux fluctuations d'orientation des molécules anisotropes qui est directement liée à R_i:

$$R_{an} = (13/6) R_i = (13/6) R \rho_n / (1 + \rho_n) \tag{III}$$

Naturellement $R = R_{is} + R_{an}$.

A ces constantes correspondent les facteurs de diffusion introduits par Kielich [5]:

F_{is}, facteur de diffusion moléculaire isotrope,

F_{an}, facteur de diffusion moléculaire anisotrope,

qui sont liés aux moments dipolaires induits par l'onde lumineuse, et donc liés, en dernière analyse, au tenseur de polarisabilité $|\alpha|$ de la molécule. Ces facteurs caractérisent le mécanisme de diffusion de la lumière isotrope et anisotrope. Ils sont définis [1] par:

$$F_{is} = d'^2 \; \bar{\alpha}^2 \; kT \; K_T = (R/C) \; (6 - 7 \; \rho_n) / (6 + 6 \; \rho_n) \quad (IV)$$

avec $K_T =$ coefficient de compressibilité isotherme et

$$C = 1/2 \; (2\pi/\lambda)^4 \; [(n^2 + 2)/3]^2$$

et par:

$$F_{an} = 5 \; d'^2 \; \bar{\alpha}^2 \; kT \; K_T / (6 - 7 \rho_n) = R_{an} / (2,6 \, C) \quad (V)$$

Divers auteurs comme Coumou et al. [12] et Kielich [5] ont tenté de déterminer le rôle des interactions moléculaires dans la partie anisotrope diffusée par les liquides de façon à mettre en évidence l'existence éventuelle d'un ordre à courte distance. Pour cela, ils ont comparé les constantes R_{an} et les facteurs F_{an} mesurés à l'état liquide et en phase vapeur. Mais à notre connaissance, il n'a pas été possible de dégager une systématique de ces travaux permettant d'exploiter facilement les mesures d'intensité diffusées par les liquides. C'est pourquoi par la suite, d'autres auteurs ont proposé de définir d'autres paramètres caractérisant l'anisotropie optique du milieu en utilisant toujours les composantes du tenseur de polarisabilité moléculaire $|\alpha|$ (polarisabilités optiques principales, α_{xx}, α_{yy} et α_{zz}, suivant les trois directions d'un systèmes d'axes trirectangle lié à chaque centre diffusant anisotrope).

Des auteurs [3] définissent l'anisotropie optique moléculaire par le rapport:

$$\delta^2 \text{ ou } \Delta^2 = 1/2 \; [(\alpha_{xx} - \alpha_{yy})^2 + (\alpha_{yy} - \alpha_{zz})^2 + (\alpha_{zz} - \alpha_{xx})^2] /$$
$$(\alpha_{xx} + \alpha_{yy} + \alpha_{zz})^2 \quad (^1)$$

quelle que soit la cause de l'anisotropie de la molécule.

(¹) Quand l'ellipsoïde des polarisabilités est de révolution, $\alpha_{yy} = \alpha_{zz}$ alors l'expression se simplifie et devient:

$$\delta \text{ ou } \Delta = (\alpha_{xx} - \alpha_{yy}) / (\alpha_{xx} + 2 \alpha_{yy}).$$

Portgal. Phys. — Vol. 17, fasc. 3-4, pp. 181-202, 1986

187

Mais à notre connaissance cette formulation n'a pas permis non plus d'aboutir à une systématique permettant la mise en évidence d'une organisation dans les liquides qui en présentent une. On a alors [3] défini l'anisotropie optique moléculaire intrinsèque d'un composé comme:

$$\gamma_0^2 = 1/2 \ [(\alpha_{xx} - \alpha_{yy})^2 + (\alpha_{yy} - \alpha_{zz})^2 + (\alpha_{zz} - \alpha_{xx})^2]$$
$$+ \ 3 \ [\alpha_{xy}^2 + \alpha_{yz}^2 + \alpha_{zx}^2]$$

Cette formulation n'étant pas d'un emploi très commode on préfère souvent utiliser un autre paramètre lié à γ_0^2: en effet, loin des bandes d'absorption, ce qui est généralement le cas en diffusion de la lumière, le tenseur de polarisabilité est symétrique; et dans le cas où $|\alpha|$ est diagonal l'anisotropie optique moléculaire prend la forme:

$$\gamma_{ap}^2 = 1/2 \ [(\alpha_{xx} - \alpha_{yy})^2 + (\alpha_{yy} - \alpha_{zz})^2 + (\alpha_{zz} - \alpha_{xx})^2] \ (^1)$$

que nous désignerons par anisotropie optique moléculaire apparente car elle dépend non seulement de la structure électronique de la molécule et de sa conformation, mais aussi des interactions moléculaires dans lesquelles elle est engagée. γ_{ap}^2 $(^2)$ peut être facilement déterminée par des mesures physicochimiques simples; ce qui explique qu'on a pu établir une systématique à partir de la détermination des γ_{ap}^2 de nombreux composés. Dès 1962 Clément et Bothorel [23] montraient que γ_{ap}^2 pouvait être déduit de la mesure de la diffusion Rayleigh dépolarisée et remarquaient que pour une série de paraffines normales, γ_{ap}^2 augmente régulièrement en fonction du nombre d'atomes de carbone de celles-ci.

(¹) Avec les réfractivités moléculaires principales A, B, C,

$$\gamma_{ap}^2 = 1/2 \ [(A\text{-}B)^2 + (B\text{-}C)^2 + (C\text{-}A)^2]$$

(²) Ne pas confondre avec le facteur d'anisotropie moléculaire de Coumou [12] défini par

$$\gamma^2 = (\alpha_{xx} - \alpha_{yy})^2 + (\alpha_{yy} - \alpha_{zz})^2 + (\alpha_{zz} - \alpha_{xx})^2$$

Cette conclusion était explicitée en 1972 par Bothorel et al. [16]: l'intensité dépolarisée (i) diffusée par un liquide est directement proportionnelle à γ_{ap}^2 :

$$i = (16\,\pi\,N\,/\,15\,\lambda^4)\ d'V\ [(\,n^2 + 2\,)/3\,]^2\ \gamma_{ap}^2\ E^2 \qquad (VI)$$

où d' est le nombre de molécules par unité de volume. Pour augmenter la précision, les mesures sont effectuées en général par rapport à l'intensité dépolarisée (i_0) diffusée par un liquide de référence [24]:

$$\lambda_{ap}^2 = \frac{135\,\lambda^4}{16\,\pi^4} \cdot \frac{M}{Nd} \cdot \frac{1}{(n^2 + 2)^2} \cdot \frac{i}{i_0} \cdot \left(\frac{n}{n_0} \right)^2\ i_0 \qquad (VII)\ (^1)$$

(l'indice o se rapportant à la substance étalon).

Les paramètres γ^2 et Δ^2 (ou δ^2) sont liés de façon simple par l'intermédiaire de la réfraction moléculaire:

$$\Delta^2\ R_M^2 = (16/81)\ \pi^2\ N^2\ \gamma^2$$

D'autre part:

$$R_{an} = (13/10)\ (2\pi/\lambda)^4\ [(n^2 + 2)/3]^2\ d'\ \overline{\alpha}^2\ \Delta^2 \qquad (VIII)$$

pour une observation à 90° et $F_{an} = d'\ \overline{\alpha}^2\ \Delta^2$ [5] ;
enfin Farinato et al. [1] montrent que pour de petites particules anisotropes, on a:

$$\rho_n (\Theta) = [\,6\,\Delta^2 + (\,5 + \Delta^2\,)\cos\Theta\,]\,/\,(\,5 + 7\,\Delta^2\,) \qquad (IX)$$

où Θ est l'angle entre faisceau incident et axe d'observation, Δ et δ étant désignés par respectivement anisotropie relative et anisotropie proprement dite, ces deux paramètres étant liés par [1]

$$\Delta^2\ =\ \delta^2\,/\,(\,9\ \overline{\alpha}^2\,) \qquad (X)$$

(^{1}) Notons que:

$$i\,/\,i_0 \simeq (\rho_n\,/\,\rho_{no})\ (2 - \rho_{no})\,/\,(2 - \rho_n) \simeq \rho_v\,/\,\rho_{vo}\,.$$

Divers paramètres d'anisotropie optique peuvent aussi être définis [1] a partir du coefficient de compressibilité isotherme K_T

$$\Delta_1^2 = 5 \, d' \, kT \, K_T \, \rho_n / (6 - 7 \rho_n) ; \qquad\qquad (XI)$$

Farinato et ses collaborateurs [1] posent également:

$$\Delta_2^2 = F_{an} / (d' \, \bar{\alpha}^2) ; \qquad\qquad (XII) \ (^1)$$

on peut aussi définir

$$\Delta_3^2 = \left[\frac{5 \, K_T \, kT \, \rho_n}{(6 - 7 \rho_n) \, \bar{\alpha}^2} \cdot F^{an} \right]^{1/2} \qquad\qquad (XIII)$$

3 — MÉTHODE

On mesure tout d'abord la constante absolue de Lord Rayleigh (R) de chaque échantillon, puis les facteurs de dépolarisation ρ_n, ρ_v et ρ_h. On calcule alors les constantes de Lord Rayleigh 'isotrope' et 'anisotrope' à l'aide des relations (II) et (III) puis les facteurs de diffusion moléculaire 'anisotrope' à partir de R_{an} à l'aide de la relation (V). Enfin on calcule les divers paramètres d'anisotropie optique moléculaire à l'aide des relations (VII) et (XI) à (XIII).

Conditions expérimentales et résultats.

Toutes les mesures ont été éffectuées à température ambiante et avec la raie 632,8 nm de lasers He / Ne.

Le diffusiomètre utilisé a été décrit précédemment [26].

Pour les composés diffusant peu, on a employé un laser O.I.P. modèle 181B (^{2}) pouvant délivrer une puissance maximale

---

(^{1}) Pour une observation à 90°, Kielich [5] établit la relation suivante:
$\rho_n = 6 \, \Delta^2 / (5 \, d' \, kT \, K_T + 7 \, \Delta^2)$:

(^{2}) Aimablement prêté par le département de Biologie du C. E. N. Saclay, que nous remercions très sincèrement.

de 150 mw à 632,8 nm (au cours des mesures sa puissance était comprise entre 75 et 100 mw).

Le phytol (phytol pour biochimie) provenait de l'entreprise Merck et a été utilisé sans purification complémentaire.

L'acétate de phytyle a été préparé de la façon suivante: dans un premier temps on prépare le phytolate de potassium par réaction du phytol en solution dans de l'hexane normal sur du potassium métallique en quantité stoechiométrique; lorsque la réaction est complètement terminée, on ajoute par petite portion une solution de chlorure d'acétyle dans de l'éther de pétrole, le ballon où s'effectue la réaction étant maintenu vers 0°C, en le plongeant dans un récipient contenant de l'eau et des glaçons. La solution est ensuite filtrée, puis les solvants sont évaporés par distillation sous vide.

Nous avons tout d'abord mesuré sur notre appareil et à 632,8 nm la valeur absolue (i_0) de l'intensité dépolarisée diffusée par le cyclohexane, que nous avons choisi comme liquide de référence. Tous les liquides ont soigneusement été dépoussièrés comme au cours du travail précédent [26].

Le Tableau 1 rassemble les grandeurs moléculaires (masse moléculaire, densité, indice de réfraction et polarisabilité moyenne) utilisées au cours de ce travail.

Dans le Tableau 2 se trouvent les facteurs de dépolarisation de différents solvants organiques, du phytol et de l'acétate de phytyle.

Le Tableau 3 rassemble les rapports de Rayleigh, les constantes de Rayleigh 'isotropes' et 'anisotropes' ainsi que les facteurs de diffusion moléculaire 'anisotropes' mesurés et calculés au cours de ce travail; dans la dernière colonne, nous avons porté les valeurs de F_{an} selon la définition de Deželič [6], qui diffèrent de celles de Kielich [5] du facteur $16 \pi^2 [(n^2 + 2)/3]^2$ [1].

Les différents paramètres d'anisotropie optique relative calculés suivant les relations (XI) à (XIII) ont été rassemblés dans le Tableau 4, sur lequel on a aussi porté les coefficients de compressibilité isotherme de la référence [4].

Enfin le Tableau 5 présente les paramètres d'anisotropie optique moléculaire apparents obtenus en utilisant la relation (VII). La précision expérimentale sur l'anisotropie optique est d'environ 6 à 7 %.

TABLEAU 1 — Grandeurs moléculaires utilisées

Composés	Massa moléculaire M	Densité d (gcm⁻³)	'Densité' d' (10^{21} cm⁻³)	Polarisabilité moyenne $\overline{\alpha}$ (10^{-24} cm³)	Indice de refraction, n
cyclohexane	84,162	0,77389	5,5378	10,95	1,42194
dodécane	170,33	0,75112	2,6347	22,843	1,41836
benzène	78,11	0,87901	6,7774	10,329	1,49493
toluène	92,142	0,86696	5,6665	12,271	1,49141
tétra-chlorure de carbone	153,823	1,58439	6,3032	10,455	1,4559
quinoléine	129,22	1,09	5,081	16,474	1,61875
phytol	296,54	0,8497	1,7256	38,530	1,46928
acetate de phytyle $C_{22}H_{42}O_2$	338,54	0,8577	1,5283	—	1,4347

192

Portgal. Phys. — Vol. 17, fasc. 3-4, pp. 181-202, 1986

TABLEAU 2 — Facteurs de dépolarisation

Composés	ρ_v	ρ_h	ρ_n [*]	ρ_{nK} [**]	Écarts en % [***]
cyclohexane	0,0476	1	0,080	0,0909	+ 12
dodécane	0,0947	1,0076	0,172	0,173	+ 0,37
benzène	0,2774	1,0395	0,426	0,4433	+ 4,1
toluène	0,3897	1,0694	0,543	0,561	+ 3,35
tétrachlorure de carbone	0,0135	0,9055	0,028	0,0266	– 5,3
quinoléine	0,3398	0,983	0,500	0,507	+ 1,38
phytol	0,2987	1,028	0,454	0,46	+ 1,38
acétate de phytyle	0,149	1,011	0,249	0,257	+ 4,8

[*] ρ_n, facteurs de dépolarisation obtenus par mesure directe à 632,8 nm.

[**] ρ_{nK}, facteurs de dépolarisation calculés par la relation de Krishnan [17]: $\rho_{nK} = (1 + \rho_h^{-1})/(1 + \rho_v^{-1})$

[***] Écarts en %: $100 \cdot (\rho_{nK} - \rho_n)/\rho_{nK}$

TABLEAU 3 — Rapports de Rayleigh, constantes de Rayleigh isotropes et anisotropes et facteurs de diffusion moléculaire anisotropes

Composés	R (10^{-6} cm^{-1})	R_{an} 10^{-6} cm^{-1} (a)	R_{is} (10^{-6} cm^{-1}) (b)	C (10^{19} cm^{-4}) (c)	F_{an} (10^{-25} cm^3) (d)	F'_{an} (10^{-25} cm^3) (e)
cyclohexane	2,69	0,48	2,21	$8,830_1$	$0,020_8$	5,895
dodécane	1,65	$0,240_4$	$1,409_6$	$8,690_6$	$0,010_4$	3,117
benzène	9,04	6,017	$3,02_3$	$9,683_9$	$0,238_5$	75,04
toluène	11,02	6,03	4,99	$9,63_6$	$0,240_7$ à $0,342_4$	$75,35_9$ à $107,20_6$
tétra-chlorure de carbone	3,073	0,810	2,263	$9,164_3$	0,034	1,013
quinoléine	45,54	$33,206_9$	$12,33_3$	11,5275	1,108	$415,00_3$
phytol	$8,35_1$	5,701	2,65	$9,339_3$	$0,234_8$	$71,25_4$
acétate de phytyle	3,72	1,555	$2,16_5$	$8,89_4$	0,067	19,42

(a) $R_{an} = 13R_i / 6$ [16]. (b) $R_{is} = R - R_{an}$ [1, 5]. (c) $C = 1/2 \ (2\pi/\lambda)^4 \ [(n^2 + 2)/3]^2$ [1]. (d) $F_{an} = R_{an} / (2,6\,C)$ d'après [1] et [5]. (e) $F'_{an} = F_{an} \cdot 16\,\pi^2 \ [(n^2 + 2)/3]^2$ [1].

TABLEAU 4 — Paramètres d'anisotropie optique relative Δ^2.

Composés	K_T (10^{-11} cm² dyne^{-1})	$\Delta_3^2 \times 10^2$ (1)	$\Delta_3^2 \times 10^3$ (2)	$\Delta_2^2 \times 10^3$ (3)	$\Delta_1^2 \times 10^3$ (4)	$\Delta_1^2 \times 10^3$ (5)
cyclohéxane	8,197	5,143	5,93	3,16	1,591	6,012
dodécane	3,680	13,788 (7,134)	—	0,772	0,720	—
benzène	8,719	27,449	20,977	33,05	19,597	29,8
toluène	5,834	30,284	31,237 (36,7)	28,21 (40,13)	18,375	32,365 (38)
tétra-chlorure de carbone	8,131	9,851	10,456	4,93	2,491	11,247
quinoléine	16,480	58,713	—	80,36	35,552	—
phytol	10,900	7,801	—	9,16 (9,5)	6,399	—

(1) $\Delta_3^2 = \left[\dfrac{5K_T\, kT\, \varrho_n}{(6\text{-}7\varrho_n)\,\bar{\alpha}^2} \cdot F_{an} \right]^{1/2}$ avec les valeurs de K_T de la première colonne de ce tableau, tirées de [4].

(2) Δ_3^2 calculées avec les valeurs de K_T de la référence [2].

(3) $\Delta_2^2 = F_{an} / (d'\,\bar{\alpha}^2)$.

(4) $\Delta_1^2 = 5d'\, kT\, K_T \varrho_n /(6\text{-}7\varrho_n)$ avec les valeurs de K_T de la référence [4].

(5) Δ_1^2 avec les valeurs de K_T de la référence [22].

Portgal. Phys. — Vol. 17, fasc. 3-4, pp. 181-202, 1986

195

TABLEAU 5 — Paramètres d'anisotropie optique moléculaire apparents

Composés	i / i_0 (*)	γ_{ap}^2 ($\mathring{A}^6$)
cyclohexane	1	3,22
dodécane	2,258	15,15
benzène	6,49$_6$	17,02
toluène	8,94$_4$	28,04
tétra-chlorure de carbone	0,34$_1$	0,98
quinoléine	8,0	27,55
phytol	7,048	72,66
acétate de phytyle	3,382	39,48

(*)   Avec $(i_0)_{cyclohexane} = 20,75.10^{-8}$ cm^{-1} à 632,8 nm.

Pour compléter cette étude, nous avons enregistré le spectre infrarouge du phytol entre faces de bromure de potassium. Comme prévu, on observe deux absorptions dues aux vibrateurs OH à 3340 cm^{-1} et à 3615 cm^{-1}. Cette dernière est d'une intensité relative très faible, le rapport des intensités intégrées de ces bandes étant de 260.

4 – DISCUSSION

Il n'existe que très peu de mesures de diffusion de la lumière à 632,8 nm. Néanmoins on peut faire les remarques suivantes:

— Nous avons obtenu $R = 9,04.10^{-6}$ cm^{-1} pour le rapport de Rayleigh du benzène alors qu'il est égal à $16,3.10^{-6}$ cm^{-1}, lorsqu'on

196

Portgal. Phys. — Vol. 17, fasc. 3-4, pp. 181-202, 1986

le mesure à 546,1 nm [16]; le rapport de ces deux valeurs est pratiquement égal au rapport des longueurs d'onde servant à effectuer les mesures élevé à la puissance 4.

— Toujours avec le benzène, nous mesurons $\rho_n = 0,426$, en bon accord avec la mesure de Bothorel, Such et Clement [16], $\rho_n = 0,42$ à 541,6 nm, et avec celle que l'on peut déduire du travail de Lalanne et Bothorel, $\rho_n = 0,42$ à 632,8 nm [27], mesure également effectuée avec un laser He/Ne ([1]).

— En ce qui concerne les γ_{ap}^2 : pour le dodécane, la valeur 15,15 Å^6, obtenue au cours de ce travail, est très voisine de celle rapportée dans la référence [23] (15,29 Å^6).

Avec le benzène $\gamma_{ap}^2 = 17,02$ Å^6, valeur qui est en accord raisonnable avec la valeur calculée (19,6 Å^6) [24]; tandis que cette anisotropie optique est nettement plus élevée en solution: 36 Å^6 dans le tétrachlorure de carbone [23], alors qu'en extrapolant à dilution infinie elle serait égale à 38,7 Å^6 [24].

Cet accord avec les résultats antérieurs nous a incité à voir de quelle façon les résultats obtenus avec le phytol et l'acétate de phythyle s'insèrent dans la systématique développée à propos des hydrocarbures par les auteurs qui viennent d'être cités. D'autant plus que cette systématique permet effectivement d'avoir des renseignements sur la structure de ces corps à l'état liquide.

Auparavant rappelons qu'un liquide, loin d'être un état parfait, présente généralement un certain ordre à courte distance, qui se manifeste soit par le diatropisme (les molécules ont tendance à se placer perpendiculairement les unes aux autres), soit par le paratropisme (qui caractérise la tendance des molécules à se placer parallèlement les unes aux autres); dans le premier cas l'ordre obtenu a tendance à diminuer la valeur de l'anisotropie optique moléculaire; dans le second, qui se produit le plus souvent avec des molécules de forme allongée, l'anisotropie optique moléculaire a tendance à augmenter.

([1]) De la valeur de ρ_v donnée par Farinato et Rowell [1], on déduit: $\rho_n = 0,425$ a 546 nm par la relation de Krishnan [17].

On a d'ailleurs montré qu'il existe une relation quasi linéaire entre les γ^2 des hydrocarbures linéaires purs et le nombre d'atomes de carbone de ces molécules [23]. Cette linéarité a été attribuée à des corrélations d'orientation moléculaire: les molécules d'alcanes normaux tendent à se placer parallèlement les unes aux autres [16 et 24].

L'anisotropie optique moléculaire apparente γ_{ap}^2 du phytol est, à notre connaissance, la valeur la plus élevée obtenue pour cette 'observable' avec les liquides organiques. Cependant la comparaison de cette valeur avec la série de valeurs obtenues par Clement et Bothorel [23] avec des alcanes normaux et ramifiés nous semble intéressante: le point représentatif du phytol se trouve sur la droite $\gamma^2 = f$ (nombre d'atomes de carbone) obtenue par ces auteurs, à condition de considérer que la chaîne étendue du phytol comprend 32 carbones au moins, au lieu des 16 prévus. Or la spectrométrie infrarouge montre qu'à l'état liquide le phytol est autoassocié et que dans cet état il n'existe pratiquement pas de molécules non liées par liaison hydrogène. A l'état liquide, le phytol existe donc probablement sous forme de dimères, ceux-ci étant sans doute liés par des forces de Van der Waals.

Cette interprétation est confirmée par le fait que l'anisotropie optique moléculaire apparente de l'acétate de phytyle (dont la chaîne étendue est plus longue que celle du phytol) n'est que de $39,48 \, \text{Å}^6$ (donc 1,84 fois plus petite que celle du phytol); ce qui peut s'expliquer par le fait que l'acétate de phytyle peut interagir avec lui-meme par des liaisons de Van der Waals, mais qu'il ne peut s'autoassocier par liaison hydrogène. En reportant la valeur de γ_{ap}^2 obtenue avec cet ester sur la courbe de Clement et Bothorel, on constate d'ailleurs que la chaîne étirée de cette molécule serait equivalente à une chaîne d'alcane a 23 chaînons environ.

La comparaison des γ_{ap}^2 du phytol et de l'acétate de phytyle avec les anisotropies moléculaires apparentes des alcanes non ramifiés n'est donnée qu'à titre indicatif. En effet sur le diagramme $\gamma^2 = f$ (nombre d'atomes de carbone) [23] le point représentatif d'un composé comme l'hexaméthyl-tétracosane n'est pas aligné avec ceux des alcanes normaux. Par contre, ceux des trimethyl-pentanes, du methyl-2-butane et du methyl-3-heptane le sont.

De toute façon, le γ_{ap}^2 du phytol est presque le double de celui de l'acétate de phytyle.

Des autres grandeurs déterminées au cours de ce travail ne se dégage aucune conclusion nette permettant d'avoir une idée de la structure du phytol à l'état liquide:

— Le facteur de diffusion moléculaire anisotrope (F_{an}) du phytol est plus élevé que ceux du dodécane, du tétrachlorure de carbone et du cyclohexane et est voisin de celui du benzène. Le manque de données dans la littérature ne permet pas de dépasser cette simple constatation.

De même aucune systématique ne se dégage de la comparaison des divers paramètres d'anisotropie optique (δ^2 ou Δ^2) relevés dans la littérature [5 à 7]. Mais ceci est peut-être en grande partie dû au fait que l'imprécision est très grande. Nous avons (par exemple) noté des écarts de 390 % entre les valeurs δ^2 du cyclohexane mesuré par [5] et [6], il est vrai que le cyclohexane est peu anisotrope et que les mesures sont donc peu précises. Mais dans le cas du benzène, l'écart entre les valeurs de ces auteurs atteint 382,5 %.

Dans ces conditions, il aurait été surprenant que nous puissions tirer des renseignements sur la conformation du phytol a partir des valeurs des paramètres Δ_1^2, Δ_2^2 et Δ_3^2 rassemblés sur le tableau 4.

Par contre, les constantes de Rayleigh 'isotropes' et 'anisotropes' mesurées par Kielich [5] et par Coumou et coll. [12] avec une série de solvants organiques sont suffisamment voisins pour nous avoir incité a calculer les rapports R_{an} / R_{is} à partir de leurs valeurs (^{1}). Ce rapport augmente bien suivant la séquence n-hexane, n-octane, n-décane, n-hexadécane et il est particulièrement faible dans le cas du cyclohexane.

Cependant, apparemment, il n'y a pas de rélation simple entre ce rapport et la longueur ou la conformation de ces molécules hydrocarbonées.

Avec les valeurs portées sur le tableau 3 on trouve $R_{an} / R_{is} = 2,15$ pour le phytol, 0,217 pour le cyclohexane, 0,17 pour le dodécane et 0,75 pour l'acétate de phytyle.

(^{1}) Ces auteurs ont aussi mesuré R_{an} et R_{is} à l'état vapeur et donnent les rapports R_{an} (liquide) / R_{an} (vapeur) et R_{is} (liquide) / R_{is} (vapeur). Mais la comparaison de grandeurs caractérisant l'anisotropie mesurées dans des états différents a été critiqué [23] et ne permet de toute façon pas d'en tirer les éléments d'une systématique des polarisabilités principales.

En accord avec les conclusions tirées des valeurs de γ_{ap}^2, ce rapport est donc spécialement élevé pour le phytol, la partie relative aux fluctuations d'orientation étant relativement importante dans le rapport de Rayleigh. Cependant il est surprenant que ce rapport soit plus élevé dans le cas du cyclohexane que dans le cas du dodécane.

5 – CONCLUSIONS

La détermination des anisotropies optiques moléculaires apparentes par diffusion Rayleigh dépolarisée (D.R.D.) d'un certain nombre de solvants organiques, du phytol et de l'acétate de phytyle à l'état liquide permet de confirmer que l'étude de l'intensité dépolarisée diffusée par ces liquides donne non seulement des renseignements sur l'anisotropie intrinséque des molécules (due à leur conformation ou a leur structure electronique) mais aussi sur leurs corrélations de translation ou d'orientation, autrement dit sur les interactions dirigées entre molécules liquides (c'est à dire finalement sur tout ce qui modifie le 'champ interne' autour de la particule diffusante considérée).

L'étude par D.R.D. du phytol et de son ester acétique montre que ces molécules à l'état liquide tendent à se placer parallèlement les unes aux autres, comme les alcanes ayant une chaîne hydro-carbonée suffisament longue.

Mais, alors que l'anisotropie optique moléculaire apparente de l'acétate de phytyle correspond à peu près à celle attendue pour un alcane ayant le même nombre d'atomes de carbone, celle du phytol correspondrait a un alcane ayant environ deux fois plus d'atomes de carbone.

Ce résultat inattendu résulte sans doute du fait que toutes les molécules de phytol sont auto-associées par liaison hydrogène comme l'a montré le spectre infrarouge.

Les polymères du phytol (sans doute en majorité des dimères) sont evidémment des entités plus longues que les molécules monomères. Il peut donc en resulter une augmentation de la tendance au paratropisme, puisque celui-ci apparaît pour les hydrocarbures saturés non cycliques dés que la chaîne dépasse 7 a 8 atomes de carbone.

De toute façon, la comparaison des anisotropies optiques moléculaires apparentes du phytol et de l'acétate de phytyle

200

Portgal. Phys. — Vol. 17, fasc. 3-4, pp. 181-202, 1986

E.S.R. STUDY OF MAGNETIC INTERACTIONS IN GLASSES CONTAINING IRON

E. Guedes de Sousa, S. K. Mendiratta

Centro de Física, Universidade de Aveiro, 3800 Aveiro, Portugal

J. M. Machado da Silva

Centro de Física, Universidade do Porto, 4000 Porto, Portugal

ABSTRACT — Electron Spin Resonance (ESR) provides a useful tool not only as a probe of local structure and short range order in glasses but also of magnetic interactions in the glasses containing suitable magnetic ions. We have analysed the spectra of many glasses in the series $xFe_2O_3(PbO \cdot 2B_2O_3)$. The results of computer simulation of the spectra and the experiments on the temperature dependence of the parameters of relevant lines can be summarised as follows. For low concentration $(x < 0.1)$ the peak at $g = 4.3$ is due to isolated Fe^{3+} ions in a distorted octahedral or tetrahedral coordination. The broadening of this peak can be adequately accounted for by considering temperature effects and dipolar interaction. For intermediate concentrations (approximately $0.1 \leqslant x \leqslant 0.4$) the model of superexchange interaction between strongly coupled ions, forming a pair (pair-wise interaction model) gives reasonable results in explaining, qualitatively, broad $g = 2$ absorption. For high concentrations where a fraction of iron ions is in the precipitated a-Fe_2O_3 crystalline phase, the spectra have interesting features of Ferromagnetic Resonance (FMR) and the $g = 4.3$ peak, typical of isolated Fe^{3+} ions, is more intense, indicating that these ions, left over in the glassy matrix, are comparatively diluted.

1 – INTRODUCTION

The ESR spectra of transition metal (TM) ions in the oxide glasses, specially in silicate and borate glasses have been the subject of many studies [1-9]. ESR has been used primarily as a tool to draw conclusions about valence state, coordination and the crystal field symmetry of the ion. Although there have been

some studies of the resonance line shape which take the exchange interaction between magnetic ions as the dominant part of the Hamiltonian describing the states of resonance centre [10-12], we describe here an attempt to study systematically the magnetic interaction between iron ions when the concentration of the ions is varied through a wide range in the same base glass matrix.

Three ESR peaks for Fe^{3+} ions in glasses have been reported in the literature [1-4]: $g = 6$, $g = 4.3$ and $g = 2$. We did not observe $g = 6$ peak in our samples, and therefore do not discuss it. From the point of view of their microscopic origin, the spectra are determined mainly by: A) the symmetry of the crystal field at the ion and B) the interaction between the ions. There are two major symmetry environments of the ion: T_d and O_h; T_d corresponding to Fe^{3+} ion going as network former substituting boron in BO_4 tetrahedra. Since in glass exact symmetry is rarely encountered, the spectra are due to axial ($g = 6$) or rhombic ($g = 4.3$) distortions of T_d and O_h fields. The rhombic distortion leads to $g = 4.3$ peak of Fe^{3+} ions [2]. The interaction between the ions can be magnetic dipole-dipole or exchange interaction. At large inter-ion separation we expect dipole-dipole interaction to be dominant [13-a] and at small inter-ion distances, where Fe-O-Fe configurations are possible, the dominant interaction will be the exchange interaction. As we vary the concentration of Fe_2O_3 in the glass composition we expect changes in ESR spectra to reflect in a systematic manner the resulting changes in the interactions.

A rather important issue in these glasses is that of clustering. The question has two aspects. The first one can be formulated as follows: at any given concentration is it possible that all (or a major fraction of) iron ions are in a special geometrical relation to one another or are they perfectly randomly distributed? It is clear that even in a homogeneous distribution there will be some ions, owing to statistical nature of the distribution, in a geometry favorable to exchange interaction, but these will be very few. The second aspect of the question is the following: if the special geometry configurations (clusters) start in a significant way at a definite concentration, what is that concentration? Again, the concentration which permits exchange configurations from a purely geometrical point of view will not be specially interesting. We hope that by our ongoing study of electrical [14], magnetic [13, 15]

and resonance [13] properties of these glasses we can say something about this interesting question. It is expected that since some features of ESR depend on magnetic interactions resulting from special geometry, ESR can throw some light on the question of clustering.

The technique of ESR analysis we have applied for low concentrations consists, essentially, of simulating ESR spectra on a computer using a suitable but manageable Hamiltonian. A similar technique is applied to the high concentration, $x = 0.5$ sample, this time using a ferromagnetic resonance model [16, 17]. On the computer we can also generate the temperature variation of the intensities, expected from a given interaction model [10-13]. Despite this rather powerful technique, it is needless to say that due to uncertainties on some basic issues (like possible sites of Fe^{3+} ion) we can draw unambiguously only qualitative conclusions; and even that only when supplemented by information from other measurements.

2 — EXPERIMENTAL PROCEDURE

The standard technique of glass melting in air was used and the only detail worth mentioning is that we used a twice melting procedure to ensure homogeneity. The X-band (9.5 GHz) ESR spectra were taken on a Varian E-109 machine capable of fields up to 10 Kilogauss. A circulating Nitrogen cryostat permits cooling up to approximately 100 K.

3 — LOW AND INTERMEDIATE CONCENTRATION

3.1 — *Peak intensities and widths*

From the point of view of magnetic interaction, we can discuss the results in three concentration regimes:

1. Low concentration ($0.01 \leqslant x \leqslant 0.1$): In this region the line-width is dominated by weak long range dipole-dipole inter-action between the magnetic moments of Fe^{3+} ions. As the con-centration of ions in the glass increases, the average distance between Fe^{3+} ions decreases. This results in an increased dipolar

interaction and consequently the width ΔH of the $g = 4.3$ line is expected to increase with concentration [13-a]. In Fig. 1a, 1b we show two typical spectra ($x = 0.01$, 0.02) and indicate the corresponding values of $(\Delta H)_{4.3}$.
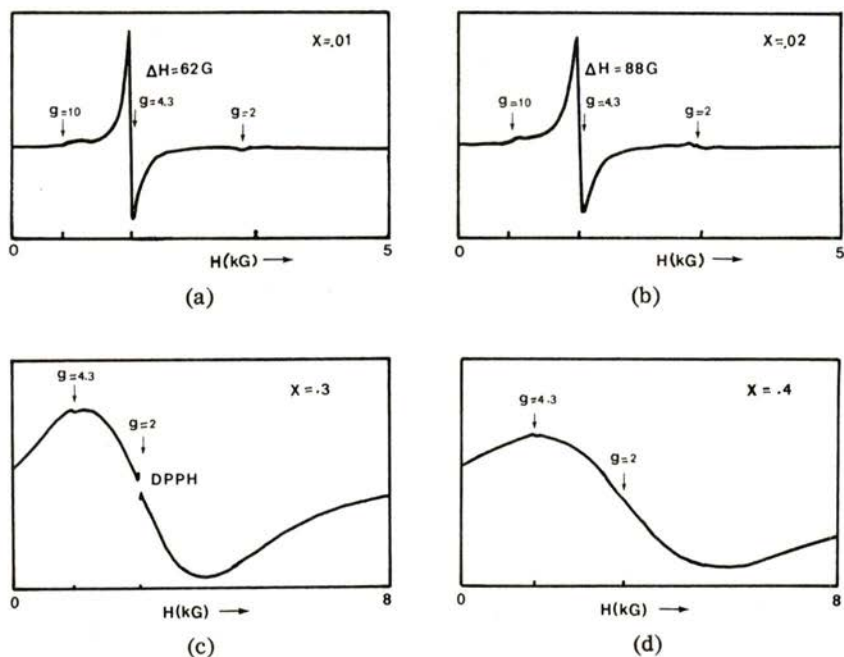
Fig. 1 — E.S.R. spectra of $x = 0.01$, 0.02, 0.3, 0.4 samples, at room temperature, of the glass system $xFe_2O_3(PbO \cdot 2B_2O_3)$.

2. Intermediate concentration ($0.1 \leqslant x \leqslant 0.4$): In this region the effect of exchange interaction between Fe^{3+} is noticeable. This manifests itself in two different ways: A) effect on the $g = 4.3$ peak; B) appearance and evolution of a broad $g = 2$ absorption. So far as the $g = 4.3$ peak is concerned the width does not change visibly within this region. Moreover, as the number of ions participating in the exchange pairs increases, the number of isolated ions contributing to the dipole broadened $g = 4.3$ peak decreases leading to a loss of intensity in that resonance. The presence of a broad resonance at $g = 2$ is due to exchange interaction [9-13], direct or superexchange via bridging oxygen ion,

between the Fe^{3+} ions. As expected, the intensity of this peak increases with concentration. In Fig. 1c, 1d we show two typical spectra of intermediate concentrations, $x = 0.3$ and 0.4. From this
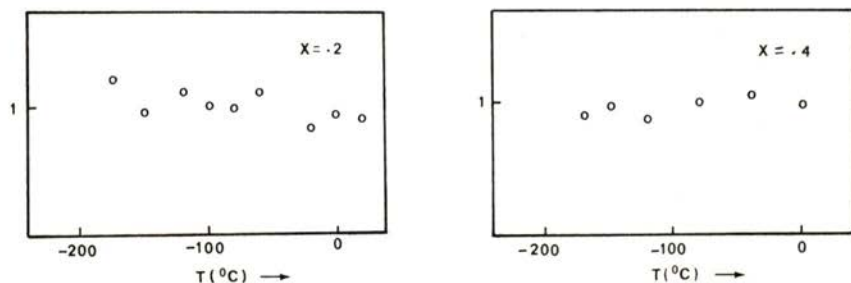
Fig. 2 — Variation of the intensity of $g = 2$ absorption line with temperature, in arbitrary units, for $x = 0.2$ and $x = 0.4$.

and other spectra, the relative increase in the intensity of the $g = 2$ peak at the cost of $g = 4.3$ peak is clearly evident. Room temperature values of the intensity ratios, $I_{g=2} / I_{g=4.3}$, for different values of x, are shown below.

x	0.1	0.2	0.3	0.4
$I_{g=2} / I_{g=4.3}$	0.35	5	100	100

3.2 – Temperature effects

The effect of temperature variation on the spectra of $x = 0.2$ and $x = 0.4$ specimens can be summarised as follows:

1. The intensity of the $g = 4.3$ peak decreases with the increase of temperature (see Fig. 5 for $x = 0.2$ sample). This behaviour is easily attributed to interaction with the phonons.

2. The intensity of the $g = 2$ peak remains relatively constant in the temperature region 100 K - 300 K. Actually, for the sample $x = 0.2$ the intensity slightly decreases with increasing temperature, while for $x = 0.4$ there is a marginal increase (Fig. 2).

If we assume that the dominant interaction between the ions is pair-wise exchange [11, 12] of antiferromagnetic type, we can attribute the appearance of the observed $g = 2$ peak to this inter-

action. The peak becomes broader if, along with the exchange field, the original distorted crystal field of isolated ions is also included in the Hamiltonian. Thus we verify the qualitative features of the observed peak in the pair exchange interaction model, except the temperature behaviour of the resonance centered at $g = 2$. Within this model, where exchange interaction is assumed to be dominant, an increase in the peak intensity with temperature is predicted [10-12]. In our case the peak in the glass $x = 0.4$ follows the predicted behaviour if we assume very small values of J, but the observed temperature variation in the $x = 0.2$ sample, though weak, is in the opposite sense. This leads us to suspect that, in the present case, the exchange interaction is not sufficiently large; we estimate $J < 0.5\ \mathrm{cm}^{-1}$.

4 – HIGH CONCENTRATION

For samples $x = 0.5$ and $x = 0.6$ a Mössbauer study [15] indicates the presence of crystalline α-Fe_2O_3 (Hematite) in these glasses. This introduces major changes in the corresponding ESR spectra. The room temperature spectra of these two glasses are shown in Fig. 3a and 3b. In both spectra we notice a background signal spread over a rather large range of the applied field. However, the most interesting feature of these samples is the behaviour of the sharp $g = 2$ peak.

In the sample $x = 0.5$ the pronounced $g = 2$ peak can be attributed to the superparamagnetic behaviour of the small particles of Hematite. This has also been observed in other glasses where a segregated phase is present [18-20]. In order to interpret and draw some conclusions from the temperature behaviour of this peak we recall some rather well known facts about α-Fe_2O_3. The bulk form of Hematite shows weak ferromagnetism at room temperature, when the spins lie in the c-plane. At about 260 K (T_M) Morin transition takes place and the pure antiferromagnetic phase corresponding to the configuration of all spins lining up along the c-axis is more stable. The behaviour of small particles of α-Fe_2O_3 is, however, different. T_M decreases with the decreasing size of the particles [21-24], so much so that Yamamoto [23] did not observe any transition in the sintered sample with particle diameter less then 200 Å. For small particles, a gradual decrease is generally

observed in the properties characteristic of superparamagnetism with increasing particle size. The spectra of the x = 0.5 sample taken at different temperatures confirm the above mentioned general behaviour. In Fig. 3c and 3d we show two of these spectra (T = − 120°C, T = − 60°C).

(a)

(b)

(c)

(d)

(e)
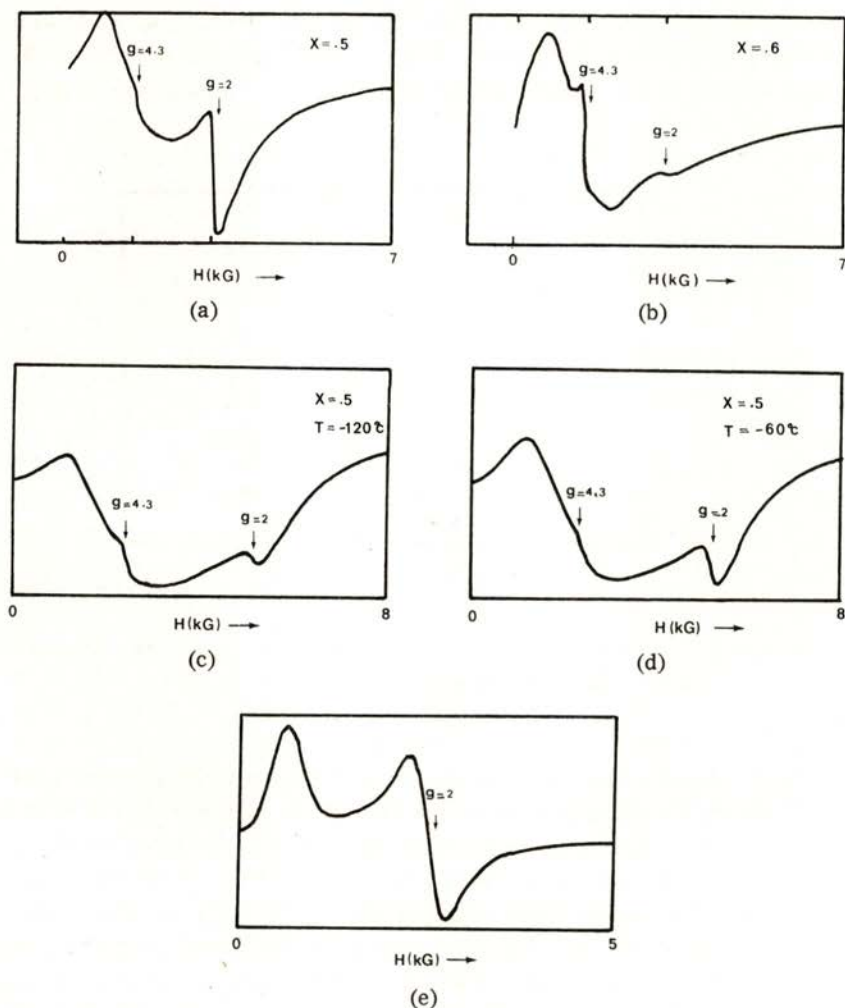
Fig. 3 — (a) (b) Room temperature E.S.R. spectra for x = 0.5 and x = 0.6; (c) (d) Spectra for x = 0.5, at −120 and −60°C; (e) Simulated spectrum of ferromagnetic resonance, in the cubic model, with $2K_1 / M_s = 2500$ Gauss.

The temperature dependence of the superparamagnetic properties of small particles, has been given by Néel [25]. This was applied by Kündig et al. [24] to the Mössbauer spectra of the particles and from their data they calculated the anisotropy constant to be $K_1 = 4.7 \times 10^4$ erg cm^{-3}. If we apply a similar procedure to our ESR intensities and make the Arrehenius plot of $\log_e (I)_{p-p}$ versus $1/T$ ($(I)_{p-p}$ being the difference between maximum and minimum, proportional to the absorption intensity) for the $g = 2$ sharp resonance of the $x = 0.5$ sample we obtain the graph shown in Fig. 4, where the slope gives the anisotropy energy.
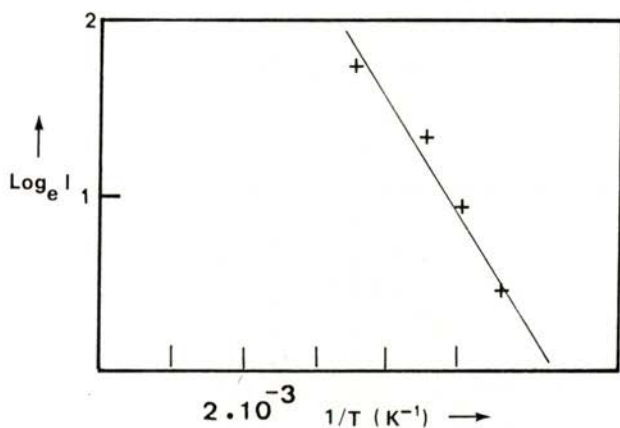
Fig. 4 — $\log_e (I)_{p-p}$ vs. $1/T$, for $g = 2$ peak of the $x = 0.5$ sample. Anisotropy energy, calculated from the slope, is 8.7×10^{-14} erg.

We can estimate the diameter of the particles employing the value of K_1 given by Kündig et al. [24]. This gives a value of 120 Å and therefore the observation of a gradual decrease in the intensity of the $g = 2$ peak instead of Morin transition agrees with the observations of Yamamoto [23] and Kündig et al. [24] on such small particles. Although the anisotropy energy for small particles can account for the results, the exact physical origin of this anisotropy is not clear; it may be due to some interactions inside the particles or simply because of the demagnetising field.

We have looked at the $g = 2$ resonance from yet another point of view. We have simulated a ferromagnetic resonance spectrum

for spherical particles assuming all possible relative orientations of the applied field and the anisotropy field. The resonance condition for the cubic symmetry is given by [17, 18]

$$H(\Theta, \phi) = H_0 + (2K_1 / M_s)(1 - 5F)$$

where

$$F(\Theta, \phi) = \cos^2\Theta \sin^2\Theta + \sin^4\Theta \sin^2\phi \cos^2\phi$$

The simulated spectrum is shown in Fig. 3e. This points to a value of the anisotropy field of 2500 Gauss and from the results of Komatsu and Soga [22] for the value of effective magnetic moment in α-Fe_2O_3, we deduce that the value of K_1 as 1.4×14^4 erg cm^{-3}. Using this value the estimated particle diameter would be 180 Å. Still neither of the analyses, Néel model or computer simulation of ferromagnetic resonance, takes into account the interactions and structure specific to Hematite. We are working on a model which takes into account these features.

The fact that the sample $x = 0.6$ hardly shows the features of superparamagnetism is again in agreement with the Néel theory, according to which the anisotropy energy depends upon the volume. As a matter of fact the size of the particles in this sample is so large that their diameter, from X-ray, may be estimated to be about 1000 Å. The most noteworthy observation which we have made in this sample is the increase in the intensity of the $g = 4.3$ peak relative to the situation in the samples $x = 0.5$. From the similarity in the temperature variation of this peak in samples $x = 0.2$ and $x = 0.5$ (Fig. 5) we conclude that the peak indeed corresponds to isolated Fe^{3+} ions. However, the problem of this peak of isolated ions being more intense and sharper than in the sample $x = 0.5$ needs a more thorough analysis of the physical situation and is currently under study.

5 — CONCLUSIONS

The physical picture we deduce is the following. At very low concentration (approximately $x < 0.1$) the Fe^{3+} ions behave as independent spins and the principal interaction is dipolar. There is no noticeable clustering at this low level of concentration, barring a few exchange coupled ions allowed on statistical grounds.

As the concentration is increased, the dipolar interaction increases, but, more importantly, a significant fraction of ions form exchange coupled pairs. The dominant interaction is superexchange (anti-ferromagnetic) via a bridging oxygen ion. Analysis of the temperature variation of the g = 2 resonance shows that a pair-wise
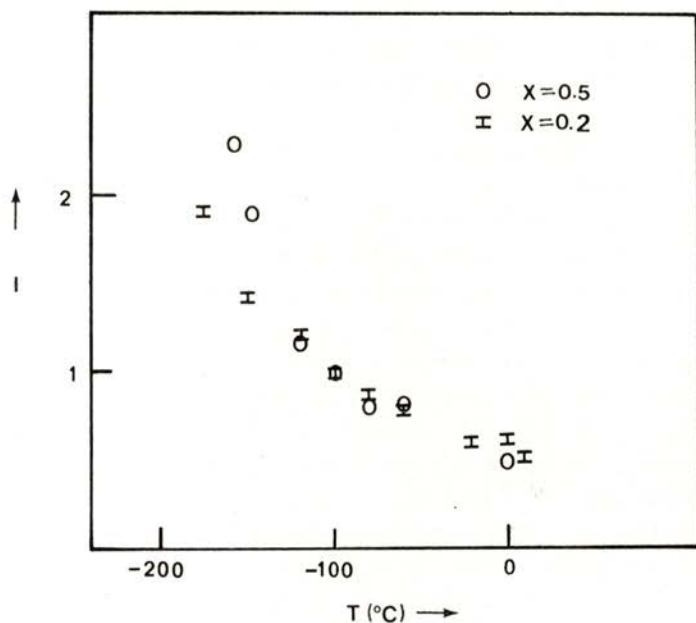
Fig. 5 — Variation of peak-to-peak intensity of g = 4.3 peak, for the x = 0.2 and x = 0.5 samples, in arbitrary units.

exchange interaction model, where the exchange term is dominant, is not adequate to explain all the experimental details. The onset of crystallite (α-Fe$_2$O$_3$) formation with increased concentration is accompanied by a sudden appearance of a sharp g = 2 peak arising from small crystallites behaving essentially like superparamagnetic particles. The size and anisotropy energy of these particles are consistent with the results obtained by other authors. As more ions go into crystallites the latter become bigger and, probably, the large anisotropy energy prevents the precession of the small magnetic moment and, therefore, no typical superparamagnetic

behaviour is observed. On the other hand the $g = 4.3$ peak of isolated Fe^{3+} ions becomes sharper and more intense. This and some other details of spectra of these glasses with a crystalline phase, which are currently under study, cannot be explained at this moment.

REFERENCES

[1] SANDS, P. H., *Phys. Rev.* **99**, 1222 (1955).

[2] CASTNER, T., NEWELL, G. S., HOLTON, W. C. and SLICHTER, P. C., *J. Chem. Phys.* **32**, 668 (1960).

[3] KURKIJAN, C. R. and SIGETY, E. A., *Phys. and Chem. of Glasses* **9**, 73 (1968).

[4] LOVERIDGE, D. and PARK, S., *Phys. and Chem. of Glasses* **12**, 19 (1971).

[5] CAMARA, B., *J. de Physique* (Paris) C9 **43**, 165 (1982).

[6] HIRAYAMA, C., CASTLE, J. G. and KURYAMA, M., *Phys. and Chem. of Glasses* **9**, 109 (1968).

[7] MOON, D. W., AITKEN, J. M., MACRONE, R. K. and CIELOSZYK, G. S., *Phys. and Chem. of Glasses*, **16**, 91 (1975).

[8] BURZO, E., ARDELEAN, I. and URSU, I., *J. of Mat. Sci.*, **15**, 581 (1980).

[9] KISHORE, N., BANSAL, T. K., KAMAL, R. and MENDIRATTA, R. G., *Phys. and Chem. of Glasses* **25**, 52 (1984).

[10] LANDRY, R. J., FOURNIER, J. T. and YOUNG, C. G., *J. of Chem. Phys.* **46**, 1285 (1967).

[11] FOURNIER, J. T., LANDRY, R. J. and BARTRAM, R. H., *J. of Chem. Phys.* **55**, 2522 (1971).

[12] OWEN, J., *J. Appl. Phys. Suppl.* 10 **32**, 2135 (1961).

[13] GUEDES DE SOUSA, E., MENDIRATTA, S. K. and MACHADO DA SILVA, J. M., «*Proceedings of the 1st International Workshop on Non-Crystalline Solids*» — *San Feliu Guixols* — Spain (1986), editors M. Baró and N. Clavaguera, (World Scientific Publishing — Singapore — 1986);
MENDIRATTA, S. K., HORNE, R. and VAN DUYNEVELDT, A. J., *Solid State Commun.* **52**, 371 (1984);
MENDIRATTA, S. K. and VALENTE, M., «*XIV International Congress on Glass*» — New Delhi (1986).

[14] MENDIRATTA, S. K., *Phys. Status Solidi* **93a**, 293 (1986).

[15] WAERENBORGH, J., private commun.

[16] KITTEL, C., *Rev. Mod. Phys.* 21, 541 (1949).

[17] SCHLÖMANN, E., *J. Phys. and Chem. of Solids* 6, 257 (1958).

[18] TSAY, F. D., CHAN, S. I. and MANATT, S. L., *Geochim. et Cosmochim. Acta* 35, 865 (1971).

[19] TSAY, F. D., MANATT, S. L. and CHAN, S. I., *Geochim. et Cosmochim. Acta* 37, 1201 (1973).

[20] GRISCOM, D. L., *Geochim. et Cosmochim. Acta* 38, 1509 (1974).

[21] BANDO, Y., KYIAMA, M., YAMAMOTO, N., TAKADA, T., SHINJO, T. and TAKAKI, H., *J. Phys. Soc. Japan* 20, 2086 (1965).

[22] KOMATSU, T. and SOGA, N., *J. Mat. Sci.*, 19, 2355 (1984).

[23] YAMAMOTO, N., *J. Phys. Soc. of Japan*, 24, 23 (1968).

[24] KÜNDIG, W., BÖMMEL, H., CONSTABARIS, G. and LINDQUIST, R. H., *Phys. Rev.* 142, 327 (1966).

[25] NÉEL, L., in «*Physique des Basses Temperatures*», Les Houches (1961), editors C. de Witt, B. Dreyfus and P. G. de Gennes (Presses Universitaires de France — Paris).

AN O$_2^+$ PRIMARY ELECTRON COLLISION ION SOURCE
FOR THE STUDY OF HARPOONING TRANSITIONS AT SURFACES

Pan Haochang (*), T. C. M. Horn, P. H. F. Reijnen and A. W. Kleyn

FOM - Institute for Atomic and Molecular Physics,
Kruislaan 407, 1098 SJ Amsterdam, The Netherlands

ABSTRACT — This paper describes a primary electron collision ion (Nier) source for producing an O$_2^+$ molecular beam, which is used in experiments to study harpooning transitions in the interaction of O$_2^+$ with a Ag (111) surface. The beam energy is 100-400 eV with an energy spread of about 0.01-0.03. The beam current density is about $10^{-10} - 10^{-9}$ A/cm^2 at a distance of 100 cm from the source. The O$^+$ fraction can be as mall as 0.01. The operation of the source in a surface scattering experiment is described. Some experimental results of harpooning transitions at surfaces are presented.

1 — INTRODUCTION

Harpooning reactions are well known chemical reactions in the gas phase [1]. The reactions proceed via an ionic intermediate, e. g. K + Br$_2$ → K$^+$ + Br$_2^-$ → KBr + Br. The ionic intermediate can be formed at the crossing seam of the potential energy surfaces for the neutral (covalent) and ionic states at large separation of the reactants. The formation of free ion-pairs has been observed as soon as there is enough energy to form the pair in an (endothermic) harpooning reaction. From studies of ion-pair formation much information has been obtained about the understanding of harpooning reactions [2]. Research of this type is also currently being performed in Portugal by Moutinho's group [3].

(*) Permanent address: Institute of Nuclear Research, Academia Sinica, P. O. Box 8204, Shanghai, China.

For collisions in the gas phase the electron jump can enlarge the reactive cross section considerably with respect to gas-kinetic cross sections. In molecule-surface collisions this increase is irrelevant, because the molecule will hit the surface anyway. In surface collisions the importance of harpooning is that it turns on an attractive force, i. e., the electrostatic image force, that can initiate trapping, sticking, dissociation or even a reaction of the molecule, whereas otherwise elastic scattering occurs. This is indicated schematically in Fig. 1. Theoretical work has indicated

Elastic Scattering　　　　　　**Harpooning Reaction**

crossing seam
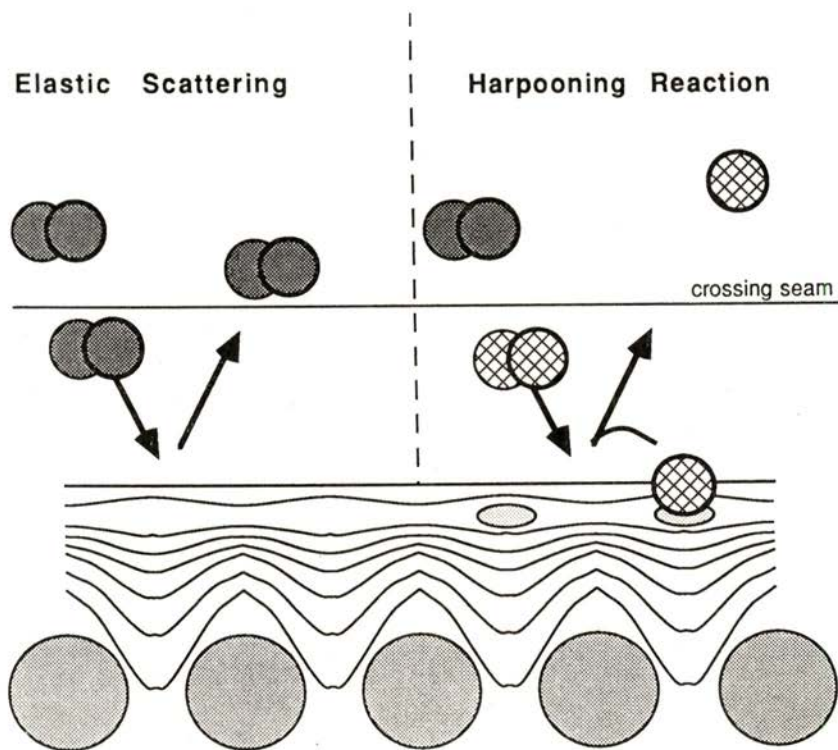
Fig. 1 — Schematic representation of a harpooning-reaction at a surface. A sideview of a part of the surface with 5 atoms is given. The contours around the atoms indicate the potential energy for the incoming particle. At the left an elastic collision is shown. At the right the molecule picks up an extra electron after passing the crossing seam. An attractive force is turned on, which is strongest in the egg-shaped regions. The situation drawn represents the case when the molecular bond is weakened by the harpooning, which results in dissociation of the molecule and subsequent sticking of an atom. The picture does not refer to any particular situation encountered experimentally.

that harpooning can occur in molecule surface collisions [4]. The curve crossing needed could be induced by the electrostatic image force.

To study the dynamics of harpooning at surfaces one should perform experiments in which the important step of the reaction, i. e. the negative ion formation, occurs and in which the collision energy is sufficiently high to prevent subsequent sticking. O_2 scattering from Ag is a good system for the study of these processes. It is known that molecularly chemisorbed O_2 is negatively charged [5]. Consequently, the neutral state of the system can be expected to cross the potential of the ionic ($Ag^+ + O_2^-$) at a reasonably large molecule-surface distance. Therefore we have studied O_2 scattering from Ag [6]. Because it is very difficult to make O_2 beams in the eV range. we use an O_2^+ beam, assuming that it neutralizes into the ground state of O_2 when approaching the surface. Energetic beams are necessary because the process of negative ion formation is endothermic by a few eV.

The experimental setup is a modified version of the one used by Tenner et al. [7] to study alkali ion scattering. The positive ions are produced by an electron impact ionization (Nier) type gun that will be described in detail in this paper. The crystal is mounted in a two axis goniometer. The scattered ions are detected using a 90° cylindrical electrostatic energy analyzer, which can be rotated around the crystal. The set-up is shown schematically in Fig. 2.

The requirements for the ion source are as follows:

(1)   The beam should consist exclusively of O_2^+.

(2)   Because it is connected, via a pumping resistance, with an UHV chamber, with a base pressure of 1×10^{-10} mbar, the working pressure of the source chamber should be around 10^{-6} mbar.

(3)   The source should operate at a distance from the target of about 100 cm.

(4)   A small energy spread of the ion beam is required for studying dynamics of surface processes.

(5)   Finally, although the gas introduced into the source is oxygen, the filament should have a reasonable lifetime.
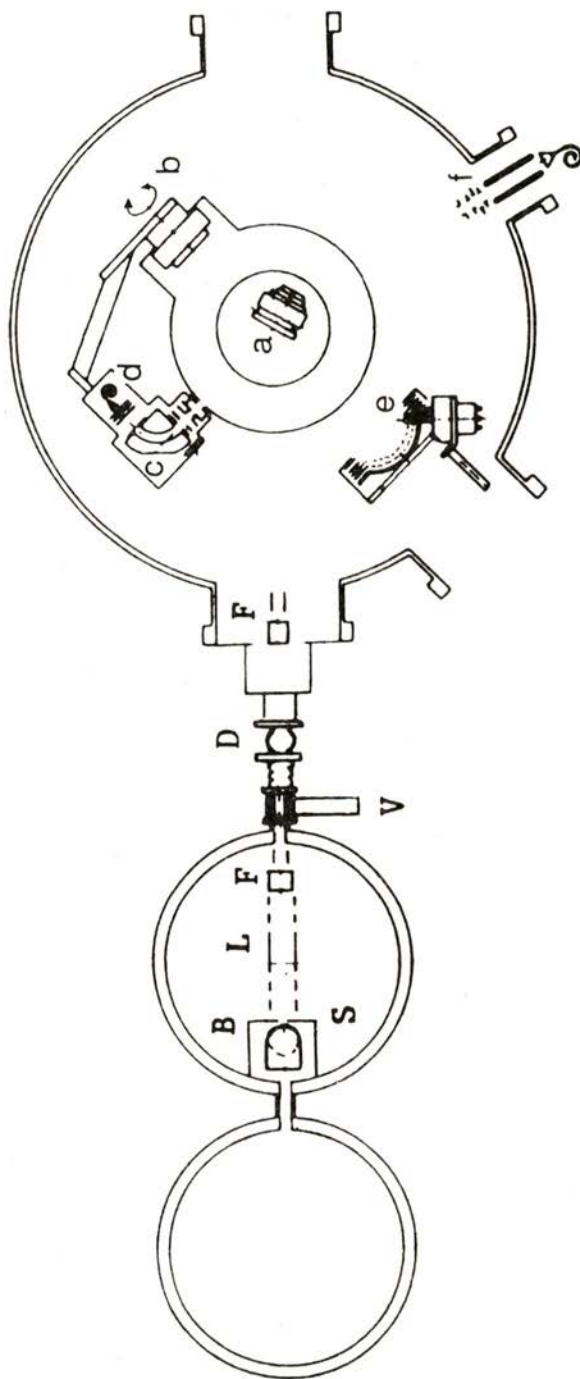
Fig. 2 — A schematic diagram of the experimental set-up. The source part contains the following elements: S = ion source, B = screen box, L = lens system, F = deflectors, V = valve and D = diaphragm. The UHV chamber contains: a = target manipulador, b = detector manipulador, c = energy analyzer, d = open channeltron, e = LEED system and f = quadrupole residual gas spectrometer.

Based on the requirements mentioned above we have decided to use a primary electron collision ion (or Nier) source [8]. A useful overview of available ion sources is given in [9].

In the following sections we will describe: the principle and construction of the ion source in section 2, measurement of the beam current and factors which influence the beam current in section 3, measurement of energy spread of the ion beam in section 4, measurement of ratio $O^+/(O_2^+ + O^+)$ by using a Wien filter in section 5, the application of the source in surface scattering experiments in section 6, some results on harpooning transitions in section 7, and conclusions in section 8.

2 — PRINCIPLE AND CONSTRUCTION

In a primary electron collision ion source atomic or molecular ions are created by collisions of energetic electrons with gas molecules. There are four steps in the process: (1) Production of electrons by thermal emission and acceleration of the electrons to a certain energy; (2) Production of ions by collisions of the energetic electrons with gas molecules in a small ionization chamber; (3) Extraction of the ions from the ionization chamber and their acceleration to the required energy; (4) Focusing and transmission of the ion beam by a lens system. The pressure in the chamber being low enough and the electron beam sufficiently confined (by an axial magnetic field) no double collisions of electrons or ions occur. This is in contrast to plasma sources.

When electrons collide with gas molecules several processes may happen according to the electron energy, such as elastic collisions, excitation or ionization of gas particles, or dissociation of gas molecules. If the energy of the primary electrons greatly exceeds the ionization energy of the particles, multiple ionization may occur.

In order to produce an O_2^+ ion beam the electron energy should be higher than the ionization energy of O_2^+ (12 eV) and should not be too high to avoid dissociation of molecules, production of O^+ and multiple ionization [10].

Portgal. Phys. — Vol. 17, fasc. 3-4, pp. 215-237, 1986

219

When an electron beam passes through a gas the ion yield is given by [11]:

$$n_+ = j^- \, p \, l \, S_e / e \qquad (cm^{-2} \, s^{-1}) \qquad\qquad (1)$$

where j^- is the electron current density (A/cm^2), p is the gas pressure (Torr), l is the length of the electron beam in the ionization volume (cm), and S_e is the differential ionization coefficient ($cm^{-1} \, Torr^{-1}$), which depends on electron energy and gas species.

Fig. 3 illustrates our O_2^+ ion source. The filament F is a pure rhenium ribbon with dimension $6 \times 0.07 \times 0.05 \, mm^3$. The operating current is 6A. The electron energy is determined by V_e, the voltage between the filament and the ionization chamber. The emission of the filament consist of the electron beam entering the ionization chamber and the electrons hitting the outside wall of the chamber. To obtain an emission limited beam the distance between the filament and the ionization chamber is smaller than 1 mm. The ionization chamber is a small stainless steel box, of depth and diameter 8 mm and 15 mm, respectively. It has an electron entrance, a gas inlet, a repeller, a hole facing a collector and an exit through which the ions are extracted from the ionization chamber. The ion beam energy is determined by V_{ext}, the voltage between the extractor and the ionization chamber. The distance between the extractor and the ionization chamber is about 7 mm. In front of the exit, at a distance of 1 mm, there is a slit which consists of two plates which can be supplied with different voltages to deflect and focus the beam. In addition, those voltages can make the extraction field more homogeneous. If the repeller inside the ionization chamber is put at a positive potential, V_{rep}, with respect to the chamber, the repeller can increase the extraction efficiency of ions, enhancing the beam current effectively, but this will influence the energy spread of the ion beam.

A strong magnetic field parallel to the electron beam makes the electrons spiral and will increase the electron path length in the ionization chamber (see Fig. 3; M is a permanent magnet). The magnetic field strength is 500 G near the magnet and 150 G at the center of the ionization chamber.

The distance from the source to the target in the UHV chamber is about 100 cm. A lens system L is used to improve the

220

Portgal. Phys. — Vol. 17, fasc. 3-4, pp. 215-237, 1986
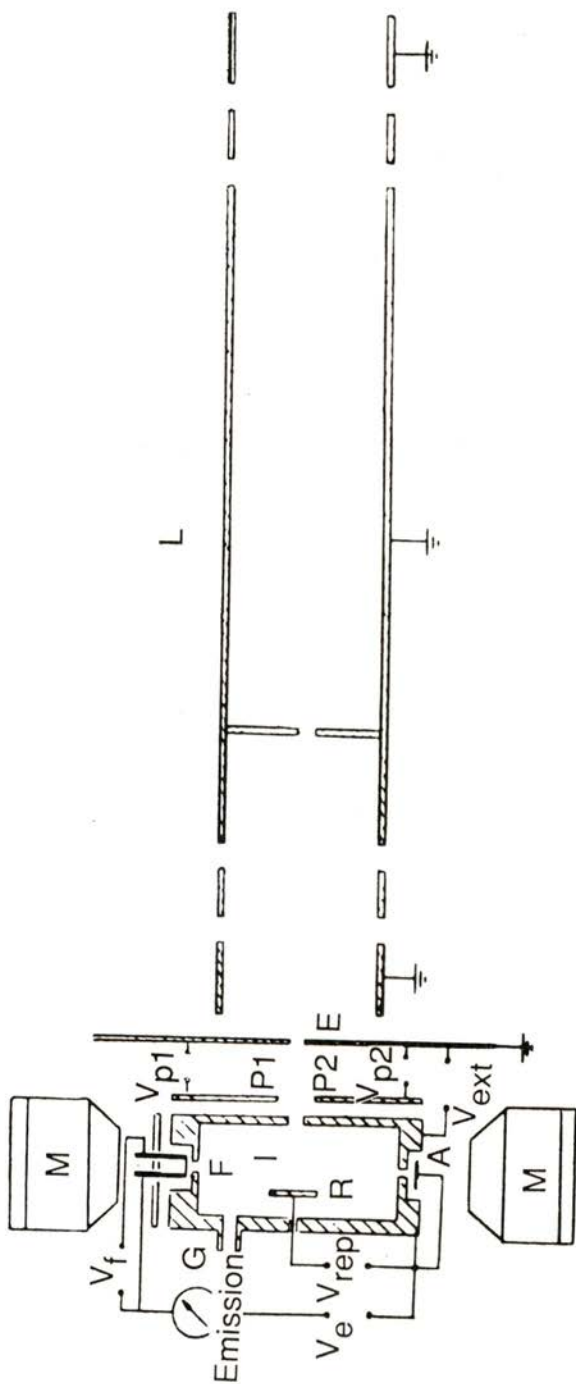
Fig. 3 — A schematic diagram of the ion source and the lens system: I = ionization chamber, F = filament or cathode, G = gas inlet, E = extractor, P1 and P2 = focusing plates, R = repeller, A = collector, M = magnet and L = lens system.

Portgal. Phys. — Vol. 17, fasc. 3-4, pp. 215-237, 1986

221

beam current density. The lens system has two lenses which are made up of five cylinders of 20 mm diameter. The first, third and fifth cylinder are grounded. At the end of the lens system and at the entrance of the UHV chamber X and Y deflectors are mounted. Between the source chamber and the UHV chamber there is a pumping resistance, a pipe 5 mm in diameter and 40 mm long.

To test the performance of the source, measurements of the beam intensity, its energy spread and its composition have been performed. For measuring the beam intensity a wire or a plate collector is mounted in the wall of the source chamber after the lens system and the X and Y deflectors. A grid is mounted between the deflector and collector to measure the energy distribution of the beam using the retarding method. The set-up to measure the energy spectra and composition of the beam is shown in Figure 4.
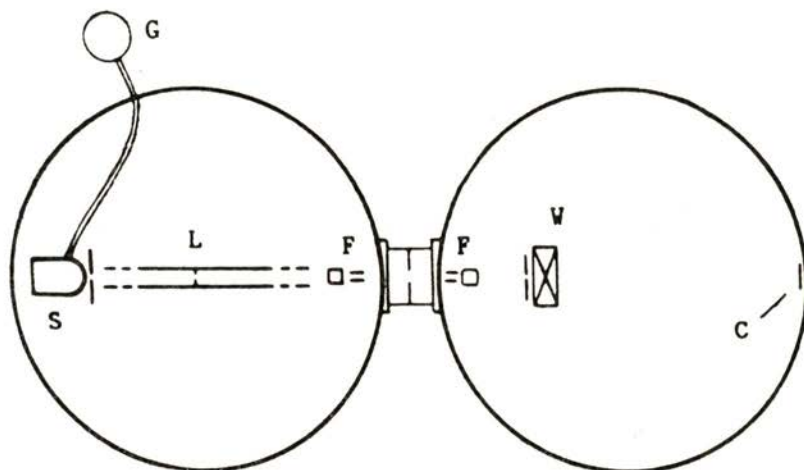
Fig. 4 — A schematic diagram of the test set-up to measure the energy spread and the composition of the beam, where S = ion source, G = gas bottle, L = lens system, F = deflectors, W = Wien filter and C = wire collector.

At the entrance of the second vacuum chamber there is another pair of X and Y deflectors. A wire collector is mounted at the other side of this chamber. A Wien filter behind a 1 mm diaphagm is placed near the deflectors.

3 — MEASUREMENT OF THE ION BEAM CURRENT

There are several factors which can influence the ion beam current (I), such as the emission of the filament, the electron energy, the extractor voltage, the repeller voltage and the voltages on the lens system. In order to make the best choice for those parameters, the dependence of I on the above-mentioned factors has been measured.

Fig. 5 shows the dependence of I on the emission. According to equation (1) I is proportional to emission. The small deviation of the curve from a straight line may be due to effects of the
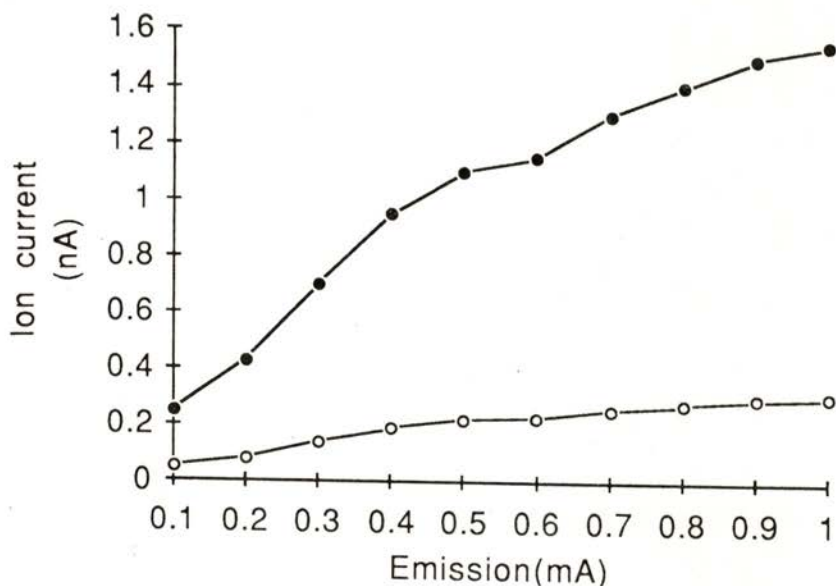
Fig. 5 — The ion current as a function of the emission; $p(O_2) = 5.10^{-6}$ torr, $V_e = 60$ V, $V_{ext} = 100$ V, $V_{rep} = 0$ V (open dots) or 20 V (filled dots).

change of the shape of the electron beam with emission, but the source can be operated at all emission values. So the choice of the operating value of the emission is limited by the lifetime of the filament. The suggested emission value is 0.5 to 2.0 mA. The current measured on the collector is about 0.1 of the emission current, which may be due to the fact that most electrons are not entering the ionization chamber at all.

Portgal. Phys. — Vol. 17, fasc. 3-4, pp. 215-237, 1986

223

Fig. 6 shows the dependence of I on the repeller voltage (V_{rep}). The decrease of I at the beginning of the curve can be explained as follows. When a positive voltage is added on the
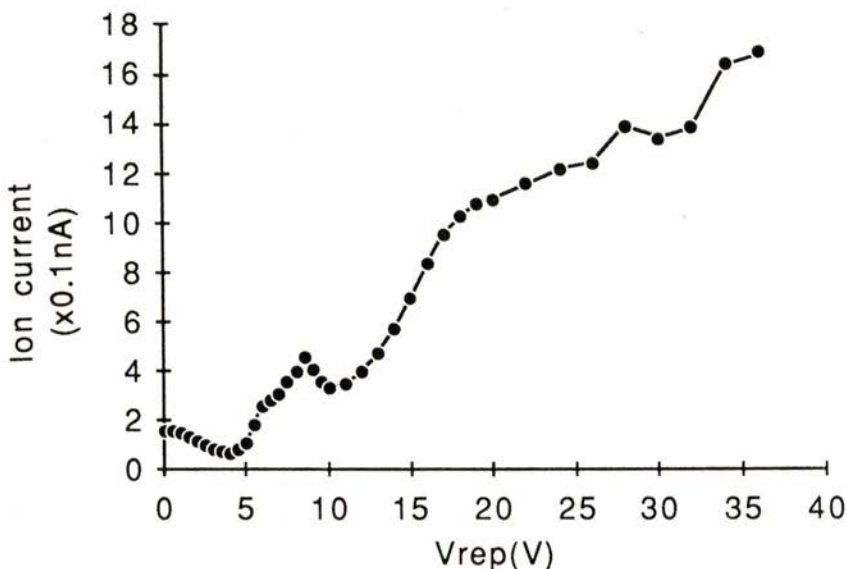
Fig. 6 — The ion current as a function of the repeller voltage; $p(O_2) = 3.10^{-6}$ torr, Emission $= 0.5$ mA, $V_e = 60$ V, $V_{ext} = 100$ V.

repeller, it attracts electrons, which decreases the electrons beam intensity. At low V_{rep} the effect of attracting electrons is larger than the effect of repelling ions. When choosing V_{rep} its influence on the energy spread of the ion beam should be taken into acount. This will be discussed in section 4.

Fig. 7 shows the dependence of I on the extraction voltage V_{ext}. Above a threshold, I increases proportionally to V_{ext}. When the extractor voltage is lower than the threshold, I will almost be zero. So it is not possible to get an ion beam with energy lower than 20 eV. Of course, the choice of V_{ext} is determined by the required ion beam energy. By using a Heddle lens system [12] it is possible to increase the energy range of operation considerably.

Fig. 8 shows the dependence of I on V_e. Its shape is similar to the results published earlier [11].
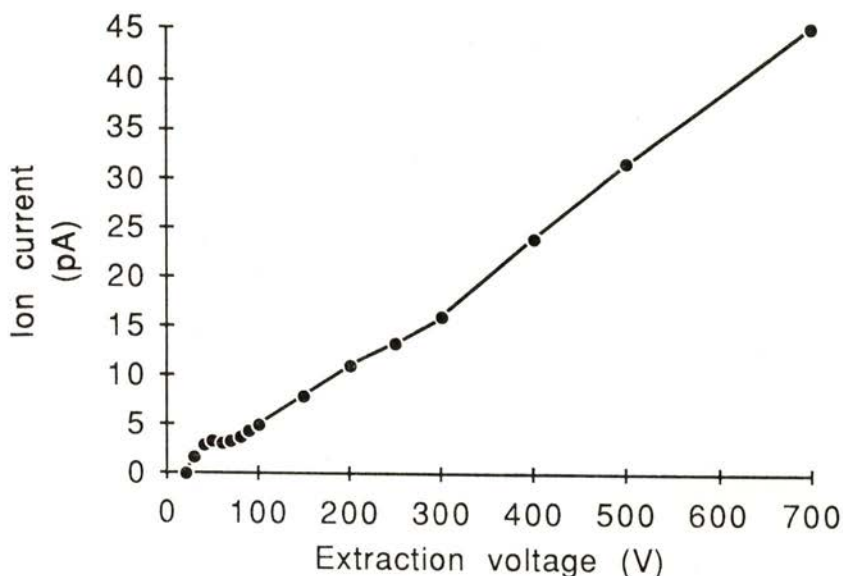
Fig. 7 — The ion current as a function of the extraction voltage; p (O_2) = 3.10⁻⁶ torr, Emission = 0.2 mA, V_{rep} = 0 V, no voltages applied on the lens system.
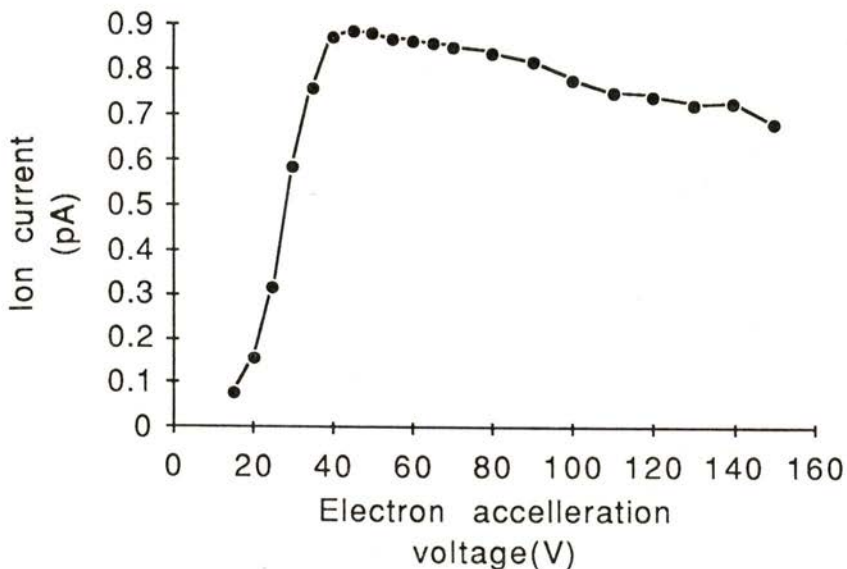
Fig. 8 — The ion current as a function of the electron acceleration voltage; p (O_2) = 3.10⁻⁶ torr, Emission ≃ 0.2 mA (the emission was adjusted for each point), V_{ext} = 100 V, V_{rep} = 0.07 V.

4 — MEASUREMENT OF THE ENERGY SPREAD
OF THE ION BEAM

In experiments to study the dynamics of surface scattering a small energy spread of the ion beam is required. We used a retarding method to measure the energy spread. A grid is mounted at the end of the lens system. Behind the grid is a collector which is a wire of 0.5 mm diameter or a plate. The measured (integral) curves and the differentiated curves (directly showing the energy distribution) are presented in Fig. 9. The measurements are performed with focussing plate voltages $V_{p1} = V_{p2} = 0$. With a plate collector the energy spread is about 0.015 when $V_{rep} = 0$ V and about 0.029 when $V_{rep} = 15$ V. Another characteristic of these curves is that they all have a small peak at an energy lower than the main peak. The origin of this peak is not clear. Energy spectra of the beam have been measured using the energy analyser in the UHV chamber. Due to its worse resolution (0.1) the effects seen in Fig. 9 have not been confirmed (see also Fig. 13).

An appreciable repeller voltage can obviously increase the spread in beam energy. If $V_{rep} = 0$ V every point in the ionization chamber has equal potential. In addition, in the ionizing collisions the ions hardly can get any momentum from the electrons due to the large mass difference. Consequently, we can get a very small energy spread of the ion beam. But if V_{rep} is not zero, there will be a potential distribution between the repeller and the exit of the ionization chamber. Then, the ions extracted from different points inside the chamber will have different energy, which causes an increase of the energy spread.

5 — MEASUREMENT OF THE RATIO $O^+ / (O_2^+ + O^+)$
USING A WIEN FILTER

A Wien filter is a velocity selector for an ion beam [13]. It consists of an electric field E, and a magnetic field B, perpendicular to each other. An ion moving in a direction perpendicular to both fields experiences an electric and a magnetic force, which balance when the velocity is $v = E/B$; ions with this velocity pass through the Wien filter without deflection. Ions with a different velocity will be deflected. By fixing B and scanning E, a velocity spectrum can be obtained. The velocity resolution depends on the magnitude
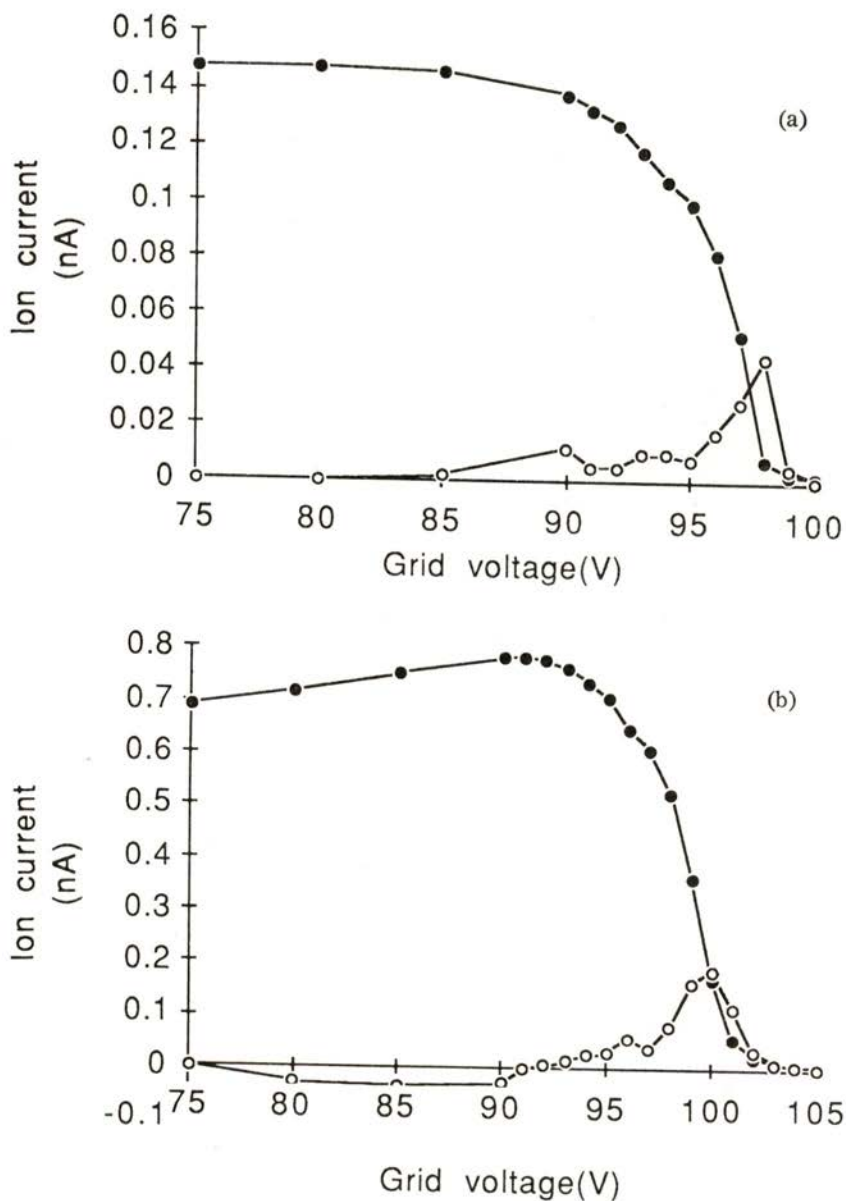
Fig. 9 — The ion current as a function of the retarding grid voltage (filled dots), measured using a plate collector and different repeller voltages; the differentiated curves (open dots) give the energy spread of the beam. $p(O_2) = 3.10^{-6}$ torr, Emission $= 0.5$ mA, $V_e = 60$ V, $V_{ext} = 100$ V, $V_{rep} = 0$ V (a) or $V_{rep} = 15$ V (b).

Portgal. Phys. — Vol. 17, fasc. 3-4, pp. 215-237, 1986

227

of E and B, the length of the Wien filter, the diameter of the diaphragm which is in front of the Wien filter, the size of the beam collector and the distance between the Wien filter and the beam collector.

Figure 10 shows the velocity spectra of O_2^+ and O^+ as a function of the voltage generating the electric field. Figures 11 and 12 show some velocity spectra of He^+, Ar^+ and Ar^{++}. The velocity spectra of He^+, Ar^+ and Ar^{++} are measured to calibrate the velocity or mass scale. Table 1 presents the mass assignment of the species associated with the peaks in figures 10-12, according to I_B, V_E, and beam energy, E_i. I_B is the current in the coil generating the magnetic field, V_E is the voltage associated with the electric field and v is the velocity of the ions, which is proportional to V_E / I_B, ($E_i = 200$ eV). The mass M is proportional to $E_i V^{-2}$ or $E_i (V_E / I_B)^{-2}$. Using the calibration by He^+ and Ar^+ we obtain the mass of the main peak in Fig. 10. It is about 32, which means that the beam consists of O_2^+.

The O^+ fraction is determined by V_e in the ionization process. Table 2 shows the ratio $O^+ / (O_2^+ + O^+)$ which is cal-
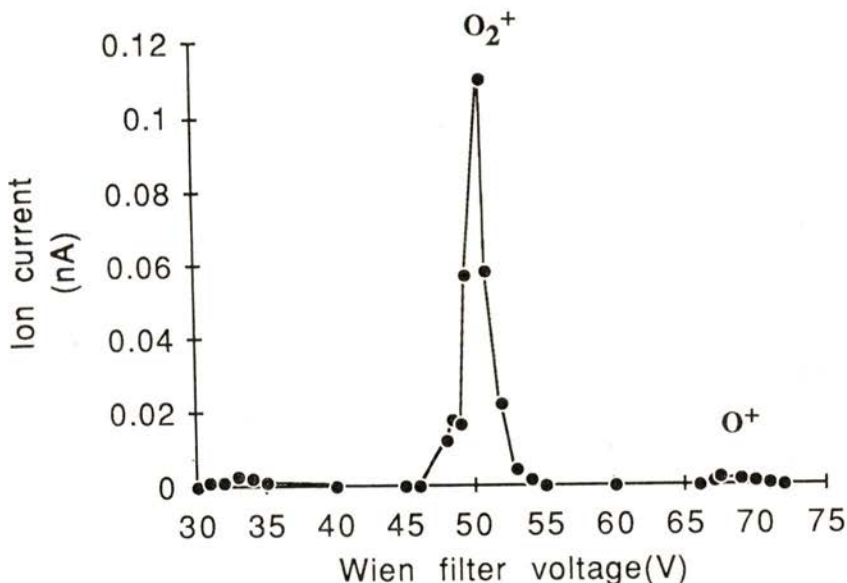
Fig. 10 — Velocity spectra of oxygen as a function of the Wien filter voltage, when a wire collector is used; $p(O_2) = 6.10^{-6}$ torr, $V_e = 50$ V, $V_{ext} = 200$ V, $V_{rep} = 0$ V, $I_B = 1.5$ A.
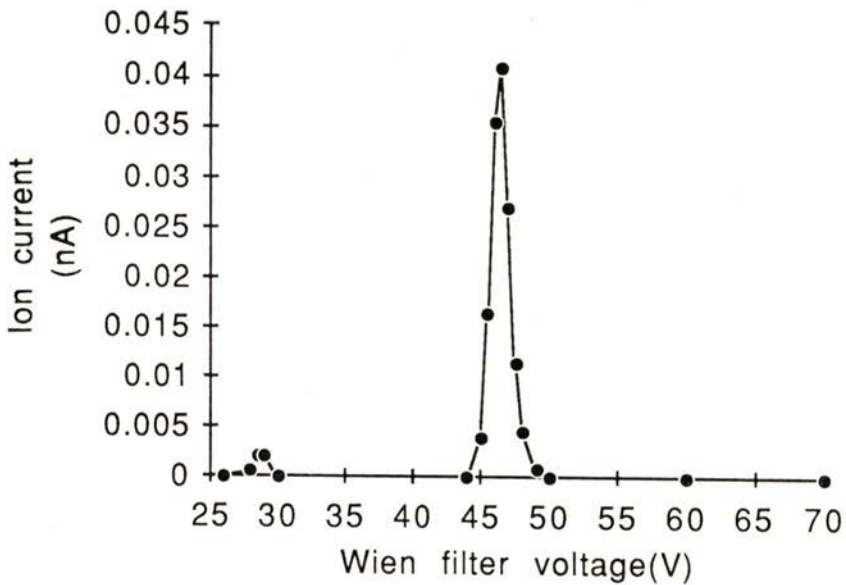
Fig. 11 — Velocity spectrum of helium as a function of the Wien filter voltage, when a wire collector is used; p (He) = 7.10⁻⁶ torr, $V_e = 60$ V, $V_{ext} = 200$ V, $V_{rep} = 0$ V, $I_B = 0.5$ A.
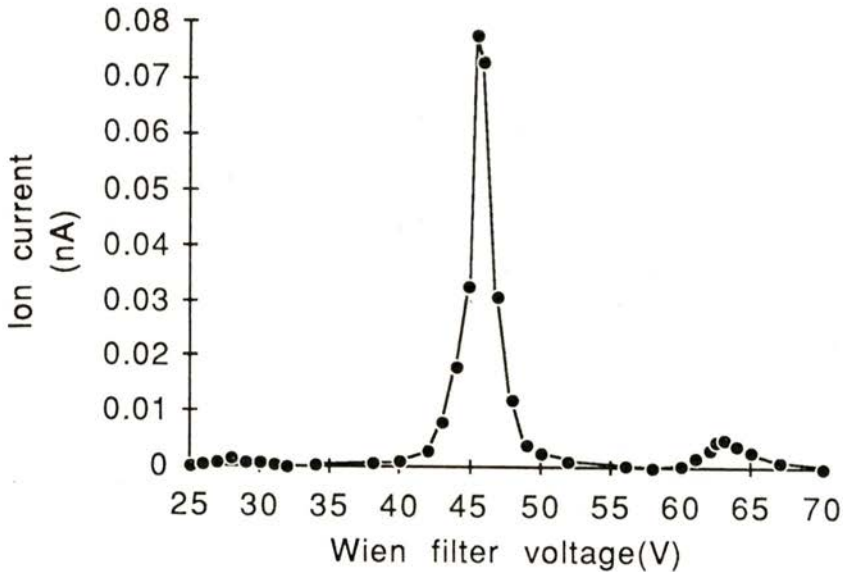
Fig. 12 — Velocity spectrum of argon as a function of the Wien filter voltage, when a wire collector is used; p (Ar) = 6.10⁻⁶ torr, $V_e = 60$ V, $V_{ext} = 200$ V, $V_{rep} = 0$ V, $I_B = 1.5$ A.

culated from the velocity spectra of O_2^+ and O^+ at several V_e values. Near each O_2^+ or O^+ peak there is a small shoulder at slightly lower velocity, visible in Fig. 10. This corresponds to the

TABLE 1 — The assignment of the mass M for the peaks in Figures 10-12

I_B (A)	V_E (V)	V_E / I_B ($\propto v$)	Energy/v^2 ($\propto M$)	Assignment of M
0.50	46.5	93.0	0.023	4 (H_e^+)
1.50	45.5	30.3	0.22	40 (Ar^+)
1.50	63.0	42.0	0.11	40 (Ar^{++})
1.50	50.2	33.5	0.18	32 (O_2^+)
1.50	69.0	46.0	0.09	16 (O^+)

TABLE 2 — The O^+ fraction in the oxygen beam for different values of the electron energy

V_e (V)	20	30	40	50	60	80
$O^+ / (O_2^+ + O^+)$ (%)	0	0.78	0.84	1.55	2.36	9.8

small peak in the energy spectra in Fig. 9. The origin of these small peaks is not known. The origin of the peaks at much lower E, around 30 V, may be due to hydrocarbon contaminants.

6 – APPLICATION OF THE SOURCE IN SURFACE SCATTERING EXPERIMENTS

After the experiments described, the source was aimed at a Ag (111) crystal in the UHV chamber of the MOBI apparatus, as shown in Fig. 1. Because of space limitations, the Wien filter, which was not really necessary for O_2^+ beams, has not been used.

Operating conditions of the source for 100, 200, 300 and 400 eV O_2^+ beams are listed in Table 3. The energy spectra of the beam, directly measured by the 90° cylindrical electrostatic energy analyser in the UHV chamber, are shown in Fig. 13. The width

Table 3 — Operating conditions for the O_2^+ beam used in the experiments

E_i (eV)	V_e (V)	V_{ext} (V)	V_2 (V)	V_4 (V)	V_{p1} (V)	V_{p2} (V)	emission (mA)	P_1 (10^{-6} torr)	P_2 (10^{-9} mbar)	I (10^{-9} A)
100	40	100	98	65	50	46	1.9	5	4	.15
200	40	200	196	122	79	72	2	5	4	.65
300	40	300	277	161	145	135	1	4.6	4	1
400	40	400	359	211	323	321	1	5	4	.8
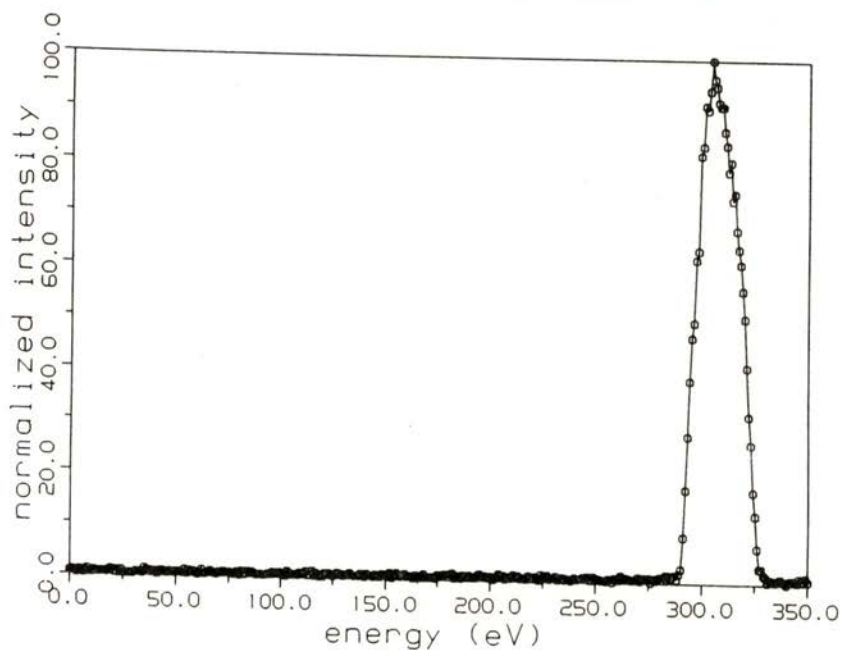
Fig. 13 — A measurement of the energy spectrum of the oxygen beam of 300 eV measured directly by the 90° cylindrical electrostatic energy analyser in the UHV chamber.

of the peak is determined by the resolution of the energy analyser ($\delta E/E \doteq 0.1$), and is much larger than seen in Fig. 9.

In $O_2^+ - Ag(111)$ surface scattering experiments, scattered ions could get negatively charged [6]. A typical energy spectrum of negative ions (O_2^- and O^-) after specular scattering of 300 eV O_2^+ from Ag(111) at an angle of incidence of 70 degrees with respect to the surface normal is shown in Fig. 14. The peak at
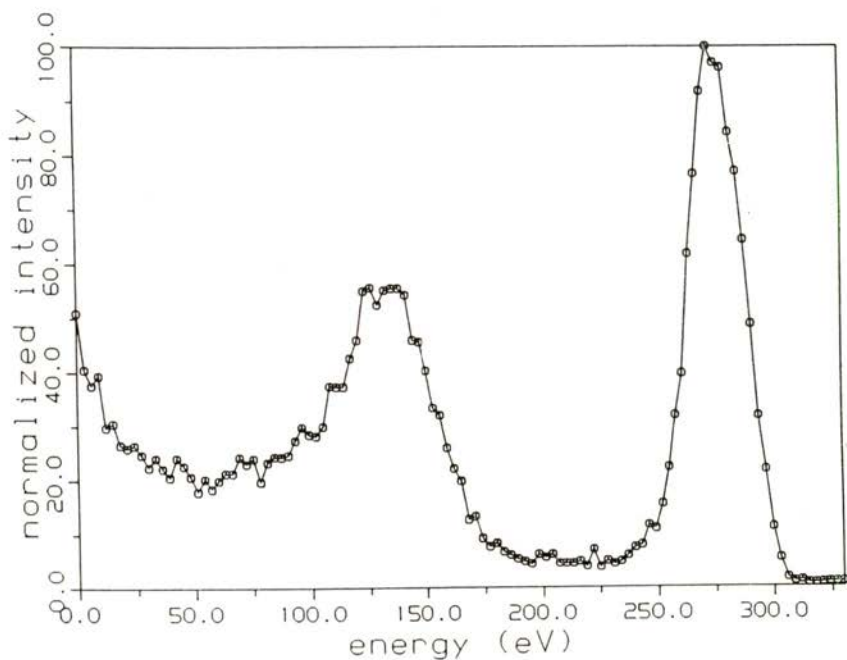
Fig. 14 — A typical energy spectrum of negative ions (O_2^- and O^-) after scattering of 300 eV O_2^+ from Ag(111), when the angles of incidence and detection (with respect to the surface normal) are both equal to 70 degrees.

275 eV is assumed to be O_2^- since it corresponds to an oxygen molecule having roughly lost the energy corresponding to two binary collisions with silver atoms as a consequence of the glancing incidence. The peak at half this energy is correspondingly due to O^-, carrying about half of the energy of the molecule [14].

Scanning the azimuth of the crystal over 360° shows a very nice symmetry corresponding to the hexagonal structure of the unit cell of Ag (111). This azimuthal dependence of O_2^- peak is shown in Fig. 15. The symmetry of this spectrum nicely shows that the crystal has been prepared properly, and turned out to be much more sensitive to the quality of the crystal surface than low energy electron diffraction (LEED).
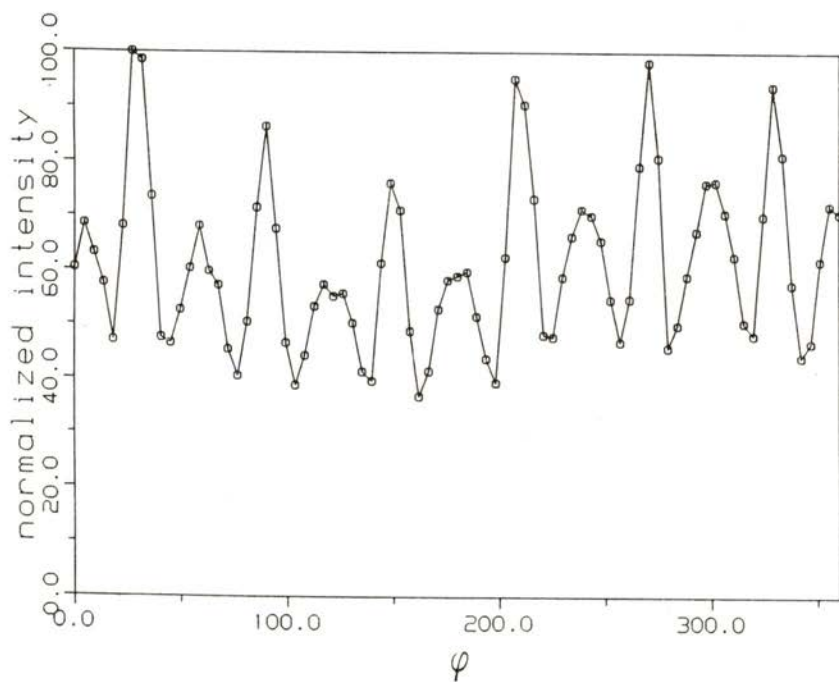
Fig. 15 — The azimuthal dependence of the O_2^- peak from the scattering as measured in fig. 14.

The O_2^+ beam seems pure because of the low background measured between the O_2^- and O^- peaks. O_2 gas efficiently removes contamination from the source, whereas in case of, for example, Ne the beam may contain H_2O^+, hydrocarbon ions and oxide ions. So, for those species a Wien filter is necessary.

7 – HARPOONING TRANSITIONS

The result for scattering of a beam of O_2^+ with an energy of 300 eV from Ag (111) leading to negative ions is shown in Fig. 16. The angle of incidence Θ_i measured from the surface normal is 70°. The figure shows the angular and energy spectrum of the negative ions. Two peaks are visible, at 130 and 275 eV,
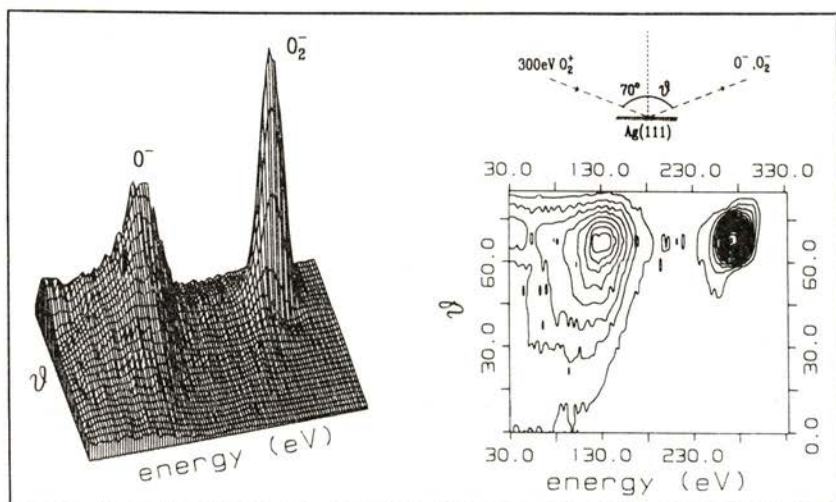
Fig. 16 — Intensity distribution for negative ions formed in glancing collisions ($\Theta_i = 70°$) of 300 eV O_2^+ ions with Ag (111). The measured intensity is plotted 3-dimensionally and in contour representation as a function of the final energy and polar scattering angle. The axes are identical for both representations. No correction for the energy dependent transmission of the energy analyser has been made. The inset shows the scattering geometry and the definition of the angles.

for the specular direction. These clearly can be identified with O^- and O_2^-, assuming that for scattered O^- each of the atoms carries half of the translational energy of the corresponding O_2^-. By varying the incident energy and Θ_i we find that the O^- yield seems to scale with the normal component of the impact velocity, and can exceed the O_2^- yield.

234

Portgal. Phys. — Vol. 17, fasc. 3-4, pp. 215-237, 1986

The count rates are an order of magnitude lower for positive than for negative ions. This large negative to positive ion ratio indicates that the probability for negative ion formation dominates and that negative ions are not formed at defect sites. A crude estimate shows that the total scattered negative ion yield is of the order of a few percent of the primary beam. The scattered neutrals could not be detected in our apparatus.

Three important events take place during the collision: 1) the neutralization of the positive ion, 2) the (hard) collision with the surface, 3) the attachment of a second electron. It seems likely that the first event occurs before the other two. For the first step resonant neutralization followed by Auger deexcitation and Auger neutralization are the most likely processes in view of the low beam energy. This would lead to neutralization into molecules in the ground state, which in turn leads to O_2^-. A subsequent event is the hard collision. The probability for impulsive energy transfer in this collision, leading to dissociation, seems small for specular scattering. However, classical trajectory calculations indicate that the dissociation of O_2^- observed in the figure can entirely be due to the collision with the surface. Calculations with an ab-initio potential show even more dissociation than observed experimentally [15]. This suggests that the most important step, i. e., the attachment of another electron to the molecular ion or atomic ions, proceeds more easily when molecular ions are the final product. It could be due to an orientational dependence of the charge transfer probabilities.

Having demonstrated that harpooning transitions occur for the O_2 / Ag (111) system, we now turn to the relevance of our observations to chemisorption. It is very likely that, for a slow O_2 molecule approaching the surface, the harpooning transition can take place along the way towards the surface, leading to chemisorption as O_2^-. A potential diagram suggested by Campbell indicates that the binding energy of O_2^- to Ag (111) is 0.3 eV [16]. The low sticking probability of O_2, in the order of 10^{-6}, indicates that the negative ion state is not accessible for thermal molecules, because of a barrier. Clearly the high translational and possibly also vibrational energy of the initial O_2^+ is sufficient to overcome this barrier, since the O_2^- relative yield is much larger than 10^{-6}. It also indicates that indeed the harpooning transition is responsible for the chemisorption of molecular oxygen on Ag surfaces. From

Portgal. Phys. — Vol. 17, fasc. 3-4, pp. 215-237, 1986

235

this we conclude that the importance of harpooning transitions in energy transfer processes at surfaces has been established experimentally and will add another dimension to these processes which traditionally are being thought of as collisions of hard spheres.

8 – CONCLUSION

The performance parameters of the O_2^+ ion source considered in this paper are the beam current and its current density, the energy and energy spread, the pressure in the source chamber and the lifetime of the filament. The source parameters we generally used are as follows: $V_e = 40$-50 V, resulting in $O^+ / (O_2^+ + O^+) \simeq 0.01$; the lifetime of the filament is a few tens of hours (it takes about 1 hour to change the filament); the beam current density is about $10^{-10} - 10^{-9}$ A/cm^2 at a distance of 100 cm.

Using this source, a significant contribution to the understanding of the dynamics of chemisorption of molecules at surfaces has been made, via the observation of so-called harpooning transitions.

REFERENCES

[1] D. R. Herschbach, *Adv. Chem. Phys.* **10** (1966), 319.
[2] A. W. Kleyn, J. Los and E. A. Gislason, *Phys. Repts.* **90** (1982), 1.
[3] A. M. C. Moutinho, *Portgal. Phys.* **15** (1984), 157;
     E. E. B. Cowan, M. A. D. Fluendy, A. M. C. Moutinho and A. J. F. Praxedes, *Mol. Phys.* **52** (1984), 1125.
[4] J. W. Gadzuk, *Comm. At. Mol. Phys.* **16** (1985), 219.
[5] C. Backx, C. P. M. de Groot and P. Biljoen, *Surf. Sci.* **104** (1981), 300;
     C. T. Campbell, *Surf. Sci.* **173** (1986), L641.

[6] Pan Haochang, T. C. M. Horn and A. W. Kleyn, *Phys. Rev. Letters* **57** (1986), 3035.

[7] A. D. Tenner, K. T. Gillen, T. C. M. Horn, J. Los and A. W. Kleyn, *Phys. Rev. Letters* **52** (1984), 2183; *Surf. Sci.* **172** (1986), 90.

[8] C. Brunnee and H. Voshage, *Massenspektrometrie* (Karl Thiemig, Muenchen, 1964).

[9] Robert G. Wilson and George R. Brewer, *Ion Beams With Application to Ion Implantation* (John Wiley and Sons, New York, 1973) Chap. 2.

[10] G. J. Schulz, *Rev. Mod. Phys.* **45** (1973), 423.

[11] A. Von Engel, *Ionized Gases* (Oxford University Press, London, 1965).

[12] D. W. O. Heddle, *J. Phys. E: Sci. Instr.* **4** (1971), 981.

[13] E. H. A. Granneman and M. J. van der Wiel, in: *Handbook on Synchroton Radiation*, ed. E. E. Koch (North-Holland, Amsterdam, 1983), p. 367.

[14] W. Heiland and E. Taglauer, in: *Methods of Experimental Physics*, vol. 22, chap. 6.

[15] P. J. van den Hoek, T. C. M. Horn and A. W. Kleyn, to be published in *Surf. Sci.*

[16] C. T. Campbell, *Surf. Sci.* **157** (1985), 43.

CONTENTS

FASCÍCULO 1-2

CONTENTS

FASCÍCULO 3-4

AUTHOR INDEX

PORTUGALIAE PHYSICA publishes articles or research notes with original results in theoretical, experimental or applied physics; invited review articles may also be included.

Manuscripts, with an abstract, may be written in English or French; they should be typewritten with two spaces and in duplicate. Figures or photographs must be presented in separate sheets and be suitable for reproduction with eventual reduction in size; captions should make the figures intelligible without reference to the text. Authors are requested to comply with the accepted codes concerning references.

There is no page charge. Author(s) will get 50 free reprints (without covers); these are to be shared among all the authors of the article. Authors interested in more reprints should say so when sending their manuscripts; quotations shall be sent with the proofs.

Subscription rates for volume 17:

3.600 Escudos (US$24) — individuals
9.000 Escudos (US$60) — libraries

PORTUGALIAE PHYSICA may also be sent on an exchange basis; we wellcome all suggestions to such effect.

All mail to be addressed to

PORTUGALIAE PHYSICA

C/O LABORATÓRIO DE FÍSICA, FACULDADE DE CIÊNCIAS
PRAÇA GOMES TEIXEIRA
4000 PORTO PORTUGAL

PORTUGALIAE PHYSICA

VOL. 17 · NUMB 3/4 · 1986

CONTENTS